universität wien

DISSERTATION / DOCTORAL THESIS

Titel der Dissertation/ Title of the Doctoral Thesis

"Probes of sub-GeV Dark Sector Physics – Two Showcases"

verfasst von/ submitted by

Jui-Lin Kuo

angestrebter akademischer Grad/in partial fulfilment of the requirements for the degree of

Doktor der Naturwissenschaften (Dr. rer. nat.)

Wien, 2021/ Vienna, 2021

Studienkennzahl lt. Studienblatt/ degree programme code as it appears on the student record sheet:	UA 796 605 411
Dissertationsgebiet lt. Studienblatt/ field of study as it appears on the student record sheet:	Physik
Betreut von / Supervisor:	Dr. Josef Pradler
	Univ.-Prof. Dr. André Hoang

Statement of the thesis advisor

I hereby confirm that Jui-Lin Kuo has contributed substantially to the following four publications, which are part of his thesis:

[1] X. Chu, J.-L. Kuo, J. Pradler and L. Semmelrock, *Stellar probes of dark sector-photon interactions*, Phys. Rev. D100 (2019) no. 8, 083002, arXiv:1908.00553 [hep-ph]

[2] X. Chu, J.-L. Kuo and J. Pradler, *Dark sector-photon interactions in proton-beam experiments*, Phys. Rev. D101 (2020) no. 7, 075035, arXiv:2001.06042 [hep-ph]

[3] C. Bœhm, X. Chu, J.-L. Kuo and J. Pradler, *Scalar Dark Matter Candidates - Revisited*, Phys. Rev. D103 (2021) no. 7, 075005, arXiv:2010.02954 [hep-ph]

[4] J.-L. Kuo, M. Pospelov and J. Pradler, *Terrestrial Probes of Electromagnetically Interacting Dark Radiation*, Phys. Rev. D (submitted), arXiv:2102.08409 [hep-ph]

According to the common practice in particle physics, the authors are listed in alphabetical order.

Dr. Josef Pradler

Acknowledgements

First of all, I would like to express my special gratitude to my research supervisor Josef Pradler, not only for guiding me to become a good physicist but also for his kind support and help during my Ph.D. study. His door is always open for me to ask questions when I cannot figure out the next move, no matter how trivial or strange they may be. I truly enjoy the collaboration with him and all the inspiring discussions that we had. I would also like to thank André Hoang at the University of Vienna for being my corresponding official supervisor for my thesis and his help on the administration.

I am thankful for the colleges at the Institute of High Energy Physics and from the DK-PI doctoral program, who create a vibrant environment for performing research. Among them, I am most indebted to Xiaoyong Chu, who is not only a senior researcher to me but also a great friend of mine. He is always there for me when I feel down either by the academy life or daily life (I would say 24/7), and patiently offers handy advice and solutions toward my numerous concerns and questions. I certainly learn a lot from the daily discussion about physics with him and his discerning insights into the research.

For all the interesting conversation and their help in taking courses and translating German documents, which makes my life in a foreign country a lot easier and more fun, I would also like to thank my officemates, Lukas Semmelrock, Marko Nikolic, Gerhard Ungersbäck, Lukas Matzi, Alicia Wongel, and other students that I met in the institute and university, Priya Hussain, Janik Andrejkovic, Sebastian Templ and Jan Lüdtke.

During my Ph.D. study, I am grateful to work with Yue-Lin Sming Tsai, Wei-Chih Huang, Céline Bœhm and Maxim Pospelov in addition to my local collaboration. I would like to thank them for bringing me into different research areas and their countless great research ideas. In addition, I would like to thank my academic referees, Kingman Cheung and José W. F. Valle, for their strong support during my postdoc application.

I want to thank Yumin Su, for all the encouragement and companion toward completing this thesis. Finally, I want to sincerely thank my family, especially my parents, for encouraging me to do things that I enjoy, for their unconditional support all along, and for always reminding

me to be happy. They always tell me that, no matter what happens, I can go home any time I want, which makes me at ease whenever I encounter any obstacle during my Ph.D. study.

To myself and the memory of Wang-Shih Huang-Lin.

Abstract

Besides the visible and known sectors of particles and interactions described by the Standard Model, it is possible that there exists a dark sector of light, sub-GeV particles attributable to dark matter. A rich phenomenology can be expected in laboratories, astrophysics and cosmology, when visible and dark sectors are connected. In this thesis, we scrutinize two dark sector scenarios. First, we study a so-called vector-portal model, in which fermionic dark states carry electromagnetic form factors and thus can interact with the photon. Second, we then focus on a fermion-portal model containing a scalar dark matter candidate coupled to Standard Model leptons via a new heavy fermion. The latter model has been entertained to explain the long-standing INTEGRAL 511 keV excess and the muon $g-2$ anomaly. With detailed derivations of the current and future experimental sensitivity, we constrain the coupling strengths between the visible sector and dark sectors through a large number of probes. Concretely we consider collider and fixed-target/beam-dump experiments, Standard Model precision observables, direct/indirect detection, astrophysical/cosmological implications such as the stellar energy loss and extra relativistic degrees of freedom in the early universe. The combination of these results establish that 1) sub-GeV dark sector particles can only have feeble electromagnetic form factor interactions, and 2) the parameter space of the fermion-portal model for explaining the two mentioned anomalies is ruled out. In the bigger scheme of things, we develop a detailed framework to study light (sub-GeV) dark sectors, demonstrated with two minimal extensions of the Standard Model. Such a framework may be readily adjusted to accommodate more complicated dark sectors.

Zusammenfassung

Neben dem sichtbaren und bekannten Teilchensektors des Standardmodells ist es möglich, dass der dunkle Materie Sektor aus leichten Teilchen, mit sub-GeV Massen, existiert. Wenn beide Sektoren miteinander wechselwirken, ist damit eine reichhaltige Phänomenologie im Labor, in der Astrophysik und in der Kosmologie zu erwarten. In dieser Arbeit untersuchen wir zwei Szenarien des dunklen Sektors: Zunächst betrachten wir ein sogenanntes Vektorportal-Modell, bei dem fermionische neue Teilchen mit dem Photon über elektromagnetische Formfaktoren interagieren. Zweitens konzentrieren wir uns dann auf ein Fermion-Portal-Modell, das einen skalaren dunkle Materie Kandidaten enthält, der über neue schwere Fermionen an Standardmodell-Leptonen gekoppelt ist. Das letztere Modell wurde in der Vergangenheit herangezogen, um den INTEGRAL 511 keV Photonenfluss aus den zentralen Regionen der Milchstraße, sowie die Myon $g-2$ Anomalie, zu erklären. Mittels detaillierten Herleitungen der aktuellen und zukünftigen experimentellen Sensitivität setzen wir in einer Vielzahl an teilchenphysikalischen Tests (zu erwartende) Schranken an die Kopplungsstärken zwischen dem sichtbaren und dunklen Sektor. Konkret betrachten wir Beschleuniger- sowie sog. Fixed-Target- und Beam-Dump-Experimente, Präzisions-Observablen des Standardmodells, direkte/indirekte Detektion, astrophysikalische/kosmologische Konsequenzen wie anomaler Energieverlust im Inneren von Sternen und zusätzliche relativistische Freiheitsgrade im frühen Universum. Die Kombination dieser Ergebnisse zeigt, dass 1) sub-GeV-Teilchen des dunklen Sektors nur äußerst schwache Wechselwirkungen mit elektromagnetischen Formfaktoren aufweisen können und 2) der Parameterraum des Fermion-Portal-Modells zur Erklärung der beiden genannten Anomalien ausgeschlossen ist. Anhand der zwei Szenarien—die minimalen Erweiterungen des Standardmodells entsprechen—wird damit ein detailliertes Framework zur Untersuchung von leichten (sub-GeV) dunklen Sektoren entwickelt. Dieses ist leicht anpassbar, um komplizierte dunkle Sektoren zu untersuchen.

Summary

This thesis entertains the possibility of light, sub-GeV mass dark sectors beyond the Standard Model and scrutinizes their phenomenology in terrestrial experiments, in astrophysical environments, and in cosmology. We present in detail the calculation of relevant interaction processes in various probes and derive constraints or forecasts of sensitivity on the dark sector parameter space. The results presented in this thesis have been published in [P1–P4], listed on the next page.

The thesis is organised as follows:

Chapter 1: we start with a brief introduction into the Standard Model for particle physics and standard cosmology, followed by motivation and historical development for the renewed interest in light dark sector physics. An overview of experiments and environments that we investigate in this thesis is also given.

Part I: in this part, we study the *photon portal*. It purports, that the Standard Model photon connects the dark sector and the observable sector, by dark sector particles χ carrying electromagnetic form factors, such as a millicharge or magnetic/electric dipole moment. In Chap. 2, we introduce the Lagrangians describing the possible interactions between χ and the photon as well as their possible origins. We then study three scenarios in which these electromagnetic interactions can manifest themselves: in Chap. 3, we compute the production of χ in stellar environments in great detail, taking into finite-temperature effects and examining potential double countings between various processes. These dark states, if escaping from the stellar interiors, can result in additional energy loss. The non-observation of these anomalous energy sinks gives us leverage to constrain the dark sector physics. In Chap. 4, we test the photon portal against the data from proton-beam experiments, in which χ may be produced from the Drell-Yan processes and meson decays, and detected via electron recoil or hadronic shower events. Finally, in Chap. 5, the case that χ plays the role of "dark radiation" sourced through the decay of long-lived dark matter is studied. We investigate the sensitivity of direct detection and large-volume neutrino experiments to this dark radiation, through the electron or nuclear recoils it causes. In addition, the relativistic description of scattering between dark sector particles and SM particles is derived.

Part II: we revisit a dark sector model comprised of a sub-GeV leptophilic scalar dark matter particle ϕ and a mediator that couples ϕ to Standard Model particles, either a heavy fermion F or a new gauge boson Z'. This model has become quite popular about two decades ago for successfully addressing the 511 keV line observed at the center of the Milky Way, explaining the muon $g-2$ anomaly, and achieving the correct dark matter relic density. In light of much experimental and observational advances, we revisit this possibility and subject the models to a multitude of new probes. The particle model, together with the above hints/anomalies are discussed in Chap. 6. Subsequently, we demonstrate that intensity frontier experiments,

Standard Model precision tests and LEP (Chap. 7), as well as astrophysical and cosmological observables (Chap. 8), by now completely exclude the favored parameter space for the above hints. A summary of Part II is given in Chap. 9.

Chapter 10 summarizes the main results of this thesis and discuss future perspectives for probing the dark sector physics possibilities.

The Appendix provides further details on the calculations that are applied in different parts of this thesis. In App. A, we derive the three- and four-body phase space. The formulas for squared amplitudes, decay rates and cross sections of various processes are given in App. B and App. C, corresponding to the particle models considered in Part I and Part II, respectively.

Published references, part of this thesis:

[P1] X. Chu, J.-L. Kuo, J. Pradler and L. Semmelrock, *Stellar probes of dark sector-photon interactions*, Phys. Rev. D100 (2019) no. 8, 083002, arXiv:1908.00553 [hep-ph]

[P2] X. Chu, J.-L. Kuo and J. Pradler, *Dark sector-photon interactions in proton-beam experiments*, Phys. Rev. D101 (2020) no. 7, 075035, arXiv:2001.06042 [hep-ph]

[P3] C. Bœhm, X. Chu, J.-L. Kuo and J. Pradler, *Scalar Dark Matter Candidates - Revisited*, Phys. Rev. D103 (2021) no. 7, 075005, arXiv:2010.02954 [hep-ph]

[P4] J.-L. Kuo, M. Pospelov and J. Pradler, *Terrestrial Probes of Electromagnetically Interacting Dark Radiation*, Phys. Rev. D (submitted), arXiv:2102.08409 [hep-ph]

Contents

List of Figures

List of Tables

CHAPTER 1

Introduction

1.1 The Standard Model of particle physics and beyond

1.1.1 The Standard Model

From the atom to the sub-atomic particles such as the nucleus, to the nucleons, and to the, so far considered, elementary particles: quarks and leptons. The journey of pursuing the most fundamental physical description of known phenomena never stops. During this journey, we transit from "classical" physics with determinism to "quantum" physics with an inherent probabilistic description. Moreover, absolute Newtonian dynamics is superseded by special and general relativity for the description of space-time. With a few decades of effort, the combination of quantum mechanics and special relativity gives rise to quantum field theory (QFT). Based on QFT, the Standard Model (SM) [5] is, currently, accepted as the most fundamental framework in describing interactions of elementary particles.

The SM is comprised of fermions (quarks and leptons), gauge bosons, the Higgs boson, and their interactions governed by the gauge symmetry $\mathrm{SU}(3)_C \times \mathrm{SU}(2)_L \times \mathrm{U}(1)_Y$; the subscripts C, L and Y stands for color, left-handed and hypercharge, respectively. The three gauge groups[1] correspond to three fundamental interactions: the strong force described by quantum chromodynamics (QCD), electroweak (EW) theory, and quantum electrodynamics (QED), respectively. See Tab. 1.1 for an overview of the SM particle content and the corresponding assignment of electroweak charge, *i.e.*, the weak isospin T_3, hypercharge Y and the electric charge $Q_{\mathrm{EM}} \equiv T_3 + Y$ after EW symmetry breaking (EWSB)[2]. Note that only quarks and gluons are charged under $\mathrm{SU}(3)_C$ and transform in its fundamental representation. All particles in SM are massless initially, as the gauge symmetry forbids a mass term. However, the spontaneous breaking of the EW symmetry $\mathrm{SU}(2)_L \times \mathrm{U}(1)_Y \to \mathrm{U}(1)_{\mathrm{EM}}$ sources the vacuum expectation value (VEV) of the Higgs boson. Other particles can, therefore, obtain a mass through the *Higgs mechansim* [8–10]. In the following, we briefly discuss the SM Lagrangian before and after EWSB.

[1] The SM is gauge-anomaly free [6, 7].

[2] Note that there is alternative definition $Q_{\mathrm{EM}} \equiv T_3 + Y/2$ in the literature.

Before EWSB, the SM Lagrangian reads

$$\mathcal{L}_{\rm SM} = \mathcal{L}_{\rm QCD} + \mathcal{L}_{\rm EW} + \mathcal{L}_{\rm Higgs} + \mathcal{L}_{\rm Yukawa}\,. \tag{1.1}$$

The QCD Lagrangian can be written as

$$\mathcal{L}_{\rm QCD} = -\frac{1}{4}G^a_{\mu\nu}G^{\mu\nu}_a + \sum_q i\bar{\psi}_i\gamma^\mu\left(\partial_\mu\delta_{ij} - ig_s G^a_\mu\lambda^a_{ij}\right)\psi_j\,, \tag{1.2}$$

where G^a_μ is the 8-component $\mathrm{SU}(3)_C$ gluon field ($a = 1, \cdots, 8$), $G^a_{\mu\nu} = \partial_\mu G^a_\nu - \partial_\nu G^a_\mu + g_s f^{abc} G^b_\mu G^c_\nu$ is the gluon field strength tensor with the $\mathrm{SU}(3)_C$ coupling constant g_s and structure constants f^{abc}, ψ is the Dirac spinor for quark fields, (i, j) are color indices, γ^μ are the Dirac matrices, and λ^a_{ij} are the Gell-Mann matrices, respectively. The Lagrangian for the EW theory, $\mathcal{L}_{\rm EW}$, is

$$\mathcal{L}_{\rm EW} = -\frac{1}{4}W^b_{\mu\nu}W^{\mu\nu}_b - \frac{1}{4}B^{\mu\nu}B_{\mu\nu} + \sum_{q,l} i\bar{\psi}\gamma^\mu\left(\partial_\mu - ig\vec{\tau}\cdot\vec{W}_\mu - ig'YB_\mu\right)\psi\,, \tag{1.3}$$

where $\vec{W}_\mu$ and B_μ are 3-component $\mathrm{SU}(2)_L$ and $\mathrm{U}(1)_Y$ gauge fields with field strength tensors $W^b_{\mu\nu}$ ($b = 1, 2, 3$) and $B_{\mu\nu}$, $\vec{\tau} = \vec{\sigma}/2$ with $\vec{\sigma}$ being a vector of Pauli matrices, g is the $\mathrm{SU}(2)_L$ gauge coupling, and g' is the $\mathrm{U}(1)_Y$ gauge coupling. With the $\mathrm{SU}(2)_L$ Higgs doublet $\phi^T = (\phi^+, \phi^0)/\sqrt{2}$, the Lagrangian for the Higgs sector reads

$$\mathcal{L}_{\rm Higgs} = \left|\left(\partial_\mu - ig\vec{\tau}\cdot\vec{W}_\mu - ig'YB_\mu\right)\phi\right|^2 + \mu_H^2\phi^\dagger\phi - \lambda(\phi^\dagger\phi)^2\,. \tag{1.4}$$

The quadratic μ_H^2 and quartic λ are both positive making the ground state $\langle\phi^0\rangle = v/\sqrt{2}$ with $v \equiv |\mu_H|/\sqrt{\lambda}$ break the $\mathrm{SU}(2)_L$ symmetry. The Yukawa interactions between Higgs boson and fermions are described by

$$\mathcal{L}_{\rm Yukawa} = -Y^d_{ij}\bar{Q}^i\begin{pmatrix}\phi^+\\ \phi^0\end{pmatrix}d^j_R - Y^u_{ij}\bar{Q}^i\begin{pmatrix}\phi^{0*}\\ \phi^-\end{pmatrix}u^j_R - Y^l_{ij}\bar{L}^i\begin{pmatrix}\phi^+\\ \phi^0\end{pmatrix}e^j_R + h.c.\,, \tag{1.5}$$

with $Y^{d,u,l}_{ij}$ being the 3×3 Yukawa matrices of up-type quarks, down-type quarks and charged leptons.

Below the EW scale, we can parameterize the Higgs doublet in unitary gauge as

$$\phi = \frac{1}{\sqrt{2}}\begin{pmatrix}0\\ v+H\end{pmatrix}\,, \tag{1.6}$$

where H is the Higgs field. Replacing ϕ with Eq. (1.6) and diagonalizing the mass matrix of gauge bosons, the Higgs Lagrangian after EWSB $\mathcal{L}^{\not{\rm EW}}_{\rm Higgs}$ takes the form:

$$\mathcal{L}^{\not{\rm EW}}_{\rm Higgs} = \frac{1}{2}\partial_\mu H\partial^\mu H + (v+H)^2\left(\frac{g^2}{4}W^b_\mu W^\mu_b + \frac{g^2}{8c_W^2}Z_\mu Z^\mu\right) + \mathcal{L}_{\text{H-self}}\,, \tag{1.7}$$

where $c_W = \cos\theta_W$ with θ_W being the weak angle ($\tan\theta_W \equiv g'/g$) and $\mathcal{L}_{\text{H-self}}$ gives the Higgs self-interactions originating from Higgs potential. Equation (1.7) shows that gauge bosons, Z and $W^{\pm}$, obtain a mass after EWSB. The Lagrangian of the Yukawa interactions becomes

$$\mathcal{L}^{\cancel{\text{EW}}}_{\text{Yukawa}} = -\frac{v+H}{\sqrt{2}}\left(Y^d_{ij}\bar{d}^i_L d^j_R + Y^u_{ij}\bar{u}^i_L u^j_R + Y^j_{ij}\bar{e}^i_L e^j_R\right) + h.c.\,, \tag{1.8}$$

from which we can read off that quarks and charged leptons obtain a mass $Yv/\sqrt{2}$ with Y being the value of Yukawa couplings. On the other hand, after diagonalizing the mass matrix of gauge bosons, we can rewrite $\mathcal{L}_{\text{EW}}$ as

$$\mathcal{L}_{\text{EW}} = \mathcal{L}_{\text{kin}} + \mathcal{L}^{\gamma,Z,W}_{\text{self}} + \mathcal{L}^{\gamma}_{\text{QED}} + \mathcal{L}^{Z}_{\text{NC}} + \mathcal{L}^{W}_{\text{CC}}\,, \tag{1.9}$$

where $\mathcal{L}_{\text{kin}}$ includes the kinetic terms for fermions and gauge bosons, $\mathcal{L}^{\gamma,Z,W}_{\text{self}}$ gives the cubic and quartic self-interactions of gauge bosons,

$$\mathcal{L}^{\gamma}_{\text{QED}} = \sum_{q,l} eQ_{\text{EM}}\bar{\psi}\gamma^{\mu}A_{\mu}\psi$$

is the QED interaction Lagrangian with $e = g'c_W$ being the elementary charge and A_μ being the photon field, $\mathcal{L}^{Z}_{\text{NC}}$ gives the neutral-current weak interaction mediated by Z, and $\mathcal{L}^{W}_{\text{CC}}$ gives the charged-current weak interaction mediated by $W^{\pm}$, respectively.

In summary, after EWSB the SM Lagrangian reads

$$\mathcal{L}^{\cancel{\text{EW}}}_{\text{SM}} = \mathcal{L}_{\text{QCD}} + \mathcal{L}_{\text{kin}} + \mathcal{L}^{\gamma,Z,W}_{\text{self}} + \mathcal{L}^{\gamma}_{\text{QED}} + \mathcal{L}^{Z}_{\text{NC}} + \mathcal{L}^{W}_{\text{CC}} + \mathcal{L}^{\cancel{\text{EW}}}_{\text{Higgs}} + \mathcal{L}^{\cancel{\text{EW}}}_{\text{Yukawa}}\,. \tag{1.10}$$

$\mathcal{L}_{\text{SM}}$ (1.1) and $\mathcal{L}^{\cancel{\text{EW}}}_{\text{SM}}$ (1.10), entail a rich phenomenology ranging from the quarks' asymptotic freedom to the parity violation in the weak interactions. These phenomena can be examined in the laboratory and compared with the prediction from the SM.

On the experimental side, the validity of the SM description of nature has been strengthened from the confirmation of the existence of quarks and gauge bosons to the latest discovery of the Higgs boson at the Large Hadron Collider (LHC) [11, 12]. After the Higgs discovery, together with the absence of other "new" particles, the precision determination of SM parameters, *e.g.*, masses and couplings, have gained additional importance. The requirement of high precision guides the experimental designs aiming for efficient production of particles such as weak bosons, mesons and Higgs boson ("particle factories"), as well as detectors with high angular and energy resolution. With the measurements of the decay widths and branching ratios from these particle factories, we can decipher the three fundamental gauge interactions. It is fair to say that we are now in the *precision era* of the SM [13]. Advancing in precision also drives theorists to consider higher-order "loop" contributions, *i.e.*, radiative correction to the masses and couplings requiring the theory of *renormalization*.

In summary, so far, the SM provides a self-consistent and perturbatively renormalizable framework. Although the SM is seemingly successful in many aspects, some anomalies call for

	$L^T = (\nu_L, e_L)$	e_R	$Q^T = (u_L, d_L)$	u_R	d_R	γ	Z	$W^\pm$	g	H
T_3	$\left(\frac{1}{2}, -\frac{1}{2}\right)$	0	$\left(\frac{1}{2}, -\frac{1}{2}\right)$	0	0	0	0	± 1	0	$-\frac{1}{2}$
Y	$-\frac{1}{2}$	-1	$\frac{1}{6}$	$\frac{2}{3}$	$-\frac{1}{3}$	0	0	0	0	$\frac{1}{2}$
$Q_{\rm EM}$	$(0, -1)$	-1	$\left(\frac{2}{3}, -\frac{1}{3}\right)$	$\frac{2}{3}$	$-\frac{1}{3}$	0	0	0	0	0

Table 1.1: Particles in the SM and their electroweak charge assignment. From left to right, we have the left-handed doublet for leptons L, right-handed singlet for charged leptons e_R, left-handed doublet for quarks Q, right-handed singlet for both up(down)-type quarks $u(d)_R$, gauge bosons including photon γ, weak neutral(charged) boson $Z(W^\pm)$ and gluon g, and Higgs boson H. For leptons and quarks, there are three generations, *i.e.*, 1) leptons: electron e, ν_e, muon μ, ν_μ and tau τ, ν_τ; 2) up-type quarks: up u, charm c and top t; 3) down-type quarks: down d, strange s and bottom b. Only mass is distinct for different generations.

physics beyond the SM (BSM), introduced in the next section. The anomalies also indicate the final fundamental theory is yet to come. In this thesis, we take the SM as a given and study potential new (dark) physics upon it.

1.1.2 Beyond the Standard Model

Even if the SM is very predictive around and below the EW scale, there are some phenomena that cannot be explained by the SM, *e.g.*, the non-zero neutrino mass, the baryon asymmetry, the absence of CP violation in strong interactions, the hierarchy between the EW and Planck scales, and the omnipresent dark matter (energy). These facts suggest that the SM is a low-energy "effective" theory of a more fundamental theory at some UV scale. To address these phenomena, an enlargement of the SM particle content and/or SM gauge group are needed. For example, at a higher energy scale, we can have a Grand-Unified Theory (GUT) [14–16] and/or Supersymmetry [17–19]. In the effective field theory (EFT) approach, the SM is extended by adding operators beyond mass-dimension 4 [20] to have effective Lagrangian

$$\mathcal{L}_{\rm eff} = \mathcal{L}_{\rm SM}^{\not{\rm EW}} + \sum_{n>4} \frac{c_n}{\Lambda_{\rm UV}^{n-4}} \hat{\mathcal{O}}_n \,, \tag{1.11}$$

where $\Lambda_{\rm UV}$ is some UV scale, c_n is effective coupling, and $\hat{\mathcal{O}}_n$ is a gauge-invariant effective operator constructed of SM particles and/or new states. The validity of the EFT requires that the scale of UV completion or the mass scale of mediators that connect the SM and dark sectors are much higher than the considered energy scale under question. The scenario discussed in Part I falls in this category, *i.e.*, the model parameters are chosen such that the EFT description will be applicable. In Part II of this thesis, we shall instead work in a UV-complete extension of the SM. Finally, there are a number of gauge-invariant combinations in the SM such as $H^\dagger H$ which allow particular low-dimensional operators connecting the new physics. This possibility is often referred to as "portals" [21].

The possible formulations of BSM physics go in hand with measurements of the SM parameters. The progress of laboratory experiments and high-precision measurements provides guidance for perspective directions to go. Most of the electroweak parameters are known with sufficient precision to serve as probes for new physics [13]. On the other hand, quantities related to the $\mathrm{SU}(3)_C$ sector of the SM can be estimated using methods such as perturbative QCD [22], effective field theories of QCD [23–25] and lattice simulations [26]. The SM quantities sensitive to the electroweak interactions and discussed later in this thesis are leptonic $g-2$, the muon lifetime from the process $\mu \to e\bar{\nu}_e\nu_\mu$, Z-pole measurements (mass and decay width), and the polarization asymmetry due to the parity violation in weak interactions. All of the above observables are measured well and offer unique tests for the BSM models.

Although most of the observables are concordant with the SM prediction, some of them show abnormal outcomes, in which the most notable one is the long-standing muon $g-2$ anomaly [27]. The g-factor is intrinsic for any particle carrying a spin, and $g-2$ singles out the quantum correction with the Dirac result being $g=2$. We note that this nominal 3σ tension between the SM predicted value and the observed one [28][3] does not influence the soundness of the SM but, instead, becomes the impetus of precise higher-order calculation of SM contribution (hadronic, EW, QED), as well as potential BSM contribution. The latter case will be scrutinized in this thesis by including the loop diagrams induced by new particles from the dark sector.

Another interesting brand of SM that deserves particular attention is flavor physics. The flavor mixing of neutrinos, *neutrino oscillation* [30, 31], naturally predicts a non-zero neutrino mass, for which calls for an extension of the neutrino masses, *e.g.*, through the seesaw mechanism [32–35]. The parameters including mixing angles, a potential CP-violating phase, and potential Majorana phases in the Pontecorvo–Maki–Nakagawa–Sakata (PMNS) matrix [36], not precisely measured so far, are also popular research areas, which can yield suggestions on neutrino's nature and offer guidance for formulating a complete theory for the leptonic sector. See [37] for a recent global analysis on neutrino oscillation. On the other hand, the Cabibbo–Kobayashi–Maskawa (CKM) matrix [38, 39] entailing the flavor mixing in the quark sector has been measured precisely [5]. For charged leptons, the flavor is conserved in SM interactions; therefore, lepton flavor violating (LFV) processes such as $\mu \to e\gamma$ are an absolute indication of BSM physics.

Although not being the main focus of this thesis, we note there are many other phenomenologically intriguing aspects of the BSM physics. For example, anomalies observed in the B physics [40], the strong CP problem which may imply the existence of *axion* [41–44], and the hierarchy problem which may suggest exotic new physics [45–47].

[3] See [29] for a recent measurement of muon $g-2$. Combining the value in [29] with previous measurement [28], the muon $g-2$ anomaly is now 4.2σ.

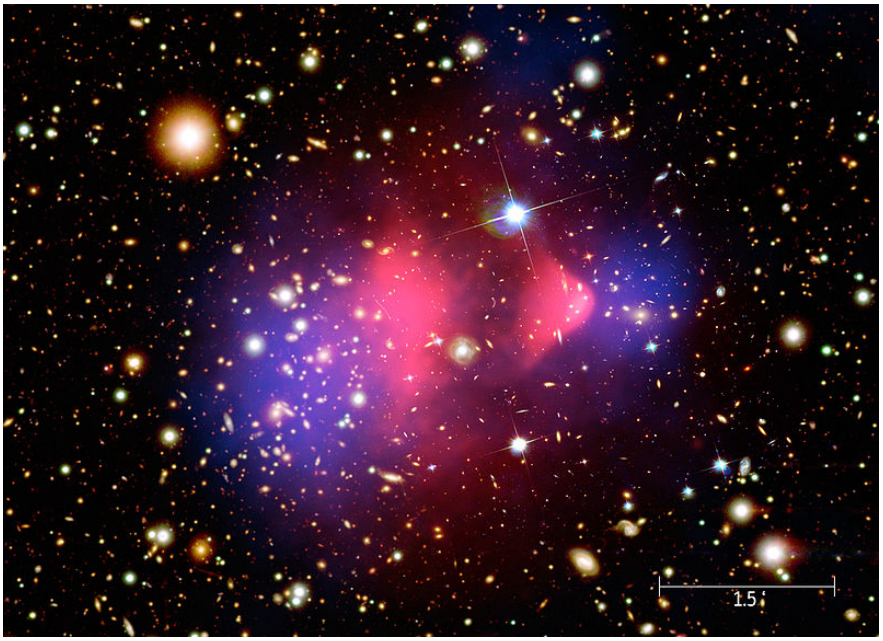

Figure 1.1: The Bullet Cluster, one of the most compelling pieces of evidence for DM. The red part is inferred from X-ray observation, while the blue part, showing the gravitational center of the clusters, obtained from lensing measurements. The offset of the two regions indicates that DM does not interact with the baryonic component. Figure credit: Chandra X-Ray Observatory: 1E 0657-56.

1.2 Dark Matter

1.2.1 Evidence and hints

With Newtonian gravity, general relativity, and observations based on electromagnetic radiation, the motion of stars and other heavenly bodies can be described and precisely measured. The earliest hint of a non-luminous matter component can be traced back to 1933; motivated by the inconsistency between the observation based on the galaxy motions and theoretical calculation using the virial theorem of the mass distribution in the Coma Cluster, Fritz Zwicky postulated that there is "dark matter" (DM) that outweighs the observed luminous matter [48]. The concept of DM did not receive much attention until the observation of anomalous galaxy rotational curves [49, 50], showing the circular speed at the galactic outskirts stays constant with the distance from the galactic center instead of decreasing. The departure from expectation implies an underlying non-luminous matter component with a diffuse mass distribution that sources the gravitational potential for constant rotational speed at large radii, currently known as the DM *halo*.

The existence of DM is further confirmed by the observation of the Bullet Cluster [51], demonstrating that the matter distribution in a system of two colliding clusters appears different in the X-ray spectrum than inferred from gravitational lensing; see Fig. 1.1 for illus-

tration. Only visible matter, including gas and stars, manifests itself in the X-ray spectrum. The gravitational lensing is universal for both visible matter and DM; the two observations' mismatch suggests that the two clusters reside in DM halos. Not only being a necessity to explain galactic-scale phenomena, it turns out that DM is also a required building block for standard cosmology. The observation of anisotropy in the Cosmic Microwave Background (CMB) and the large-scale structure (LSS) of the universe both indicate that the gravitational potential of DM is indispensable. In the early universe, the DM gravitational potential sources the *baryon acoustic oscillation*, which generates the observed CMB power spectra and leaves imprints on the LSS. Therefore, the energy budget can be determined accordingly. After the decoupling of CMB photons, the DM gravitational potential enables the growth of density perturbation which eventually enters the non-linear regime and creates the LSS we observe today.

To explain the CMB anisotropy as well as the the observed accelerated cosmic expansion [52, 53], we further need an unknown type of energy, called "dark energy" (DE) in analogy to DM [54]. The first possibility for DE is a "cosmological constant" Λ, initially introduced by Einstein for obtaining a static universe at the time. In a universe that is expanding [55], Λ rather describes the accelerated expansion of the universe. A cosmological constant has negative pressure (*i.e.*, its equation of state $w \equiv p/\rho = -1$), thus its energy density stays constant irrespective of the cosmic expansion. While we do not study the DE further in this thesis and take Λ as a given, we note there are still alternative models for DE aiming for addressing more phenomena, *e.g.*, interacting DE [56, 57], or a varying equation of state [58, 59].

DM is a necessary ingredient in standard cosmology; however, its particle nature remains largely unknown. Nevertheless, there are still some preferable characteristics of DM that we can infer from observation. First, DM appears uncharged under $\mathrm{SU}(3)_C$ and $U(1)_{\mathrm{EM}}$ to a large degree; otherwise, we can observe clear signals in various experiments and environments. That is to say, at most, DM can be "weakly-interacting" with SM particles. Second, since DM is the primary source of gravitational potential for the cosmic structure formation, we can infer that it shall be "cold", *i.e.*, with negligible velocity dispersion. Therefore, we can infer that the SM neutrino cannot be the chief DM component; its thermal velocity will smooth out nearly all small-scale density perturbations. The "warm" DM (WDM) is still allowed, though it is strongly constrained by the LSS observation [60, 61]. In summary, it is evident that the particle content of SM may not accommodate DM[4], and we need new physics to describe the DM nature.

[4] One exception are primordial black holes that form in the early universe; see [62] for a recent review.

1.2.2 Particle dark matter

Propelled by the existence of DM from observations discussed in the previous section, model building regarding the DM nature becomes a timely and popular research topic; see [63] for a general review. Following the guidelines, "cold" and "weakly-interacting", it is intuitive to postulate DM appears in the form of "weakly-interacting massive particle" (WIMP). Putting aside the *nightmare scenario* that there is no DM-SM interaction beyond gravity, it is realized that the correct DM relic abundance can be attained naturally through the thermal "freeze-out" of WIMPs with a mass of $\mathcal{O}$(GeV–TeV) if the cross section of DM-SM interaction is comparable to that of SM weak interactions[5]. This coincidence is known as the *WIMP miracle*, which has been a strong motivation for particle models that naturally yield such a candidate[6]; for example, the lightest supersymmetric particle can play the role of WIMP [64]. Besides being entertained in model building, the WIMP miracle also stimulates the progress of experimental designs with three-major directions: the collider search, indirect search, and direct detection experiments.

Although WIMPs are attractive in that they have interactions similar to the ones observed in the SM weak interactions, we note that they are not the only DM candidates. The spectrum of DM mass can span orders of magnitudes: from extremely light of $\mathcal{O}(10^{-22}\,\text{eV})$ to heavy of $\mathcal{O}(M_\odot)$; see Fig. 1.2 for a summary. In general, these models follow the rules of "cold" and extremely "weakly-interacting" and have some add-ons from either the production mechanism or the interaction pattern. For example, at the lightest mass end, the fuzzy (ultralight) DM with a mass of $\mathcal{O}(10^{-22}\,\text{eV})$ can be seen as a coherent wave with a Compton wavelength of galactic scale $\mathcal{O}$(kpc) [66, 67]; thus, the galactic structure in this scenario can be different from the prediction of cold DM (CDM). On large scale, it forms Bose-Einstein condensation, making it behave similar to a CDM component. Another interesting example is the keV sterile neutrino, which can be a WDM candidate. It is connected to SM particles through the neutrino sector and may enter the mechanism that generates the tiny neutrino mass.

It is also possible that DM does not come alone, but, instead, is part of a hidden or dark sector of particles, some of which may be weakly-interacting with SM particles [68]. Aside from accommodating a DM candidate, a dark sector can provide various dark dynamics such as light degrees of freedom that mediate a dark force [68] and their interaction with DM [69], resulting, *e.g.*, in signals of long-lived particles in experiments or in a different cosmic history of structure formation. Even though other dark states cannot dominate the energy budget, they can be non-thermally generated from DM or from the feeble interaction

[5]The required thermally averaged annihilation cross section for obtaining the correct DM relic density via freeze-out is $\langle\sigma v_M\rangle \sim 3\times10^{-26}\,\text{cm}^3\,\text{s}^{-1}$, which can be realized with $\mathcal{O}(100\,\text{GeV})$ WIMPs interacting through the EW force.

[6]Thermal freeze-out is also possible for sub-GeV DM considered in this thesis. Although the required annihilation cross section is similar to that of the WIMP scenario, model parameters such as couplings and masses of mediators need to be different; see the discussion in Sec. 6.4 of Part II.

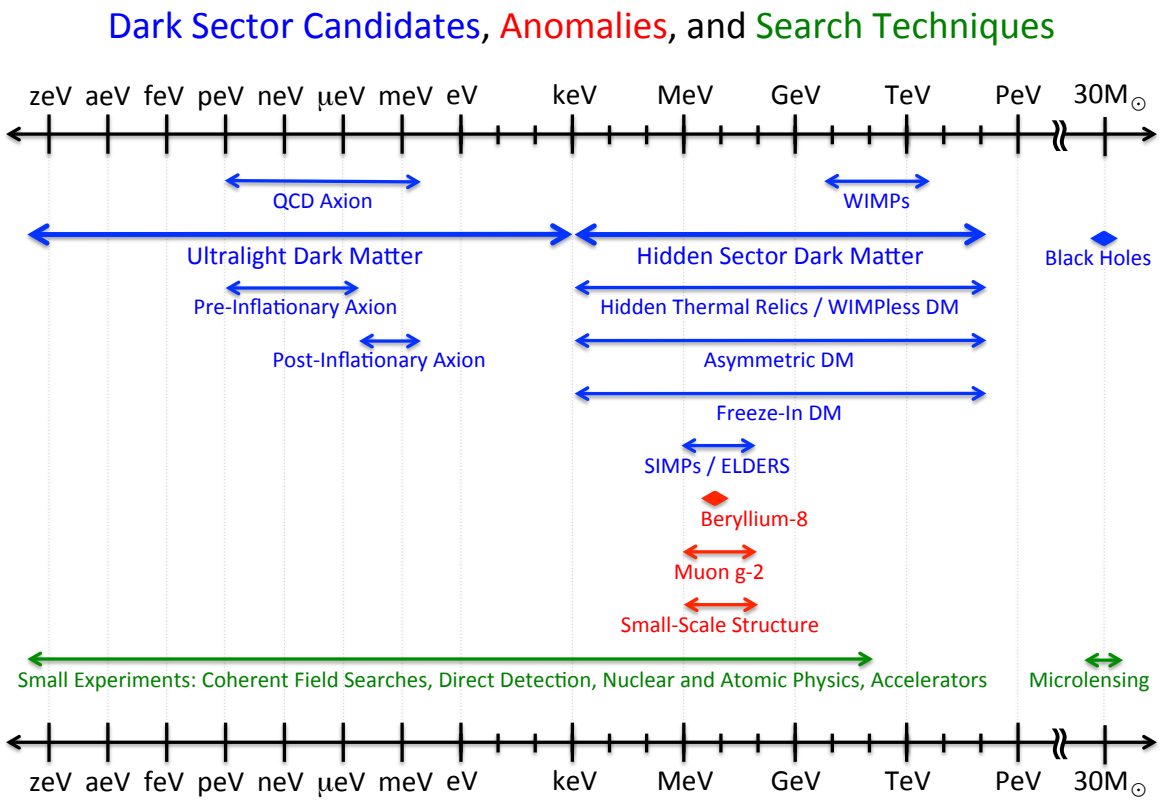

Figure 1.2: The mass spectrum of DM candidates. Figure credit: [65].

with SM particles; thus, they can have a distinct energy spectrum from the thermal bath, which may, in turn, enhance their detection potential. For example, the sensitivity to the dark radiation, sourced from the decay of DM, will be studied later.

In short, there is no "best" model for DM so far, yet there are assorted directions for model building. Some unexplained phenomena in the SM can be related to the dark sector, for instance, generating baryon asymmetry of the universe from the asymmetric DM [70] and creating a non-zero neutrino mass from dark sector dynamics [71]. In addition, anomalies observed in laboratories or astrophysical environments may be alleviated when including the contribution from the dark sector, *e.g.*, the muon $g-2$ tension mentioned before and observed photon excess (INTEGRAL 511 keV line [72, 73], 3.5 keV line [74, 75] and galactic center gamma-ray excess [76]). In this thesis, we will focus on a light, sub-GeV dark sector below the EW scale, connected to the SM via a vector (Part I) or a fermion (Part II) mediators, as well as its implications in laboratory experiments, astrophysics and cosmology.

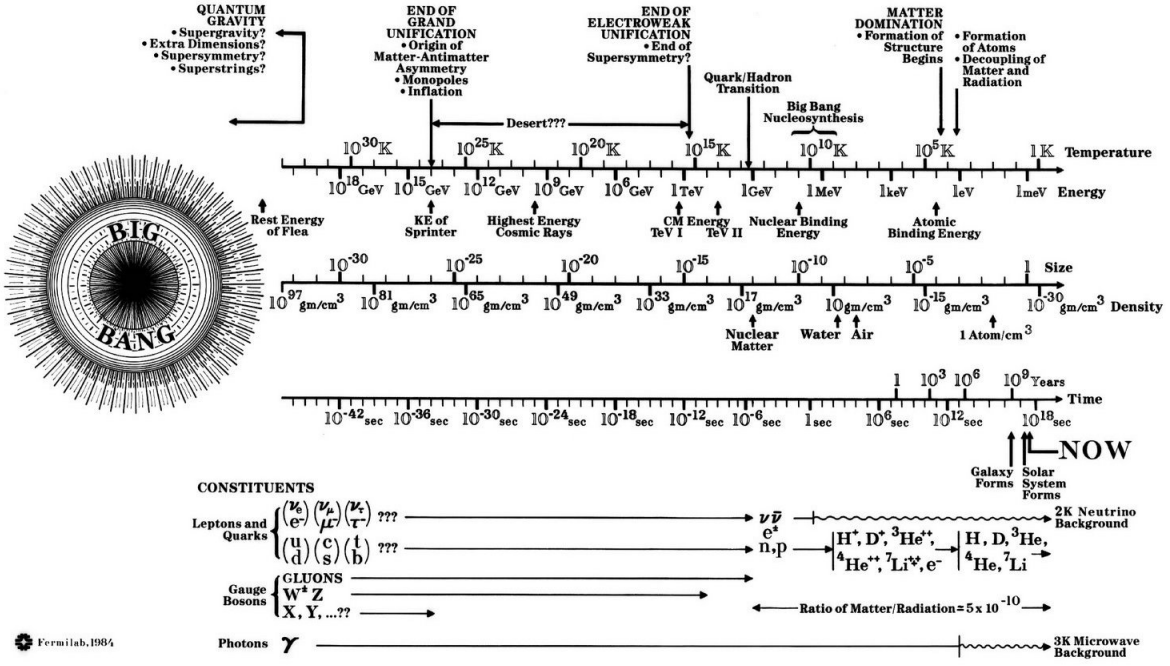

Figure 1.3: The brief history of our universe with major events noted. Figure credit: Fermilab.

1.3 Cosmology in a nutshell

1.3.1 The ΛCDM model

As DM dominates the energy budget from matter-radiation equality until the late universe when DE starts to dominate, it is also phenomenologically of key importance from the viewpoint of cosmology. To infer the DM nature cosmologically, we need to know how our universe evolves from the Big Bang to the present. In the following, we recap, in chronological order, the standard cosmology based on the ΛCDM model, *i.e.*, the Big Bang cosmological model comprised of DE (cosmological constant Λ), CDM, and ordinary matter (the SM). See Fig. 1.3 for an overview on the cosmic history and the particle content in each epoch.

Observationally, our universe is isotropic and homogeneous on the large scales beyond $\mathcal{O}(100\,\mathrm{Mpc})$. It is then described by the Friedmann-Lemaître-Robertson-Walker (FLRW) metric:

$$ds^2 = a^2(\tau)\left[d\tau^2 - \left(\frac{dr^2}{1-kr^2} + r^2 d\theta^2 + r^2 \sin^2\theta d\phi^2\right)\right], \tag{1.12}$$

with the cosmic expansion encoded in the scale factor a as a function of conformal time τ, the curvature parameter $k = -1, 0, 1$ corresponding to open, flat and closed geometry, respectively. The scale factor multiplies the *comoving* coordinate r, in which the cosmic expansion is factored out; $a(\tau)r$ is the physical distance. It is useful to define the redshift

$z = a^{-1} - 1$ with $a(0) = 1$. To address the *flatness problem*: "why our universe is flat with $k = 0$?" and the *horizon problem*: "why our universe is isotropic and homogeneous on large scales?", after the Big Bang, a period of exponential expansion by a factor e^{60} is typically postulated, termed as *inflation* [77, 78]. Not only does inflation provide an elegant solution to the cosmological fine-tuning problems mentioned above, the intrinsic quantum fluctuations of the inflaton, *i.e.*, the field responsible for inflation, becomes the seed of density perturbations.

In the inflationary paradigm, the simplest possibility is that the inflaton reheats the universe at the end of inflation by decaying into SM particles [79], providing thermal initial conditions for standard cosmology. At this stage, the universe becomes radiation-dominated, and reaches thermal equilibrium with a temperature T, typically assumed above the EW scale. As the universe expands and cools down, it goes through the electroweak phase transition (EWPT). The EWPT happened at $T \sim 200\,\mathrm{GeV}$, when the finite-temperature correction is not enough to make $\langle\phi\rangle = 0$ a true minimum, and the Higgs boson obtains a VEV of $\langle\phi\rangle \neq 0$. Therefore, the EW gauge symmetry breaks from $\mathrm{SU}(2)_L \times \mathrm{U}(1)_Y$ to the electromagnetism $\mathrm{U}(1)_{\mathrm{EM}}$. Besides, the VEV of the Higgs boson gives rise to the fermion's mass via the Yukawa coupling and the masses of the weak bosons through the covariant derivative; see the discussion about the Higgs mechanism in Sec. 1.1.1, Eqs. (1.1) and (1.10).

Later, at $T \sim 150\,\mathrm{MeV}$[7], the QCD phase transition started, during which the chiral symmetry breaks from $\mathrm{SU}(3)_L \times \mathrm{SU}(3)_R \to \mathrm{SU}(3)_V$ [81–83]. This transition leads to the quark confinement: the original quark-gluon plasma transforms to a gas of hadrons, primarily made of pions, neutrons and protons. Assuming the baryon asymmetry was created before the EWPT, baryon pair-annihilation depleted the symmetric part of the population by $T \sim 20\,\mathrm{MeV}$. The remaining neutrons and protons maintained nuclear statistical equilibrium (NSE) through the weak interactions[8]. At $T \sim 3\,\mathrm{MeV}$, the rate of the weak interactions that connect neutrinos to the thermal bath drops below the Hubble rate; hence neutrinos decouple from electrons/positrons and photons. Soon after neutrino decoupling, at a photon temperature of $T \sim 0.7\,\mathrm{MeV}$, the weak interactions freeze out, leaving a neutron to proton ratio of $n/p \sim 1/6$.

A chain of nuclear reactions is induced when T falls sufficiently below the binding energies of light nuclei; the primordial light element abundances can build up, called *Big Bang Nucleosynthesis* (BBN). At the starting point of BBN, $n/p \simeq 1/7$ as some neutrons have decayed. The first step is to synthesis deuterium D with a binding energy of 2.22 MeV through proton-neutron fusion. However, D only became abundant when $T \sim 0.08\,\mathrm{MeV}$, due to its small binding energy and the large entropy of the universe (parameterized by the baryon-to-photon ratio $\eta \equiv n_B/n_\gamma \sim 6 \times 10^{-10}$); this is referred to as the "deuterium bottleneck". Once it opens, other light elements up to ^{7}Li are synthesized rapidly. At the end of BBN,

[7] This value is obtained with QCD lattice calculation [80].

[8] At this stage, the abundance of light elements also follows NSE; however, at that point, they are negligible.

almost every neutron went into ^{4}He, resulting in a helium-4 mass fraction $Y_p \sim 1/4$. The prediction for other elements with respect of hydrogen atom are D/H $\sim$ ^{3}He/H $\sim \mathcal{O}(10^{-5})$ and ^{7}Li/H $\sim \mathcal{O}(10^{-10})$; see [84, 85] for reviews on the BBN and its implications on BSM physics.

As the universe cools and the particles' momenta redshift[9], at $T \sim 1\,\mathrm{eV}$ ($z \sim 3300$), the energy budget of radiation and non-relativistic particles equal and the universe reaches *matter-radiation equality*. After matter-radiation equality, the energy budget is dominated by matter, enabling the linear growth of density perturbation within the Hubble horizon[10]. Meanwhile, baryons—still tightly couple to photons via frequent Thomson scattering—form a baryon-photon fluid that oscillates within the gravitational potentials sourced by DM. This *baryon acoustic oscillation* (BAO) gives rise to an important "standard ruler", corresponding to the scale of the sound horizon. It becomes imprinted on both the CMB anisotropy power spectra [86] and the distribution of galaxies through density perturbations [87, 88]. At $z \sim 1200$, *recombination* took place: T falls sufficiently below the binding energy of hydrogen such that the atomic bound-state formation rate becomes faster than the dissociation rate caused by photons. After recombination, the universe became transparent to photons, *i.e.*, they have no charged particles to scatter on, and the free-streaming of photons started. This photon relic carrying the information of the last scattering surface is then the CMB we observe today.

The universe entered the *dark ages* as there are no photon sources except the background CMB after recombination. In ad interim, baryons started to fall into the DM gravitational potentials since there is no longer the back-reaction from photon pressure. Therefore, the baryonic density perturbations can also grow linearly. The main difference between baryons and DM is that baryons can cool radiatively by emitting photons. Consequently, baryonic overdensities collapse into compact objects if their scale is smaller than the so-called *Jeans scale* related to the baryon sound speed. Around $z \sim 50$–100, the first stars form, and the universe is lightened again, which marks the *cosmic dawn*[11]. Subsequently, when the star formation became effective, larger baryonic structures such as galaxies and clusters can form. Lyman-alpha photons from stars couple the *spin temperature*—a temperature parameterizing the difference in populations of triplet (parallel spin-alignment) and singlet states (antiparallel spin-alignment)—of the hydrogen atom to the gas temperature via the Wouthuysen–Field effect [91–93], creating a global 21 cm signal with the CMB as the background radiation field. The 21 cm cosmology [94] offers an essential probe of the cosmic epoch in the redshift bracket $z \simeq [10, 100]$. In addition to the 21 cm signal, the photons from stars are energetic enough to ionize the hydrogen atoms, ionizing again the universe; this process is called *reionization*. The universe became fully reionized at $z \sim 6$–9 inferred from the measurement of the CMB optical depth [86] as well as the Gunn-Peterson trough [95, 96]. The global 21 cm signal

[9] $\rho_{\mathrm{rel}} \propto T^4 \propto (1+z)^4$ while $\rho_{\text{non-rel}} \propto T^3 \propto (1+z)^3$.

[10] In the radiation-dominated era, the density perturbation can only grow logarithmically.

[11] The redshift of the formation of first stars is not settled [89]; see [90] for the details on first-star formation.

vanished when reionization was completed.

In the meantime, the small-scale DM density perturbation entered the non-linear regime, *i.e.*, the density contrast $\delta \equiv \rho/\bar{\rho} - 1 \gg 1$. Those density perturbations can virialize and form diffuse DM *halos*. As the non-linear scale became larger, mode-mode coupling enabled ubiquitous halo and galaxy mergers, forming the LSS of the universe we observe today [97, 98]; The LSS has the form of a "cosmic web" [99] composed of DM and ordinary matter, including cosmic filaments and cosmic voids. Below $z \sim 1$, the energy budget became dominated by DE, accelerating the cosmic expansion with the scale factor evolving as $a(t) \propto e^{t-t(z=1)}$, where t is the cosmic time.

1.3.2 Beyond ΛCDM

Although, the ΛCDM model is highly successful, there are several phenomena that it may not explain. One recent greatly discussed topic is the value of the Hubble constant. There exists an almost 4σ tension between H_0 inferred from CMB measurements [86] (high-z) and from the distance ladder [100] (low-z); to explain this *Hubble tension*, one needs to impose physics beyond the ΛCDM model either in the early or late universe, *e.g.*, early dark energy [59], non-standard recombination [101, 102] or modified DM-baryon scattering [103]. Another anomaly that may require new physics is the *cosmological lithium problem* [104]: the prediction of standard BBN is not concordant with the observationally inferred primordial content from metal-poor halo stars. Possible BSM solutions are, for example, the decay or annihilation of new massive particles [105], new particles engaging in nuclear reactions [106], variation of fundamental constants [107], or a non-standard cosmology [108]; we also note that solutions may come from astrophysics; a nuclear physics solution has been ruled out [109–112].

We also have observables that are predicted in the ΛCDM model but are yet to be detected. The first one is the *cosmic neutrino background* (CνB), which is the thermal neutrino radiation[12] resulting from neutrino decoupling in the early universe; see the discussion in the previous section. The resulting CνB's temperature is lower than that of the CMB by a factor of 1.4 because e^-e^+ annihilation happened after neutrino decoupling, which in turn only heats the CMB. Although there is indirect evidence of the CνB from either BBN or the CMB [113], so far, we do not have a direct detection of it. Shall the CνB be detected, we can then probe the early universe beyond the CMB [114]. The second implication of the ΛCDM model that remains unresolved is the EW phase transition (EWPT). Physics such as the process of EWPT, the EW potential (first- or second-order), and the possible signals such as stochastic gravitational wave [115, 116] are also active research fields.

Another set of observations for which their underlying origins are not fully understood

[12]The CνB is a "hot" relic as it decoupled relativistically, in contrast to a cold relic such as DM from thermal freeze-out.

are, for instance, the apparent baryon asymmetry of the universe [117]. It requires *baryogensis* [118, 119], *e.g.*, based on leptogenesis [120, 121], *i.e.*, lepton asymmetry converted to baryon asymmetry via processes that violate both baryon number B and lepton number L such as the sphaleron. On the other hand, we have observed the homogeneity and isotropy of the universe through various observations; the possible mechanism which naturally leads to this result is best-described by inflation, as discussed in the previous section. The nature of the particle driving inflation, the inflaton, and its potential remains unknown. Besides, the distinctive signal of inflation: the B-mode polarization of the CMB, originating from a stochastic gravitational wave background during inflation, is not detected so far [122].

It is well accepted that ΛCDM with collisionless cold DM is successful in describing the large-scale observables; however, observations and simulations of dwarf-spheroidal galaxies (dSphs) show that ΛCDM has difficulties in explaining the density profile (velocity dispersion) as well as the abundance of dSphs [123–127]. This is coined as the "small-scale crisis" of ΛCDM. The small-scale clustering strength is predicted to be too large. To address the crisis, several alternative DM models have been proposed, *e.g.*, WDM, fuzzy DM [66, 67], self-interacting DM [128], and dark sector interactions (see ETHOS [69]). All of the models have distinct mechanisms to suppress small-scale power, while, at the same time, keep large scales unmodified. Note that baryonic feedback within ΛCDM can also alleviate the crisis [129–132]. Taken together, simulations with high precision and resolution are needed to settle this debate. Besides the large-scale structure observed at low redshift (galaxy surveys, Lyman-alpha forest [133]), in the future, we are expecting to probe cosmic structure at cosmic dawn through the 21 cm global signal[13] as well as its fluctuation, *i.e.*, the 21 cm power spectrum [143].

An attractive mechanism to obtain the DM abundance is "thermally", produced through the freeze-out mechanism. Still, we can also obtain the correct relic density in a *non-thermal* way. One phenomenologically interesting scenario, *freeze-in* [144], is that the DM relic abundance is gradually built up from zero by feeble interactions that are slower than the Hubble rate. Further feasible scenarios are out-of-equilibrium decay of particles and interactions suppressed by a high-energy scale. For light (pseudo-)scalar ϕ, such as fuzzy DM or the axion, the correct relic density can be obtained by a so-called *misalignment mechanism* [67]: at $H \gg m_\phi$ the scalar field freezes as its Compton wavelength is much larger than the Hubble horizon, while at $H \sim m_\phi$, ϕ begins to oscillate, and when its potential is harmonic, its density evolves like a CDM component ($\rho \propto a^{-3}$). It is worth mentioning that there are also other exotic ways to produce DM abundance in the early universe, *e.g.*, using the relativistic

[13] Recently, the EDGES collaboration claimed that they detected, for the first time, the global 21 cm absorption signal [134]; however, the amplitude is lower than the expectation in the ΛCDM model. Either cooler gas from, *e.g.*, baryon-DM interactions [135] or additional radiation background [136, 137] is required to explain this anomaly. On the flip side, this signal can also be utilized to constrain DM interactions [138–141] and DM nature [142].

nature of the bubble wall during a first-order phase transition [145, 146].

To summarize, physics beyond current experimental reach or the ΛCDM framework discussed above may originate from a dark sector. In turn, precise measurements of cosmological observables in cosmic epochs can provide hints on the nature of dark states, as well as serve as probes for them. In this thesis, we will study how the benchmark dark sector models affect the early-universe observables as well as the late-time ones, and employ current measurements to constrain their parameter space.

1.4 The search for dark states: from WIMPs to sub-GeV DM

As discussed, the anomalies or deviations either from the SM or from the ΛCDM predictions may be connected with the nature of the dark sector. In this section, we review the effort that has been made in the DM search and subsequently point out the directions for probing a light, sub-GeV dark sector which is the main focus of this thesis.

Before introducing various experiments and searches, we recap the general constraints on the nature of DM. Assuming a thermal freeze-out scenario, if DM maintains thermal contact via the weak interaction, the *Lee-Weinberg bound* [147] requires the DM mass to be larger than $\mathcal{O}(2\,\mathrm{GeV})$; otherwise, it will overclose the universe. Relaxing the condition on the interaction type, we can, on the other hand, constrain the maximum value of the interaction cross section by quoting *partial-wave unitarity*, which in turn limits the thermal DM mass to be smaller than 340 TeV [148]; see, however, recent work [149]. In the local universe, dSphs are good targets for probing the DM nature, as DM is the main constituent in mass. The analysis of their phase-space density can constrain the mass of a free fermionic DM to be heavier than $\mathcal{O}(\mathrm{keV})$ based on general arguments made about the phase space structure, known as the *Tremaine-Gunn bound* [150, 151][14].

Ever since the concept of DM was introduced, several experiments were built to search for WIMPs, or in general, any dark sector particle. According to the underlying DM-SM processes, we can roughly put them into three categories:

- Collider search: if kinematically allowed, even though DM only feebly couples to SM particles, it can still have a chance to be produced by collisions between them [153]. The iconic facility is the Large Hadronic Collider (LHC) which collides two proton beams accelerated to high energy.
- Indirect detection: SM particles can also be produced from DM decay or pair annihilation. In the early universe, the injected energy can alter the black-body spectrum of CMB and ionize/heat the thermal plasma, which affects the CMB power spectra.

[14] The Tremaine-Gunn bound can be relaxed if the fermionic DM is made of many degenerate or quasi-degenerate states [152].

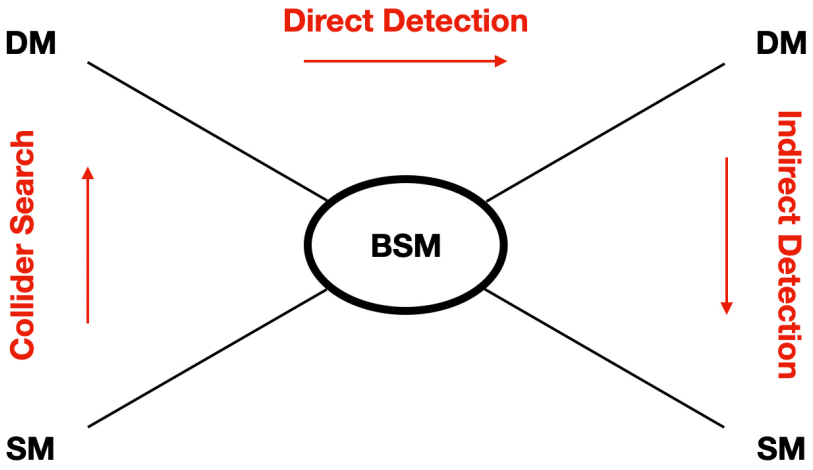

Figure 1.4: Three directions of DM search. Based on the differing composition of initial and final state particles, we can have collider search for DM production from SM particles collision, direct detection for DM-SM scattering, and indirect detection for DM pair-annihilation into SM particles.

In the local universe, we can search for an excess of (anti-)particle and/or gamma-ray line/continuous signature by pointing the telescope toward DM-abundant regions such as our Milky Way (MW) center and dSphs [154].

- Direct detection: here the targeted process is the scattering between DM and atomic nuclei and electrons. Their recoils can cause measurable signals in the form of heat, scintillation, or ionization; see [155] for a recent review.

See Fig. 1.4 for illustration on the relation of DM-SM interaction and the above categories.

Most of the conventional probes target the $\mathcal{O}$(GeV–TeV) WIMPs. No signal has been seen to date. Therefore, much attention has recently turned to a relatively unexplored mass region: *sub-GeV*, in which we can still have the correct relic abundance either through thermal freeze-out or freeze-in. A sub-GeV dark sector also provides rich phenomenology, as it can accommodate dark light degrees of freedom and the interactions between dark states.

To probe a sub-GeV dark sector in accelerator experiments, the main different strategy from searching for WIMPs is that we need to have ways to separate SM backgrounds mainly caused by neutrinos from signals caused by dark states. Still, we need to have high enough intensity or luminosity to compensate for the feeble DM-SM interactions. In this sense, low center-of-mass (CM) energy but high-intensity facilities equipped with detectors having good energy and angular resolutions, such as electron-positron colliders [156] and fixed-target/beam-dump experiments [157–159] are suited for probing a light, sub-GeV dark sector.

On the direct detection side, a non-relativistic sub-GeV particle does not carry enough energy to produce a detectable nuclear recoil. Several ways are proposed to bypass this bottleneck, *e.g.*, lowering the recoil threshold by considering DM-electron scattering [160], detecting

the photon from a bremsstrahlung process instead [161], accelerating DM by cosmic rays [162] or solar reflection [163], or utilizing the nuclear Migdal effect [164, 165]. The experimental design also progresses to use other materials such as semiconductors that have a small band-gap compared to the noble gas atom's binding energy, *i.e.*, a lower ionizing threshold. Currently, much attention is put on computing the material's response after scattering with a DM particle, such as the production efficiency of the phonons and photo-electrons; see [166] for an overview. Indirectly, we can anticipate sub-GeV signals from DM pair-annihilation. Thus, gamma-ray/radio telescopes and cosmic-ray detectors with a lower energy threshold are expected to probe this mass range [167]. In the early universe, the distortion on the CMB anisotropy power spectra still place tight constraints on the energy injection from sub-GeV DM [168, 169].

Astrophysically, "sub-GeV" is in the ballpark of the temperature or plasma frequency of stellar cores. Therefore, the interaction between DM and SM particles can lead to intriguing implications on, *e.g.*, stellar evolution, stars' morphology, and their relative composition. These effects usually originate from the energy carried away by DM, in addition to the standard coolants such as neutrinos and/or photons [170–173]. The response of the star upon energy loss as well as the production mechanism of the dark states in a thermal plasma will be explored in detail later. In addition, sub-GeV dark states can alter various cosmological observables. These dark states can be produced before/during the BBN epoch from their interactions with SM particles, contributing extra degrees of freedom parameterized by $N_{\rm eff}$. The values of $N_{\rm eff}$ are inferred at both BBN and CMB, providing leverage to constrain the light dark states abundance in the early universe. On the other hand, the self-interaction of dark states through a dark force is possible in a light dark sector. If the dark states constitute the main component of DM, their self-interaction can change the interior of the DM substructures [174]. Also, if the interaction with the SM particles is allowed, the DM has to be kinetically decoupled from the thermal bath at $T \sim \mathcal{O}(\text{keV})$ to prevent overdamping density perturbations below its mean-free-path (collisional damping). For DM with non-zero thermal velocity such as WDM, the damping on the small-scale structure due to its free-streaming (non-collisional damping) is also relevant in terms of LSS observables [60, 61].

With light dark sector physics, we note that some of the observed anomalies in the SM may be alleviated. For example, the muon $g-2$ has long been recognized as a potential sign for new physics, especially "light" new physics. Models that include light particles coupled to SM leptons can be entertained; see, *e.g.*, [68, 175] for reconciling muon $g-2$ with a dark photon. Also, we have observed a 511 keV line feature in the MW's center. Although its origin is known; electron-positron annihilation through positronium formation, the source of these nearly-stopped positrons remains a puzzle. While standard astrophysics may not solve this puzzle, the pair-annihilation of $\mathcal{O}(\text{MeV})$ thermal DM into electron-positron pairs is still an attractive BSM explanation [176].

In summary, with the theoretical and experimental developments and the absence of TeV-scale new physics, the critical question, "what is the dark matter?", is gradually superseded by "what constitutes the dark sector?" as well as "how should we probe a light dark sector". This thesis is dedicated to pondering on these questions by elaborating the implications of a light dark sector in different environments and experiments, as well as utilizing the accumulated data to constrain the nature of dark sector particles. In the rest of this thesis, through studying two minimal extensions of the SM focusing on a vector (Part I) and a fermion (Part II) portals which connect a sub-GeV dark state to the SM, we demonstrate how the light dark particles, as well as their mediators between the dark sector and SM sector, manifest themselves in laboratory experiments and astrophysical/cosmological observables. Moreover, the detection strategies and, in turn, the derivation of the constraints on the parameter space are spelled out.

Part I

The Photon as the New Physics Mediator

CHAPTER 2

The Photon Portal

2.1 Is the dark sector really dark?

To date, "dark matter" lives up to its name as we have only observed the gravitational interaction between the dark and visible sectors. Various ideas about possible *portals* that connect the DM to the SM sector beyond gravity are proposed, such as the vector portal [177], Higgs portal [178], and neutrino portal [179, 180]. Although being relatively minimal extensions of the SM, these portals so far have not manifested themselves in experiments, resulting in stringent constraints on the available parameter space [21, 181].

While the electromagnetic (EM) interactions within the SM particles are well-understood with high precision, the EM properties of DM remain largely unknown. One intuitive possibility to construct a portal is the SM photon being the mediator between the dark and visible sectors, which is usually overlooked as we in general expect DM to be electromagnetically neutral. Most astronomical observations and also many experiments heavily rely on photons as the messengers of information. Thus, if DM were to interact with photons with appreciable strength, we would already have detected DM in several observables. Nevertheless, it is perfectly possible that a coupling between DM and photons exists but is weak such that it has escaped detection.

In general, DM can originate from a more complicated dark sector comprising different dark states. Interactions between dark states and DM together with the ones between dark states and photons may yield an effective EM coupling for DM. The minimal way to entitle DM with EM interactions is to assign it a *millicharge* which is sourced from, for example, the kinetic mixing between a dark photon and SM photon [177]. Owing to the simplicity of the underlying ultraviolet (UV) model, this scenario has been well examined in particle physics and cosmology; see [182] and the references therein. However, even if DM is seemingly *electromagnetically neutral*, it can still interact directly with photon through EM form factors, such as an electric/magnetic dipole moment, an anapole moment, or a charge radius [183]. These interactions between the neutral DM and photon can, *e.g.*, arise from UV completions with additional heavy charged states.

For a broader point of view, we shall consider *any* particles χ beyond the SM that carry a millicharge or have non-vanishing EM form factors. The production and detection of χ can

have intriguing implications in astrophysics, in cosmology, in intensity frontier experiments, in direct detection experiments, and in large-volume neutrino experiments. Therefore, a detailed study of the phenomenology of the photon portal is of utmost importance in pinning down the EM nature of the dark states and serving as a starting point or driving force for considering a more involved dark sector. In the following chapters, we answer the question "is the dark sector really dark?" by quantifying the "darkness" of the dark sector through various probes mentioned above.

2.2 Effective electromagnetic interactions

We consider χ being a Dirac fermion as it allows for the richest variety of form factors. The Lagrangians that describe the χ interactions with the photon A_μ or its field strength tensor $F_{\mu\nu}$ read, in ascending order of their mass-dimensionality,

$$\mathcal{L}_\chi^{\text{dim-4}} = \epsilon e\, \bar{\chi}\gamma^\mu \chi A_\mu \,, \tag{2.1a}$$

$$\mathcal{L}_\chi^{\text{dim-5}} = \frac{1}{2}\mu_\chi\, \bar{\chi}\sigma^{\mu\nu}\chi F_{\mu\nu} + \frac{i}{2} d_\chi\, \bar{\chi}\sigma^{\mu\nu}\gamma^5\chi F_{\mu\nu} \,, \tag{2.1b}$$

$$\mathcal{L}_\chi^{\text{dim-6}} = -a_\chi\, \bar{\chi}\gamma^\mu\gamma^5\chi\partial^\nu F_{\mu\nu} + b_\chi\, \bar{\chi}\gamma^\mu\chi\partial^\nu F_{\mu\nu} \,, \tag{2.1c}$$

$$\mathcal{L}_\chi^{\text{dim-7}} \propto \frac{1}{\Lambda^3}\left(\bar{\chi}\chi F^{\mu\nu}F_{\mu\nu} + i\bar{\chi}\gamma^5\chi F^{\mu\nu}F_{\mu\nu} + \bar{\chi}\chi F^{\mu\nu}\tilde{F}_{\mu\nu} + i\bar{\chi}\gamma^5\chi F^{\mu\nu}\tilde{F}_{\mu\nu}\right) . \tag{2.1d}$$

Here ϵe is the millicharge (mQ), μ_χ and d_χ are the mass-dimension -1 coefficients of the magnetic and electric dipole moments (MDM and EDM), a_χ and b_χ are the mass-dimension -2 coefficients of the anapole moment and charge radius interaction (AM and CR), $\sigma^{\mu\nu} \equiv i[\gamma^\mu, \gamma^\nu]/2$, and Λ is a UV scale, respectively. In the following we shall study EM form factors of χ to mass-dimension 6, where the interaction entails a single photon. At mass-dimension 7, there are four Rayleigh operators that lead to two-photon interactions with $F_{\mu\nu}$ and/or its adjoint $\tilde{F}_{\mu\nu} \equiv \epsilon_{\mu\nu\rho\sigma}F^{\rho\sigma}/2$, which requires a dedicated treatment [184]. If χ is a Majorana fermion, the mQ, MDM/EDM and CR interactions with a vector bilinear vanish. For completeness, we also list EM form factors for a complex scalar ϕ to mass-dimension 6:

$$\mathcal{L}_\phi^{\text{dim-4}} = i\epsilon e\left[\phi^*(\partial^\mu\phi) - (\partial^\mu\phi^*)\phi\right] A_\mu \,, \tag{2.2a}$$

$$\mathcal{L}_\phi^{\text{dim-6}} \propto \frac{1}{\Lambda^2}\left(i\partial^\mu\phi\partial^\nu\phi^* F_{\mu\nu} + \phi\phi^* F^{\mu\nu}F_{\mu\nu} + \phi\phi^* F^{\mu\nu}\tilde{F}_{\mu\nu}\right) , \tag{2.2b}$$

which corresponds to a millicharge, a CR operator and two mass-dimension 6 Rayleigh operators. In case of a real scalar, the millicharge and CR interactions in Eq. (2.2a) vanish.

In the classical (non-relativistic) regime, the mass-dimension 5 and 6 EM form factors correspond to the interaction Hamiltonians $\mathcal{H}_{\text{MDM}} = -\mu_\chi(\vec{\sigma}_\chi \cdot \vec{B})$, $\mathcal{H}_{\text{EDM}} = -d_\chi(\vec{\sigma}_\chi \cdot \vec{E})$, $\mathcal{H}_{\text{AM}} = -a_\chi(\vec{\sigma}_\chi \cdot \vec{J})$ and $\mathcal{H}_{\text{CR}} = -b_\chi(\vec{\nabla}\cdot\vec{E})$, respectively. Here, $\vec{\sigma}_\chi$, $\vec{E}$, $\vec{B}$ and $\vec{J}$ are a vector of Pauli matrices related to the spin of χ, electric field, magnetic field and external EM current.

	$\vec{\sigma}_\chi$	$\vec{B}$	$\vec{E}$	$\vec{J}$	$\vec{\nabla}$	MDM	EDM	AM	CR
Charge Conjugation $\mathcal{C}$	$-$	$-$	$-$	$+$	$-$	$+$	$+$	$-$	$+$
Parity $\mathcal{P}$	$+$	$+$	$-$	$-$	$-$	$+$	$-$	$-$	$+$
Time-Reversal $\mathcal{T}$	$-$	$-$	$+$	$-$	$+$	$+$	$-$	$+$	$+$

Table 2.1: The $\mathcal{CPT}$ properties of the quantities in the Hamiltonian and the effective EM form factors.

From the classical expression, we can deduce the properties of the EM form factors under discrete Lorentz transformations, *i.e.*, parity $\mathcal{P}$, charge conjugation $\mathcal{C}$ and time-reversal $\mathcal{T}$, which make the phenomenology of each effective interaction distinct. The properties under $\mathcal{C}$, $\mathcal{P}$ and $\mathcal{T}$ transformations of the various quantities in the Hamiltonian are summarized in Tab. 2.1.

First, we note that both $\mathcal{C}$, $\mathcal{P}$ and their product $\mathcal{CP}$ are a good symmetry for the MDM; therefore, in a QFT, fermions naturally inherit a MDM as long as they are charged. The spin and the resulting MDM are connected by the g-factor; for example, see the discussion in Sec. 6.2. On the other hand, the EDM maximally violates $\mathcal{P}$ and sources $\mathcal{CP}$-violation. So far, no fundamental EDM for any SM particle has been observed. Accordingly, the search for EDM becomes a clean probe for new physics. The AM, first proposed in [185], violates both $\mathcal{C}$ and $\mathcal{P}$ but conserves $\mathcal{CP}$; it has been observed in nuclei [186]. Note that in this case, the particle can even be Majorana as the AM does not arise from a multipolar expansion of the charge. The CR, as the second-order expansion of the charge form factor, is omnipresent in composite particles such as baryons. In addition, much attention has been devoted to searches for CR interactions of SM leptons as new physics is required, shall it be observed. See [187] for a summary for neutrino's CR. Similar to a charge, the CR behaves like a scalar under all discrete Lorentz transformations.

For the Feynman-diagrammatic computation, one assembles the interactions into the matrix element of the effective EM current of χ,

$$\langle \chi(p_f)|J^\mu_\chi(0)|\chi(p_i)\rangle = \bar{u}(p_f)\Gamma^\mu_\chi(k)u(p_i)\,,$$

where $p_{i,f}$ and $k = p_i - p_f$ are four-momenta. The resulting vertex function reads

$$\Gamma^\mu_\chi(k) = \epsilon e\gamma^\mu + i\sigma^{\mu\nu}k_\nu\left(\mu_\chi + id_\chi\gamma^5\right) + \left(k^2\gamma^\mu - k^\mu \not{k}\right)\left(-a_\chi\gamma^5 + b_\chi\right). \tag{2.3}$$

Here we regard the various moments as being generated at an energy scale well above the energies involved in the environments or experiments considered here, *i.e.*, they are q-independent.

The matrix element summed over spins of the emitted χ-pair is given by

$$\mathcal{T}^{\mu\nu}_\chi(k) = \mathrm{Tr}\left[(\not{p}_\chi + m_\chi)\Gamma^\mu_\chi(k)(\not{p}_{\bar{\chi}} - m_\chi)\bar{\Gamma}^\nu_\chi(k)\right], \tag{2.4}$$

with $\bar{\Gamma}^{\mu}_{\chi}(k) = \Gamma^{\mu}_{\chi}(-k)$ for the interactions considered here. In the case that the direction of χ particles is not important, we can integrate the phase space of χ-pair in their rest frame:

$$\int \frac{d\Omega^{\mathrm{R}}_{\chi\bar{\chi}}}{4\pi} \mathcal{T}^{\mu\nu}_{\chi}(k) = f(s_{\chi\bar{\chi}}) \left(-g^{\mu\nu} + \frac{k^{\mu}k^{\nu}}{s_{\chi\bar{\chi}}}\right) , \tag{2.5}$$

where, for the various effective EM interactions, $f(s_{\chi\bar{\chi}})$ reads

$$\text{mQ: } f(s_{\chi\bar{\chi}}) = \frac{4}{3}\epsilon^2 e^2 s_{\chi\bar{\chi}} \left(1 + \frac{2m^2_{\chi}}{s_{\chi\bar{\chi}}}\right) , \tag{2.6a}$$

$$\text{MDM: } f(s_{\chi\bar{\chi}}) = \frac{2}{3}\mu^2_{\chi} s^2_{\chi\bar{\chi}} \left(1 + \frac{8m^2_{\chi}}{s_{\chi\bar{\chi}}}\right) , \tag{2.6b}$$

$$\text{EDM: } f(s_{\chi\bar{\chi}}) = \frac{2}{3}d^2_{\chi} s^2_{\chi\bar{\chi}} \left(1 - \frac{4m^2_{\chi}}{s_{\chi\bar{\chi}}}\right) , \tag{2.6c}$$

$$\text{AM: } f(s_{\chi\bar{\chi}}) = \frac{4}{3}a^2_{\chi} s^3_{\chi\bar{\chi}} \left(1 - \frac{4m^2_{\chi}}{s_{\chi\bar{\chi}}}\right) , \tag{2.6d}$$

$$\text{CR: } f(s_{\chi\bar{\chi}}) = \frac{4}{3}b^2_{\chi} s^3_{\chi\bar{\chi}} \left(1 + \frac{2m^2_{\chi}}{s_{\chi\bar{\chi}}}\right) , \tag{2.6e}$$

with $s_{\chi\bar{\chi}} = k^2$ being the invariant mass square of the χ-pair. This factor will repeatedly appear in the following chapters and was first obtained in [183]. Note that when contracting Eq. (2.5) with an QED amplitude, the term containing the four-momentum transfer k^{μ} does not contribute to the squared amplitude due to the Ward Identity $\mathcal{M}_{\mu}k^{\mu} = 0$.

The effective EM interactions described by Eq. (2.1) can originate from various UV completions, *e.g.*, from a compositeness of χ [188–190] such that its internal structure generates a dipole or a charge radius, or from a UV model with additional EM charged states [191]. In the latter case, MDM and EDM are, *e.g.*, generated perturbatively by loop-induced axial or vector Yukawa interactions $y_{A,V}$ of χ with additional scalars and fermions. One can estimate the strength of MDM and EDM via $\mu_{\chi} \sim Q|y_{A,V}|^2/M$ and $d_{\chi} \sim Q\,\mathrm{Im}[y_V y^*_A]/M$ where Q is the electric charge of the mediator and M is the common mass-scale of these new states. In turn, the parametric strength of AM and CR interactions are expected as a_{χ}, $b_{\chi} \sim Q|y_{A,V}|^2/M^2$. It should be noted, however, that these estimates may not be precise as the genuine strengths of these effective interactions strongly depend on the spectrum of the new states [192]. In this thesis, focusing on the phenomenology at the energy scale of $\mathcal{O}$(keV–TeV), we shall remain agnostic about the origin of these effective interactions.

CHAPTER 3

Stellar Probes

This chapter largely follows the paper [P1]. The details of the calculation of Compton production of χ-pairs are given in App. B.1.6.

3.1 Stars as laboratories for dark sector physics

Since ancient times, stars have been essential targets for observation, propelling the progress of physics on all scales, from astronomy and cosmology to nuclear and particle physics. Measurements of the properties of stars such as their size, lifetime, and motion inform us about the underlying physics, *e.g.*, the thermodynamics, Newtonian dynamics, and GR. Progress in physics is through positive feedback: observed anomalies urge physicists to revise the conventional theories, and new ideas also propel experimentalists to build new observatories. The dark sector physics, currently under substantial investigation, is no exception in this framework.

Before constructing high-energy facilities such as the LHC, stars and cosmic rays are the places where we can observe "high-energy" phenomena. Even if we now have various experimental facilities, stars still offer a clean probe of $\mathcal{O}$(keV–MeV) physics. According to standard astrophysics, the nuclear reactions in stars result in energy loss in the form of neutrinos and photons. Neutrinos free-stream since they are weakly interacting, while photons engage in a random walk by scattering with other charged particles before escaping the stellar surface. This explains that neutrinos only take 8 minutes from the Sun's core to earth, while photons need roughly 10^5 years to propagate the same distance. These emitted particles bring us a constant stream of information about stellar properties such as temperature and chemical composition. Besides, we can study underlying microscopic physics from them, for example, neutrino oscillations and the QED interaction strength.

If the dark sector is connected to the SM through some interactions, *e.g.*, the effective EM interactions considered here, dark states can also be produced in the stars by the interactions of charged particles and/or the "massive" plasmons. The resulting dark states can either behave like neutrino (free-streaming) or photon (random walk) depending on their interaction

strength with the ambient plasma[1]. There will be additional energy loss if these dark states successfully make their way out of the stellar profile. In this way, stars can be seen as "dark" sources for dark states. The associated additional energy loss alters the stellar properties, such as their lifetime.

The variation of stellar properties will give differing consequences depending on the heat capacity of stars. Active stars such as red giants (RG), horizontal branch (HB) stars, or the Sun are systems of negative heat capacity: if energy is lost, either through standard emission or through new, anomalous processes, the decrease of total energy causes the gravitational energy to become more negative. By virtue of the virial theorem, the average kinetic energy and, thereby, the photon temperature increases. The system heats up, leading to faster consumption of its nuclear fuel while the overall stellar structure remains broadly unchanged. In contrast, dead stars such as white dwarfs or the proto-neutron star (PNS) formed in core-collapse supernova (SN) are supported by degeneracy pressure, and stellar energy loss implies a cooling of the system. Constraints are then derived based on an observationally inferred cooling curve.

The non-observation of these phenomena grants us a method to constrain the nature of the dark states. In the following paragraphs, we summarize the criteria for constraining the additional energy loss.

Red giant and horizontal branch stars In globular clusters (GCs), the population of stars on the RG branch *vs.* HB is directly related to the lifetime of stars in the respective phases. Their observationally inferred number ratio agrees with standard predictions to within 10%. Anomalous energy losses shorten the helium-burning lifetime in HB stars, creating an imbalance in the number of HB *vs.* RG stars. This constrains the luminosity in non-standard channels to be less than approximately 10% of the standard helium-burning luminosity of the HB star's core [193],

$$\int_{\text{core}} dV\, \dot{Q} < 10\% \times L_{\text{HB}} \quad (\text{HB})\,. \tag{3.1}$$

Following [193], L_{HB} will be taken as $20\,L_\odot$ for a $0.5 M_\odot$ core below. The values of the Solar mass and luminosity are $M_\odot = 1.99 \times 10^{33}$ g and $L_\odot = 3.83 \times 10^{33}$ erg/s, respectively. The computation of the anomalous energy loss rate per unit volume and time, $\dot{Q}$, will be the subject of the next section.

A constraint for RG stars may be derived from an agreement between predicted and observationally inferred core masses prior to helium ignition. Energy loss delays the latter and the core mass keeps increasing as the hydrogen burning "ashes" fall onto the degenerate He

[1]Note that even neutrino can engage in a random walk through weak interactions with other SM particles in dense environments, such as in the interior of a supernova.

core. Preventing an increase in the core mass by no more than 5% yields the constraint [193]:

$$\dot{Q} < 10\,\mathrm{erg/g/s} \times \rho \quad (\mathrm{RG})\,. \tag{3.2}$$

Here, $\dot{Q}$ is to be evaluated at an average density of $\rho = 2 \times 10^5\,\mathrm{g/cm}^3$ and a temperature of $T = 10^8\,\mathrm{K} \simeq 8.6\,\mathrm{keV}$, slightly higher than that of HB stars.

The criterion (3.2) on energy loss can be improved utilizing high precision photometric observations of GCs. For example, considering the brightness of the tip of the RG branch, [194] has provided a detailed error budget and new limits on neutrino dipole moments from GC M5 were derived based on predictions of absolute brightness in the presence of anomalous energy loss that are obtained with dedicated stellar evolutionary codes. It was found, however, that previously derived limits based on Eq. (3.2) remain largely intact, as there appears to be a slight preference for anomalous energy loss channels [194]. In the following, for our purposes it will hence be entirely sufficient to employ the simple condition (3.2) to arrive at constraints on the EM form factors.

The Sun Solar neutrino fluxes are a direct measure of the nuclear fusion rates inside the Sun. For example, not only the ^{8}B neutrino flux is very well measured but also the sensitive dependence of the responsible reaction on temperature provides an excellent handle for constraining anomalous energy losses. The ensuing constraint is then phrased in terms of the total Solar photon luminosity [195, 196], as

$$\int_{\mathrm{Sun}} dV\,\dot{Q} < 10\% \times L_\odot \quad (\mathrm{Sun})\,. \tag{3.3}$$

It is important to note that Eq. (3.3) is basically insensitive to the long-standing "solar opacity problem": the measured ^{8}B neutrino flux is situated in the overlap region of the nominal error ranges between the discrepant high- and low-metallicity determinations of the Solar chemical composition [197]; see the respective references [198] and [199]. Hence, Eq. (3.3) suffices as a criterion, awaiting further developments on Solar opacity determinations.

Supernovae and proto-neutron stars New particles that are emitted from the PNS and that stream freely may quench the electroweak rates of neutrino emission during the cooling phase. The involved processes and their dynamics are highly complex. However, an approximate but very useful criterion to constrain additional energy loss is the condition that the total luminosity due to non-standard processes should not exceed the neutrino luminosity at one second after core bounce [193],

$$\int_{\mathrm{core}} dV\,\dot{Q} < L_\nu = 3 \times 10^{52}\,\mathrm{erg/s} \quad (\mathrm{SN})\,. \tag{3.4}$$

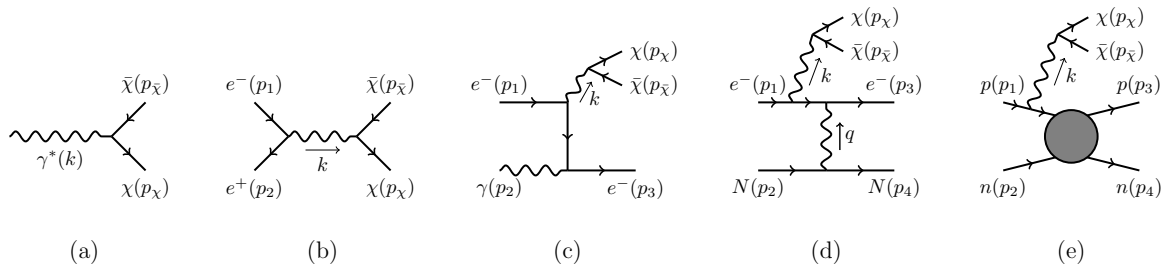

(a) (b) (c) (d) (e)

Figure 3.1: Shown are the pair production processes of $\chi\bar{\chi}$ that are calculated in this chapter, namely, (a) plasmon decay, (b) e^+e^- annihilation, (c) $2 \to 3$ Compton scattering, (d) electron bremsstrahlung and (e) nucleon bremsstrahlung; for (c)-(d) we only show one of two relevant diagrams. The four momentum of the $\chi\bar{\chi}$-producing photon is denoted by k.

The applicability of the bounds above are contingent on that the SN1987A was a neutrino-driven SN explosion[2] and that the produced particles are able to escape the dense environment of the SN remnant, assumed to be a PNS. Below, we will account for this so-called "trapping-limit" in the case of SN. For all other systems introduced above, trapping is either irrelevant, or happens in a parameter region that is excluded otherwise.

3.2 Emission of the dark states

In this section, we first provide the general formula for $\chi\bar{\chi}$ pair production in the thermal bath, before breaking it down into the most relevant pieces that dominate the in-medium production cross sections and, thereby, the stellar cooling rates. Concretely, we are considering the following fundamental dark state emission processes, highlighting in brackets the stellar system(s) for which the process is most relevant,

Plasmon decay:	$\gamma_{\rm T,L} \to \chi\bar{\chi}$	(all) ,	(3.5)
Annihilation:	$e^-e^+ \to \chi\bar{\chi}$	(SN) ,	(3.6)
Bremsstrahlung:	$e^-N \to e^-N\chi\bar{\chi}$	(RG, HB, Sun) ,	
	$n(p)\,n(p) \to n(p)\,n(p)\chi\bar{\chi}$	(SN) ,	(3.7)
Compton scattering:	$e^-\gamma_{\rm T,L} \to e^-\chi\bar{\chi}$	(all) .	(3.8)

The respective processes are decay of in-medium transverse (T) and longitudinal (L) modes of thermal photons $\gamma_{\rm T,L}$ which we will simply refer to as *plasmons*, electron-positron annihilation, electron bremsstrahlung on protons and nuclei, nucleon-nucleon bremsstrahlung (see [P1] for detailed calculations) and Compton scattering with the emission of a $\chi\bar{\chi}$-pair. Exemplary respective diagrams are shown in Fig. 3.1.

[2] For an alternative explosion mechanism where the SN1987A bounds would not apply, see [200, 201].

3.2.1 Exact formula for $\chi\bar{\chi}$ pair production

In thermal field theory, the production rate of a decoupled fermion per volume per time may be obtained from its relation to the imaginary part of its self-energy in medium [202] via

$$\dot{N}_\chi = -\int \frac{d^3\vec{p}_\chi}{(2\pi)^3}\,\frac{1}{e^{E_\chi/T}+1}\,\frac{\mathrm{Im}\,\Pi_\chi\left(E_\chi,\vec{p}_\chi\right)}{E_\chi}\,, \tag{3.9}$$

where $\mathrm{Im}\,\Pi_\chi\left(E_\chi,\vec{p}_\chi\right) = \bar{u}(p_\chi)\Sigma(E_\chi,\vec{p}_\chi)u(p_\chi)$ is the discontinuity of the thermal self-energy of χ, $\Sigma\left(E_\chi,\vec{p}_\chi\right)$; $u(p_\chi)$ and $\bar{u}(p_\chi)$ are free particle spinors with four-momentum $p_\chi = (E_\chi,\vec{p}_\chi)$. To lowest order in the dark coupling, $\Sigma(E_\chi,\vec{p}_\chi)$ is found from the one-loop diagram with a dressed photon propagator attached to the χ fermion line. A general exposition on calculating discontinuities in the thermal plasma is found in [202, 203].

Below, in Eq. (3.11), we are using a different formulation and the equivalence may be appreciated in the following way: when cutting the self-energy diagram for χ, the optical theorem implies that the production rate may also be obtained by computing all graphs where a photon γ^* of four-momentum $k = p_\chi + p_{\bar{\chi}}$ emerges from a SM current and is being dotted into the dark current of the $\chi\bar{\chi}$ pair. The SM-process that leads to the creation of γ^* is in turn related to the imaginary part of the photon self-energy in the medium, $\mathrm{Im}\,\Pi^{\mu\nu}$, where

$$\Pi^{\mu\nu} = (\epsilon^\mu_{\mathrm{T},1}\epsilon^\nu_{\mathrm{T},1} + \epsilon^\mu_{\mathrm{T},2}\epsilon^\nu_{\mathrm{T},2})\Pi_\mathrm{T} + \epsilon^\mu_\mathrm{L}\epsilon^\nu_\mathrm{L}\Pi_\mathrm{L}\,. \tag{3.10}$$

Here $\epsilon_{\mathrm{T,L}}$ are the transverse and longitudinal photon polarization vectors and $\Pi_{\mathrm{L,T}}(k)$ is the thermal photon self-energy for the respective polarization; explicit expressions are given in App. B.1.1. Identifying the leading contributions to $\mathrm{Im}\,\Pi_{\mathrm{L,T}}(k)$ in various mediums then allows to account for the dominant χ pair production channels.

The exact differential production rate per volume of $\chi\bar{\chi}$ pairs via a photon of 4-momentum $k = (\omega,\vec{k})$ emerging from *any* SM process to lowest order in the dark current can be obtained by borrowing the results from dilepton production in hot matter, see, *e.g.*, [204, 205]. Adopted to our purposes (see App. B.1.2) it reads

$$\frac{d\dot{N}_\chi}{ds_{\chi\bar{\chi}}} = -\sum_{i=\mathrm{T,L}} g_i \int \frac{d^3\vec{k}}{(2\pi)^3}\,\frac{1}{e^{\omega/T}-1}\,\frac{\mathrm{Im}\,\Pi_i(\omega,\vec{k})}{\omega}\,\frac{f(s_{\chi\bar{\chi}})}{16\pi^2|s_{\chi\bar{\chi}}-\Pi_i|^2}\sqrt{1-\frac{4m_\chi^2}{s_{\chi\bar{\chi}}}}\,, \tag{3.11}$$

where $s_{\chi\bar{\chi}} = k^2$ is the invariant mass of the χ-pair and the internal degrees of freedom of two polarization modes are $g_\mathrm{T} = 2$, $g_\mathrm{L} = 1$. The differences in the various interaction possibilities are entirely captured in $f(s_{\chi\bar{\chi}})$; see Eq. (2.6). Equation (3.11) is the general expression of the weakly coupled χ pair-production rate from the thermal medium; details are found in App. B.1.2.

The contribution to $\chi\bar{\chi}$ production to leading order in α is given by the *pole* in Eq. (3.11), *i.e.*, for $s_{\chi\bar{\chi}} = \mathrm{Re}\,\Pi_{\mathrm{T,L}}$. When this condition is met, Eq. (3.11) reduces to the decay rate of

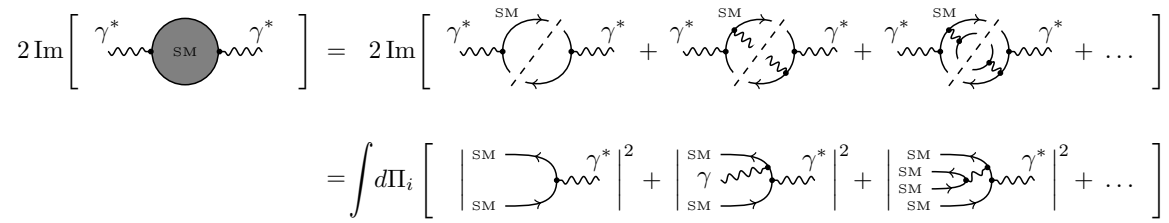

Figure 3.2: Optical theorem relating the imaginary part of the photon self energy to the sum of all SM processes that create an off-shell photon γ^*. The first equality shows the leading individual contributions to the self-energy. When the latter loop-diagrams are cut, they correspond to the scattering processes shown in the second line, where $d\Pi_i$ symbolizes the phase space integral of all external particles, except γ^*. When the scattering diagrams are deformed in a way such that two SM particles are in the initial state, the processes correspond to annihilation, Compton scattering and bremsstrahlung (from left to right). Any diagrams with χ particles involved yield contributions to the production rate in Eq. (3.11) that are of higher order in the dark coupling.

thermal photons $\gamma_{\mathrm{T,L}} \to \chi\bar{\chi}$. Hence, resonant $\chi\bar{\chi}$ production is fully accounted for by $\gamma_{\mathrm{T,L}}$ decay. The decay itself becomes possible by virtue of the in-medium (squared) mass of $\gamma_{\mathrm{T,L}}$: it is given by $\mathrm{Re}\,\Pi_{\mathrm{T,L}}(\omega_{\mathrm{T,L}}, \vec{k})$, where $\omega_{\mathrm{T,L}}$ denotes the solution of $\omega(|\vec{k}|)$ of the corresponding longitudinal and transverse dispersion relations $\omega^2 - |\vec{k}|^2 - \mathrm{Re}\,\Pi_{\mathrm{T,L}}(\omega, \vec{k}) = 0$. Plasmon decay is discussed in the following subsection, and explicitly calculated in Eqs. (B.47)–(B.50) in App. B.1. The expressions for $\mathrm{Re}\,\Pi_{\mathrm{T,L}}$ and finite-temperature dispersion relations are found in Eqs. (B.32) and (B.33).

Production *off-the-pole* to Eq. (3.11) can be elucidated by studying the contributions to $\mathrm{Im}\,\Pi_{\mathrm{T,L}}$ using the optical theorem, illustrated in Fig. 3.2. The left hand side shows the fully dressed vacuum polarization of an off-shell photon γ^*, found by considering loop-diagrams of increasing order in α illustrated in the first equality. When those loop diagrams are cut, their imaginary parts are given by the tree-level production processes for γ^* shown in the last equality. The leading α contribution to $\mathrm{Im}\,\Pi_{\mathrm{T,L}}$ is then given by the electron one-loop diagram. Although it is well known that on-shell plasmon decay $\gamma_{\mathrm{T,L}} \to e^- e^+$ remains forbidden at finite temperature [206], an electron loop still contributes to $\mathrm{Im}\,\Pi_{\mathrm{T,L}}$ in the off-shell case. The associated process is then $e^- e^+$ annihilation to $\chi\bar{\chi}$, *i.e.*, process (3.6).

The second and third diagrams in the last line of Fig. 3.2 are related to $\chi\bar{\chi}$ production in Compton scattering and bremsstrahlung. Here, it is important to note that $s_{\chi\bar{\chi}} = \mathrm{Re}\,\Pi_{\mathrm{T,L}}$ can also be met in the photon propagator that produces the χ-pair with invariant squared mass $s_{\chi\bar{\chi}}$. However, including such resonances would amount to double countings. As we have seen above, the pole contributions are already captured by plasmon decay[3]. In our

[3] A heuristic argument on such double counting was also given in the context of neutrino pair emission in Sec. 2.5 of [207]. It furthermore appears to us, that double counting may have occurred in [173] where a potentially resonant bremsstrahlung process was added to the plasmon decay contribution.

calculations, we explicitly avoid this situation by setting $\Pi_{\mathrm{L,T}} \to 0$ in the propagator if the resonance is kinematically allowed for the photon that directly couples to the dark current. We have numerically verified that our results remain otherwise unaffected by neglecting the thermal shift in the photon propagator.

Finally, we note that there is also a potential double counting between Compton scattering and bremsstrahlung processes, which happens when in the bremsstrahlung process the photon exchanged between two initial particles carries 4-momentum q (see Fig. 3.1.d) that satisfies the dispersion relation $q^2 - \mathrm{Re}\,\Pi_{\mathrm{L}}(q^0, \vec{q}) = 0$, leading to the exchange of an on-shell longitudinal plasmon. The process then becomes equivalent to Compton scattering $e/N + \gamma_{\mathrm{L}} \to e/N + \chi + \bar{\chi}$. This has been reported for axion production processes, where the contribution of latter is mostly covered by that of bremsstrahlung [208]. To avoid such double counting, we take the static approximation ($q^0 = 0$) for the thermal mass of the photon exchanged in bremsstrahlung processes, which is a valid limit as the nucleon mass is large. As $q^2 < 0$ and $\Pi_{\mathrm{L}}(q^0 = 0, \vec{q})$ is always positive, the exchanged photon cannot become on-shell in bremsstrahlung processes, thus double counting is avoided; see Sec. 3.2.4 for more details.

3.2.2 $\gamma_{\mathrm{T,L}}$ decay

The on-shell process of photon decay to $\chi\bar{\chi}$ (Fig. 3.1.a) becomes possible in the medium and has an important analogy in the literature, the plasmon decay to neutrinos. Since the dispersion relation for transverse and longitudinal thermal photons are distinct, it is again helpful to separate the two polarizations in the calculation. Explicitly, we obtain for the decay rate per degree of freedom:

$$\Gamma_{\mathrm{T,L}} = \frac{1}{16\pi} Z_{\mathrm{T,L}} \sqrt{1 - \frac{4m_\chi^2}{\omega_{\mathrm{T,L}}^2 - |\vec{k}|^2}}\, \frac{f(\omega_{\mathrm{T,L}}^2 - |\vec{k}|^2)}{\omega_{\mathrm{T,L}}}\,, \tag{3.12}$$

where $\omega_{\mathrm{T,L}} = \omega_{\mathrm{T,L}}(|\vec{k}|)$ for each polarization mode, as defined above. Details on the definition of the wave function renormalization factors $Z_{\mathrm{T,L}}$ and the calculation are again given in App. B.1. In the limit of $m_\chi \to 0$, the decay widths for MDM agree with the well-known formulas for plasmon decay to a neutrino pair [193].

For the plasmon decay processes, the energy loss rate can be expressed as [193]

$$\dot{Q}_{\mathrm{decay,T}} = \frac{2}{2\pi^2} \int_0^\infty d|\vec{k}|\, \frac{|\vec{k}|^2 \Gamma_{\mathrm{T}} \omega_{\mathrm{T}}}{e^{\omega_{\mathrm{T}}/T} - 1} \Theta(\omega_{\mathrm{T}}^2 - |\vec{k}|^2 - 4m_\chi^2)\,, \tag{3.13}$$

$$\dot{Q}_{\mathrm{decay,L}} = \frac{1}{2\pi^2} \int_0^{k_{\max}} d|\vec{k}|\, \frac{|\vec{k}|^2 \Gamma_{\mathrm{L}} \omega_{\mathrm{L}}}{e^{\omega_{\mathrm{L}}/T} - 1} \Theta(\omega_{\mathrm{L}}^2 - |\vec{k}|^2 - 4m_\chi^2)\,, \tag{3.14}$$

where Θ is the Heaviside step function. The expression for $k_{\max}$ is given in Eq. (B.34). For a non-relativistic medium (HB, RG, Sun), the dispersion relation crosses the light-cone at $|\vec{k}| =$

$k_{\rm max}$, signaling the damping of longitudinal modes, *i.e.*, Landau damping; for a relativistic plasma (SN), $k_{\rm max} \to \infty$. The relative factor of 2 between the expressions reflects the counting of polarization degrees of freedom. Finally, the last factor is a kinematic restriction on the phase space, $\omega_{\rm T,L}^2 - |\vec{k}|^2 \geq 4m_\chi^2$. For transverse mode thermal photons, the integral becomes bounded from below since $\omega_{\rm T}^2 - |\vec{k}|^2$ increases as $|\vec{k}|$ increases according to the dispersion relation. For the longitudinal case, the integral is additionally bounded from above since the trend in $\omega_{\rm L}^2 - |\vec{k}|^2$ with respect to $|\vec{k}|$ is reversed.

3.2.3 e^-e^+ annihilation

The degenerate plasma of the PNS core with temperature $T \gg m_e$ contains a population of e^+, allowing for dark state pair-production through e^-e^+ annihilation (Fig. 3.1.b). The calculation for the pair production cross section is detailed in App. B.1.5.

In terms of the invariant $s = (p_1 + p_2)^2$ and the sum/difference of incoming $e^\mp$ energies $E_{1,2}$ in the frame of the thermal bath, *i.e.*, $E_\pm \equiv E_1 \pm E_2$, the corresponding cross section mediated by the transverse polarization part of the propagator reads

$$\sigma_{\rm T} = \frac{\alpha\left[sE_-^2 + (4m_e^2 + s)(E_+^2 - s)\right]}{8\sqrt{s(s-4m_e^2)}(E_+^2 - s)(s - \Pi_{\rm T})^2}\sqrt{1 - \frac{4m_\chi^2}{s}}f(s)\,, \tag{3.15}$$

with $f(s)$ given in Eq. (2.6). For the longitudinal part we obtain

$$\sigma_{\rm L} = \frac{\alpha\left[s(E_+^2 - E_-^2 - s)\right]}{8\sqrt{s(s-4m_e^2)}(E_+^2 - s)(s - \Pi_{\rm L})^2}\sqrt{1 - \frac{4m_\chi^2}{s}}f(s)\,. \tag{3.16}$$

Note that there is no interference term between the two. Furthermore, the sum of both cross sections, $\sigma_{\rm T} + \sigma_{\rm L}$, becomes Lorentz invariant in the limit of $\Pi_{\rm T,L} \to 0$.[4]

Before using Eq. (3.15) and Eq. (3.16) in the calculation of the energy loss rate, a comment on the analytic structure is in order. Although it appears that the process may be significantly enhanced when $s = {\rm Re}\,\Pi_{\rm T,L}$, this condition is never met: for the same reason that the decay of thermal photons into an electron-positron pair ($\gamma_{\rm T,L} \to e^-e^+$) is forbidden [206], the finite-temperature corrections to m_e prevent the process (3.6) from going on-shell. It is for this reason that we have explicitly evaluated the thermal electron mass for the employed radial profile of the PNS; see App. B.1.1. In other words, we use a thermal electron mass in SN, and use the zero-temperature electron mass in HB, RG and Sun, where e^-e^+ annihilation is of little relevance. The values of chemical potential μ_e are self-consistently adjusted to match the numerical PNS profiles from the literature (see below).

[4] We use a definition of the cross section for which the Møller velocity instead of the relative velocity $|\vec{v}_1 - \vec{v}_2|$ appears. At zero temperature, this makes the cross section a Lorentz invariant quantity, see the discussion in [209].

The energy loss rate of e^-e^+ annihilation is found by weighing the emission process by the total radiated final-state energy $E_3 + E_4 = E_1 + E_2$ and by the probability of finding the initial states with the respective energies E_1 and E_2,

$$\dot{Q}_{\rm ann} = \int d\Pi_{i=1,2,3,4}\,(2\pi)^4\delta^4(p_1+p_2-p_3-p_4) g_{e^-} g_{e^+} f_{e^-} f_{e^+} \frac{1}{4}\sum_{\rm spins} |\mathcal{M}_{\rm ann}|^2 (E_1+E_2)\,. \tag{3.17}$$

Here, $f_{e^\mp}$ are the phase-space distributions of $e^\mp$, with internal degrees of freedom $g_{e^\mp} = 2$, and $|\mathcal{M}_{\rm ann}|^2$ is the squared matrix element for e^-e^+ annihilation into a dark state pair. In Eq. (3.17) a Pauli-blocking factor induced by χ and $\bar{\chi}$ is neglected; we have verified that this does not affect the derived constraints. Finally, $d\Pi_i = \prod_i d^3\vec{p}_i (2\pi)^{-3}(2E_i)^{-1}$ is the Lorentz invariant phase space element.

The energy loss rate can be written in terms of the cross sections $\sigma_{\rm T,L}$. Borrowing from the discussion on the phase space in [210], we find explicitly

$$\dot{Q}_{\rm ann} = \int_{4m_{\rm th}^2}^{\infty} ds \int_{\sqrt{s}}^{\infty} dE_+ \int_{-\sqrt{(1-4m_e^2/s)(E_+^2-s)}}^{\sqrt{(1-4m_e^2/s)(E_+^2-s)}} dE_- \,\frac{1}{64\pi^4} g_{e^-} g_{e^+} f_{e^-} f_{e^+} E_+ \sqrt{s(s-4m_e^2)}\,\sigma_{\rm T,L}\,. \tag{3.18}$$

The distribution functions f_{e^-} and f_{e^+} read

$$f_{e^\mp} = \frac{1}{e^{(E_+ \pm E_- \mp 2\mu_e)/2T}+1}\,.$$

Here, μ_e is the chemical potential of electrons and T is the temperature. The threshold mass $m_{\rm th}$ is equal to $\max\{m_e, m_\chi\}$.

3.2.4 Compton scattering

For $2 \to 3$ Compton scattering ($e^-/N + \gamma_{\rm T,L} \to e^-/N + \chi + \bar{\chi}$) with an initial $\gamma_{\rm T,L}$ (Fig. 3.1.c), we calculate the differential cross section via

$$\frac{d\sigma_{2\to3}}{ds_{\chi\bar{\chi}}} = \sigma_{2\to2}(s_{\chi\bar{\chi}}) \frac{f(s_{\chi\bar{\chi}})}{16\pi^2 s_{\chi\bar{\chi}}^2} \sqrt{1-\frac{4m_\chi^2}{s_{\chi\bar{\chi}}}}\,. \tag{3.19}$$

Here, $\sigma_{2\to2}(s_{\chi\bar{\chi}})$ is the cross section of the two-body Compton scattering with the final-state photon having a mass $\sqrt{s_{\chi\bar{\chi}}}$, given in Eqs. (B.62) and (B.63) for the two polarizations. We are only required to consider the process on electrons, $e^- + \gamma_{\rm T,L} \to e^- + \chi + \bar{\chi}$, as Compton scattering on protons is strongly suppressed. Following the treatment in [207] and our discussion above, we neglect the thermal mass of the final-state photon in $\sigma_{2\to2}$ to avoid any potential double counting with $\gamma_{\rm T,L}$ decay. For the initial-state photon in the integration

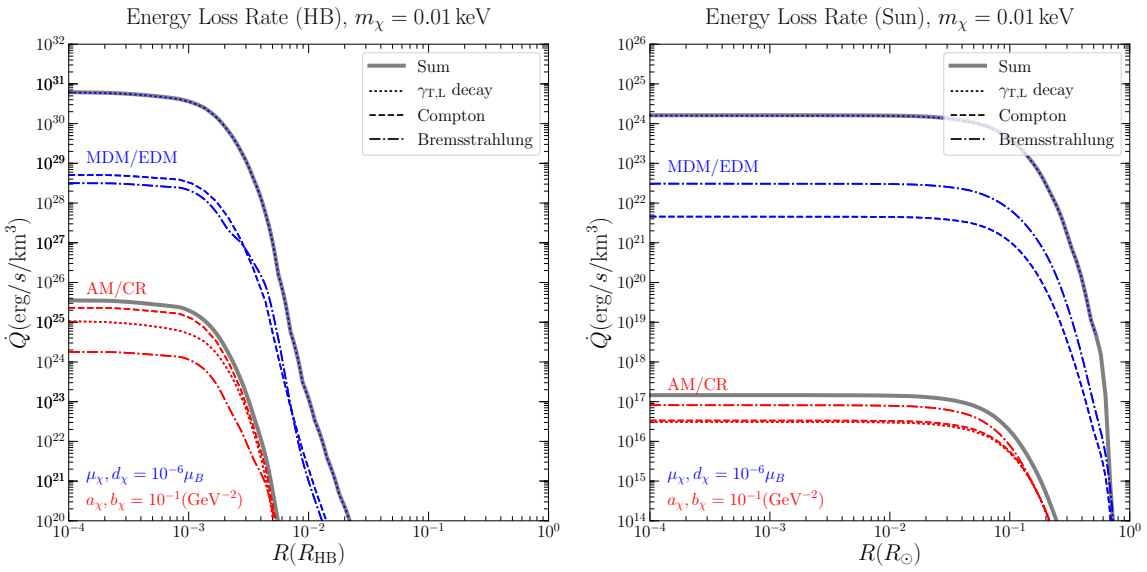

Figure 3.3: *Left:* Energy loss rates as a function of fractional stellar radius from $\gamma_{\mathrm{T,L}}$ decay (dotted lines), Compton production (dashed lines) and electron bremsstrahlung (dash-dotted lines) for $m_\chi = 0.01\,\mathrm{keV}$ and $\mu_\chi(\mathrm{or}\ d_\chi) = 10^{-6}\,\mu_B$ and $a_\chi(\mathrm{or}\ b_\chi) = 0.1/\mathrm{GeV}^2$ in the representative HB star we consider. The sum of all processes is shown by the thick gray line, which for MDM/EDM interactions practically coincides with plasmon decay. *Right:* The same processes as in the left panel but for the Sun.

of energy loss rate, Eq. (3.20) below, the thermal mass is properly taken in account through the dispersion relation stated in Eq. (B.33).

Furthermore, note that there is no double counting between the Compton process and bremsstrahlung in either of our treatment. A double counting would appear if the t-channel photon exchange in bremsstrahlung, with 4-momentum q (see Fig. 3.1.d), goes on resonance. This is in principle possible for the longitudinal mode, since Π_{L} in the propagator could become negative once the dispersion relation of γ_{L} crosses the light cone. Nevertheless, in the electron bremsstrahlung process discussed below—most relevant for RG, HB and the Sun—the proton recoil and hence the energy exchange are extremely small. Therefore, the propagator can be taken in the static limit (energy exchange $q^0 \to 0$). This limit amounts to Debye screening, characterized by $\Pi_{\mathrm{L}}(q^0 \to 0, |\vec{q}|)$. Since the screening scale is always positive, a resonance is never met. Therefore, we include the contribution from $e^- + \gamma_{\mathrm{L}} \to e^- + \chi + \bar{\chi}$ to capture the t-channel resonance contribution of electron bremsstrahlung, although it is less important than plasmon decay.

The energy loss rate from Compton scattering is calculated in a similar way as Eq. (3.17), but here E_{loss} is given by the energy carried by the virtual photon in the medium frame,

$$\dot{Q}_{\mathrm{Compton}} = \int d\Pi_{i=1,2}\, 4E_1E_2v_M g_e g_{\mathrm{T,L}} f_1 f_2 (1-f_3) E_{\mathrm{loss}} \sigma^{\mathrm{T,L}}_{2\to 3}\,, \tag{3.20}$$

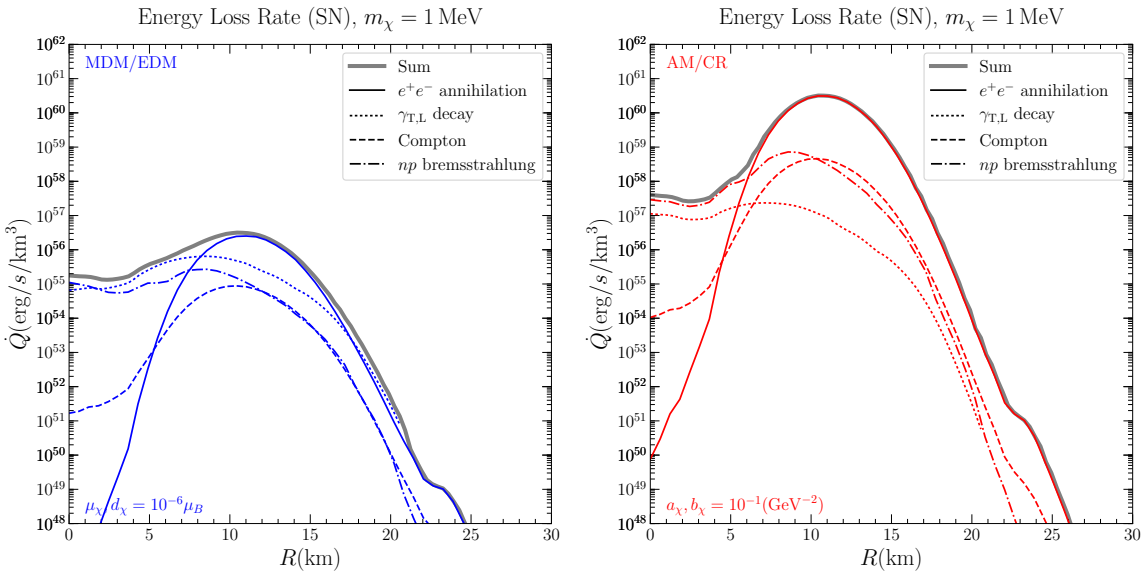

Figure 3.4: *Left:* Energy loss rates inside the PNS for MDM/EDM interactions with μ_χ(or d_χ) = $10^{-6}\,\mu_B$ and $m_\chi = 1\,\mathrm{MeV}$ are shown for all computed processes, namely, e^-e^+ annihilation (thin solid line), $\gamma_{\mathrm{T,L}}$ photon decay (dotted line), Compton production (dashed line) and np bremsstrahlung (dash-dotted line). The sum of all contributions is the thick solid line. *Right:* The same processes as in the left panel but for AM/CR interactions with a_χ(or b_χ) = $0.1/\mathrm{GeV}^2$.

where $f_{1,2,3}$ are the distribution functions of the incoming electron, $\gamma_{\mathrm{T,L}}$ and outgoing electron, respectively, with $g_e = g_{\mathrm{T}} = 2$ and $g_{\mathrm{L}} = 1$ being the internal degrees of freedom for the incoming electron and $\gamma_{\mathrm{T,L}}$. Pauli blocking is accounted for by including the factor $(1 - f_3)$. The energy loss $E_{\mathrm{loss}} = E_\chi + E_{\bar{\chi}}$ can be expressed in terms of variables defined in the medium frame; see Eq. (B.64). Moreover, for RG, HB and the Sun, the relativistic corrections induced by transforming from the CM frame to the medium frame are very small, and are neglected for simplicity.

3.2.5 eN bremsstrahlung

In this subsection, we consider dark state pair production from bremsstrahlung of electrons on protons or other nuclei (Fig. 3.1.d). Similar to the Compton scattering above, we also relate the $2 \to 4$ cross section to a $2 \to 3$ process of $eN \to eN + \gamma^*_{\mathrm{T,L}}$ in which the emitted photon, $\gamma^*_{\mathrm{T,L}}$, has an invariant mass $\sqrt{s_{\chi\bar{\chi}}}$,

$$\frac{d\sigma_{2\to4}}{ds_{\chi\bar{\chi}}} = \sigma_{2\to3}(s_{\chi\bar{\chi}})\frac{f(s_{\chi\bar{\chi}})}{16\pi^2 s^2_{\chi\bar{\chi}}}\sqrt{1 - \frac{4m_\chi^2}{s_{\chi\bar{\chi}}}}\,. \tag{3.21}$$

In the following we shall only consider photon-emission from electrons, as the emission from the nuclear leg is suppressed by a factor of $(Zm_e/m_N)^2 \ll 1$ where Z and m_N are the charge

and mass of the proton/nucleus. Furthermore, ordinary electron-electron bremsstrahlung is a quadrupole emission process and correspondingly smaller in practice. We therefore also neglect such production channel.

The eN process is sensitive to the details of in-medium corrections. To this end, recall that the t-channel photon exchange in Fig. 3.1.d has a well-known Coulomb divergence in the limit of vanishing momentum transfer. This issue is mitigated by two factors: first, the divergence is not met kinematically as long as $m_\chi \neq 0$ since a minimum momentum transfer is necessary to create the final-state pair. Second, the medium itself regulates the process through the Debye screening of bare charges characterized by a momentum scale k_D. The latter appears as the static limit of $\Pi_{\rm L}(q^0 \to 0, \vec{q})$ and for a classical plasma reads

$$k_D^2 = \frac{4\pi\alpha n_e}{T} + \text{ion-contributions}, \tag{3.22}$$

where n_e is the electron number density.

For the numerical results, we have calculated $\sigma_{2\to3}$ in Eq. (3.21) using the propagator (B.31), neglecting, for simplicity, ion contributions. We separate the squared amplitude into transverse and longitudinal parts and include the static limits of $\Pi_{\rm T,L}$ in the respective propagators. For the longitudinal part, the zero-temperature propagator q^{-2} is replaced by $(q^2 - k_D^2)^{-1}$. In contrast, there is no magnetic screening in the static limit ($\Pi_{\rm T}(q^0 \to 0, |\vec{q}|) = 0$), hence there is no thermal screening for the propagator of the transverse mode. We find that in the non-relativistic limit the contribution of the longitudinal mode dominates.

To avoid any double counting between this process and $\gamma_{\rm T,L}$ decay, we need to subtract the contribution when the virtual photon that directly couples to χ goes on-shell. As stated above, this is achieved by setting $\Pi_{\rm T,L}$ in the corresponding propagator to zero. Since this should over-estimate the production rate at $s_{\chi\bar{\chi}} \leq \Pi_{\rm T,L}$, we have also tested an opposite option of choosing $\Pi_{\rm T,L} \to -\Pi_{\rm T,L}(E_\chi + E_{\bar{\chi}})$ to avoid the singularity, which under-estimates the production rate. We find that both prescriptions lead to same results at percent level, which justifies our simplification of taking $\Pi_{\rm T,L} = 0$ for the photon that directly couples to the dark states.

For dark state pair production in e^- bremsstrahlung on protons and nuclei, the energy loss rate is expressed as

$$\dot{Q}_{\rm brem} = \int d\Pi_{i=1,2}\, 4E_1E_2v_M g_1g_2f_1f_2(1-f_3)E_{\rm loss}\sigma_{2\to4}\,, \tag{3.23}$$

where $f_{1,2,3}$ are the distribution functions of the incoming electron, proton/nucleus and outgoing electron, with $g_{1,2}$ the internal degrees of freedom for the incoming particles. We have neglected the Pauli blocking factor for final-state proton/nucleus as it plays little role. The Møller velocity $v_M = F/(E_1E_2)$ is given in terms of the flux factor F found in Eq. (B.60).

The energy carried-away by the dark states is $E_{\rm loss} = E_\chi + E_{\bar\chi}$ and its expression in the medium frame is given in Eq. (B.69).

Making the approximation that protons and other nuclei are at rest, their phase-space integral gives $\int d\Pi_2\, f_2 = n_N/(2m_N g_2)$ where n_N is the number density of the protons/nuclei. Hence, we arrive at

$$\dot{Q}_{\rm brem} = \int_{m_e+2m_\chi}^{\infty} dE_1\, \frac{2n_N E_1 E_2 v_M}{(2\pi)^2 m_N} |\vec{p}_1| g_1 f_1 (1-f_3) E_{\rm loss} \sigma_{2\to 4}, \tag{3.24}$$

with $|\vec{p}_1| = \sqrt{E_1^2 - m_e^2}$ and where $\sigma_{2\to4}$ is obtained from integrating Eq. (3.21) over appropriate boundaries (see App. B.1.7). Generically, bremsstrahlung is less effective when pair annihilation or plasmon decay are open as production channels, but it can be dominant at low temperatures where the latter processes are kinematically suppressed.

Before ending this subsection, it is worth commenting on the so-called soft-photon approximation, which states that in the limit that the emitted photon energy is small compared to the available kinetic energy (*i.e.*, $\omega \ll E_{\rm kin}$), the process of $eN \to eN + \gamma^*_{\rm T,L}$ factorizes into a product of elastic scattering times a factor describing the additional emission of $\gamma^*_{\rm T,L}$. While this approximation works well for the emission of a massless photon, it breaks down if the off-shell photon's *effective* mass is large, $\sqrt{s_{\chi\bar\chi}} \sim E_{\rm kin}$. Overall, we find that the soft photon approximation describes the $2 \to 4$ process well for small m_χ in the non-relativistic limit. However, for $2m_\chi \sim E_{\rm kin}$ or for relativistic initial states the approximation fails, and it is ultimately related to the UV-sensitivity of the cross section; see App. B.1.8 for details. Even though calculations simplify considerably in the soft photon limit, it cannot be applied for the whole m_χ-range in electron bremsstrahlung and we therefore calculate $\sigma_{2\to4}$ exactly, relegating details of the calculation to App. B.1.7. However, the soft-photon approximation is adopted in its region of validity to estimate the energy loss from nucleon-nucleon bremsstrahlung in [P1].

3.3 Constraints on the effective coupling

After calculating the energy loss rates induced by the above discussed processes in each stellar environment (*e.g.*, see Figs. 3.3 and 3.4), we apply the luminosity criteria introduced in Sec. 3.1 to obtain the upper bounds on the EM form-factors of light dark states. Here we focus on mass-dimension 5 and 6 operators and refer the reader to [170, 173] for constraints on the mass-dimension 4 mQ interaction.

3.3.1 Limits from RG, HB, and Sun

In this subsection, we derive the constraints coming from HB and RG stars utilizing the above calculated anomalous energy loss rates. For HB, we consider a representative star of

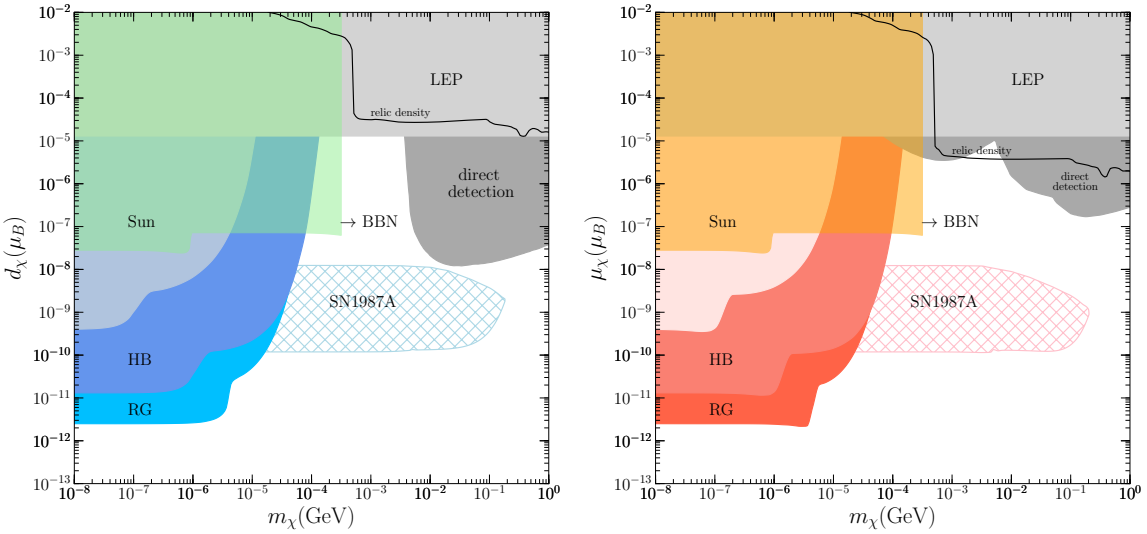

Figure 3.5: Summary of constraints on the EM form factors for mass-dimension 5 operators, *i.e.*, EDM (left) and MDM (right). Colored exclusions are derived in this chapter. Direct detection (only applying to dark matter) and LEP bounds are taken from [183]. On the solid black line the thermal freeze-out abundance matches the DM density.

$0.8\,M_\odot$ and utilize the stellar profiles for density, temperature and chemical partition between hydrogen and helium from [193, 211], reproduced in Fig. B.3 in App. B.1.1. The luminosity of its helium-burning core is $L_{\rm HB} = 20 L_\odot$ to which Eq. (3.1) is then applied. For RG we use the prescription detailed below Eq. (3.2): a $0.5\,M_\odot$ helium core with a constant density of $\rho = 2 \times 10^5\,{\rm g/cm}^3$ and a temperature $T = 10^8\,{\rm K}$.

For the Sun, we use the standard Solar model BP05(OP) [212] to calculate the total power radiated into $\chi\bar{\chi}$ which in turn is constrained from Eq. (3.3). For bremsstrahlung we take the contribution of electron scattering on H, ^{4}He and other less abundant nuclei (^{3}He, C, N, and O). For simplicity, we assume all targets are in a fully ionized state. We find numerically that the contribution from the less abundant nuclei constitutes 10% of the total energy loss rate from bremsstrahlung, as the coherent enhancement from atomic charge number Z somewhat compensates for their scarcity in number.

The energy loss rates as a function of fractional stellar radius for HB stars (Sun) for mass-dimension 5 and 6 operators are shown in the left (right) panel of Fig. 3.3 for $m_\chi = 10\,{\rm eV}$ and μ_χ(or d_χ) $= 10^{-6}\,\mu_B$ and a_χ(or b_χ) $= 0.1\,{\rm GeV}^{-2}$. MDM and EDM as well as AM and CR lines essentially yield identical results. This is owed to the fact that production proceeds in the kinematically unsuppressed region $T \gg m_\chi$ for which the energy loss rates match; the γ^5 factor discriminating the interactions of same mass-dimension only plays a role when χ particles become non-relativistic, hence close to kinematic endpoints. As can be seen, for mass-dimension 5 operators the decay process (dotted lines) dominates over bremsstrahlung (dash-dotted lines) and Compton scattering (dashed lines) processes in both HB stars and

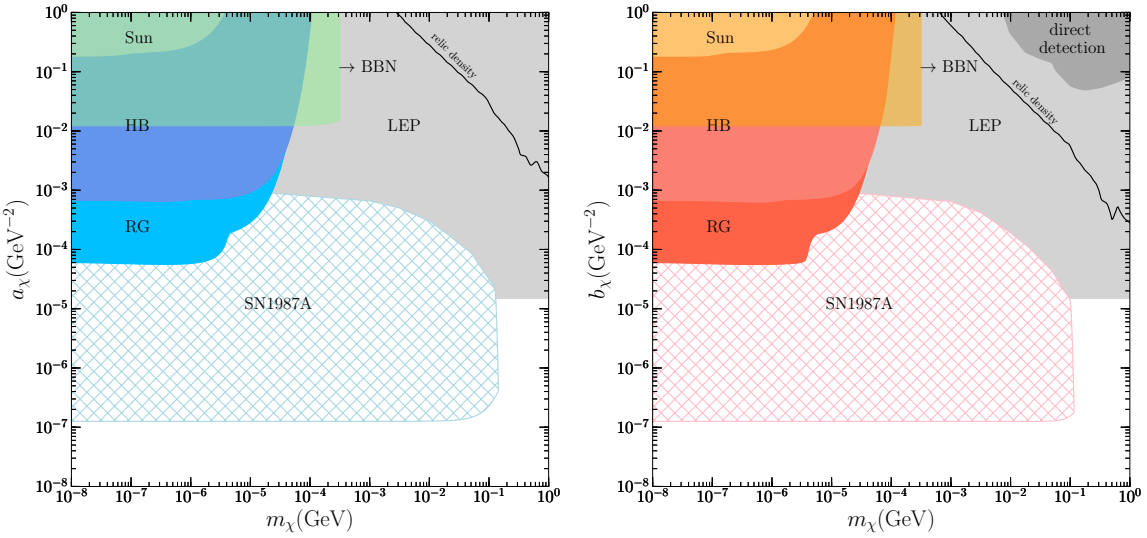

Figure 3.6: Summary of constraints on the EM form factors for mass-dimension 6 operators, *i.e.*, AM (left) and CR (right); labels are the same as in Fig. 4.4.

Sun. For mass-dimension 6 operators, the contribution of Compton scattering is comparable to that of decay processes in HB stars while in the Sun all three processes are of comparable importance.

Applying the criteria for the maximum allowable energy loss of Sec. 3.1, we obtain the excluded shaded regions in Figs. 4.4 and 4.5 as labeled. The strongest limits are provided by RG stars. They have a higher core temperature, $T = 8.6\,\mathrm{keV}$, compared to HB stars or the Sun, favoring an emission process that is UV-biased because of the considered higher-dimensional operators. In the low mass region, for $2m_\chi < \omega_p$, the limits are governed by $\gamma_{\mathrm{T,L}}$ decays, and become independent of χ mass quickly. Once the decay process is kinematically forbidden, the limits become determined by the bremsstrahlung and Compton scattering processes. As can be seen, the critical values of m_χ where this happens for RG stars, HB stars, and the Sun are reflective of the differing core-plasma frequencies (B.30) of the respective systems. Furthermore, the mass-dimension 5 constraints on MDM and EDM are practically identical; differences only appear in the kinematic endpoint region.

3.3.2 Limits from SN1987A

Limits on χ-photon interactions from SN1987A have previously been estimated in [183], largely following the approach of [173], and considering e^-e^+ annihilation but with plasmon decay neglected. Here we revisit these constraints in light of a more detailed calculation. Dark state pairs with mass $m_\chi \lesssim 400\,\mathrm{MeV}$ can be efficiently produced inside the PNS, predominantly through e^-e^+ annihilation as positrons are thermally supported. Nevertheless,

we will consider all processes in Fig. 3.1 except for electron bremsstrahlung as it is significantly weaker than the others; see Fig. 3.4 for one example with $m_\chi = 1\,\mathrm{MeV}$.

When the particles stream freely after production and are hence able to escape from the PNS core, the limit Eq. (3.4) applies. We set the size of the PNS core to be $r_{\mathrm{core}} = 15\,\mathrm{km}$ and model the PNS from which $\chi\bar{\chi}$ pairs are emitted using the simulation results of a $18\,M_\odot$ progenitor in [213]; see Fig. B.3 in App. B.1.1. Notice that such simulation results are based on an artificial neutrino-driven explosion method and should be taken with a grain of salt. We adopt the total energy density $\rho(r)$, temperature $T(r)$ and electron abundance $Y_e(r)$ profiles at 1 s after the core bounce. The number density of baryons can be computed as $n_b(r) \simeq \rho(r)/m_p$ and the number density of electrons can be written as $n_e(r) \simeq n_b(r)Y_e(r)$. Other quantities such as chemical potential of electrons $\mu_e(r)$, plasma frequency $\omega_p(r)$ and effective electron mass $m_e^{\mathrm{eff}}(r)$ are derived from $n_e(r)$ and $T(r)$. $m_e^{\mathrm{eff}}(r)$ is recursively solved at each radius using Eq. (B.41); see App. B.1.1 for details. In the calculations that relate to the anomalous emission, m_e is understood to be m_e^{eff}.

The result is shown by the lower boundary of the region labeled SN1987A in Figs. 4.4 and 4.5. Compared to the results in [183] where only e^-e^+ annihilation was taken into account, the constraint for MDM and EDM is improved. This is traced back to the fact that the energy loss rate of $\gamma_{\mathrm{T,L}}$, nucleon-nucleon bremsstrahlung and Compton scattering for MDM and EDM are comparable to e^-e^+ annihilation into a $\chi\bar{\chi}$ pair. For AM and CR, however, the results from [183] remain largely unchanged, as $\gamma_{\mathrm{T,L}}$ decay, nucleon-nucleon bremsstrahlung and Compton scattering are less efficient. Once the effective coupling becomes large enough, the produced χ particles will eventually come into thermal equilibrium with SM particles and become trapped. In this case, the energy loss argument does not apply, resulting in upper boundaries of SN1987A exclusion limits shown in Figs. 4.4 and 4.5; see [P1] for the derivation.

3.3.3 Related works

Stellar bounds on the EM properties of light dark states have been studied in the literature, mostly in the context of EM properties of eV-scale (SM) neutrinos; see [187, 214] and references therein. In these studies, the mass of neutrino is essentially zero. Therefore, in the limit $m_\chi \to 0$ our results can be compared with previously derived constraints on neutrino EM interactions.

For instance, based on similar energy loss arguments, bounds on the neutrino MDM have been obtained by calculating the plasmon decay process, from RG stars as $\mu_\nu \leq (2\text{–}4) \times 10^{-12}\,\mu_B$ [215–217], from HB stars as $\mu_\nu \leq (1\text{–}3) \times 10^{-11}\,\mu_B$ [218, 219], from the Sun as $\mu_\nu \leq 4 \times 10^{-10}\,\mu_B$ [220]. Indeed, all these bounds are in essential agreements with our newly derived ones once the limit $m_\chi \to 0$ is taken. Similar constraints on mass-dimension 5 operators have also been obtained in Ref. [221].

For higher-dimensional operators, Ref. [222] estimated the anomalous energy loss rate in the PNS through electron-positron pair annihilation into light right-handed neutrinos, limiting its charge radius to be below $3.7 \times 10^{-34}\,\mathrm{cm}^2$, that is $9.5 \times 10^{-7}\,\mathrm{GeV}^{-2}$, about seven times weaker than the one presented above. This is partially due to the fact that Ref. [222] assumed an one order of magnitude larger luminosity as the maximum permissible energy loss.

3.3.4 Cosmological constraints

Light dark states may lead to extra radiation in the early Universe, and thus its coupling to the SM bath is constrained by both the predictions from BBN and CMB observvations. On the one hand, for the mass region considered here the CMB bounds depend on how χ-pairs annihilate/decay. On the other hand, primordial abundance measurements of D and ^{4}He suggest that extra relativistic degrees of freedom need to be less than that of one chiral fermion during the nucleosynthesis (see, *e.g.*, [223–225]). Thus here we require that the Dirac fermion χ is thermally diminished at $T \sim 100\,\mathrm{keV}$, either due to a feeble EM form-factor coupling or by a Boltzmann-suppression induced by its mass.

The relevant bounds are also given in Figs. 4.4 and 4.5. They only constrain the parameter region with $m_\chi \ll 1\,\mathrm{MeV}$. In the same figures, we also show the line which corresponds to the thermal freeze-out scenario which generates the observed dark matter abundance, although such scenario has been excluded by various constraints for this model; see [183]. The dominant annihilation channel is into two photons at $m_\chi < m_e$ and into a electron-positron pair at $m_\chi \geq m_e$, which explains the sharp decrease of the relic density curve at $m_\chi \sim m_e$ seen in Fig. 4.4. The freeze-in parameter region for $m_\chi \ll 1\,\mathrm{MeV}$ is also constrained by the stellar energy loss argument; see [221].

3.4 Summary of Chapter 3

In this chapter, we explore the sensitivity of stellar systems to neutral dark states that share higher-dimensional interactions with the SM photon. To this end, we choose a Dirac fermion χ that is coupled to mass-dimension 5 MDM and EDM operators with respective dimensionful coefficients μ_χ and d_χ, and mass-dimension 6 AM and CR operators with respective coefficients a_χ and b_χ. We consider anomalous energy losses from the interior of RG and HB stars, of the Sun, and of the PNS core of SN1987A. Together with previously derived direct, indirect, and cosmological limits in [183], this chapter adds astrophysical constraints to draw a first comprehensive overview of light dark states with masses (well) below the GeV-scale and EM moment interactions.

The thermal environments of stellar interiors significantly affect (or enable) production processes of $\chi\bar{\chi}$ pairs. Before breaking it down to individual contributions, we establish the exact formula, Eq. (3.11), for the pair-production rate in leading order of the dark coupling. The expression factorizes into a piece that represents the probability to produce an off-shell photon γ^* from a SM current, and a piece that describes the production of the $\chi\bar{\chi}$ pair from that photon. The former is proportional to the imaginary parts of the transverse and longitudinal thermal photon self-energies $\mathrm{Im}\,\Pi_{\mathrm{T,L}}$. The latter are model-dependent but otherwise universal factors that represent the choice of interaction, Eq. (2.6). The optical theorem then allows us to identify all major production processes by studying the contributions to $\mathrm{Im}\,\Pi_{\mathrm{T,L}}$. The approach also allows us to clarify the role of thermal resonances in these processes, *i.e.*, the kinematic situation when the pair-producing photon goes on-shell, $k^2 = \mathrm{Re}\,\Pi_{\mathrm{T,L}}$. We find that resonant production is entirely captured by the decay of transverse and longitudinal thermal photons or "plasmons", $\gamma_{\mathrm{T,L}} \to \chi\bar{\chi}$.

We compute the rates of χ-pair production and its ensuing energy loss from plasmon decay and Compton production for all systems. In addition, we evaluate eN bremsstrahlung for RG stars, HB stars and the Sun, and e^-e^+ annihilation and nucleon-nucleon bremsstrahlung for SN1978A. For MDM and EDM interactions, plasmon decay dominates in HB and RG stars and in the Sun. For the interactions of increased mass-dimension, AM and CR, the Compton (bremsstrahlung) production dominates in HB and RG stars (Sun). In the PNS core, e^-e^+ annihilation dominates the anomalous energy loss for $r \gtrsim 7\,\mathrm{km}$. In the most inner region the population of positrons becomes extremely Boltzmann suppressed by a decrease in temperature, and plasmon decay and np bremsstrahlung take over as the most important production channels. For all processes we have taken into account all important finite-temperature effects. Furthermore, in the evaluation of rates, we explicitly avoid any double counting between plasmon decay and an on-shell emitted photon in bremsstrahlung and between Compton production and an on-shell exchanged t-channel photon in bremsstrahlung.

The rates when integrated over stellar radius then become subject to the observationally inferred limits on anomalous energy loss. The resulting restrictions on the parameter space are found in Figs. 4.4 and 4.5. In the kinematically unrestricted regime $m_\chi \lesssim 1\,\mathrm{keV}$, the stellar limits are dominated by RG stars with $\mu_\chi, d_\chi \leq 2\times10^{-12}\,\mu_B$ and $a_\chi, b_\chi \leq 6\times10^{-5}\,\mathrm{GeV}^{-2}$. All interactions are additionally constrained from SN1987A, in the windows $10^{-10}\,\mu_B \leq \mu_\chi, d_\chi \leq 10^{-8}\,\mu_B$ and $10^{-7}\,\mathrm{GeV}^{-2} \leq a_\chi, b_\chi \leq 10^{-3}\,\mathrm{GeV}^{-2}$ for $m_\chi \lesssim 10\,\mathrm{MeV}$. The SN1987A constraining region is bounded from above by the trapping of χ particles, which is evaluated in [P1]. The presented astrophysical constraints add to a program that has started in [183] and that aims at charting out the experimental and observational sensitivity to effective dark state-photon interactions. The stellar constraints on anomalous energy loss derived in this chapter yield the most important limits on the existence of effective dark sector-photon interactions for χ-particles below the MeV-scale.

CHAPTER 4

Proton-beam Experiments

This chapter is based on Ref. [P2]. For the study on the same interactions but with electron-beam facilities, we refer the reader to [183].

4.1 Dark sector physics at the intensity frontier

For the conventional $\mathcal{O}$(GeV–TeV) WIMP, the best laboratory probe are high-energy colliders due to their high CM energy. In contrast, for lighter dark states, the energy threshold is less demanding. The essential quantity rather becomes the intensity or luminosity of the experiments. Even if the CM energy is much less than that of high-energy colliders, the sensitivity of experiments at the *intensity frontier* is boosted with a high-intensity particle beam, quantified by the number of *particles on target*. In addition, individual backgrounds can sometimes be better isolated in intensity frontier experiments, making them a competitive probe for sub-GeV dark sectors.

On the particle theory side, the connection between the SM sector and the light dark sector is often made by the introduction of portals, as discussed in previous chapters. Assuming the UV scale is well beyond the CM energy, the interaction between dark states and SM particles can be expressed in terms of *effective operators* with different mass-dimensions n depending on the nature of the portal, *e.g.*, the various EM form factors considered here. The details of the effective EM interactions can be found in Chap. 2. In addition to the stellar systems studied in Chap. 3, dark states can be produced in laboratories through these effective operators.

The estimation in [157] shows that the typical production rates of dark states, per SM particle collision, of intensity frontier experiments can win over or be comparable to that of high-energy colliders for $n \leq 6$ effective operators. Nevertheless, for $n > 6$ effective operators, since the interaction is suppressed by the higher power of the UV scale, the dependence on CM energy eventually dwarf the intensity. Other than the production rate, we also need to take the detector acceptance into account. A typical intensity frontier experiment usually consists of a downstream detector. Contrary to the nearly 4π detector coverage in high-energy colliders, the detectors in intensity frontier experiments cannot encompass all the emitted

$E_{\text{beam}} \setminus$ meson	π^0	η	η'	ρ	ω	ϕ	J/Ψ
8.9 GeV	8.6×10^{-1}	8.2×10^{-2}	4.9×10^{-3}	6.9×10^{-2}	7.4×10^{-2}	1.1×10^{-4}	0
120 GeV	2.9	3.2×10^{-1}	3.4×10^{-2}	3.7×10^{-1}	3.7×10^{-1}	1.1×10^{-2}	5.0×10^{-7}
400/450 GeV	4.1	4.6×10^{-1}	5.1×10^{-2}	5.4×10^{-1}	5.4×10^{-1}	1.9×10^{-2}	8.0×10^{-6}

Table 4.1: The number of mesons produced per POT from a `PYTHIA 8.2` simulation for different beam energies. MiniBooNE-DM corresponds to $E_{\text{beam}} = 8.9\,\text{GeV}$, DUNE is in the category of $E_{\text{beam}} = 120\,\text{GeV}$, and $E_{\text{beam}} = 400/450\,\text{GeV}$ are for SHiP, E613/CHARM II, respectively.

dark states, even though it is highly collimated along the beam axis. Nevertheless, even after weighting the production rate with the detector's angular acceptance, the sensitivity of intensity frontier experiments for $n < 6$ effective operators surpasses that of high-energy colliders. The scaling of sensitivity with respect to CM energy can be seen later in the result section.

We note that the intensity frontier experiments were first devised to study neutrino oscillation parameters with neutrinos produced at the beam dump and later detected via (in)elastic scattering on nucleons or electrons. Neutrinos share part of the dark states' nature: long-lived and weakly-interacting. Therefore, these neutrino experiments are also proper facilities for dark state searches, in which neutrinos become the primary source of background. In this chapter, we focus on proton-beam facilities and study, in detail, the production mechanism of the dark states χ as well as their signals in a downstream detector, assuming the effective EM interactions. The main production channels are the Drell-Yan (DY) process and/or meson decay, depending on the mass-dimension of portal interaction; for detection, we study electron recoil and hadronic shower signals. We point the reader to Ref. [183] for tests in electron-beam facilities. A discussion of electron-beam facilities is relegated to Sec. 7.1, with the particle model formulated in Sec. 6.4.

4.2 Dark states production

At proton-beam experiments, dark states coupled to the photon can be produced via prompt processes (*e.g.*, in DY process or proton bremsstrahlung) and secondary processes (*e.g.*, in meson decays or secondary collisions). In this section, we discuss these production processes and provide the calculations of dominant channels. Numerical results, taking the SHiP experiment as an example, are shown in Fig. 4.1. The relative importance of the individual contributions does not change significantly from experiment to experiment.

4.2.1 Drell-Yan production

Dark states with effective couplings to the photon can be pair-produced directly through quark-antiquark annihilation. To correctly estimate the χ production from proton-proton collision, we utilize the event generator `MadGraph 5` [226], to obtain the energy spectrum and angular distribution of dark states per collision in the lab frame, denoted as $d^2\hat{N}_\chi^{\rm DY}/(dE_\chi d\cos\theta_\chi)$, as a function of χ energy E_χ and the angle between their momentum and the beam axis, θ_χ.

We then take the thick target limit, and calculate the total yield of dark states from the DY process via

$$\frac{d^2N_\chi^{\rm DY}}{dE_\chi d\cos\theta_\chi} = {\rm POT}\times A^{\alpha_1-\alpha_2}\times\frac{d^2\hat{N}_\chi^{\rm DY}}{dE_\chi d\cos\theta_\chi}\,, \tag{4.1}$$

where the proton on target (POT) number is known for each experiment and A is the atomic mass number of the target; α_1, α_2 are scaling-indices induced by scattering off a nucleus instead of a proton for the DY cross section, and the total scattering cross section, respectively. DY processes can be treated as incoherent and thus $\alpha_1 \simeq 1$. The value of α_2, for inclusive proton-nucleus scattering, typically of the order $\mathcal{O}(0.8)$, depends on the exact target material, and only mildly affects the final results. Here we take $\alpha_2 = 0.9, 0.88, 0.8, 0.71, 0.6$, for graphite, beryllium, iron, molybdenum, and tungsten, respectively [227].

4.2.2 Meson decay

Another important process is the secondary production of a χ-pair in the decays of scalar/vector mesons through an off-shell photon. Here we consider the scalar mesons π^0, η and η', as well as vector mesons ρ, ω, ϕ and J/Ψ.

Typically, if the decays of mesons into dark states are kinematically allowed, they tend to dominate the production rate. For example, [228] shows that the production of millicharged particles from meson decay is several orders of magnitude larger than that from DY. Among them, the π^0 decay contribution is most important. However, this picture changes when one considers higher-dimensional operators. This is because the decay rate of light mesons into χ-pairs will receive additional suppression from their masses, as shown below.

For scalar mesons, the dominant decay channel of producing dark states is a three-body decay with final states $\gamma\chi\bar{\chi}$. By factorizing out the dark current part, we infer that

$${\rm Br}({\rm sm}\to\gamma\chi\bar{\chi}) = \frac{\Gamma_{{\rm sm}\to\gamma\chi\bar{\chi}}}{\Gamma_{{\rm sm}\to\gamma\gamma}}\times{\rm Br}({\rm sm}\to\gamma\gamma)\,, \tag{4.2}$$

where the subscript "sm" denotes "scalar meson". The branching ratios, ${\rm Br}({\rm sm}\to\gamma\gamma)$, are taken from the PDG [214]. It is worthwhile pointing out that in this step we neglect the mild q^2-dependence induced by the meson transition form factors $F_{{\rm sm}\gamma\gamma^*}(q^2,0)$. Such

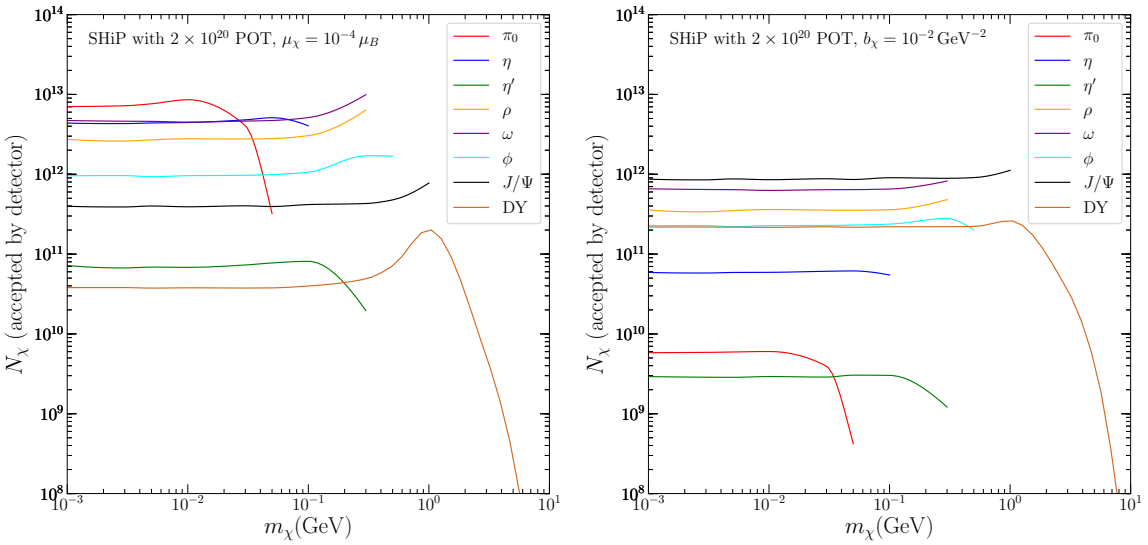

Figure 4.1: The number of produced dark states reaching the SHiP detector and produced by a 400 GeV proton beam, broken down into the individual contributing channels, for mass-dimension 5 (left panel) and mass-dimension 6 (right panel) operators. Here we only select 2 operators (MDM and CR) for demonstration.

approximation is particularly justified for the lighter mesons: the photon virtuality is limited by kinematics, $q^2 \leq m_{\rm sm}^2$ and corrections enter at the level of q^2/m_ρ^2 where m_ρ is the ρ-meson mass; see, *e.g.*, [229–231] and Fig. B.4 in App. B.2.1. To calculate $\Gamma_{\rm sm\to\gamma\chi\bar{\chi}}$ and thus the ratio of the two channels, we follow our previous methodology in [183] and [P1], and provide the corresponding expressions in App. B.2.1.

A vector meson, in turn, can decay into a χ pair directly. Thus we compute the branching ratios $\mathrm{Br}(\mathrm{vm} \to \chi\bar{\chi})$, where "vm" stands for "vector meson". For two-body decays, one can separate the decay amplitude and phase space factors to obtain

$$\mathrm{Br}(\mathrm{vm} \to \chi\bar{\chi}) = \mathrm{Br}(\mathrm{vm} \to e^- e^+)\,\frac{f(m_{\rm vm}^2)}{f_e(m_{\rm vm}^2)}\sqrt{\frac{m_{\rm vm}^2 - 4m_\chi^2}{m_{\rm vm}^2 - 4m_e^2}}\,, \tag{4.3}$$

where the last two factors count the differences induced by the interaction type and the phase space, respectively. The expression of $f(m_{\rm vm}^2)$ for each interaction type is given in App. B.2.1, and has previously been derived in [183] and [P1]. In contrast to the (milli)charge case (f_e), the function $f(m_{\rm vm}^2)$ depends more strongly on the meson mass for higher-dimensional operators, and the χ production rate becomes enhanced for heavier meson decay; for more details see Eq. (2.6).

Besides the normalized meson distribution discussed above, we also require the total number of produced mesons in each experiment. For this, we use `PYTHIA 8.2` [232, 233] to simulate pp collisions, and list the average number of mesons produced per POT for each experiment in Tab. 4.1. We assume that these meson production rates per POT remain the same for pN

collisions; for the latter, current detailed simulations yield differing results, see, *e.g.*, [234] for a recent discussion[1]. The meson multiplicities of our Tab. 4.1 lie within the range of their adopted values in previous works, *e.g.*, [234, 236–241], and we estimate the uncertainties only affect the final bounds by a factor of 1.2 at most. Finally, we have also extracted the information on their momentum and angular distributions from `PYTHIA 8.2`, which is consistent with the fitted distributions mentioned above [241].

For the final distribution function of χ particles from meson decay in the lab frame we find

$$\frac{d^2N_\chi}{dE_\chi d\cos\theta_\chi} = \sum_{m=\pi^0,\cdots} \int \frac{d\cos\theta^* d\phi^*}{4\pi} dE_\chi^* \frac{d\hat{N}_\chi^m}{dE_\chi^*} \frac{d^2N_m}{dE_m d\cos\theta_m} \left| \frac{\partial(E_m, \cos\theta_m)}{\partial(E_\chi, \cos\theta_\chi)} \right| , \tag{4.4}$$

where E_χ^*, θ^* and ϕ^* are defined in the meson rest frame and denote, respectively, the χ energy, the polar and azimuthal angles of the χ momentum with respect to the direction of the boosted meson. In contrast, E_χ and θ_χ are defined in the lab frame, and represent the energy of χ and the angle of the χ momentum with respect to the beam axis. At last, E_m and θ_m, the energy of the meson and the angle of the meson momentum with respect to the beam axis in the lab frame, are functions of θ^*, ϕ^*, E_χ^*, E_χ and θ_χ. The dark state spectrum from each meson decay, $d\hat{N}_\chi^m/dE_\chi^*$, is defined as

$$\frac{d\hat{N}_\chi^m}{dE_\chi^*} \equiv 2\frac{d\mathrm{Br}_\chi}{dE_\chi^*}, \tag{4.5}$$

where the factor 2 accounts for the pair production of dark states and Br_χ is the aforementioned $\mathrm{Br}(\mathrm{sm} \to \gamma\chi\bar{\chi})$ or $\mathrm{Br}(\mathrm{vm} \to \chi\bar{\chi})$, depending on the spin of the meson. Their exact expressions are given in App. B.2.1. Note that to obtain Eq. (4.4) we have used the fact that the meson decay at rest is isotropic.

In practice, we perform Monte Carlo simulations to numerically obtain the distribution function of χ from meson decay, instead of integrating Eq. (4.4) directly, as the latter is prohibitively time-consuming.

4.2.3 Other production mechanisms

Here we discuss additional channels of χ-pair production. Prominently, pN bremsstrahlung contributes to the production of χ particles. The process can, *e.g.*, be estimated using the Fermi-Weizsäcker-Williams method [242–244], as has been done in [245–248]. However, for the higher-dimensional interactions studied here, the production of χ-pairs through pN

[1] Although photo-production of light scalar mesons is known to scale as $A^{2/3}$ [235] and the scaling-index for inclusive pN scattering is about $\mathcal{O}(0.8)$ as mentioned above, effects of showers and the nuclear medium require dedicated simulations/measurements.

bremsstrahlung is generally dominated by the contribution of the vector meson resonance at $s_{\chi\bar{\chi}} \simeq m^2_{\rho,\omega}$ [249]. Since we have already taken into account the resonant contribution through the vector meson decay processes above, we will not consider the proton-nucleus bremsstrahlung any further; thereby we also avoid any double counting.

Another source of χ-pair production is the capture of pions onto nuclei or protons via $p\pi^- \to n\gamma^* \to n\chi\bar{\chi}$. This process will mostly result in low-energy χ-particles and is not considered further here. At last, secondary collisions, *e.g.*, between secondary electrons/photons and the target, should not appreciably contribute to the χ yield in our framework. We always neglect the latter contributions in this work.

4.3 Dark states detection

The dark states, produced in proton-nucleus collisions, travel relativistically and unhindered through the shield into the downstream detector, leading to observable signals. Here we focus on their elastic scattering with electrons in the detector (LSND, MiniBooNE-DM, CHARM II, DUNE, SHiP) and hadronic shower signals caused by deep inelastic scattering (DIS) in E613.

For simplicity, we will approximate the detector-shapes as cylinders with a constant transverse cross-sectional area and a certain depth. Thus, the geometric acceptance of the dark states is determined by the target-detector distance and an effective size. For the nearly spherical detector in MiniBooNE-DM, we take the spherical geometry into account in deriving the signal rate.

4.3.1 Scattering on electrons

When entering the detector, χ particles may scatter with electrons and cause detectable recoil signals. Following [183], the master formula to calculate the number of signal events reads

$$N_{\rm sig}^{(e)} = n_e \int_{E_R^{\rm min}}^{E_R^{\rm max}} dE_R \int_{E_\chi^{\rm min}} dE_\chi \, L_{\rm det} \epsilon_{\rm eff} \frac{dN_\chi}{dE_\chi} \frac{d\sigma_{\chi e}}{dE_R} \,, \tag{4.6}$$

where n_e is the electron number density of the target, $L_{\rm det}$ is the effective depth of the detector, E_R is the electron recoil energy with respective experimental threshold and cutoff energies $E_R^{\rm min}$ and $E_R^{\rm max}$, E_χ is the initial χ energy in the lab frame, and $\epsilon_{\rm eff}$ is the detection efficiency. The minimal energy of dark states $E_\chi^{\rm min}$ to produce a recoil with E_R can be expressed as

$$E_\chi^{\rm min} = \frac{E_R}{2} + \frac{\sqrt{m_i(E_R + 2m_i)(E_R m_i + 2m_\chi^2)}}{2m_i} \,, \tag{4.7}$$

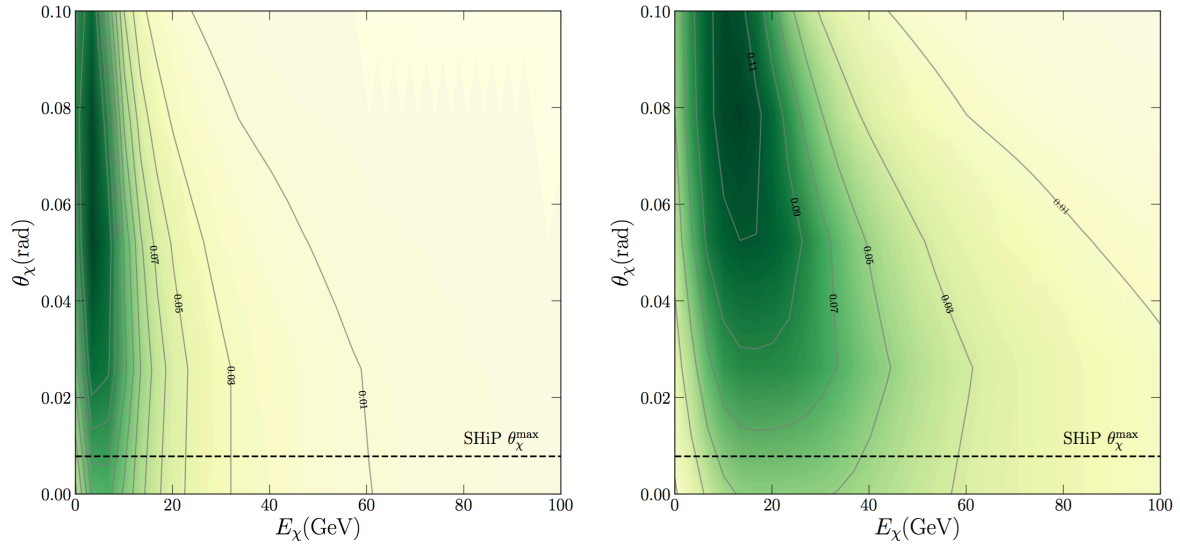

Figure 4.2: Normalized energy and angular distribution of χ particles, $d^2\hat{N}_\chi/(dE_\chi d\theta_\chi)$, for SHiP with 400 GeV incident protons. Here we only select 2 operators, MDM (left) and CR (right) and $m_\chi = 1\,\text{MeV}$ for demonstration.

where m_i is target mass, *i.e.*, the electron mass in this case. The differential scattering cross section, $d\sigma_{\chi e}/dE_R$, is found in App. B.3.2.

The energy spectrum of dark states, *i.e.*, the number of χ per unit energy, that have entered the detector, dN_χ/dE_χ, is obtained by summing up all production processes in the previous section, and applying the detector geometric cut,

$$\frac{dN_\chi}{dE_\chi} = \int_{\cos\theta_\chi^{\max}}^{1} d\cos\theta_\chi \, \frac{d^2N_\chi}{dE_\chi d\cos\theta_\chi} \,. \tag{4.8}$$

The maximum opening angle $\theta_\chi^{\max}$ is obtained from the target-detector distance and the effective size of the detector. This is illustrated in Fig. 4.2 for the SHiP experiment (400 GeV proton) and Fig. 4.3 for the MiniBooNE-DM experiment (8 GeV proton), where only χ particles below the horizontal dashed line ($\theta_\chi \leq \theta_\chi^{\max}$) enter the detector. For the purpose of illustration, the two figures give the contours of $d^2\hat{N}_\chi/dE_\chi d\theta_\chi$, normalized as per χ particle via

$$\frac{d^2\hat{N}_\chi}{dE_\chi d\theta_\chi} \equiv -\frac{\sin\theta_\chi}{N_\chi}\frac{d^2N_\chi}{dE_\chi d\cos\theta_\chi} \,, \tag{4.9}$$

which is obviously independent of the values of form factor couplings.

As shown by the figures, only about 0.1–10^{-5} of the total number of χ particles produced reach the detectors, and this strongly suppresses the number of final events at low-energy experiments, such as at MiniBooNE-DM[2]. Moreover, such reduction becomes more severe

[2]This is also one of the motivations for off-axis detectors in proton-beam experiments; see, *e.g.*, [250–252].

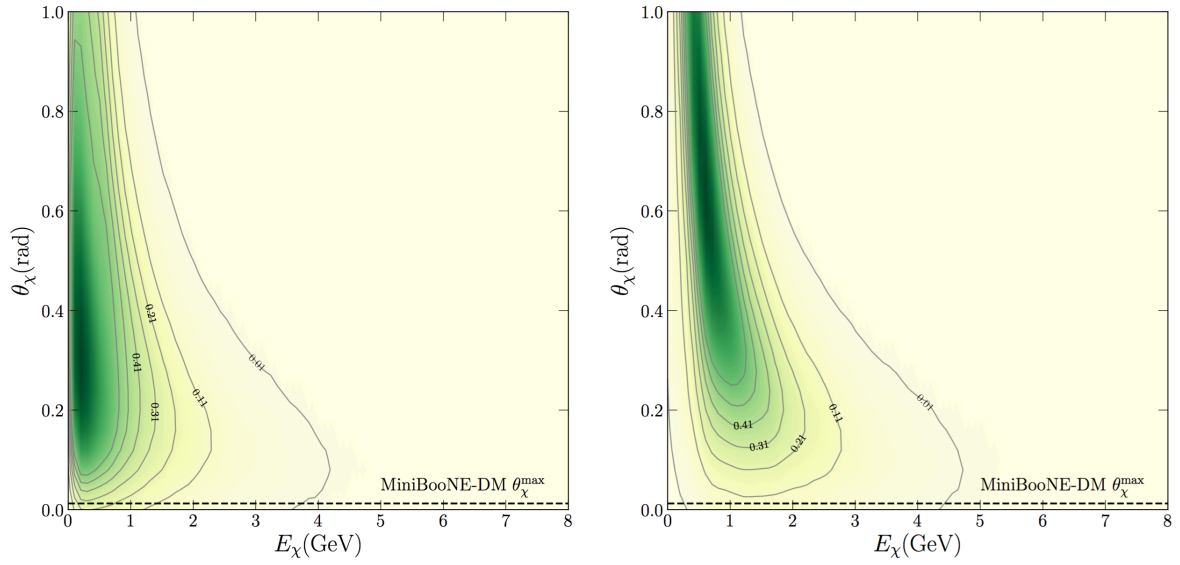

Figure 4.3: Same as Fig. 4.2 for MiniBooNE-DM with 8 GeV incident protons: MDM (left) and CR (right) and $m_\chi = 1\,\text{MeV}$.

for dark particles generated from heavy meson decay, and is largely insensitive to m_χ for χ particles from DY processes. Besides, for higher-dimensional operators, a preference for more energetic χ particles can also be observed by comparing the left and right panels in Fig. 4.2 (also in Fig. 4.3). This is due to their different energy-dependence in the production rate, and will be further discussed in Sec. 4.5.1.

4.3.2 Hadronic showers

The dark states may also cause hadronic showers, which is relevant for E613. Following [253] we consider the deep inelastic scattering of χ with nucleons (N) as the energy deposition process, while neglecting any coherence effects since the typical momentum transfer is larger than the QCD confinement scale. It is worth pointing out that we do not consider the possibility of multiple scatterings in the detector, since the coupling between the χ particle and the photon is assumed to be weak; see Sec. 4.3.3.

To derive the expected number of signal events, we first compute the differential cross section of χN deep inelastic scattering. The 4-momentum of χ before (after) scattering is denoted as p_χ (p'_χ). The momentum transfer carried by the intermediate photon is defined as $q = p_\chi - p'_\chi$, which is spacelike. Following the DIS formalism for leptons, we introduce the Bjorken variable $x \equiv Q^2/(2m_N\nu)$, with $m_N \simeq m_p$ being the nucleon mass, $Q^2 \equiv -q^2 > 0$ and ν being the energy transfer in the rest frame of the nucleons. The differential cross section is then written as

$$\frac{d^2\sigma_{\chi N}}{d\nu dQ^2} = \frac{\alpha}{4m_N(E_\chi^2 - m_\chi^2)} \frac{L_{\mu\nu}W^{\mu\nu}}{Q^4}\,, \tag{4.10}$$

where $L^{\mu\nu}$ is the trace of the dark current,

$$L_{\mu\nu} = \frac{1}{2}\mathrm{Tr}\left[\left(\not{p}_\chi + m_\chi\right)\Gamma_{\chi,\mu}(q)\left(\not{p}'_\chi + m_\chi\right)\Gamma_{\chi,\nu}(-q)\right], \tag{4.11}$$

with the factor 1/2 coming from an average over initial-state χ-spins and the vertex factors given in Eq. (2.3). The hadronic tensor $W^{\mu\nu}$ may be expressed as [253]

$$W^{\mu\nu} = \left(-g^{\mu\nu} + \frac{q^\mu q^\nu}{q^2}\right)F_1(x,Q^2) + a^{\mu\nu}F_2(x,Q^2), \tag{4.12}$$

in which

$$a^{\mu\nu} \equiv \frac{1}{p_N\cdot q}\left(p_N^\mu - \frac{p_N\cdot q}{q^2}q^\mu\right)\left(p_N^\nu - \frac{p_N\cdot q}{q^2}q^\nu\right), \tag{4.13}$$

with p_N being the 4-momentum of the nucleon before the scattering. The two structure functions F_1 and F_2 may be written as[3]

$$F_1 = \frac{1}{2x}\sum_q e_q^2 x f_q(x,Q^2), \quad F_2 = 2xF_1, \tag{4.14}$$

where e_q is the charge of quarks in unit of electron charge. We sum over flavors of light quarks/antiquarks, $q = u,\bar{u},d,\bar{d},s,\bar{s}$, and use the values of parton distribution function $xf_q(x,Q^2)$ averaged over nucleons for each corresponding nucleus, provided at the leading order by Hirai-Kumano-Nagai [254].

The expected number of signal events is given by

$$N_{\mathrm{sig}} = n_N L_{\mathrm{det}}\epsilon_{\mathrm{eff}}\int dE_\chi \int d\nu dQ^2 \frac{dN_\chi}{dE_\chi}\frac{d^2\sigma_{\chi N}}{d\nu dQ^2}, \tag{4.15}$$

where n_N is the number density of nucleons in the detector. The integration boundaries for ν and Q^2 are derived from kinematics as

$$E_{\mathrm{cut}} < \nu < E_\chi - m_\chi,$$

where E_{cut} is the experiment-specific threshold energy. The squared momentum transfer Q^2 lies in the range:

$$2\left(E_\chi^2 - E_\chi\nu - m_\chi^2\right) \mp 2\sqrt{E_\chi^2 - m_\chi^2}\sqrt{\left(E_\chi-\nu\right)^2 - m_\chi^2}.$$

Finally, there is the general requirement $x < 1$.

[3]Such parameterization is numerically equivalent to $F_{\mathrm{T}} = F_1$ and $F_{\mathrm{L}} = [1 + 2xm_N^2/(p_N\cdot q)]F_2 - 2xF_1$ of [253] in the limit of $\nu^2 \gg Q^2$, which is the case in E613 ($\nu > 20\,\mathrm{GeV}$).

Experiments	POT (10^{20})	$\lvert\theta_\chi^{\max}\rvert$	Signal process and cuts	$N_{\rm bkg}$	$\epsilon_{\rm eff}$	on/off axis	Reference
LSND	1800	-	e-recoil ($E_R \in [18, 52]\,\text{MeV}$, $\theta_R \leq \pi/2$)	$N_{\rm sig} \leq 110$	0.16	31°	[237, 255]
MiniBooNE-DM	1.86	12.4 mrad	e-recoil ($E_R \in [75, 850]\,\text{MeV}$, $\theta_R \leq 140\,\text{mrad}$)	0	0.2	0°	[256]
CHARM II	0.25	2.1 mrad	e-recoil ($E_R \in [3, 24]\,\text{GeV}$, $E_R\theta_R^2 \leq 1\,\text{MeV}$)	5429	~ 1	0°	[257, 258]
DUNE (10 yr)	11/yr	3.4 mrad	e-recoil ($E_R \in [0.6, 15]\,\text{GeV}$, $E_R\theta_R^2 \leq 1\,\text{MeV}$)	8930/yr	0.5	0°	[259, 260]
SHiP	2	7.8 mrad	e-recoil ($E_R \in [1, 20]\,\text{GeV}$, $\theta_R \in [10, 20]\,\text{mrad}$)	846	~ 1	0°	[261, 262]
E613	0.0018	12.8 mrad	had. shower ($E_N^{\rm dep} \geq 20\,\text{GeV}$ per event)	$N_{\rm sig} \leq 180$	~ 1	0°	[253, 263]

Table 4.2: Summary of key parameters from each proton-beam experiment. Here $\theta_\chi^{\max}$ is the maximal angle between χ's momentum and the beam axis in order for χ to pass through the detector, E_R is the recoil energy of the target, θ_R is the recoil angle of the target with respect to the χ momentum and $\epsilon_{\rm eff}$ is the detection efficiency of considered signal.

4.3.3 Mean-free-path of dark states

As already mentioned above, our calculations are based on the assumption that χ particles travel freely, both in the shield and in the detector. This may be validated by estimating the mean-free-path of χ, using transport cross section $\sigma_{\chi p}^{\rm t}$ of χ-proton scatterings,

$$\lambda_\chi \sim \left(n_p \sigma_{\chi p}^{\rm t}\right)^{-1} , \tag{4.16}$$

where n_p is the proton number density. The transport cross section is used as it removes the influence of soft scatterings that would not attenuate the flux of dark particles.

To obtain an estimate, we use the elastic scattering processes for which the formulas can be found in App. E of [183]. Here we take the typical distance between the collision point and the detector to be 100 m and the dump/shield mass density to be $10\,\text{g/cm}^3$. By requiring $\lambda_\chi \geq 100\,\text{m}$, one can see that these proton-beam experiments are sensitive to the EM form factor parameters,

$$\mu_\chi, d_\chi \leq 0.005\,\mu_B\,, \quad \text{and} \quad a_\chi, b_\chi \leq 0.1\,\text{GeV}^{-2}\,, \tag{4.17}$$

for sub-GeV χ particles with $E_\chi = 5\,\text{GeV}$. As parameters larger than these values above are already excluded by other probes, we may always assume that χ particles scatter at best once inside the entire experimental setup.

4.4 Experimental setups

In this section, we briefly review the relevant details of each experiment under consideration. In order to derive the ensuing 90% C.L. limits, we require that the number of events generated by the dark states,

$$N_{\rm sig} \leq \text{Max}[0, N_{\rm obs} - N_{\rm bkg}] + 1.28\sqrt{N_{\rm obs}}\,, \tag{4.18}$$

where $N_{\rm obs}$ is the number of actual observed events and $N_{\rm bkg}$ is the expected number of background events. When making forecasts for future experiments, we assume $N_{\rm obs} = N_{\rm bkg}$. The standard criterion $N_{\rm sig} \leq 2.3$ is adopted if no events were observed. For each experiment, the summary of relevant parameters can be found in Tab. 4.2.

LSND At the Liquid Scintillator Neutrino Detector (LSND) experiment, a proton beam of 800 MeV kinetic energy was conducted onto water or a high-Z target such as copper [255]. The detector was located at a distance of 35 m from the beam dump, with an off-axis angle of 31°, and an active volume comprised of an 8.3 m long cylinder with a diameter of 5.7 m, filled with 167 ton of mineral oil CH_2 [264].

Due to the low beam energy, we consider π^0 decay as the only χ production channel in LSND as other heavier mesons decay and DY channels are suppressed. As it is difficult to generate the total production rate of π^0 in `PYTHIA 8.2` at such low energy, we instead estimate it via the ratio $(\sigma_{pp\to X+\pi^0} + 2\sigma_{pp\to X+2\pi^0})/\sigma_{pp}$, which measurements put at a value of approximately 0.1 [265, 266]. Under the assumption that this ratio remains unchanged for proton-nuclear scattering, we adopt the value $0.1\,\pi^0$/POT as our fiducial value in the calculation. This is close to the production rate of positively charged mesons in LSND, about $0.08\,\pi^+$/POT [267], as well as the value used in COHERENT experiment, $0.09\,\pi^0$/POT [268].

In the MDM case with $m_\chi \ll m_\pi$, the χ flux entering the detector is then approximately

$$\phi_\chi \simeq 2.2 \times 10^5\,{\rm cm}^{-2} \left(\frac{\mu_\chi}{2\times 10^{-5}\,\mu_B}\right)^2 , \tag{4.19}$$

yielding the constraint $\mu_\chi \leq 2\times 10^{-5}\,\mu_B$. This can be rescaled to compare with the LSND results [269], which estimates that the ν_e flux entering the detector, ϕ_{ν_e}, is about $1.2 \times 10^{14}\,{\rm cm}^{-2}$, leading to a bound on ν_e's MDM at $\mu_{\nu_e} \leq 10^{-9}\,\mu_B$ [269]. One can see the equality,

$$\left(\phi_\chi \times \mu_\chi^2\right)\Big|_{\mu_\chi = 2\times 10^{-5}\,\mu_B} \simeq \phi_{\nu_e} \times (10^{-9}\,\mu_B)^2 ,$$

is approximately satisfied, suggesting that our treatment of the detector works well.

MiniBooNE-DM The Booster Neutrino Experiment, MiniBooNE, operates at the Fermi National Accelerator [270]. The Booster delivers a proton beam with kinetic energy $E_{\rm beam} = 8\,{\rm GeV}$ ($\sqrt{s} \sim 4.3\,{\rm GeV}$) on a beryllium ($A_{\rm Be} = 9$) target. The center of the spherical on-axis detector is placed 490 m downstream from the beam dump with a diameter of 12.2 m filled with 818 ton of mineral oil C_nH_{2n+2} ($n \sim 20$). In practice, we are more interested in the off-target mode of MiniBooNE, where the proton beam hits directly the steel beam dump, with an ensuing smaller high-energy neutrino background. This is referred to as MiniBooNE-DM, which has data with 1.86×10^{20} POT [256]. By only focusing on electrons with extremely small

recoil angles, the background was effectively reduced to zero in this off-target mode [256]. That is, we derive the 90% C.L. limits on the couplings of dark states to the photon by requiring $N_{\rm sig} \leq 2.3$.

It is well known that in the on-target mode with 1.3×10^{21} POT, MiniBooNE reported a significant excess of electron-like events [271]. In addition, the background event of a single electron recoil is estimated to be about one hundred, after the same cuts as above [272]. Substituting these values into Eq. (4.15) in turn suggests that the on-target mode should lead to slightly weaker limits than those from MiniBooNE-DM, despite its larger POT number.

CHARM II CERN High energy AcceleRator Mixed field facility II (CHARM II) was a fixed-target experiment designed for a precision measurement of the weak angle. It utilized a 450 GeV proton beam on a Be target, and collected data with 2.5×10^{19} POT during 1987–1991 [258]. The main detector is a 692 ton glass calorimeter (SiO_2, on average $\langle A \rangle \simeq 20.7$ per nucleus), and has an active area of $3.7 \times 3.7\,{\rm m}^2$, about 870 m away from the target along the beam axis [257]. In this study, we focus on the single electron recoil signals, as the detector has an almost 100% efficiency to record EM showers for recoil energy $E_R \in [3,\, 24]\,{\rm GeV}$.

To estimate the number of background events, we take $N_{\rm obs} = 5429$ reported in [258], largely induced by electron scattering with energetic $\nu_\mu + \bar{\nu}_\mu$ particles. This estimation is conservative, as CHARM II was able to determine the value of the Weinberg angle with the uncertainty below several percents.

DUNE The Deep Underground Neutrino Experiment (DUNE) is proposed to be performed at the Long-Baseline Neutrino Facility (LBNF), and can be used to probe light dark particles [273, 274]. At DUNE, a graphite ($A_{\rm C} = 12$) target is hit by a proton beam with an initial energy $E_{\rm beam} = 120\,{\rm GeV}$. The near detector (75 ton fiducial mass) will be placed 574 m downstream from the target. It is on-axis and a parallelepiped with a size $4 \times 3 \times 5\,{\rm m}^3$ and we use 5 m as its effective depth [228]. The detector is filled with liquid Argon (LAr).

We take a 10-year run of the DUNE experiment, with a total POT of 1.1×10^{22}. The observable signals we consider for DUNE are single electron events caused by χe scatterings. The detection efficiency is assumed to be $\epsilon_{\rm eff} = 0.5$ for the LAr time projection chamber. Following [240, 260], we require the cut on the electron recoil angle to satisfy $E_R \theta_R^2 \leq 1\,{\rm MeV}$, which significantly reduces the number of background events from charged-current $\nu_e n$ scattering; see Tab. 4.2 for details of the parameters.

SHiP A fixed-target facility to Search for Hidden Particles (SHiP) is proposed at the CERN super proton synchrotron (SPS) accelerator [261]. At the SPS facility, a proton beam with $E_{\rm beam} = 400\,{\rm GeV}$ ($\sqrt{s} \sim 27.4\,{\rm GeV}$) is deployed to collide with the titanium-zirconium doped

molybdenum target ($A_{\rm Mo} = 95.95$). An emulsion cloud chamber detector will be located 56.5 m downstream from the target, and it will be filled with layers of nuclear emulsion films. Following the latest SHiP report [275], the size of the detector (~ 8 ton) is set to be $80 \times 80 \times 100\,{\rm cm}^3$. We assume a 100% detection efficiency for simplicity[4].

The detection process we consider for SHiP is also χe scattering. With 2×10^{20} POT after 5-years of operation, the number of background events is estimated to be 846, which is dominated by ν_e quasi-elastic scattering with a soft final-state proton [275].

E613 E613 was a beam dump experiment at Fermilab, set up to study neutrino production, with a 400 GeV proton beam hitting a tungsten target [263]. The detector, 55.8 m away from the target, consisted of 200 ton lead plus liquid scintillator. Its size was $1.5 \times 3 \times 3\,{\rm m}^3$, with a mass density of about $10\,{\rm g/cm}^3$. In order to compare with the previous results [253, 277], we only consider a circular region of the detector with a radius of 0.75 m along the beam axis. Moreover, for nucleon-recoil events in E613, the energy deposit needs to be larger than 20 GeV, in order to be recorded. We require the number of such events to be below 180 during its 1.8×10^{17} POT run to obtain the constraints.

We assume a thick target so that each incident proton scatters once. This is different from the treatment by [253, 277], which estimated the number of scatter events per POT following the scaling:

$$L_T \times n_T \sigma_{pT}\,, \tag{4.20}$$

with L_T (n_T) being the total length (the nucleon number density) of the target, and σ_{pT} the scattering cross section between proton and target. For E613, where L_T is much larger than the mean-free-path of a 400 GeV proton (a few cm in tungsten), Eq. (4.20) significantly over-estimates the total number of produced χ particles. As a result, our limits are weaker than those derived in [277]. We revise the previous results in the next section.

Other experiments There also exist many other proton-beam experiments which adopt similar setups to those we have studied above, such as COHERENT with a 1 GeV proton beam [278], JSNS^2 with a 3 GeV proton beam [279], NOνA with a 120 GeV proton beam [280], as well as WA66 with a 400 GeV proton beam [281]. Nevertheless, these experiments are in general not expected to provide noticeably stronger (projected) bounds than those obtained above (see, *e.g.*, [239, 268, 282–286]), and are thus not further studied in this work.

A different new bound on light dark states comes from the NA62 experiment, which has recently improved the constraint on $\pi^0 \to \gamma + \text{inv.}$ by three orders of magnitude [287]. This puts upper bounds on the MDM/EDM interactions of our interest as

$$\mu_\chi, d_\chi \lesssim 2.4 \times 10^{-4}\,\mu_B\,, \tag{4.21}$$

[4] A unity efficiency was also used in [262, 276].

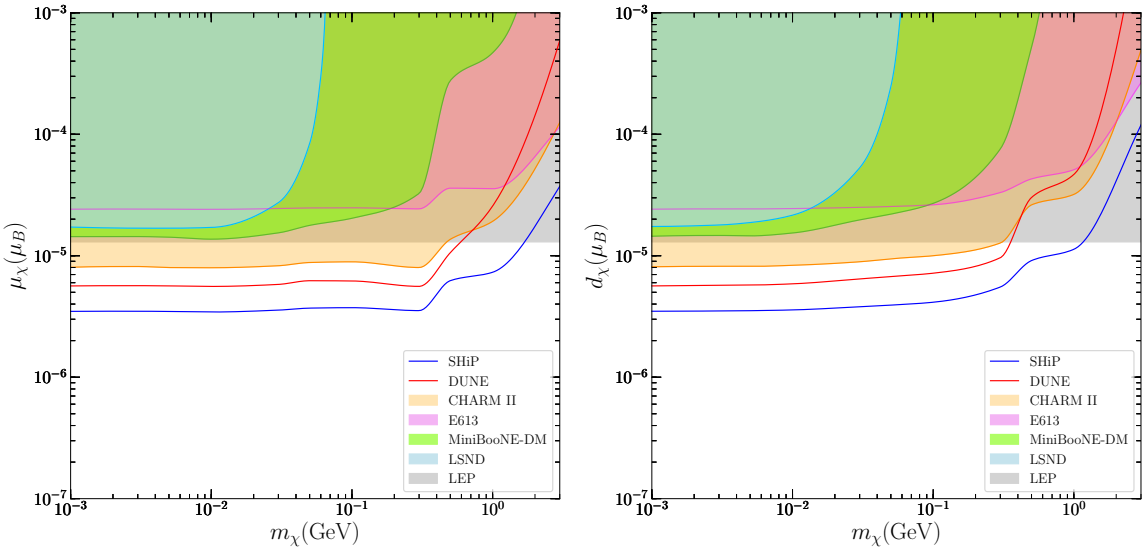

Figure 4.4: Summary of 90% C.L. excluded regions on the EM form factors for the mass-dimension 5 operators MDM (left) and EDM (right). Shaded regions are excluded; projected sensitivities from future experiments are shown as solid lines. The LEP bound is taken from [183].

for $m_\chi \ll m_\pi/2$. They are weaker than the bounds obtained above, and become even weaker for higher-dimensional operators, *i.e.*, the AM/CR interactions.

High-energy colliders become more important for χ particles heavier than pions. For instance, at LHC, the upgrade of the MoEDAL experiment will be equipped with three deep liquid scintillator layers [288]. In addition, there will be the milliQan detector [289, 290] which will be composed of three stacks of plastic scintillators[5]. Both experiments are designed to be sensitive to millicharged dark particles, of which the scattering cross section with electron/nucleus is dramatically enhanced at low momentum-transfer. As suggested in [292, 293], such experiments will constrain the EDM form factor of dark states, where there also exists an enhancement—although milder—in low momentum-transfer $\chi e\,(\chi N)$ region of elastic scattering. Moreover, proposed future colliders, such as HL-LHC and ILC, will be able to further improve the experimental sensitivity on all the EM form factors studied here; see, *e.g.*, [294–296]. It is worth mentioning that the FASER experiment [247] that will be on board in 2021 can also be relevant for the considered interactions.

4.5 Results of Chapter 4

In this section, we first compare the production efficiency of various channels, and then summarize our bounds on the EM form factors of dark states.

[5] See also the proposed FORMOSA detector [291].

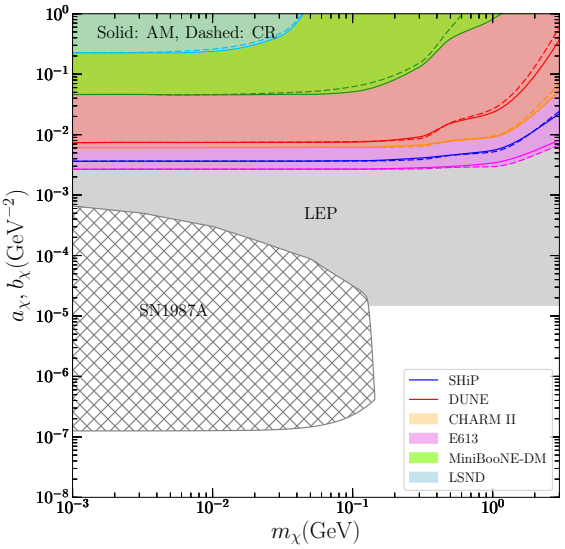

Figure 4.5: Same as Fig. 4.4 but for mass-dimension 6 operators (AM/CR). The SN1987A bound is taken from Chap. 3.

4.5.1 Comparison of production channels

In contrast to dark state-photon interactions through millicharge, higher-dimensional operators are considered in this work. Therefore, dimensional analysis demands an extra energy scale E to compensate for the presence of the dimensionful coupling (E for mass-dimension 5 operators and E^2 for mass-dimension 6 operators) in cross sections and branching ratios, in comparison to the mass-dimension 4 case. This typically suppresses the yield of dark states.

For DY, the relevant energy scale is of the order of the pp collision energy, $\sqrt{s}$. We can then infer that for mass-dimension 5 (mass-dimension 6) operators the resulting cross section will contain a dimensionless factor $\mu_\chi^2 s$ and $d_\chi^2 s$ ($a_\chi^2 s^2$ and $b_\chi^2 s^2$)[6]. Thus, the cross sections involving mass-dimension 5 and 6 operators are further suppressed relative to mass-dimension 4 interactions for $d_\chi^{-1}, \mu_\chi^{-1} \gg \sqrt{s}$ and $a_\chi^{-1}, b_\chi^{-1} \gg s$, which incidentally are also required for the treatment of Eqs. (2.1b) and (2.1c) as effective operators. As a result, the DY process gains in relevance relative to the meson decay in the production of χ particles, especially for mass-dimension 6 operators as for the latter, the relevant energy scale is roughly the meson mass.

In addition, because of the mass-scaling, the relative importance of decaying meson contributions is also modified. The branching ratios into χ-pairs from light mesons become suppressed. Therefore, we can see that although heavier mesons are produced at lower rates,

[6]The use of effective operators is justified when these products do not exceed unity. This is not guaranteed in the top portions of Figs. 4.4 and 4.5, but we expect that the region remains excluded by associated LEP bounds that resolve the UV particle content. We leave a derivation of such UV-dependent high-energy collider constraints for dedicated future work.

as shown in Tab. 4.1, the final yields of dark states from their decay are comparable to (dominate over) those from light mesons for mass-dimension 5 (mass-dimension 6) operators.

The χ production rate of each channel, after applying the geometric cut, is demonstrated in Fig. 4.1. One can see that due to the reasons above, the overall pattern in our χ production rate becomes very different from those of millicharged particles (see, *e.g.*, [228]) and dark photons (see, *e.g.*, [246]), where light meson decay is the most important production channel unless it is kinematically suppressed[7].

4.5.2 Constraints

The 90% C.L. constraints on the EM form factors derived above are shown by the colored regions in Fig. 4.4 (MDM and EDM) and Fig. 4.5 (AM and CR), together with our previous constraints (gray regions); see [183] and [P1]. As explained above, the strengths of higher-dimensional interactions are energy-sensitive, and constraints derived from current proton-beam experiments, with $\sqrt{s}$ below several to tens of GeV, turn out not to be competitive with the constraint from LEP [183]. For mass-dimension 5 operators, future experiments such as DUNE (10-year) and SHiP will improve the sensitivity by a factor of 2–3, and become stronger than LEP for $m_\chi < 1\,\text{GeV}$ due to their high intensity. It is worth pointing out that the astrophysical bound from SN1987A constrains the MeV-region below $10^{-8}\,\mu_B$ [P1], well below the current and projected experimental sensitivity.

For mass-dimension 6 operators, the production and detection rates of light dark states are even more sensitive to the CM energy, suggesting it is unlikely for low-energy experiments to play any role in the foreseeable future. In E613 the initial energy of χ needs to be above 20 GeV to trigger an observable signal, but such large E_χ also enhances the χ-proton scattering, making it difficult for χ particles to travel through the shield unless $a_\chi, b_\chi \ll 10^{-2}\,\text{GeV}^{-2}$.[8] Thus, future high-energy colliders have better potential to probe mass-dimension 6 dark state interactions.

At last, as we adopt thick target limit for E613, we also revise the E613 bound on millicharged particles from [253], although it has been surpassed by bounds derived from later experiments [183, 297–300]. Our derivation also improves with respect to a much earlier work [301], by adding the production through decays of scalar mesons and by imposing the BMPT distribution for mesons. As shown in Fig. 4.6, if only DY processes are taken into account, our bound is weaker than that from [253] by about a factor of 7. By adding contributions from vector meson decay, the bound becomes stronger, approximately in agreement with [301] (dashed lines). Our final exclusion limit, taking into account all these contributions, is shown as the pink shaded region in the figure.

[7] We have checked that our code reproduces Fig. 2 of [228] when switching the effective operators to the millicharge interaction.

[8] In this region, the validity of the use of effective operators is also in question.

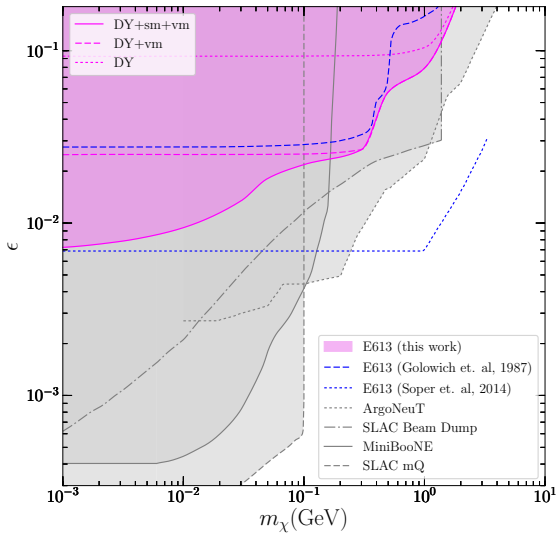

Figure 4.6: Revised upper bounds from E613 on milli-charged dark states from DY production only (pink dotted line), DY + vector meson decay (pink dashed) and DY + vector/scalar meson decay (pink solid). This corrects a previously derived limit from DY production (blue dotted) [253] and improves previous work utilizing DY + vector meson decay only (blue dashed) [301]. Other bounds shown are from the ArgoNeuT [302] (dotted grey), MiniBooNE [298] (solid gray), SLAC beam dump (dash-dotted gray) and mQ experiment [297] (dashed gray) experiments. See [298, 303] for the sensitivity reach of BaBar, BESIII, and future experiments.

4.6 Summary of Chapter 4

In this chapter, we study the production and detection of neutral fermionic dark states χ that carry EM form factors in proton-beam experiments. We consider the production of $\chi\bar{\chi}$-pairs in the collision of high-intensity protons on nuclear targets through prompt Drell-Yan scattering and in secondary meson decays. The detectable signals considered are single electron recoil events at LSND and MiniBooNE-DM, CHARM II, as well as at the proposed DUNE and SHiP experiments, and hadronic showers caused by deep inelastic scatterings at E613.

Owing to the higher dimensionality of the considered operators (mass-dimension 5 and 6), the relative importance of production channels is biased towards processes with larger intrinsic energy. As a consequence, Drell-Yan production and production in *heavy* meson decays gain prominence when compared to the millicharged and dark photon cases, for which pion decays dominate the dark state yield.

We compute in detail the energy and angular distribution of the produced dark state flux and set the strongest constraints on the existence of χ-particles with MDM and EDM interactions in the MeV–GeV mass bracket, excluding dimensionful coefficients $\mu_\chi, d_\chi \gtrsim 8 \times 10^{-6}\,\mu_B$, corresponding to an effective scale $\Lambda_5 < 0.4\,\text{TeV}$. For the mass-dimension 6 AM and

CR interactions, we find $a_\chi, b_\chi \gtrsim 3\times10^{-3}\,\mathrm{GeV}^{-2}$ are excluded, pointing towards a comparably lower effective scale of $\Lambda_6 < 20\,\mathrm{GeV}$. In the latter case, the constraint is superseded by LEP. Finally, as a by-product of our study, we also revise previously obtained proton-beam dump bounds on millicharged particles.

With a strong connection to the neutrino program, proton-beam experiments constitute an active and diverse field, with a number of new experiments such as SHiP and DUNE. However, because the interactions considered here are higher-dimensional, we find that the prospects of significantly improving the direct sensitivity on EM form factor couplings rather hinges on the future of high-energy collider experiments and their ability to produce collisions with an ever increased CM energy.

CHAPTER 5

Terrestrial Probes

The content of this chapter follows [P4].

5.1 Light dark degrees of freedom: dark radiation

Besides massive DM, a generic dark sector may further comprise nearly massless particles often called *dark radiation* (DR). They may constitute extra radiation degrees of freedom, in addition to the SM photon and neutrinos. DR (and its interaction with DM) can affect different cosmic epochs, such as BBN and CMB, or, at a later time, the cosmic dawn and structure formation. A population of the quanta can build up thermally, through the standard freeze-out framework with an energy spectrum similar to other cosmic radiation backgrounds; or, it can be created non-thermally, *e.g.*, sourced through the decay of some particle. In the latter case, the DR can have distinct energy spectra compared to the standard CMB such that $\omega_{\rm DR} \gg \omega_{\rm CMB}$, changing its phenomenology in various aspects and boosting its detection potential in terrestrial experiments.

In the literature, a primary observable for DR is the number of relativistic degrees of freedom in the early universe, parameterized by $N_{\rm eff}$. The contribution from DR, in addition to the standard relativistic degrees of freedom (photon and neutrinos), can be singled out by defining

$$\Delta N_{\rm eff} \equiv N_{\rm eff} - N_{\rm eff}^{\rm SM} \,,$$

where the SM-predicted value $N_{\rm eff}^{\rm SM} \simeq 3.044$ [304, 305]. The value of $\Delta N_{\rm eff}$ is constrained by the light element abundance from BBN as well as the CMB anisotropy power spectrum. From the current sensitivity $\Delta N_{\rm eff} \lesssim 1$ from BBN [223, 225, 306] and $\Delta N_{\rm eff} \lesssim 0.3$ from measurements of CMB+BAO [86], we infer that DR can only constitute a limited energy fraction in the early universe.

Even if DR has no appreciable impacts on the early-universe physics, in the local universe, interactions between DR and SM particles enable the detection of DR on Earth, for example, in direct detection experiments and neutrino experiments. The ensuing signals may arise from the scattering between DR and SM particles and the absorption of DR by SM particles,

depending on the particle nature of DR. These experiments typically have an energy threshold above $\mathcal{O}(\text{keV})$, thus a DR background needs to be energetic enough to be detectable. Considering that a thermal radiation background has a typical energy of $\mathcal{O}(\text{meV})$, a population of DR needs to build up non-thermally to go beyond the energy threshold as discussed above.

In this chapter, we consider the possibility of probing interacting DR χ on Earth with particle recoil events. We assume fermionic DR that is produced by the late-time two-body decay of DM X, which is one way to create a non-thermal population of DR. Furthermore, following the same narrative as previous chapters, the DR interacts with the photon via the EM form factor interactions given by Eq. (2.6). Owing to the low energy scales involved in the following, we use effective operators to describe the EM interactions. In general, the experimental sensitivity depends on the progenitor's mass and lifetime which determine the energy spectrum and flux of the DR, and the effective EM coupling strength between χ and photon. Based on where the decay takes place, the DR flux can be separated into two categories: Galactic and extragalactic. As we consider a two-body decay, in the former case, the energy of χ is monochromatic, because of the small velocity dispersion of the progenitor. On the contrary, the extragalactic DR flux develops a continuous energy spectrum due to the cosmic expansion.

In the following, we collect the ingredients for the calculation of the DR flux from decaying DM (DDM). For simplicity, we assume a single decay channel for X. In that case, the $X\bar{\chi}\chi$ coupling can be traded for the lifetime of X. The expected Galactic energy differential flux is given by

$$\frac{d\phi_\chi^{\text{gal}}}{dE_\chi} = \frac{e^{-t_0/\tau_X}}{m_X \tau_X} \frac{dN_\chi}{dE_\chi} R_\odot \rho_\odot \langle J \rangle \,, \tag{5.1}$$

where t_0 is the age of the universe, m_X and τ_X are the DM mass and lifetime, $R_\odot \simeq 8.33\,\text{kpc}$ is the distance between the Sun and the Galactic Center, $\rho_\odot = 3 \times 10^5\,\text{keV/cm}^3$ is the local DM energy density and $\langle J \rangle \simeq 2.1$ is the averaged J-factor assuming a Navarro–Frenk–White (NFW) profile [307]. For simplicity, we consider a 100% decaying fraction of DM, placing us in the long-lifetime regime with respect to t_0; if this is not the case, the formulas are to be dressed with the DDM fraction in an obvious way. The DR injection spectrum is given by

$$\frac{dN_\chi}{dE_\chi} = 2\delta\left(E_\chi - \frac{m_X}{2}\right) , \tag{5.2}$$

with a negligible spread by the parent DM velocity dispersion.

In turn, the energy differential DR flux that originates from DDM cosmologically reads [308]

$$\frac{d\phi_\chi^{\text{ext}}}{dE_\chi} = \frac{2\Omega_X \rho_c}{m_X \tau_X H_0 p_\chi} \frac{e^{-t(\xi-1)/\tau_X}}{\sqrt{\xi^3 \Omega_m + \Omega_\Lambda}} \Theta(\xi - 1) \,, \tag{5.3}$$

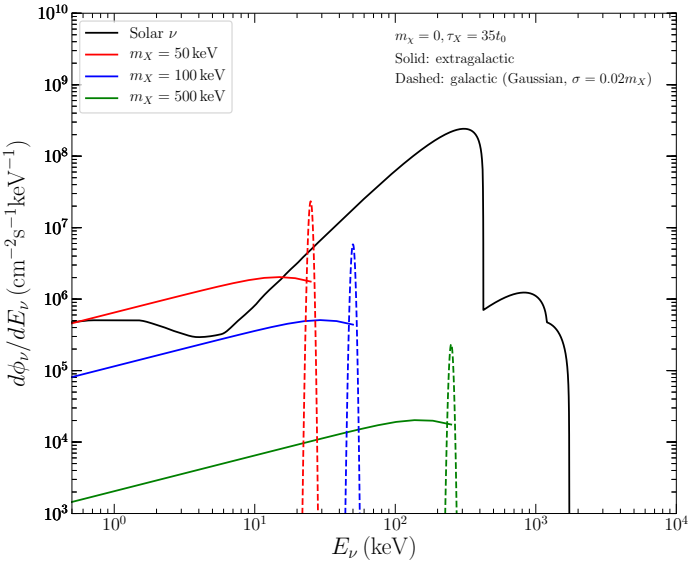

Figure 5.1: The solar neutrino flux (solid black) and the DR flux from the DDM for $\tau_X = 35t_0$ and various choices of m_X. Both, Galactic and extragalactic DR flux from DDM can reach comparable levels of flux with respect to the solar neutrinos.

where $\Omega_X = 0.2607$ is the DM density parameter [86] and $\rho_c = 4.82\,\mathrm{keV\,cm}^{-3}$ is the critical density of the Universe at present, $\Theta(\xi - 1)$ is a Heaviside step function, and $\xi \equiv p_{\mathrm{in}}/p_\chi$ is the ratio of injected momentum p_{in} to arriving momentum p_χ, $p_{\mathrm{in}}^2 = (m_X/2)^2 - m_\chi^2$. In the exponential $t(\xi - 1)$ is the cosmic time at redshift $z = \xi - 1$. For a spacially flat cosmology and for $z \lesssim 10^3$, it is given by

$$t(z) = \frac{1}{3H_0\sqrt{\Omega_\Lambda}} \ln\left[\frac{\sqrt{1 + (\Omega_m/\Omega_\Lambda)(1+z)^3} + 1}{\sqrt{1 + (\Omega_m/\Omega_\Lambda)(1+z)^3} - 1}\right], \tag{5.4}$$

where $\Omega_m = 0.3111$, $\Omega_\Lambda = 0.6889$ are the cosmological density parameters for matter and dark energy, respectively; $H_0 = 67.66\,\mathrm{km\,s}^{-1}\,\mathrm{Mpc}^{-1}$ is our adopted present day Hubble rate [86].

As a benchmark value for the DM lifetime, we take $\tau_X = 35t_0$ [309], which saturates the limit on invisibly DDM from a joint data set that includes CMB measurements [86, 310], the Pantheon data of type Ia supernovae [311] and baryon acoustic oscillation measurements [312–314]; for previous constraints on τ_X or the fraction of DDM, see [315–317]. The DR mass is not entering the analysis in an appreciable way, as we focus on the relativistic daughter particles; in our analysis, we do take into account its effect when the value of m_χ is explicitly stated. Therefore, we have two free parameters: the DM mass m_X and the coupling between the DR and the SM sector.

In Fig. 5.1, we compare the solar neutrino flux and the expected Galactic DR flux (dashed lines) and the extragalactic DR flux (solid lines) originating from DDM with mass

	Exposure (ton×yr)	Signal Range	Signal Type	Reference
XENON1T (fit)	0.65	$[1, 10]$ keV	ER	[321]
XENON1T (S1+S2)	0.65	$[3, 66]$ $\mathrm{PE_{S1}}$	ER	[321]
XENON1T (S2)	0.06	$[150, 526]$ PE	ER	[322]
Borexino	2.1×10^2	$[0.32, 2.64]$ MeV	ER, NR	[323, 324]
Super-Kamiokande	9.2×10^4	$[16, 88]$ MeV	ER	[325]
	1.6×10^5	$[0.1, 1.33]$ GeV	ER	[326]
Hyper-Kamiokande*	2.3×10^6	$[16, 88]$ MeV	ER	[327, 328]
	4.0×10^6	$[0.1, 1.33]$ GeV	ER	[327, 328]
DUNE* (10/40 kton)	7.2×10^4 (2.9×10^5)	$[0.03, 1.33]$ GeV	ER	[329]

Table 5.1: Summary of experiments with (effective) exposures, our considered signal ranges, signal type, and main reference for the reported data used in this work; the star indicates that a forecast on the sensitivity is derived.

$m_X = 50, 100, 500$ keV; we apply a 2% Gaussian smearing on the monochromatic Galactic flux for visualization. The fluxes are compared to the solar neutrino flux (solid black line) taken from [318–320]; below 10 keV, we include the contribution from plasmon decay, photoproduction, and bremsstrahlung from [207]. As can be seen, both Galactic and extragalactic DR fluxes are, in magnitude, in roughly the same ballpark as the solar neutrino flux.

5.2 Terrestrial experiments

In this section, we outline the considered experiments and the way to derive constraints and forecasts of sensitivity on the parameter space. For electron recoil (ER) in the $\mathcal{O}$(keV) energy ballpark, we consider the scattering of DR in the XENON1T detector. Neutrino experiments such as Borexino, Super-Kamiokande (SK) as well as the future Hyper-Kamiokande (HK) and Deep Underground Neutrino Experiment (DUNE) have larger energy threshold, MeV–GeV range, and we consider DR-electron scattering for which the solar neutrinos ($E_R < 30$ MeV) and atmospheric neutrinos ($E_R > 30$ MeV) become the main background. For Borexino, we consider DR-proton scattering, *i.e.*, nuclear recoil (NR), in addition. See Tab. 5.1 for a summary of experimental details.

XENON1T The XENON1T detector, located underground at the Gran Sasso laboratory, is a dual-phase time projection chamber with liquid and gaseous xenon. The registered signals include prompt scintillation (S1) and secondary scintillation from ionization (S2). In a recent analysis [321], an excess of events was identified in the S1 data at $\mathcal{O}$(keV). Although poorly understood backgrounds exist [321, 330], the possibility that this signal is due to new

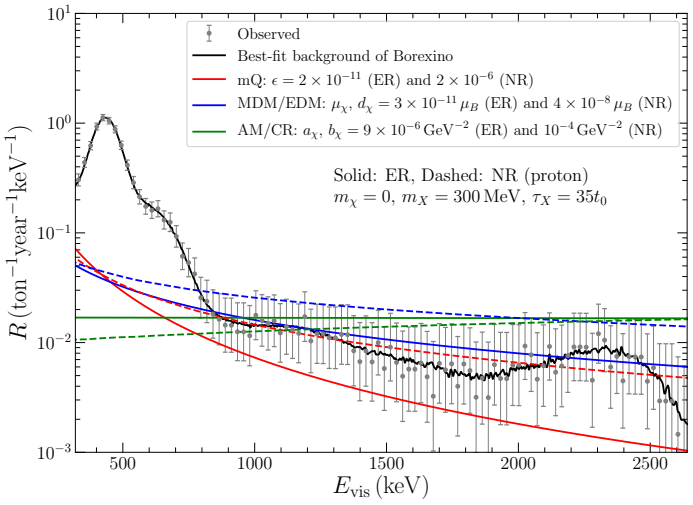

Figure 5.2: The Borexino observed event rate together with the reported best-fit background model (solid black), and exemplary event rates for mQ (red), MDM/EDM (blue) AM/CR (green) as a function of the visible energy E_{vis}. Solid lines are for ER, while dashed ones are for NR. The differing energy-dependence of the operators of differing dimensionality can be clearly observed.

physics has been entertained abundantly. The excess is not in conflict with an earlier S2-only analysis by the experiment [322]. Here we derive both, the favored region for the anomaly and the constraints on the parameter space using the S1+S2 and S2-only data. Details on the limit-setting procedure can be found in [331] which we follow here; see also [163].

Borexino The Borexino experiment features a liquid scintillator-based detector with 280 ton fiducial mass, primarily designed to measure solar neutrinos in the quasi-elastic scattering signal with electrons [332]. We use the latest data from the CNO neutrino search of phase-III [323, 324] of the experiment, with an exposure of 209.4 ton-yr. Between the threshold energy 320 keV and 2640 keV, the observed event rate and the best-fit background plus solar neutrino-induced rate are reported for each energy bin. Note that the standard neutrino events are a background in our consideration. The detection efficiency is assumed to be unity. We derive 95% C.L. limits using the CL_s method [333].

For heavier progenitor masses, we further consider the proton recoil signal in the Borexino detector. Here, we adopt Birk's law to account for the energy quenching in the organic scintillator,

$$E_{\mathrm{vis}} = \int_0^{E_R} \frac{dE}{1 + k_B dE/dx}\,, \tag{5.5}$$

where E_{vis} is the visible energy, $k_B \simeq 0.01\,\mathrm{cm/MeV}$ is Birk's constant and dE/dx is the stopping power which we compute using the `SRIM` computer package; see also [334]. For

the scintillator pseudocumine C_9H_{12} with a mass density of $\rho = 0.88\,\mathrm{g/cm}^3$, the stopping power for protons is roughly $dE/dx \sim \mathcal{O}(100)\,\mathrm{MeV/cm}$, albeit energy-dependent. For electrons, $dE/dx \sim \mathcal{O}(10^{-3})\,\mathrm{MeV/cm}$ so that we are allowed to neglect the energy quenching since $dE/dx \ll k_B^{-1}$. We utilize the same data and method presented above to derive the corresponding constraint. See Fig. 5.2 for a demonstration of the event rate from different operators and the Borexino data.

Super-Kamiokande Super-Kamiokande (SK) is a neutrino experiment with a water-based Cherenkov detector located 2.7 km underground in Japan. The fiducial mass is 22.5 kton. First, we consider the low-energy e^--recoil data with $E_R = (16\text{–}88)\,\mathrm{MeV}$ from a diffuse supernova neutrino background search in the SK-I run [325]. With 1497 days of observation, 239 events are reported with $N_{\mathrm{bkg}} = 238$ from the best-fit model, which has also been utilized to set bounds on neutrino DR [308] and cosmic-ray upscattered DM [335]. The corresponding efficiency is taken from [325]. At the higher recoil energy range, a recent analysis [326] provides three energy bins of 161.9 kton-yr fiducialized fully-contained data from the SK-IV run, with cuts applied for a single relativistic electron and no accompanying nuclear interaction. We use the first energy interval ranging from 100 MeV to 1.33 GeV with a total number of $N_{\mathrm{obs}} = 4042$ events and an efficiency $\epsilon(0.5\,\mathrm{GeV}) = 0.93$. The estimated background is 3993 e^--recoil events during its data-taking time [326]. The ensuing 90% C.L. limits on the various signal strengths can be derived by requiring that the DR-induced events $N_{\mathrm{sig}}^{\mathrm{DR}}$ satisfy Eq. (4.18).

Hyper-Kamiokande Hyper-Kamiokande (HK) will be equipped with 25 times larger fiducial mass than SK [327, 328]. It will provide supreme sensitivity to solar, atmospheric and supernova neutrinos. We consider the same low and high recoil energy ranges as in SK. The background estimation is done by rescaling the background events of SK according to their difference in the fiducial mass. Under the assumption of same data-taking time as SK and a constant efficiency of 0.8, we derive the projected sensitivity of HK by imposing $N_{\mathrm{sig}}^{\mathrm{DR}} \leq 1.28\sqrt{N_{\mathrm{bkg}}}$ assuming $N_{\mathrm{obs}} = N_{\mathrm{bkg}}$.

DUNE DUNE is a proposed long-baseline neutrino facility, which serves as the far detector for the neutrino beam generated from 1300 km away [274]. As an add-on, its liquid argon (LAr)-based detector can also probe light dark sector physics [273]. DUNE will be comprised of four 10 kton detectors. In the following we consider both the 10 kton and 40 kton configurations. To avoid the immense solar neutrino background, the electron energy threshold is set to 30 MeV [329]. The expected (all-sky) number of e^--recoil background events per year is $N_{\mathrm{bkg}} = 128\,(512)$ for the $10\,(40)$ kton detector [329]. The detection efficiency for the LAr time projection chamber is assumed to be 0.5. Finally, we obtain the future projection on the couplings for each progenitor mass by the condition $N_{\mathrm{sig}}^{\mathrm{DR}} \leq 1.28\sqrt{N_{\mathrm{bkg}}}$, assuming

$N_{\rm obs} = N_{\rm bkg}$ and the same data-taking time as well as the upper boundary of recoil energy as the SK high-E_R data.

5.3 Event rate

5.3.1 Scattering on bound electrons

For small progenitor mass, the resulting DR is low-energetic enough that we need to account for bound state effects in the DR-electron scattering and resulting atomic ionization process. Combining the DR flux from Sec. 5.1 and the differential cross section given in App. B.3.1, the differential event rate for scattering with the electrons is

$$\frac{dR}{dE_R} = \kappa N_T \varepsilon(E_R) \int_{q_-}^{q_+} dq \int_{p_\chi^{\rm min}}^{p_\chi^{\rm max}} dp_\chi \, \frac{p_\chi}{E_\chi} \frac{d\phi_\chi}{dE_\chi} \frac{d\sigma v}{dq dE_R} \,, \tag{5.6}$$

where κ is the exposure of the experiment, N_T is the number of targets per detector mass, $\varepsilon(E_R)$ is the detection efficiency, and $d\phi_\chi/dE_\chi$ is the differential χ flux from DDM that includes both, the Galactic and extragalactic components. The minimum χ-momentum for a given recoil energy E_R and momentum transfer q is

$$p_\chi^{\rm min} = \frac{q}{2x} \left[x + \frac{\Delta E}{q} \sqrt{x \left(x + \frac{4m_\chi^2}{q^2} \right)} \right] \,, \tag{5.7}$$

where $x = 1 - \Delta E^2/q^2$ with $\Delta E = E_R + |E_B^{n,l}|$ being the deposited energy and $E_B^{n,l}$ is the binding energy of the bound state orbital (n,l). The upper boundary of the p_χ integration is given by $p_\chi^{\rm max} = p_{\rm in}$. The integration boundaries of q are given by

$$q_+ = p_\chi^{\rm max} + \frac{\sqrt{(m_X - 2\Delta E)^2 - 4m_\chi^2}}{2} \,, \; q_- = \Delta E \,. \tag{5.8}$$

To obtain the total event rate, we sum up the contributions from all kinematically available (n,l) shells.

5.3.2 Scattering on free particles

For larger progenitor mass, the $\mathcal{O}$(MeV–GeV) ER signals induced by DR are best probed in the large-volume neutrino experiments mentioned in Sec. 5.2. For such recoil energies, the initial electron can be considered as a free particle. With the recoil cross section given in App. B.3.2, the total differential event rate reads

$$\frac{dR}{dE_R} = \kappa N_T \varepsilon(E_R) \int_{p_\chi^{\rm min}}^{p_\chi^{\rm max}} dp_\chi \frac{p_\chi}{E_\chi} \frac{d\phi_\chi}{dE_\chi} \frac{d\sigma}{dE_R} \,. \tag{5.9}$$

Here, the lower integration boundaries of p_χ is given through $p_\chi^{\rm min} = \sqrt{(E_\chi^{\rm min})^2 - m_\chi^2}$ with

$$E_\chi^{\rm min} = \frac{E_R}{2} + \frac{1}{2m_e}\sqrt{m_e(E_R+2m_e)(E_R m_e + 2m_\chi^2)}\,, \tag{5.10}$$

and the upper boundary as before. The expected number of events is given by

$$N_{\rm sig}^{\rm DR} = \int_{E_{\rm th}}^{E_R^{\rm max}} dE_R \frac{dR}{dE_R}\,, \tag{5.11}$$

where $E_{\rm th}$ is the threshold recoil energy. The maximal recoil energy $E_R^{\rm max}$ is either given by the energy range of the experimental data or half of the progenitor mass.

For large enough m_X, the DR is energetic enough to generate $\mathcal{O}$(keV–MeV) NR in direct detection and neutrino experiments. The framework for NR is the same as scattering on free electrons discussed above, but the recoil cross section become target-dependent; see [183] for detailed formulas of the nuclear recoil cross section.

5.4 Results of Chapter 5

5.4.1 Constraints on the effective interactions

We show the resulting constraints (shaded regions) and forecasts of sensitivity (lines) for millicharged DR in the left panel of Fig. 5.3, for MDM/EDM interactions in the right panel of Fig. 5.3 and for AM/CR interactions in the left panel of Fig. 5.5. We also show the XENON1T excess favored region, with details on the fitting procedure given in Sec. 5.4.2. Previous constraints derived from the anomalous energy loss in red giant (RG) stars and SN1987A cooling are included for comparison ([170] and [P1]), which apply when m_χ is smaller than the plasma frequency in the stellar environment: $m_\chi \leq 10\,{\rm keV}(20\,{\rm MeV})$ for RG stars (SN1987A); see also [173, 221] and Chap. 3. For mQ, we note that there exist additional bounds from galaxy cluster magnetic fields [336] and the timing of radio waves [337]. However, both of them scale with the DR mass, thus they are not included in the figures.

Due to the energy dependence in the cross sections, the experiments with higher threshold are more important for higher-dimensional operators. We see that current SK and future HK and DUNE can all provide better sensitivity than current best limit from the stellar energy loss for mass-dimension 5 and 6 operators, assuming $\tau_X = 35 t_0$. For mQ, the improvement of sensitivity between experiments that probe free-electron scattering and XENON1T is not so notable compared to higher-dimensional operators.

5.4.2 XENON1T excess

In light of the recent excess in the $\mathcal{O}$(keV) recoil energy range observed by XENON1T [321], we also explore the possibility of explaining the excess with DR, assuming the background

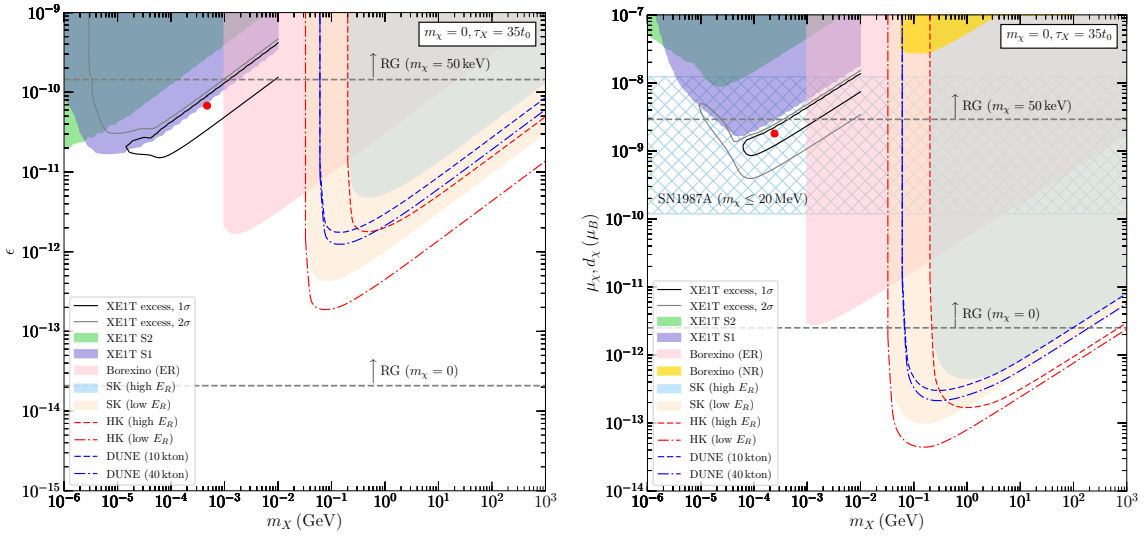

Figure 5.3: The constraints and the forecasts of sensitivity on the mQ (left panel) and effective MDM/EDM (right panel) interaction of the DR. In addition, the best-fit values (indicated by the red dots) and the favoured regions explaining the XENON1T excess are shown. The strongest bounds in the literature, taken from [170] and [P1], from the anomalous energy loss inside red giant stars are included for comparison; their strength depends on the DR mass. For mass-dimension 5 operators, we also show the constraints from the anomalous cooling of SN1987A. See Chap. 3 for the derivation of stellar bounds.

modelling is correct. This lines up with several other new physics scenarios and their constraints that have been investigated in this context. Moreover, PandaX-II reports for its own data that it is both, consistent with a new physics contribution as well as with a fluctuation of background [338]. Thus the observational status of an excess in XENON1T remains unclear at the moment.

In Fig. 5.6, we show the best-fit event rate induced by DR and the data in the energy range $[0, 10]$ keV in two fitting scenarios, including and excluding the first bin. By excluding the first bin, the recoil spectrum can better fit to the peak of excess, but at the expense of significantly overshooting the first bin. When the first bin is included in the fit, the second bin cannot be filled but the overall fit is still satisfactory, similar to the anomalous neutrino magnetic dipole moment explanation [321, 339]. The corresponding best-fit parameters and χ^2/dof are given in Tab. 5.2. We observe that higher-dimensional operators yield improved fits to the excess, as their recoil spectra are less peaked at low E_R. We also note that the best-fit coupling of mass-dimension 5 operator is consistent with the best-fit anomalous magnetic dipole moment of neutrino [339], *i.e.*,

$$\phi_\chi^{\text{best}} \times \left(\mu_\chi^{\text{best}}\right)^2 \simeq \phi_\nu^{\text{solar}} \times \left(\mu_\nu^{\text{best}}\right)^2 , \tag{5.12}$$

although the free-electron approximation is adopted in [339].

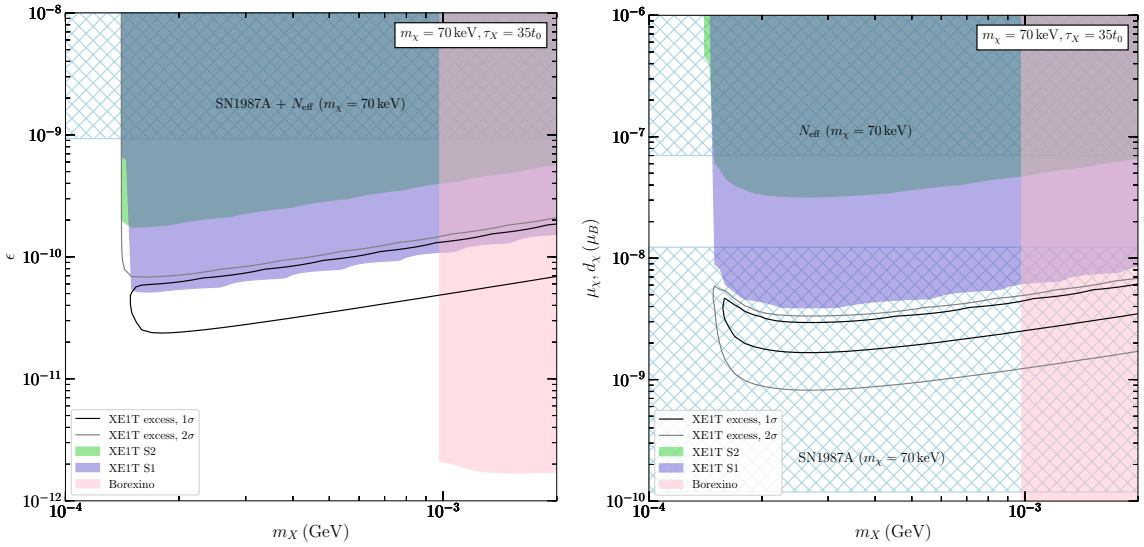

Figure 5.4: Zoom-in figures with massive DR ($m_\chi = 70\,\mathrm{keV}$) for the parameter space favoured by the XENON1T excess. Left panel (mQ): the parameter space for explaining the XENON1T excess is not constrained by either stellar energy loss arguments or $N_{\rm eff}$. Right panel (MDM/EDM): the parameter space is fully covered by the SN1987A bound. The SN1987A and $N_{\rm eff}$ constraints are adopted from [170] and [P1]. The difference between EDM and MDM is neglected as it is not resolved except at the very kinematic endpoint $m_X \simeq 140\,\mathrm{keV}$ as DR remains (semi-)relativistic everywhere else.

For massless DR, the favoured parameter space for the excess is excluded by stellar energy loss constraints, such as RG stars for mass-dimension 4 and 5 operators and SN1987A for mass-dimension 6 operators, shown in Fig. 5.3, and taken from [170] and [P1]; see also [173, 221]. However, stellar energy loss is effective only when χ production is kinematically allowed. Taking DR with $m_\chi = 70\,\mathrm{keV}$, the constraints from the stellar energy loss are alleviated. Finally, we consider the constraint from the measured number of relativistic degrees of freedom $N_{\rm eff}$, as χ particles are also populated in the early universe through plasmon decay and electron-positron annihilation; see [170, 221] and [P1]. As shown in Fig. 5.4 for mQ (left panel) and MDM/EDM (right panel), and in the right panel of Fig. 5.5 for AM/CR (right panel), there remains allowed parameter space for explaining the XENON1T excess for mass-dimension 4 and 6 operators. For mass-dimension 5 operators, the viable parameter space is covered by the SN1987A bound.

5.5 Summary of Chapter 5

In this chapter, we have considered the possibility that DM X is unstable and decays to a $\bar{\chi}\chi$-pair which itself couples to the SM through effective interactions mediated by the photon.

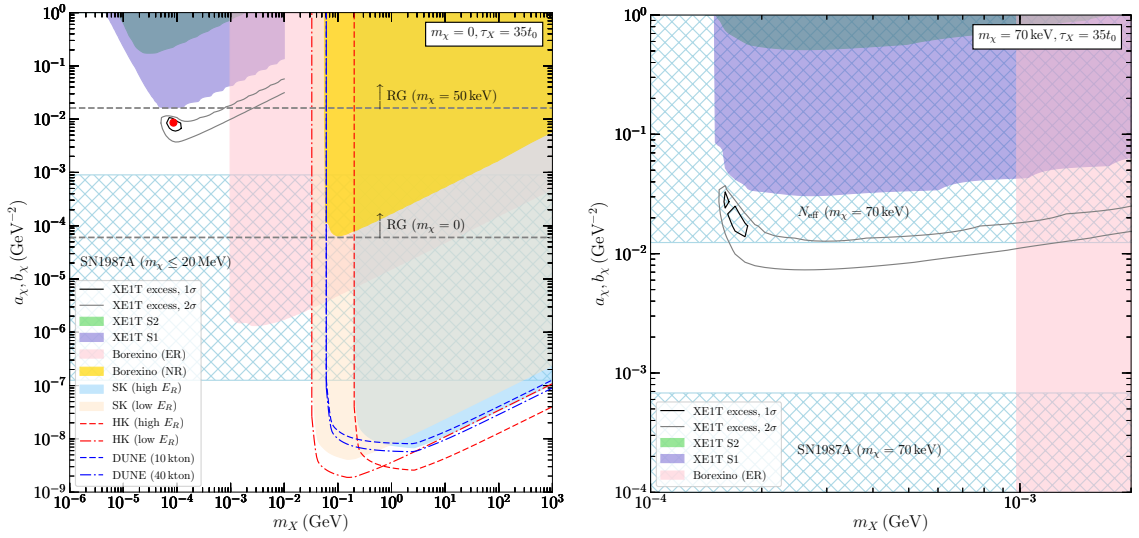

Figure 5.5: *Left:* The constraints and the forecasts of sensitivity on the effective AM/CR interaction as labeled. The hatched region shows the anomalous cooling constraint from SN1987A and dashed lines are constraints from the energy loss inside RG stars [P1]. *Right:* Zoom-in figures with massive DR ($m_\chi = 70\,\text{keV}$, AM/CR) for the parameter space favoured by the XENON1T excess. Part of the parameter space is ruled out by $N_{\rm eff}$. The difference between AM and CR is neglected as well.

We consider the possibility of millicharge of χ, magnetic and electric dipole moments, and the less familiar anapole moment and charge radius interaction. The emerging DR flux from DDM is then probed in underground rare-event searches. For $m_X \lesssim 1\,\text{MeV}$ direct detection experiments offer the best sensitivity with their ability of registering keV-scale energy depositions and below. Heavier progenitors are better probed with neutrino experiments, as χ-induced events leave MeV-scale signals. For concreteness, in this chapter we have chosen a benchmark value of $\tau_X = 35t_0$ with the bulk of DM still to decay in the distant future.

The scattering of χ on electrons is the most important signal channel. We demonstrate that the recent (S1+S2) data from the XENON1T experiment yields $\epsilon \lesssim 2\times10^{-11}$ at $m_X \simeq 10\,\text{keV}$, and $d_\chi, \mu_\chi \lesssim 2\times10^{-9}\,\mu_B$ as well as $a_\chi, b_\chi \lesssim 2\times10^{-2}\,\text{GeV}^{-2}$ at $m_X \simeq 100\,\text{keV}$. In addition, we find that it is also possible to reach a satisfactory fit to the reported excess of events seen in the XENON1T data at few keV energy. The fit improves by increasing the dimensionality of the operator, as the lowest energy bin in the data prohibits too strong of an IR-biased signal. The AM/CR interaction thereby yields the best fit. The DR mass-dependence is relatively mild in those drawn conclusions as these particles retain their (semi-)relativistic nature except at the very kinematic edge $2m_\chi \simeq m_X$. However, stellar and cosmological constraints critically depend on m_χ. By choosing a benchmark value of $m_\chi = 70\,\text{keV}$ we demonstrate that a XENON1T explanation remains intact for mQ and for the mass-dimension 6 AM and CR operators, evading bounds from the anomalous energy loss inside RG stars, of the proto-neutron star of SN1987A and from the cosmological $N_{\rm eff}$ limit.

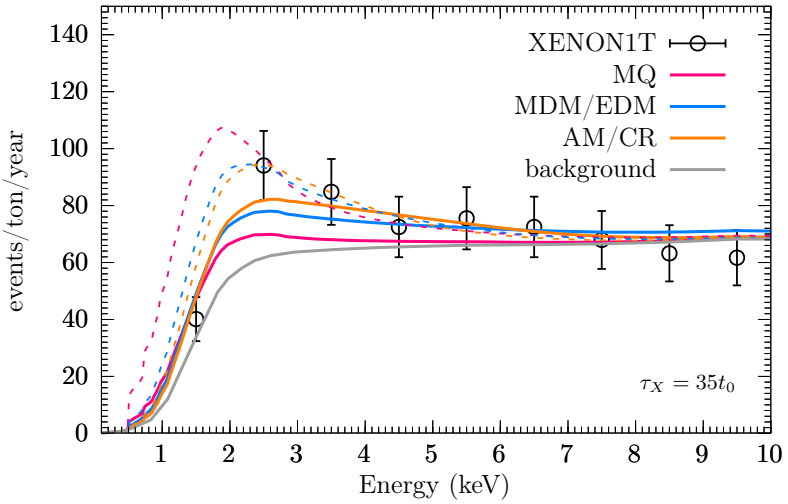

Figure 5.6: Best-fit event rate to the XENON1T excess for each effective EM interaction. We demonstrate cases including (solid) and excluding (dashed) the first bin in the fitting.

	m_X (keV)	coupling	χ^2/dof
mQ	472	$\epsilon = 6.8 \times 10^{-11}$	9.2/7
excl. first bin	183	$\epsilon = 8.9 \times 10^{-11}$	1.5/6
MDM, EDM	243	$\mu_\chi, d_\chi = 1.8 \times 10^{-9}\,\mu_B$	5.8/7
excl. first bin	81	$\mu_\chi, d_\chi = 1.8 \times 10^{-9}\,\mu_B$	1.1/6
AM, CR	86	$a_\chi, b_\chi = 8.6 \times 10^{-3}\,\text{GeV}^{-2}$	3.6/7
excl. first bin	71	$a_\chi, b_\chi = 1.1 \times 10^{-2}\,\text{GeV}^{-2}$	1.1/6

Table 5.2: Best-fit values of m_X and strength of the EM interaction as well as the corresponding χ^2/dof. A lifetime of $\tau_X = 35t_0$ is assumed.

For progenitor masses $m_X \gtrsim 1\,\text{MeV}$ Borexino has the best sensitivity reaching $\epsilon \lesssim 10^{-12}$, $d_\chi, \mu_\chi \lesssim 3 \times 10^{-12}\,\mu_B$ and $a_\chi, b_\chi \lesssim 2 \times 10^{-6}\,\text{GeV}^{-2}$ at $m_X \simeq 1\,\text{MeV}$. These limits rely on the detailed modeling of Borexino backgrounds and its solar neutrino-induced events. The limits are eventually surpassed by the ones from SK, once DR induces electron recoils above the solar neutrino background. Best sensitivity is attained for $m_X \simeq 100\,\text{MeV}$ with $\epsilon \lesssim 4 \times 10^{-13}$, $d_\chi, \mu_\chi \lesssim 10^{-13}\,\mu_B$ and $a_\chi, b_\chi \lesssim 4 \times 10^{-9}\,\text{GeV}^{-2}$. Finally, we also provide forecasts for HK and DUNE, with relatively mild expected improvements.

Part II

Sub-GeV Scalar Dark Matter Candidates

CHAPTER 6

Motivations and Hints for sub-GeV Dark Matter

In this chapter, we first recap two tantalizing hints for sub-GeV DM: the Integral 511 keV line and the muon $g-2$. Furthermore, we discuss the thermal freeze-out scenario for obtaining the DM relic density. Then we introduce the details of the particle model that we will visit and review how they can potentially account for these phenomena.

6.1 Integral 511 keV line

The SPI spectrometer on board of the INTEGRAL satellite detected a strong flux of 511 keV photons at the level of almost $10^{-3}\,\mathrm{cm}^{-2}\mathrm{s}^{-1}$ [72, 73] (see also [341, 342] and Fig. 6.1) coming from the galactic bulge. Based on those results, a MeV-scale DM origin was suggested on the basis of its spatial morphology and its general compatibility with the relic density requirement [176] while at the same time obeying soft gamma-ray constraints [343–345]. Concretely, the signal, especially its high bulge-to-disk ratio, is unexpected from known astrophysics [341, 346] and calls for a new production mechanism of low-energy positrons. This can be achieved through DM annihilation into e^-e^+ pairs.

Here we provide a lighting review on the status of the INTEGRAL line in its connection to annihilating DM into e^-e^+ pairs. Decomposing the annihilation cross section in terms of the relative velocity as $\sigma_{\mathrm{ann}}v = a + bv^2$ and assuming a NFW DM halo profile [307], the observations suggest that the best-fit values for the a or b parameters are [347]

$$a \simeq 2.2 \times 10^{-31} \left(\frac{m_\phi}{\mathrm{MeV}}\right)^2 \mathrm{cm}^3\,\mathrm{s}^{-1}\,, \tag{6.1a}$$

$$b \simeq 3.4 \times 10^{-25} \left(\frac{m_\phi}{\mathrm{MeV}}\right)^2 \mathrm{cm}^3\,\mathrm{s}^{-1}\,, \tag{6.1b}$$

with a strong preference for a constant cross section (a-value) [348] albeit large uncertainties and an additional dependence on the cuspiness of the inner DM halo profile [349] exist. With these numbers in mind, the p-wave is roughly commensurate with the value required for a successful thermal relic $\sigma_{\mathrm{ann}}v \sim \text{few} \times 10^{-26}\,\mathrm{cm}^3\,\mathrm{s}^{-1}$ (where $v \sim 0.3$ at freeze-out).

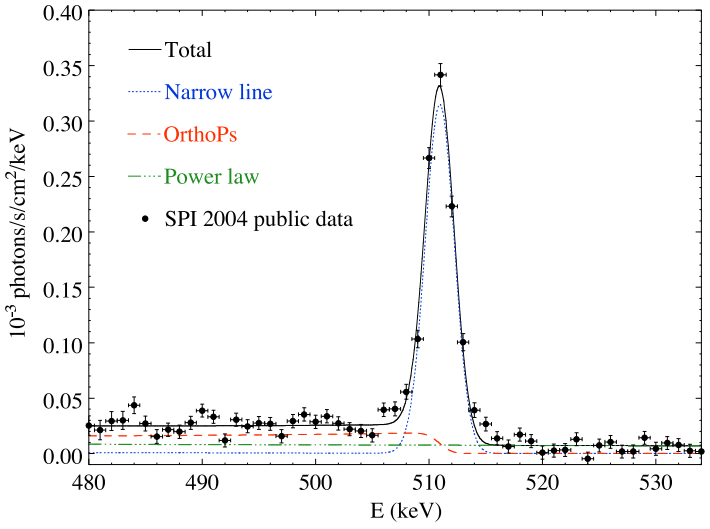

Figure 6.1: The illustration of the 511 keV flux observed by the INTEGRAL satellite. The data points can be fitted by a narrow line from direct annihilation of electron-positron pair at rest with a low-energy continuum from positronium decay. Figure credit: [340].

The question of viable DM mass is an involved one. The injected positrons produced in DM annihilation need to decelerate to non-relativistic speeds before annihilating to explain the 511 keV INTEGRAL line. Because of substantial uncertainties in astrophysical propagation modelling [350, 351], the maximal DM mass that can explain the line remains uncertain; see [352] for a recent summary. There are, however, several quantitative results with regard to spectral features:

1) Extra photons created by bremsstrahlung in the annihilation process suggest $m_\phi \lesssim 20\,\text{MeV}$ [344] although more detailed calculations relax this bound to $m_\phi \lesssim 30$–$100\,\text{MeV}$ [353]. This is comparable to the Voyager 1 bound based on local $e^\mp$ measurements [354].

2) The most stringent constraint on the DM mass is obtained when considering the in-flight annihilation, implying $m_\phi \lesssim 3$–$7.5\,\text{MeV}$ [355, 356], mostly from the COMPTEL diffuse γ-ray background measurements. The constraint is derived from the X-ray background inside the gas-dense region of the Galactic Center.

3) Recently, Ref. [357] has re-visited the extra photon emission (mainly via inverse Compton scattering) from DM annihilation at higher latitudes, where in-flight annihilation is sub-leading. Such treatment leads to a much weaker bound from the INTEGRAL data, $m_\phi \lesssim 70\,\text{MeV}$, when normalizing on the 511 keV line strength. Furthermore, Ref. [358] considers both bremsstrahlung and in-flight annihilation, showing that a future e-ASTROGAM experiment is able to probe the DM mass down to 4 MeV.

6.2 Muon anomalous magnetic moment

The Dirac equation predicts the g-factor, which connects the magnetic moment and the internal angular momentum of a fermion, to be $g = 2$. However, the Dirac magnetic moment only accounts for the "tree-level" result; g receives higher-order contributions from "loop diagrams". To quantify the radiative corrections, the anomalous magnetic dipole moment of a fermion is defined as $a \equiv (g-2)/2$, for which the Dirac magnetic moment is subtracted.

For SM charged leptons l, the 1-loop diagram of QED yields $a_l = \alpha/(2\pi)$ where α is the fine-structure constant. The analytical result was first derived by Schwinger, and is generally perceived as an essential milestone of QED. At present, we have a theoretical value of a_l by computing the diagrams at a higher-order of α precisely. In addition to the QED contribution, one needs to include electroweak and hadronic contributions for obtaining the SM-predicted value; see [359, 360] for reviews on the calculation of a_μ and [5] for the present theoretical values of a_l.

The anomalous magnetic moments of electron and muon are measured with high accuracy. While the measured value of a_e is roughly in concordance with the SM predicted value, at the time of writing, there is a $3.5\,\sigma$ tension in a_μ,

$$a_\mu^{\text{exp}} - a_\mu^{\text{SM}} = (290 \pm 90) \times 10^{-11}\,, \tag{6.2}$$

with a_μ^{exp} given by the E821 experiment [28]. This tension is usually called the "$(g-2)_\mu$ anomaly", and it may either hint of missing SM contribution or BSM physics. Therefore, to address the $(g-2)_\mu$ anomaly, three strategies can be envisioned: re-measuring a_μ^{exp}, re-checking the SM contribution or imposing BSM physics coupled to muons. In this thesis, we study the third case with dark sector particles participating in the loop diagrams.

We mainly focus on the 1-loop contribution of new physics (see Fig. 6.3 for example), as higher-order contributions are suppressed by the coupling between dark states and muons. The contribution to a_μ of any 1-loop diagram can be analytically expressed in terms of the projection operators detailed in App. C.1. Note that this $(g-2)$ contribution is UV-finite, inferred from the power of loop momentum included in the loop integral.

6.3 Dark matter as a thermal relic

As discussed in Sec. 1.2, we know that, currently, about 26% of the energy budget is in the form of DM. An elegant way to explain the correct DM relic abundance is *thermal freeze-out*: DM is thermalized with the SM particles via some interactions in the early universe and decouples from the thermal bath during freeze-out, after which its comoving number density is conserved. The thermal freeze-out scenario works very well for $\mathcal{O}$(GeV–TeV) DM, often

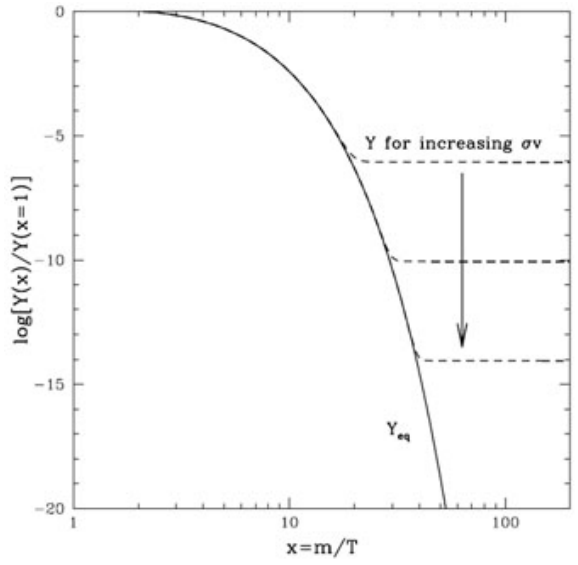

Figure 6.2: The thermal freeze-out scenario. The vertical axis represents the abundance Y, and the horizontal axis is parameterized by $x = m/T$. The positive time flow corresponds to increasing x. The larger an interaction cross section is, the longer DM in the thermal bath is, resulting in a smaller abundance today. Figure credit: [361].

referred to as the WIMP miracle: a cross section similar to a SM weak process naturally leads to the correct abundance. However, even for sub-GeV DM considered here, the thermal freeze-out is feasible. In the following, we recap the essential ingredients in computing the relic abundance; see [209] for the detailed derivation.

The thermodynamic evolution of a particle species in an isotropic and homogeneous FLRW universe is described by the Boltzmann equation:

$$\frac{\partial f_1}{\partial t} - H\frac{|\vec{p}_1|^2}{E_1}\frac{\partial f_1}{\partial E_1} = \frac{1}{E_1}C[f_1]\,, \tag{6.3}$$

where f_1 is the momentum distribution function of the species of interest. In Eq. (6.3), the left-hand side is the Liouville operator with H being the Hubble parameter and the right-hand side is the collision integral encoding the interactions of "1". For a 2-to-2 scattering with momentum assignments $p_1 + p_2 \leftrightarrow p_3 + p_4$, the collision integral reads

$$C[f_1] = -\frac{Sg_2}{2}\int d\Pi_{i=2,3,4}\,(2\pi)^4\delta^4(p_1+p_2-p_3-p_4)\times J\frac{1}{g_1 g_2}\sum_{\text{spins}}|\mathcal{M}_{12\leftrightarrow 34}|^2\,, \tag{6.4}$$

in which the factor 2 in the denominator ensures energy-momentum conservation in each collision, S is a symmetry factor, g_i is the internal degree of freedom of particle i, and $|\mathcal{M}_{12\leftrightarrow 34}|^2$ is the squared amplitude of the interaction summed over initial and final-state spins, with the factor J expressed as

$$J = f_1 f_2(1\pm f_3)(1\pm f_4) - (1\pm f_1)(1\pm f_2)f_3 f_4\,,$$

where "+(−)" is for bosons(fermions).

Assuming pair-annihilation, after performing the phase-space integral[1], we can obtain the equation governing the time evolution of the number density n as

$$\dot{n} + 3Hn = -S\langle\sigma v_M\rangle(n^2 - n_{\rm eq}^2)\,, \tag{6.5}$$

where $\langle\sigma v_M\rangle$ is the thermal-averaged cross section with v_M being the Møller velocity [209]. For pair-annihilation of identical particles $S = 1$ and $S = 1/2$ for non-identical ones. From Eq. (6.5), it follows that the process of freeze-out is controlled by two rates: rate of the cosmic expansion H, and rate of annihilation $\Gamma \sim n\langle\sigma v_M\rangle$. The moment of the decoupling can be estimated as the cosmic time at which $H = \Gamma$. In a detailed treatment, one usually solves Eq. (6.5) numerically.

In practice, it is more intuitive to quantify the abundance through $Y \equiv n/s$ where the dilution due to expansion is factored out; s is the entropy density. Therefore, after freeze-out, Y becomes a constant. After solving for the freeze-out temperature T_f numerically, the abundance today, Y_0, reads

$$Y_0^{-1} = Y_f^{-1} + \left(\frac{45}{\pi}G\right)^{-1/2} \int_{T_0}^{T_f} dT\, g_{\rm eff}^{1/2}\langle\sigma v_M\rangle\,, \tag{6.6}$$

where G is the Newton constant and

$$g_{\rm eff}^{1/2} \equiv \frac{g_{*S}}{g_*^{1/2}}\left(1 + \frac{1}{3}\frac{T}{g_{*S}}\frac{dg_{*S}}{dT}\right)\,,$$

with g_* being the total relativistic degrees of freedom (related to the energy density) and g_{*S} being the total entropy degrees of freedom (related to the entropy density). From Eq. (6.6), we can infer that $Y_0 \propto 1/\langle\sigma v_M\rangle$ if neglecting the details of the freeze-out process and assuming $Y_f \gg Y_0$. An illustration of the thermal freeze-out scenario is shown in Fig. 6.2.

6.4 Representative models

In this part, we shall focus on a complex scalar DM candidate. The Galactic 511 keV gamma-ray line can then be explained by either t-channel or s-channel annihilation processes [362]. The former process necessarily involves an electrically charged particle, taken as a fermion below. Without loss of generality, the s-channel case assumes the presence of an intermediate gauge boson, which we shall take as leptophilic. The correct DM relic density can also be obtained via standard freeze-out scenario with the same annihilation processes. In addition, the new fermion and leptophilic gauge boson contributes to $(g-2)_\mu$ through the usual triangle loop diagram, depending on the details of the model.

[1]When performing the phase space integral, we neglect the statistical factor of f and use the principle of detailed balance: $f_1^{\rm eq} f_2^{\rm eq} = f_3^{\rm eq} f_4^{\rm eq}$.

6.4.1 Heavy fermion mediator *F*

In the first model that we consider, the scalar DM particle, denoted by ϕ, couples to the Standard Model (SM) via heavy fermionic mediators. For the sake of generality we take ϕ to be complex, but mention applicable formulas for real ϕ along the way. Concretely, ϕ and its antiparticle ϕ^* may couple to the SM charged and neutral leptons $l = (l_L^-, l_R^-)^T$ and ν_l through a Yukawa-like interaction with the introduction of new electrically charged and neutral fermions $F^\pm$ and F^0, arranged as part of a $\mathrm{SU}(2)_L$ doublet (F_L^0, F_L^-), as well as singlets F_R^0 and F_R^-. Written in terms of Dirac fields $F = (F_L^-, F_R^-)^T$ and $F^0 = (F_L^0, F_R^0)^T$, the Lagrangian reads

$$\mathcal{L}_F = -c_L^l \, \phi \bar{F} P_L l - c_R^l \phi \bar{F} P_R l - c_L^l \phi \bar{F}^0 P_L \nu_l + h.c.\,. \tag{6.7}$$

Here, (ν_l, l_L^-) and l_R^- are the $\mathrm{SU}(2)_L$ doublets and singlets of lepton flavor $l = e, \mu, \tau$; $P_L = (1 - \gamma^5)/2$ and $P_R = (1 + \gamma^5)/2$ are the projection operators. We take all couplings to be real. In the presence of right-handed neutrinos ν_R, additional interactions become possible,

$$\mathcal{L}'_F = -c_R^l \, \phi (\bar{F}_R^0 \nu_R) + h.c.\,. \tag{6.8}$$

For the purpose of this thesis, we shall not consider the latter option in any detail, but mention applicable results in passing.

There are a number of options related to Eq. (6.7), see, *e.g.*, [363–369]. In what follows, we usually drop the superscript on $c_{L,R}^l$ for the coupling to electrons and electron-neutrinos as we consider them as always present, $c_{L,R} \equiv c_{L,R}^e$. Non-zero couplings to the second and third generations are *a priori* not the main focus of the thesis, but they lead to further interesting consequences. Among them is a contribution to the anomalous magnetic moment of the muon, discussed below. If there is a single generation of heavy fermions F—which is the way how the Lagrangian is written—one may additionally induce lepton flavor violating processes between the electron sector and muon or tau sector for $c^\mu \neq 0$ or $c^\tau \neq 0$, respectively (see below). At the expense of considering three generations of heavy fermions, F_l, the flavor symmetry can be restored. Finally, we note that there is also a global dark U(1)- or Z_2-symmetry in Eq. (6.7) between ϕ and F; the former (latter) applies for F^0 being Dirac (Majorana).

Because of collider bounds on charged particles [370], the fermions F have to be above the EW scale. Therefore, we take the advantage that they never appear on-shell in any process considered here, and derive constraints on the effective UV-scale $\Lambda_F = (c_L c_R / m_F)^{-1}$. Before constraining the model, we infer the normalization points for the couplings from two particularly important predictions: the contribution to the anomalous magnetic lepton moment, as well as the DM annihilation cross section corresponding to the INTEGRAL signal and the thermal relic.

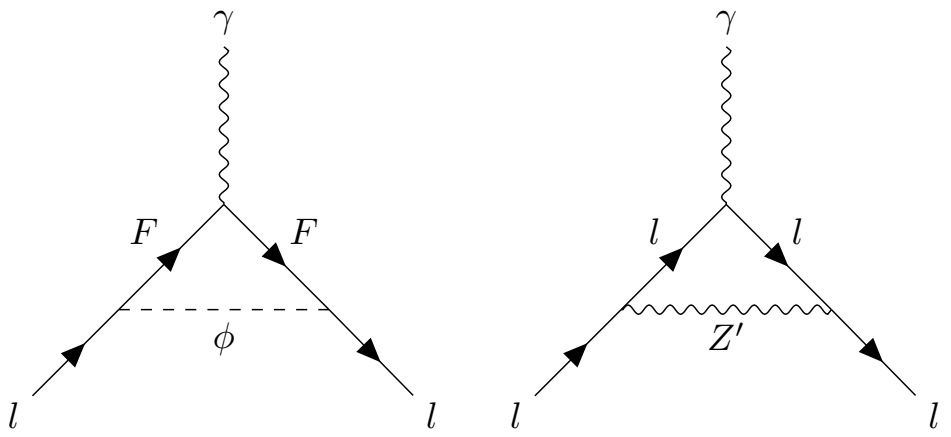

Figure 6.3: *Left*: contribution to $(g-2)_l$ from ϕ and F particles. *Right*: contribution to $(g-2)_l$ from new Z' interaction.

Anomalous magnetic moment Under the assumption that $m_F \gg m_\phi \geq m_l$ and that all c^l-couplings are real, the one-loop contribution to the leptonic anomalous magnetic moment, shown in the left panel of Fig. 6.3, is given by

$$\Delta a_l^F = \frac{c_L^l c_R^l}{16\pi^2}\frac{m_l}{m_F}\,, \tag{6.9}$$

in agreement with previous calculations [362, 371]; note that $a_l \equiv (g_l-2)/2$. Therefore, to address the long-standing muon $g-2$ anomaly [28] (see Eq. (6.2)), the corresponding favoured region is $c_F^\mu \equiv \sqrt{|c_L^\mu c_R^\mu|} \sim (5.5\text{–}7.6)\times 10^{-2}$ with $m_F = 1\,\text{TeV}$. The full expression without assuming the mass hierarchy is given in App. C.1. In anticipation of the constraints to be derived below, we point out that the contribution (6.9) to the electron anomalous magnetic moment will be of central importance when assessing the viability of explaining various anomalies.

DM annihilation In the model with heavy fermionic mediators $F^\pm$ and F^0, the non-relativistic DM annihilation cross section into e^-e^+ via $F^\pm$ exchange or into Dirac electron-neutrinos via F^0 exchange with the participation of a (kinematically unsuppressed) light right-handed state given in Eq. (6.8), $\bar\nu_e\nu_R$ or $\bar\nu_R\nu_e$, reads

$$\sigma_{\text{ann},F} v_M = \frac{c_L^2 c_R^2}{4\pi m_F^2}\left(1-\frac{m_l^2}{m_\phi^2}\right)^{\frac{3}{2}} + \frac{3c_L^2 c_R^2 m_l^2 v_{\text{rel}}^2}{32\pi m_F^2 m_\phi^2}\sqrt{1-\frac{m_l^2}{m_\phi^2}}\,, \tag{6.10}$$

where $v_M = 2(1-4m_\phi^2/s)^{1/2}$ is the Møller velocity. The s-wave component agrees with the one in Eq. (1) in [362], while the p-wave component is different, due to the fact that we expand in the Lorentz-invariant product $\sigma_{\text{ann},F} v_M$ rather than $\sigma_{\text{ann},F} v_{\text{rel}}$; see App. C.1.1 for the full expressions, as well as those for real scalar DM. Above we have omitted terms that are

suppressed by $(m_{l,\phi}/m_F)^4$ as well as higher-order terms. For the special case $c_L c_R = 0$ and for $m_l \to 0$ the above cross section vanishes, and the process becomes d-wave dominated [372–374], scaling as $v_{\rm rel}^4 m_\phi^6/m_F^8$. Given a TeV-scale F and $m_{l,\phi}$ well below GeV-scale, the latter terms do not contribute to the annihilation cross section in any appreciable way. Finally, for real scalar ϕ, a factor of four should be multiplied to the expression in Eq. (6.10) as both t- and u-channel processes contribute.

The annihilation to a pair of left-handed neutrinos $\bar{\nu}_l \nu_l$, mediated by F^0, is either suppressed by neutrino mass or $1/m_F^4$ or $v_{\rm rel}^2/m_F^4$. For Dirac neutrinos, the annihilation cross section is given in Eqs. (C.97) and (C.98) for complex and real ϕ. However, if neutrinos are Majorana fermions, one may additionally annihilate to $\nu_l \nu_l$ or, equivalently, $\bar{\nu}_l \bar{\nu}_l$ with an s-wave cross section similar to Eq. (6.10) [375]. We comment on this possibility when considering cosmological constraints.

While we do not presume any production mechanism of the observed DM relic abundance, we will show the required parameters for thermal freeze-out below. Here, the DM abundance is $\Omega_\phi h^2 = 0.1198$ [86], where Ω_ϕ is the density parameter of ϕ and h is the Hubble constant in units of 100 km/s/Mpc. The observed relic density is achieved with $c_F^2 \sim 0.01$–0.1 for $m_\phi < \mathcal{O}(\text{GeV})$ and $m_F \sim \mathcal{O}(100\,\text{GeV})$–$\mathcal{O}(\text{TeV})$ [362]. The parameter regions that yield the required annihilation cross section within uncertainties for both the thermal freeze-out and the INTEGRAL 511 keV line [376] are shown in Fig. 7.3 for $m_F \gg m_\phi$.

Although, as detailed in Sec. 6.1, the 511 keV line prefers a DM mass below several to tens of MeV, we scan over the entire MeV–GeV mass range as our results bear greater generality. In Figs. 7.3 and 7.4 below, we indicate by a lighter shading of the INTEGRAL favored bands the weakest constraint on m_ϕ that is derived from the INTEGRAL X-ray data itself [357], $m_\phi \geq 70\,\text{MeV}$.

6.4.2 Leptophilic vector mediator Z'

Turning now to the model with a gauge boson Z', both the DM particle ϕ and SM leptons are charged under the new U(1). The interactions have the form:

$$\mathcal{L}_{Z'} = g_\phi^2 Z'_\mu Z'^\mu \phi^* \phi - i g_\phi Z'_\mu \left[\phi^* (\partial^\mu \phi) - (\partial^\mu \phi^*)\phi\right] - Z'_\mu \bar{l} \gamma^\mu (g_L P_L + g_R P_R) l \,. \tag{6.11}$$

The couplings $g_{L,R}$ and g_ϕ are understood as a product of gauge coupling g and charge assignments $q_{L,R}$ and q_ϕ so that $g_{L,R} = g q_{L,R}$ and $g_\phi = g q_\phi$, respectively. Again, there are many options available with Eq. (6.11). They generally differ by the Z' mass $m_{Z'}$, by their chiral couplings, by the absence or presence of family universality and/or kinetic mixing, by their (extended) Higgs sector, by potential additional fields that are required to cancel associated gauge anomalies in the UV and so forth; see, *e.g.*, [377] and references therein.

Here, we are primarily focused on the phenomenology associated with the Z' coupling to electrons, and shall take g_L and g_R as flavor blind for when muons are involved. The special cases $g_l \equiv g_L = g_R$ and $g_L = -g_R$ correspond to a pure vector and axial-vector interactions, respectively[2]. For the purpose of illustration, we consider $m_{Z'} \geq 10\,\text{GeV}$ in most of our discussions. As will be shown, only a Z' below the EW scale is of relevance for the INTEGRAL signal, so appears on-shell at high-energy colliders. As a result, although Z' is generally off-shell for the low-energy phenomenology, and bounds derived below can be represented using $\sqrt{g_\phi g_l}/m_{Z'}$, results from LEP need to be treated with caution. For the latter, we provide bounds both on $\sqrt{g_\phi g_l}/m_{Z'}$ in the heavy mediator limit, and on $\sqrt{g_\phi g_l}$ for $m_{Z'} \ll m_Z$; see Sec. V of Ref. [P3] for the possibility of a Z' below 10 GeV.

Anomalous magnetic moment Similarly as above, for the case $m_{Z'} \gg m_l$, the one-loop contribution to $(g-2)_l$ is given by

$$\Delta a_l^{Z'} = \frac{6 g_L g_R - 2(g_L^2 + g_R^2)}{24\pi^2} \frac{m_l^2}{m_{Z'}^2}\,, \tag{6.12}$$

in agreement with [381, 382] if a pure vector coupling $g_L = g_R \equiv g_l$ is assumed. The full expression of Eq. (6.12) is found in App. C.1. The associated diagram of interest is shown in the right panel of Fig. 6.3, and the $(g-2)_\mu$ favoured parameter space is $g_l/m_{Z'} \sim (4.6\text{–}6.4)\,\text{TeV}^{-1}$. The constraint from $(g-2)_e$ will be evaluated in Sec. 7.3.1.

For a flavor-blind g_l assumed here, the combination of several experiments excludes the possibility that this simple model explains the muon $g-2$ anomaly. This conclusion holds irrespective of if Z' decays dominantly into SM leptons or into DM particles, as the leading constraint comes from the measurements of electron-neutrino scattering [383][3].

DM annihilation For the annihilation cross section via a s-channel Z', the s-wave component vanishes as scalars have no spin, and the p-wave component reads

$$\sigma_{\text{ann},Z'} v_M = v_{\text{rel}}^2 g_\phi^2 \frac{4m_\phi^2(g_L^2+g_R^2) - m_l^2(g_L^2 - 6 g_L g_R + g_R^2)}{48\pi(m_{Z'}^2 - 4m_\phi^2)^2} \sqrt{1 - \frac{m_l^2}{m_\phi^2}}\,. \tag{6.13}$$

It agrees with Eq. (3) in [362] when taking $v_{\text{rel}} \simeq 2 v_\phi$, where v_ϕ is the DM velocity. Since the cross section only varies by about a factor of two when either $g_R = 0$ or $g_L = 0$, we do not distinguish the left- and right-chiral couplings any further for annihilation, and simply take $g_L = g_R \equiv g_l$ in the remainder. For real scalar DM, the annihilation would be extremely suppressed since the Z' does not couple to a pair of real scalars at tree level.

[2] For GeV fermionic DM with a leptophilic Z', see, *e.g.*, [378–380].

[3] Other Z'-options such as $U(1)_{L_\mu - L_\tau}$ remain allowed for resolving $(g-2)_\mu$, as most recently illustrated in [384]. For bounds on other relevant DM models, see, *e.g.*, [382].

Taking the DM annihilation $\phi\phi^* \to Z'^* \to l^- l^+$ with cross section as above, for $m_{Z'} \gg m_\phi > m_l$, the parameter region of interest for the INTEGRAL signal is shown by the red and blue bands in Fig. 7.4 for NFW and Einasto profiles, respectively. Finally, we note that the observed DM relic abundance is achieved when [362]

$$g_\phi g_l \sim (3\text{–}12) \times \left(\frac{m_{Z'}}{10\,\mathrm{GeV}}\right)^2 \left(\frac{m_\phi}{\mathrm{MeV}}\right)^{-1} , \tag{6.14}$$

in the limit of $m_{Z'} \gg m_\phi$. Obviously, $m_{Z'}$ around or above the EW scale puts us into the non-perturbative regimes and is not of interest for us. Depending on the Z' decay width, resonant annihilation at the point $m_{Z'} \simeq 2m_\phi$ introduces additional velocity dependence in the annihilation. A detailed investigation of the resonant point, such as performed in [385–387], is beyond the scope of this thesis. Due to these reasons, we focus on $m_{Z'} \geq 2.1 m_\phi$.

6.5 Content outline

In light of the significant amount of activities in the past two decades that has gone into the exploration of the MeV–GeV mass range and the large amount of results, it seems timely to revisit the originally proposed models of sub-GeV scalar DM [362] and confront them to this new wealth of data. Concretely, we and Ref. [P3] add the following new pieces that were not presented previously in this context:

- sensitivities of current and future intensity-frontier experiments are derived for the first model, and re-visited for the second;
- in addition to an update of the $g-2$ constraint from electrons, limits from lepton flavor violation, parity violation, and the invisible decay of the Z-boson are established;
- the astrophysical cooling constraint from SN1987A is derived in detail for the free-streaming regime.
- the bound from astrophysical DM self-scattering is derived, while we adopt the limits on DM annihilation at the CMB epoch and from Voyager 1 data at present time in the literature.
- the high-redshift constraint from the collisional damping of DM primordial fluctuations is considered and from extra radiation degrees of freedom is re-visited;
- latest constraints from the leading direct detection experiments are summarized to apply to the models;
- the sensitivity of the high-energy colliders, LEP and LHC, is provided;
- an improved velocity expansion for the annihilation cross section for one of the models is presented.

Taken together, this part will provide a more comprehensive assessment as whether light DM particles could explain the INTEGRAL signal or the anomalous magnetic moment of the muon in this setup. It is important to stress, however, that although these anomalies serve as good and timely motivations, our study has the broader aspect that it presents a complete and self-contained survey on the viability of rather minimal models of scalar DM below the GeV-scale. A summary of results for an exemplary DM mass of 10 MeV is shown in Figs. 6.4 and 6.5. The details of each experiment and observable will be given in following chapters.

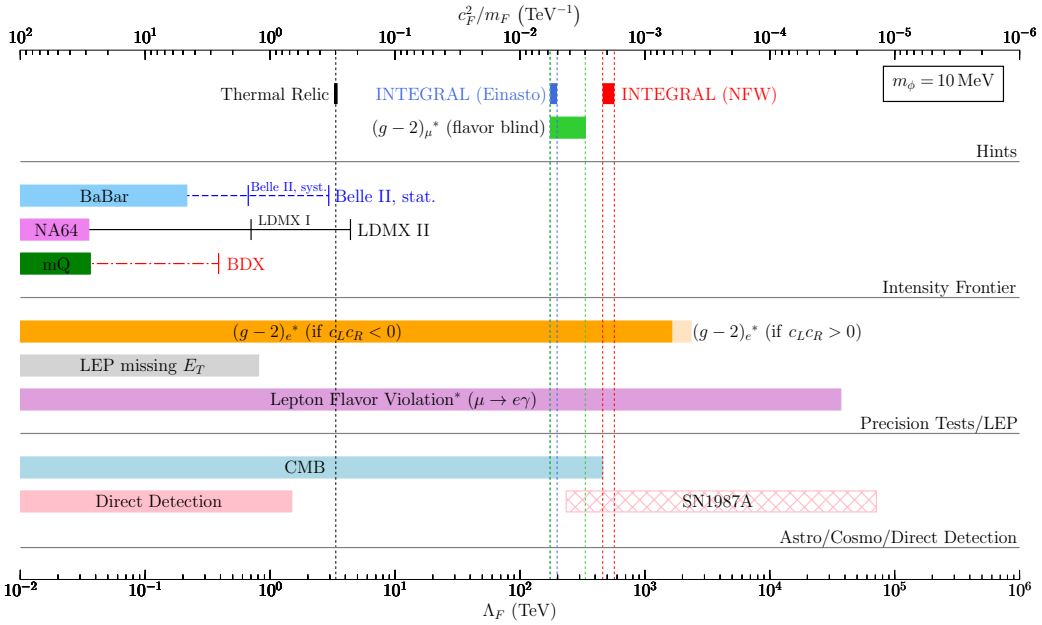

Figure 6.4: Summary of constraints obtained in this part for the fermion-mediated model as a function of the effective UV-scale $\Lambda_F = (c_F^2/m_F)^{-1}$ for a fixed DM mass of $m_\phi = 10\,\mathrm{MeV}$ in heavy mediator limit; $c_F = \sqrt{|c_L^e c_R^e|}$. A star indicates, that the bound only applies under certain conditions. The top section "Hints" shows the regions of interest for the explanation of the INTEGRAL signal, for the $(g-2)_\mu$ anomaly assuming flavor-blind couplings and same F masses between the first two generations, and the point for achieving the correct relic density through DM freeze-out. The next section "Intensity Frontier" shows constraints (projections) from searches for missing momentum in e^-e^+ collisions at BaBar (Belle II), for missing energy in the e^- fixed target experiment NA64 (LDMX), and for direct ϕe^- scattering of ϕ produced in the e^- fixed target experiment mQ (BDX). The section "Precision Tests/LEP" shows the conservative constraint from the loop-induced contribution to $(g-2)_e$ for either sign of the product of couplings as labeled [388, 389], the limit on missing energy searches at LEP and, in the case of a single generation of F and assuming flavor-blind couplings, the limit from the lepton flavor violating $\mu \to e\gamma$ transition. The final section "Astro/Cosmo/Direct Detection" is devoted to CMB limits on energy injection, to direct detection limits from ϕ-electron scattering and from anomalous energy loss in SN1987A. Weaker limits such as from the invisible width of the Z, from structure formation, from DM self-scattering, from the running of α, from the left-right asymmetry in polarized electron-electron scattering are not shown (see main text instead). The INTEGRAL interpretation is excluded.

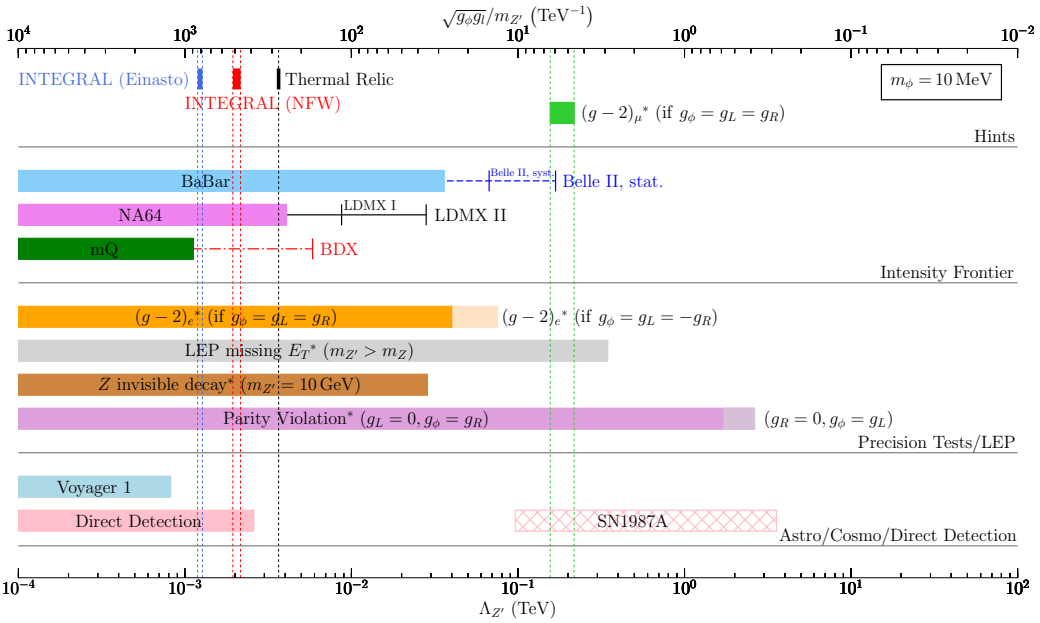

Figure 6.5: Summary of constraints obtained in this part for the vector-mediated model as a function of the effective scale $\Lambda_{Z'} = (\sqrt{g_\phi g_l}/m_{Z'})^{-1}$ for a fixed DM mass of $m_\phi = 10\,\mathrm{MeV}$ in heavy mediator limit, similar to Fig. 6.4. A star indicates, that the bound only applies under certain conditions. The new/additionally shown bounds here are from the Z-invisible width (for $m_{Z'} = 10\,\mathrm{GeV}$ only) and from parity violation using E158 under the assumption $g_\phi = g_L$ in the section "Precision Tests/LEP". Section "Astro/Cosmo/Direct Detection" now shows the annihilation constraint from Voyager 1 data. The region of interest for $(g-2)_{e,\mu}$, where the bound for $(g-2)_e$ is based on [388, 389], also requires further assumptions of couplings $g_\phi = g_L = \pm g_R$. The INTEGRAL interpretation is excluded.

CHAPTER 7

Laboratory Constraints

The scalar DM considered in this part can be produced in the laboratory, especially at electron-beam facilities[1], through electron-positron annihilation in colliders (see Fig. 7.1) or electron-nucleus bremsstrahlung in fixed-target and beam-dump experiments (see Fig. 7.2). Moreover, they can also appear virtually through loops, affecting EW precision measurements. Such considerations thus put upper bounds on the coupling of SM particles to the dark sector.

We briefly introduce the experimental data of interest and our methods to derive the related constraints below, and refer to the appendices for further details of relevant cross sections.

7.1 Electron-beam facilities

We first consider intensity frontier experiments, including low-energy electron-positron colliders and electron-beam fixed-target and beam-dump experiments. For the values of m_F and $m_{Z'}$ considered above, we can only produce ϕ via off-shell mediators in these experiments.

Following Ref. [183], we derive the expected number of signal events and constraints from current experiments such as BaBar [390], NA64 [391, 392] and mQ [297, 393], as well as projected sensitivities for future ones, including Belle II [394, 395], LDMX [396] and BDX [397]. Depending on the observable signatures, these experiments can be put in three categories described below.

7.1.1 Electron-positron colliders

The first category is to look for large missing transverse momentum/energy, accompanied by a mono-photon signal, in low-energy electron-positron colliders, such as BaBar and Belle II. The differential cross section of the signal process, weighted with the energy fraction carried away

[1] The scalar DM is assumed to be leptophilic in order to explain the INTEGRAL 511 keV line, thus we focus on electron-beam facilities. Nevertheless, if one relaxes this assumption, ϕ can in principle be probed in proton-beam experiments as well; see Chap. 4 for searches along those lines.

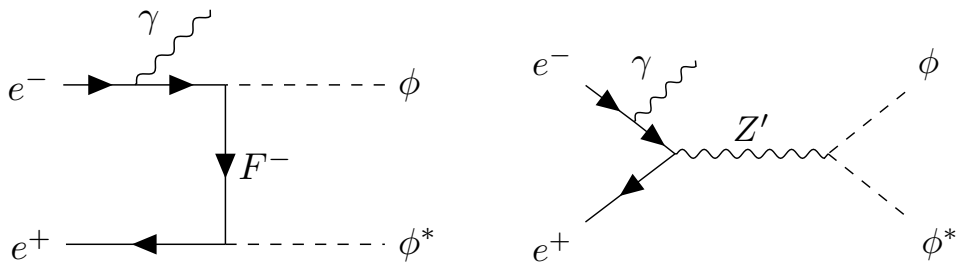

Figure 7.1: Pair production of ϕ in electron-positron annihilation in association with ISR. Photon emission from the intermediate charged F is suppressed and hence neglected.

by initial-state radiation (ISR) $x_\gamma = E_\gamma/\sqrt{s}$ and its angular distribution, can be factorized into

$$\frac{d\sigma_{e^-e^+\to\phi\phi\gamma}}{dx_\gamma\, d\cos\theta_\gamma} = \sigma_{e^-e^+\to\phi\phi}(s_{\phi\phi})\mathcal{R}^{(\alpha)}(x_\gamma, \cos\theta_\gamma, s)\,, \tag{7.1}$$

with the improved Altarelli-Parisi radiator function [398, 399] expressed as

$$\mathcal{R}^{(\alpha)}(x_\gamma, \cos\theta_\gamma, s) = \frac{\alpha}{\pi}\frac{1}{x_\gamma}\left[\frac{1+(1-x_\gamma)^2}{1+4m_e^2/s-\cos^2\theta_\gamma} - \frac{x_\gamma^2}{2}\right],$$

where s and $s_{\phi\phi} = (1-x_\gamma)s$ are the squared CM energy of e^-e^+ and ϕ-pair, respectively. The e^-e^+ annihilation cross section without ISR can be found in App. C.1.2. Integrating over the squared CM energy of the ϕ-pair and the angular distribution of the photon, the expected number of signal events in each energy bin reads

$$N_{\text{sig}}^{(i)} = \epsilon_{\text{eff}}\mathcal{L}\int_{\text{bin},i}\frac{ds_{\phi\phi}}{s}\int_{\cos\theta_\gamma^{\min}}^{\cos\theta_\gamma^{\max}} d\cos\theta_\gamma \frac{d\sigma_{e^-e^+\to\phi\phi\gamma}}{dx_\gamma\, d\cos\theta_\gamma}\,, \tag{7.2}$$

where ϵ_{eff} is the efficiency, $\mathcal{L}$ is the integrated luminosity, $\theta_\gamma^{\max,\min}$ are the cuts on the photon angle in CM frame with respect to the beam axis. The main SM backgrounds are $\gamma\not{\gamma}$ (peak), $\gamma\not{\gamma}\not{\gamma}$ (continuum) and $\gamma\not{e}^-\not{e}^+$ (continuum).

For BaBar, we take the data of the analysis of mono-photon events in a search for invisible decays of a light scalar at the $\Upsilon(3S)$ resonance [390]. The CM energy is 10.35 GeV, with two search regions of $3.2\,\text{GeV} \le E_\gamma \le 5.5\,\text{GeV}$ and $2.2\,\text{GeV} \le E_\gamma \le 3.7\,\text{GeV}$.[2] The corresponding integrated luminosities for the high and low energy bands are $28\,\text{fb}^{-1}$ and $19\,\text{fb}^{-1}$ with an efficiency 0.3 and 0.55. The angular cuts are $-0.31 < \cos\theta_\gamma < 0.6$ (high energy) and $-0.46 < \cos\theta_\gamma < 0.46$ (low energy).

For Belle II, we follow [400] and derive the projection by scaling up the BaBar background for both high and low energy data to an integrated luminosity of $50\,\text{ab}^{-1}$ with a similar

[2] We do not consider possible resonant conversion of $\Upsilon(3S) \to Z'$ plus a low-energy photon, as $m_{Z'} = 10\,\text{GeV}$ is chosen arbitrarily.

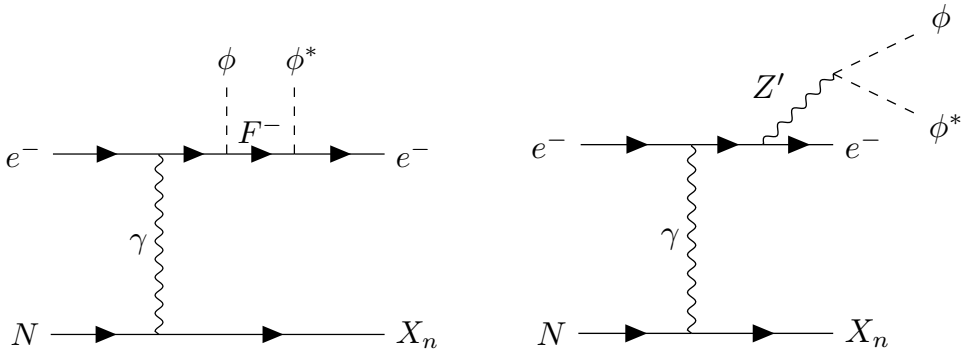

Figure 7.2: Pair production of ϕ in electron-beam fixed-target and beam-dump experiments. We consider ϕ emission from both initial- and final-state electrons (but not from the heavy F particle). Note that a global dark symmetry in Eq. (6.7) forbids the diagram with ϕ and ϕ^* interchanged for the left process; see main text.

CM energy ($E_{\rm CM} = 10.57\,\text{GeV}$) and an efficiency 0.5. The geometric cuts are assumed to be the same as BaBar. In Figs. 7.3 and 7.4, we present conservative and aggressive projections for Belle II. The conservative one is derived assuming there are intrinsic systematic uncertainties in both the peak and continuum background, while the other only includes statistical fluctuations. The actual sensitivity of Belle II is expected to lie between the two.

7.1.2 Fixed-target experiments

The second category comprise missing energy searches in electron-beam fixed-target experiments, such as NA64 and future LDMX. The expected number of signal single-electron events is given by

$$N_{\rm sig} = N_{\rm EOT}\frac{\rho_{\rm target}}{m_N}X_0\int_{E_{\rm min}}^{E_{\rm max}} dE_3\,\epsilon_{\rm eff}(E_3)\int_{\cos\theta_3^{\rm min}}^{\cos\theta_3^{\rm max}} d\cos\theta_3\frac{d\sigma_{2\to4}}{dE_3\,d\cos\theta_3}\,, \tag{7.3}$$

in the thin target limit[3], where $N_{\rm EOT}$ is the number of electrons on target (EOT), $\rho_{\rm target}$ is the mass density of the target, m_N is the target nucleus mass, X_0 is the radiation length of the target, E_3 is the energy of the final-state electron, and θ_3 is the scattering angle with respect to the beam axis of the final-state electron in the lab frame, with its detection efficiency given by $\epsilon_{\rm eff}(E_3)$. The differential cross section is derived in App. C.1.3. The background in such experiments is usually negligible after imposing stringent selection criteria.

The NA64 experiment uses an electron beam with $E_{\rm beam} = 100\,\text{GeV}$ and has collected data of $N_{\rm EOT} = 4.3\times10^{10}$. The target is an electromagnetic calorimeter (ECAL) consisting of lead and scandium plates. Since the radiation length of scandium is roughly an order larger than that of lead, the interaction between the beam and the scandium nuclei is neglected.

[3]The DM is produced within the first radiation length.

We select events only with a final-state electron, with its energy between $[0.3, 50]\,\text{GeV}$ and $\theta_3 \leq 0.23\,\text{rad}$ (to make sure the electron is stopped inside the ECAL). The parameter space resulting in $N_{\text{sig}} > 2.3$ is excluded, as no events are reported.

For the proposed LDMX experiment, we use the benchmark values of phase I with $N_{\text{EOT}} = 4 \times 10^{14}$ on a tungsten target at $E_{\text{beam}} = 4\,\text{GeV}$, and phase II with $N_{\text{EOT}} = 3.2 \times 10^{15}$ on an aluminium target at $E_{\text{beam}} = 8\,\text{GeV}$. The energy and geometry cuts on final-state electrons are $50\,\text{MeV} < E_3 < 0.5E_{\text{beam}}$ and $\theta_3 < \pi/4$. A constant $\epsilon_{\text{eff}} = 0.5$ is taken for both phases. The projection of LDMX is done by requiring $N_{\text{sig}} \leq 2.3$, assuming null signal.

7.1.3 Beam-dump experiments

The last category includes mQ and BDX, which are electron-beam beam-dump experiments designed to directly observe ϕe (or ϕ-nucleon) recoil events in a downstream detector. The expected number of electron recoil events is given by

$$N_{\text{sig}} = n_e L_{\text{det}} \int_{m_\phi}^{E_\phi^{\max}} \int_{E_R^{\text{th}}}^{E_R^{\max}} dE_R\, \epsilon_{\text{eff}}(E_R) \frac{dN_\phi}{dE_\phi} \frac{d\sigma_{\phi e}}{dE_R}\,, \tag{7.4}$$

where n_e is the electron number density in the detector, L_{det} is the detector depth. The threshold recoil energy E_R^{th} depends on the experiment and $E_R^{\max}$ reads

$$E_R^{\max} = \frac{2m_e(E_\phi^2 - m_\phi^2)}{m_e(2E_\phi + m_e) + m_\phi^2}\,,$$

with the exact differential recoil cross section given in App. C.1.4. The production spectrum of ϕ is computed by

$$\frac{dN_\phi}{dE_\phi} = 2N_{\text{EOT}} \frac{\rho_{\text{target}}}{m_N} X_0 \int_{E_\phi}^{E_{\text{beam}}} dE \int_{\cos\theta_\phi^{\min}}^{\cos\theta_\phi^{\max}} d\cos\theta_\phi\, I(E) \frac{d\sigma_{2\to4}}{dE_\phi\, d\cos\theta_\phi}\,, \tag{7.5}$$

in which the factor 2 accounts for the production of the ϕ-pair, θ_ϕ is the scattering angle with respect to the beam axis of the produced ϕ in the lab frame with boundaries given by the geometry of the downstream detector and

$$I(E) = \frac{1 + \left(\frac{E_{\text{beam}} - E}{E_{\text{beam}}}\right)^{\frac{4t_0}{3}} \left[\frac{4t_0}{3} \ln\left(\frac{E_{\text{beam}} - E}{E_{\text{beam}}}\right) - 1\right]}{\frac{4}{3}(E_{\text{beam}} - E) \ln^2\left(\frac{E_{\text{beam}} - E}{E_{\text{beam}}}\right)}\,,$$

with $t_0 \equiv L_{\text{target}}/X_0$ being the target length to radiation length ratio, is the integrated energy distribution of electrons during their propagation in the target [183]. The differential cross section for the ϕ-energy distribution is listed in App. C.1.3.

For the mQ experiment, the incoming electron with energy $E_{\text{beam}} = 29.5\,\text{GeV}$ impinges on a tungsten target ($t_0 \simeq 6$) with $N_{\text{EOT}} = 8.4 \times 10^{18}$. The detector is 110 m downstream of the

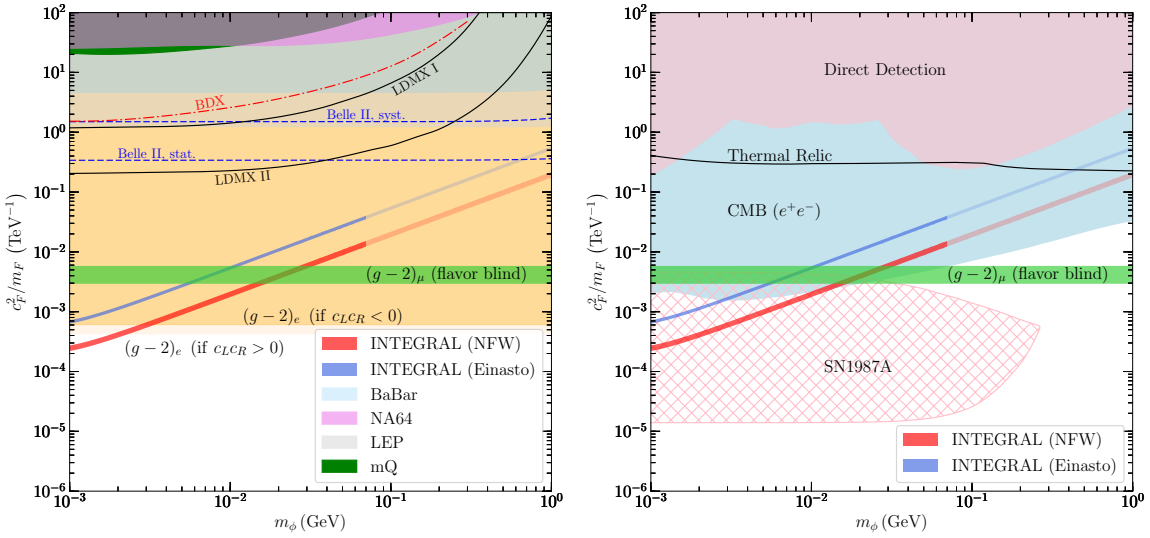

Figure 7.3: Bounds on the inverse of effective UV-scale $\Lambda_F^{-1} = c_F^2/m_F$ in the F-mediated model from laboratory experiments (left panel) and from astrophysical observations including direct detection (right panel). The parameter regions of interest for the INTEGRAL excess are shown as thin blue and red bands; for $m_\phi \geq 70\,\text{MeV}$ the DM interpretation is disfavored from INTEGRAL itself [357] as indicated by a lighter shading. The green horizontal band where $(g-2)_\mu$ is explained carries the assumption $c_F^\mu = c_F^e$. The $(g-2)_e$ constraint is the conservative one based on [388, 389], for both $c_L^e c_R^e < 0$ and $c_L^e c_R^e > 0$.

target with angular coverage $\theta_\phi < 2\,\text{mrad}$ and a depth $L_{\text{det}} = 1.31\,\text{m}$. The collaboration has reported 207 recoil events above the background, which is below the uncertainty of the latter $\sigma_{\text{bkg}} = 382$ within the signal time window. Assuming a detection efficiency of 100% [393], we derive the upper bounds on the dark sector couplings from events with electron recoil energy $E_R \geq 0.1\,\text{MeV}$ by requiring $N_{\text{sig}} < 207 + 1.28\sigma_{\text{bkg}}$, corresponding to the 90% C.L. exclusion limit.

For the proposed BDX experiment, electrons with $E_{\text{beam}} = 11\,\text{GeV}$ are incident on an aluminium target ($t_0 \simeq 15$) which comprises 80 layers with thickness of (1–2) cm each. The angular coverage of the downstream ECAL is $\theta_\phi < 12.5\,\text{mrad}$ and $L_{\text{det}} = 2.6\,\text{m}$. The BDX collaboration estimated that,x for $N_{\text{EOT}} = 10^{22}$, the number of background events with $E_R \geq 0.35\,\text{GeV}$ is about 4.7 [401]. Again, we only consider electron recoil events, with a constant efficiency of 20% [401]. We derived the 90% C.L. projection by requiring $N_{\text{sig}} \leq 18$, assuming a benchmark that $N_{\text{obs}} = 15$ and $\sigma_{\text{bkg}} = 10$.

7.2 High-energy colliders

With higher CM energy, high-energy colliders are the best probes of heavy new particles. The large electron-positron (LEP) collider holds the record of the leptonic collider with the

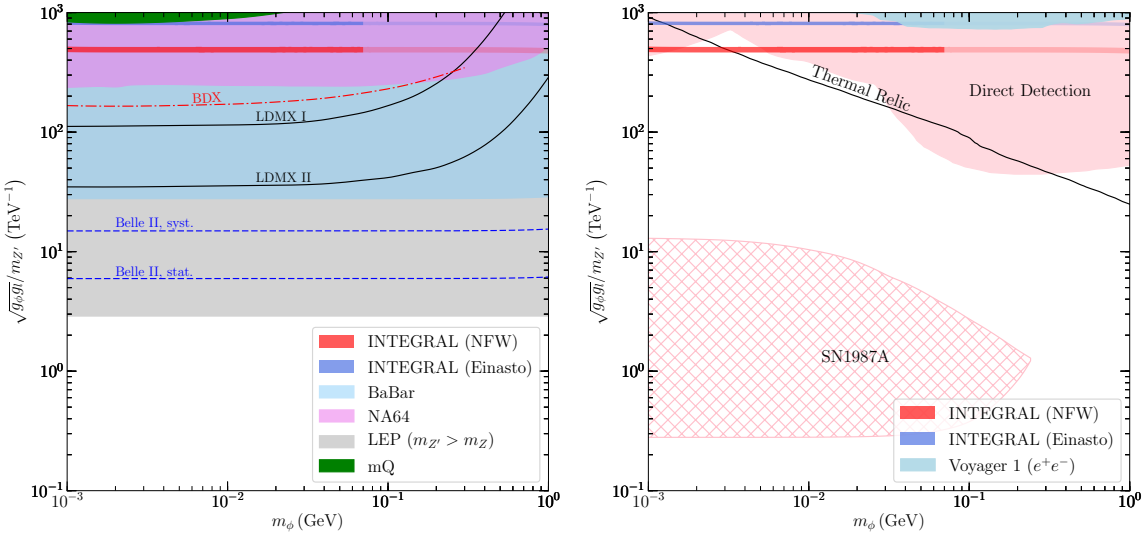

Figure 7.4: Bounds on the inverse of effective UV scale $\Lambda_{Z'}^{-1} = \sqrt{g_\phi g_l}/m_{Z'}$ for the Z'-mediated model from laboratory tests (left panel) and from cosmological and astrophysical probes including direct detection (right panel). The parameter regions of interest for the INTEGRAL excess are shown as thin blue and red bands; for $m_\phi \geq 70\,\text{MeV}$ the DM interpretation is disfavored as indicated by a lighter shading. LEP bound only applies for $m_{Z'}$ above the EW scale, below which Eq. (7.8) applies instead. We do not show a band for $(g-2)_\mu$, which would need an assumption on g_ϕ/g_l, since it is already excluded elsewhere (see main text and Fig. 6.5).

highest CM energy (close to the Z-pole). Currently, the LHC is the collider with the highest operating CM energy (13 TeV). With the validation of the SM, the data from the high-energy colliders can also be employed in constraining light dark sector physics. In the following, we focus mainly on the constraint from missing energy signatures in LEP and point the reader to references regarding the LHC or future colliders.

High-energy colliders may produce any of the dark sector particles studied here, leading to missing energy signatures. In the F-mediated model, a TeV-mass charged fermion F remains largely unconstrained by current bounds from LEP or LHC data, while the missing energy search in LEP [402] is able to constrain the overall coupling as

$$c_F^2/m_F \lesssim 1.23\,\text{TeV}^{-1}\,, \tag{7.6}$$

which can be improved by investigating DM production via Drell-Yan processes with high-luminosity LHC [367], as well with ILC [403]; note that in this regime, we can no longer write the interaction as an effective operator.

For the Z'-mediated model, the LEP bound varies depending on the Z' mass. For a heavy Z' above the LEP energy scale, we obtain a bound from missing energy events induced by DM pair production as

$$\sqrt{g_\phi g_l}/m_{Z'} \lesssim 2.89\,\text{TeV}^{-1}\,, \tag{7.7}$$

in agreement with previous results [404, 405], which is stronger than the reach of low-energy electron-beam experiments. Although this is shown in Fig. 7.4, it does not apply to $m_{Z'}$ below the LEP energy scale, where a more proper LEP bound may come from missing energy induced by on-shell Z' production, requiring $g_l \lesssim 0.01$ [406]. Its combination with the perturbative condition $g_\phi^2/(4\pi) \lesssim 10$ results in

$$\sqrt{g_\phi g_l} \lesssim 0.335\,, \tag{7.8}$$

being comparable to the BaBar bound for $m_{Z'} = 10\,\text{GeV}$. Naively speaking, these two LEP bounds, valid for different parameter regions of $m_{Z'}$, converge at $m_{Z'} \sim m_Z$. Projected sensitivities on a leptophilic Z' portal have also been derived for future colliders; see [380, 407–410].

7.3 Precision observables

In this section, we discuss the implications of SM precision observables such as $(g-2)_e$, Z invisible decay, parity violation and lepton flavor violation on the particle models considered in this part. For a Z' boson that couples to quarks/leptons with appreciable strength, precision observables were also investigated in [411, 412]; note however that stringent constraints from dilepton resonance searches derived in the latter work are avoided, as in our setup Z' dominantly decays into a ϕ-pair.

7.3.1 Electron $g-2$

The $(g-2)_e$, although not posing a notable tension like $(g-2)_\mu$ anomaly, also provides great insights in potential new physics contribution. In general, we can directly measure the value of a_e or, indirectly, derive it with measured fine-structure constant α being the input. Recently, the measurement of α has been improved significantly with Cs atom interferometers [388]. Taking as input $\alpha \equiv \alpha^{(\text{Cs})}$, the SM prediction of the electron anomalous magnetic moment $a_e^{(\text{Cs})} = a_e^{\text{SM}}(\alpha^{(\text{Cs})})$ is now in 2.5σ tension with the direct measurement of a_e [413], $a_e^{(\text{meas.})} - a_e^{(\text{Cs})} = -0.88(0.36)\times 10^{-12}$. At face value, this puts a stringent requirement on a new physics contribution:

$$\Delta a_e^{\text{BSM}}\Big|_{\text{Cs}} \in (-0.88 \pm 3\times 0.36)\times 10^{-12} = [-1.96, 0.20]\times 10^{-12}\,, \tag{7.9}$$

with a nominal 3σ requirement.

Another experiment, using the recoil velocity on a Rb atom, has measured the value of the fine-structure constant with similar uncertainty [389]. Its value of α suggests a smaller a_e, in

better agreement with the direct measurement, $a_e^{(\text{meas.})} - a_e^{(\text{Rb})} = 0.48(0.30) \times 10^{-12}$. From this we can obtain a similar constraint on the new physics contribution:

$$\Delta a_e^{\text{BSM}}\Big|_{\text{Rb}} \in [-0.42, 1.38] \times 10^{-12}\,. \tag{7.10}$$

These differences above could also be rephrased in tensions between α extracted from Cs/Rb experiments and from direct a_e measurements using the SM-prediction, $\alpha(a_e^{\text{SM}})$, *i.e.*, in $\alpha^{(\text{Cs/Rb})} - \alpha(a_e^{\text{SM}})$. Both models—through their contribution to a_e—then imply an inferred shift in the value of α. One should obtain the same constraints from both.

In the F-mediated model, positive (negative) $c_L c_R$ yields a positive (negative) contribution; *cf.*, Eq. (6.9) or the full expression in App. C.1. As shown in Fig. 7.3, either sign then puts a strong constraint on the model with a F mediator. In the Z'-mediated model, $g_L = g_R$ and $g_L = -g_R$ can also give a distinct contribution to a_e; see Eq. (6.12). A conservative limit can be given by combining the weaker of each limits of (7.9) and (7.10), *i.e.* the lower bound from $\Delta a_e^{\text{BSM}}\Big|_{\text{Cs}}$ and the upper bound from $\Delta a_e^{\text{BSM}}\Big|_{\text{Rb}}$. This yields

$$\begin{aligned} -6.1 \times 10^{-4}\,\text{TeV}^{-1} \leq c_L c_R/m_F \leq 4.3 \times 10^{-4}\,\text{TeV}^{-1}\,, \\ -178\,\text{TeV}^{-2} \leq g_L g_R/m_{Z'}^2 \leq 625\,\text{TeV}^{-2}\,, \end{aligned}$$

for the F- and Z'-mediated model. In contrast, the combination of the stronger limits results in

$$\begin{aligned} -1.3 \times 10^{-4}\,\text{TeV}^{-1} \leq c_L c_R/m_F \leq 6.2 \times 10^{-5}\,\text{TeV}^{-1}\,, \\ -38\,\text{TeV}^{-2} \leq g_L g_R/m_{Z'}^2 \leq 91\,\text{TeV}^{-2}\,. \end{aligned}$$

For the Z'-mediated model, the $(g-2)_e$ constraint is always surpassed by the LEP bound above, for both $m_{Z'} \gg m_Z$ and $m_{Z'} \leq m_Z$, and is hence not included in Fig. 7.4; see Fig. 6.5[4].

One may exercise some caution if exclusively applying Eq. (7.9), as it takes a positive half-σ shift to rule out any model by increasing the 2.5σ tension to 3σ. Here we stress that both the F- and Z'-mediated models allow for both signs in their contributions. Therefore, going in the other direction, one may first bring both measurements into reconciliation and in a further consequence, allow for a particularly large shift before the lower boundary in Eq. (7.9) is reached. In this sense, Eq. (7.9) entails both, an aggressive and conservative limit. In Fig. 7.3 we show the conservative limits that arise from the combination of Eqs. (7.9) and (7.10).

[4] Another observable is the running of the fine-structure constant, given by the photon vacuum polarization induced by the charged F-loop, $\Pi(-M_Z^2) - \Pi(0)$. This number needs to be below 0.00018 [214], requiring $m_F \gtrsim 80\,\text{GeV}$. The formula for $\Pi(p^2)$ is given in Eq. (C.120) with g_l replaced by e. A dark U(1) gauge boson Z' does not contribute to the running at one-loop.

7.3.2 Z invisible decay

The SM contribution to the Z invisible decay is through neutrinos. Thanks to the LEP, we now have measured the value of the Z invisible width $\Gamma(Z \to \text{inv})_{\text{SM}}$ to high precision, which can be inferred by 1) subtracting the total width with the visible width or 2) measuring the mono-photon events from $e^- e^+ \to \nu\bar{\nu}\gamma$. Since particles that are not charged under the SM gauge groups are also invisible, the deviation from the SM predicted value of $\Gamma(Z \to \text{inv})_{\text{SM}}$ can be evidence of new physics contribution. Under current precision, such additional contribution is bounded by experiments [5] to satisfy

$$\Gamma(Z \to \text{inv})_{\text{new}} \lesssim 0.56\,\text{MeV} \quad \text{at } 95\%\,\text{C.L.}\,. \tag{7.11}$$

In this thesis, we consider the invisible decay $Z \to \phi\phi^*$ induced by the 1-loop diagram containing F or Z' will alter the decay width of Z; see Fig. C.5. Explicit calculation of the relevant loop diagrams, detailed in App. C.2, reveals that the ensuing constraints ($c_F/m_F < 26.6\,\text{TeV}^{-1}$ and $\sqrt{g_\phi g_l} < 0.35$ for $m_{Z'} = 10\,\text{GeV}$) are weaker than those above from general missing energy searches discussed in Sec. 7.2. We hence do not show this constraint in Figs. 6.4, 7.3 and 7.4.

7.3.3 Parity violation

The properties of a particle field under discrete Lorentz transformations, *e.g.*, parity $\mathcal{P}$, time-reversal $\mathcal{T}$, and charge conjugation $\mathcal{C}$, are of ultimate importance in the formulation of QFT. Although a particle field shall be symmetric under the combination of $\mathcal{CPT}$, as a guiding principle of QFT, these symmetry can be violated individually. The example in the SM is the weak interaction, with its parity violation measured in the decay of cobalt atom [414]; on the other hand, the electromagnetic and strong interactions respect parity. Subsequently, from the measurement of kaon decay, it is realized that $\mathcal{CP}$-symmetry is violated in weak interaction; this is also confirmed in other meson decay [415]. Currently, we have measured the parameters regarding the parity violation in weak interaction with high precision. Therefore, the parity violation measurement can be employed to probe any new physics based on a chiral theory, *e.g.*, the scalar DM model considered here. In Fig. 6.5, we show the constraint based on the measurement of polarized electron-electron scattering in the E158 experiment [416, 417]; see Ref. [P3] for details.

7.3.4 Lepton flavor violation

The lepton flavor violation is a smoking gun for the new physics, as it is not predicted in the SM. Here, if only one generation of F is present, non-zero couplings to the muon and tau sector induce lepton flavor violation, similar to flavored DM [363]. For example, one may have

the decay $\mu \to e\gamma$ by closing the ϕ-loop, effectively via the magnetic dipole interaction [418]. Another example is the decay $\mu \to e\phi\phi$, but its sensitivity is likely superseded by the radiative decay above, and only applies to $m_\phi \leq m_\mu/2$. The current strongest limit is from the MEG experiment [419], shown in Fig. 6.4. We refer the reader to our paper [P3] for detailed calculations.

CHAPTER 8

Astrophysical and Cosmological Observables, and Direct Detection

As the scalar ϕ is assumed to be the dominant DM component, the models are also constrained by astrophysical and cosmological observables, as well as from DM direct detection experiments. These constraints and how to derive them are discussed in the following.

8.1 BBN/CMB ΔN_{eff} bounds

Here we take into account the BBN/CMB bounds on N_{eff} from early Universe observations, while at the same time remaining agnostic about the state of the Universe for $T \gtrsim$ MeV. Since $m_\phi \sim \mathcal{O}(\text{MeV})$, ϕ can still be relativistic and contribute to the radiation density at the onset of BBN. The effective number of relativistic degrees of freedom N_{eff} is proportional to the ratio of the energy density of relativistic particles (except photons) to the energy density of photons. Recall that we always set $m_{Z'} \geq 2.1 m_\phi$, so Z' only plays a sub-leading role in the radiation density budget, even though it has three degrees of freedom. Currently, two relativistic degrees of freedom, like from a thermalized complex scalar, are still considered to be marginally allowed by BBN which requires $\Delta N_{\text{eff}} \lesssim 1$ [223, 225, 306].

In contrast, the Planck measurement of the cosmic microwave background (CMB) spectrum requires that $N_{\text{eff}} = 2.99 \pm 0.33$ at the last scattering surface [86]. This limits the residual DM annihilation after neutrino-decoupling that injects energy either into the visible or into the neutrino sector [420, 421]. In the F-mediated model, ϕ pairs annihilate into electrons. Under the assumption of a sudden neutrino decoupling at 1.41 MeV [422], we obtain a lower bound from N_{eff} as $m_\phi \geq 5.1\,\text{MeV}$ for a complex scalar, consistent with previous results [376][1]. However, the CMB bounds from N_{eff} become much weaker if the scalar DM annihilates into both electrons and neutrinos, which happens in the F-mediated model with Majorana neutrinos, as well as in the Z'-mediated model. The underlying reason is that

[1] In the case of Dirac SM neutrinos with a kinematically accessible right-handed neutrino (as alluded to when introducing the models), one also would need to verify that ν_R decouples early enough from the thermal bath, so that, overall, the upper bound on N_{eff} is satisfied.

both, the photon- and neutrino-fluid are being heated so that the ensuing offset in the ratio of their respective temperatures is milder; see, *e.g.*, [423–425] for recent discussions. In a flavor-blind set-up assuming DM annihilates to electrons and each species of SM neutrinos equally, we then estimate that the Planck bound on $N_{\rm eff}$ only requires $m_\phi \gtrsim 2.0\,{\rm MeV}$. The latter possibility was not considered in [376].

Given the fact that, in the near future, CMB-S4 may reach the precision $\Delta N_{\rm eff} \sim 0.06$ at 95% C.L. [426], we are currently studying the effect of a dark sector, interacting with both neutrinos and electrons comparably, on the neutrino decoupling, *i.e.*, on the value of $N_{\rm eff}$, in details.

8.2 Direct detection

Direct detection experiments search for the scattering of DM with atomic nuclei or electrons. The energy deposition of DM gives rise to signals in scintillation, ionization and heat (phonons). The parameter space of EW-scale WIMP models has been probed efficiently by nuclear recoils. However, the sensitivity on the sub-GeV mass range remains insufficient due to finite energy thresholds. Several scenarios have been proposed to extend the sensitivity to the sub-GeV mass range; see a recent review [155]. Here we focus on the scattering between ϕ and the atomic electrons, which demands a lower threshold on DM mass, and consider the non-relativistic ($v \sim 10^{-3}$) DM flux from the halo; see Chap. 5 for the direct detection with a relativistic flux.

Exclusion limits are customarily presented in terms of a reference scattering cross section in the non-relativistic limit [160],

$$\bar{\sigma}_e = \frac{1}{16\pi(m_e+m_\phi)^2}\overline{|\mathcal{M}_{\phi e}(q)|}^2_{q^2=\alpha^2 m_e^2}\,, \tag{8.1}$$

where $\overline{|\mathcal{M}_{\phi e}(q)|}^2_{q^2=\alpha^2 m_e^2}$ is the squared matrix element of ϕ scattering on a free electron, summed over final-state spins and averaged over initial-state spin, evaluated at a typical atomic momentum transfer $q = \alpha m_e$. To order $\mathcal{O}(v_{\rm rel}^2)$ it is given by

$$\begin{aligned}\overline{|\mathcal{M}_{\phi e}(q)|}^2_{F} &= \frac{16 c_L^2 c_R^2 m_e^2}{m_F^2}\,,\\ \overline{|\mathcal{M}_{\phi e}(q)|}^2_{Z'} &= \frac{16 g_\phi^2 g_l^2 m_\phi^2 m_e^2}{m_{Z'}^4}\,,\end{aligned} \tag{8.2}$$

for the two representative models; see Chap. 5 for general formulation. Note that bounds on $\bar{\sigma}_e$ have been obtained for the present case of a constant DM form factor, most recently in SENSEI [427]. See also previous bounds from XENON10 [428, 429] and XENON1T [322], as well as from considering a solar-reflected DM flux [163]. The corresponding constraints, combining the results of experiments mentioned above, are shown in Figs. 7.3 and 7.4.

8.3 Indirect search

To explain the INTEGRAL signal, ϕ has to be a symmetric DM candidate, implying that ϕ can annihilate into SM leptons also during the epochs of BBN and CMB, as well as in the late universe. The pair-annihilation of ϕ can then source an excess of photons and/or (anti-)matter. Deriving constraints from the observational data necessitates the understanding of, *e.g.*, the propagation of cosmic rays and the relevant astrophysical environments. The prime targets to point the telescope at are objects with high DM density, such as our Milky Way and dwarf spheroidal galaxies. With the data from current experiments, we can constrain a fair fraction of the parameter space of EW-scale WIMP models. For sub-GeV DM, indirect searches still serve as an essential probe.

In this section, we translate the current best limits in the literature to constrains on the parameter space. Note that although the ϕ-pair annihilation to neutrinos is generic, in the models considered in this part (see Sec. 6.4), bounds on this channel from BBN observables [424, 430] are very weak, and are not further considered in this thesis. Since in the considered models ϕ does not annihilate into photons at tree-level (except when accompanied by final-state radiation), we focus on the channel $\phi\phi^* \to e^- e^+$. For the F-mediated case, in which both s-wave and p-wave annihilation are present, see Eq. (6.10), it turns out that the constraint from CMB [431] is in general stronger than that from Voyager 1 data [432]. In the Z'-mediated case, since the leading contribution of $\phi\phi^* \to e^+ e^-$ is p-wave, see Eq. (6.13), the annihilation at the CMB epoch is velocity suppressed and the bounds from present-day data such as from Voyager 1 [354, 433] are more stringent, disfavoring DM masses above $\mathcal{O}(30)\,\mathrm{MeV}$ to explain the INTEGRAL 511 keV line. This will be further improved by about one order of magnitude in the annihilation cross section in future experiments, such as e-ASTROGAM [358, 434] and AMEGO [435]. The CMB constraint for the F-mediated case and the Voyager 1 constraint for the Z'-mediated case are shown in Figs. 7.3 and 7.4, respectively.

8.4 Structure formation and DM self-scattering

To avoid the collisional damping of DM primordial fluctuations [436, 437], DM has to kinetically decouple from the observable sector in the early Universe. In the considered models, DM couples to electrons and neutrinos with similar strength. Since the number density of electrons is much lower than that of background neutrinos once $T \ll m_e$, the scattering on neutrinos hence governs the ensuing constraint. Here we take the bounds derived in [438, 439] for both energy-independent and energy-dependent DM-neutrino scattering cross sections. Concretely, we require that for the F-mediated model,

$$\sigma^F_{\phi\nu} \simeq \frac{c_F^4}{8\pi m_F^2} \lesssim 10^{-36} \left(\frac{m_\phi}{\mathrm{MeV}}\right) \mathrm{cm}^2\,, \tag{8.3}$$

and for the Z'-mediated model,

$$\sigma_{\phi\nu}^{Z'} \simeq \frac{E_\nu^2 g_\phi^2 g_l^2}{2\pi m_{Z'}^4} \lesssim 10^{-41} \left(\frac{m_\phi}{\mathrm{MeV}}\right) \left(\frac{E_\nu}{\mathrm{eV}}\right)^2 \mathrm{cm}^2 \,.$$

The requirement consequently leads to

$$c_F^2/m_F \lesssim 0.25 \left(\frac{m_\phi}{\mathrm{MeV}}\right)^{1/2} \mathrm{TeV}^{-1} \,,$$

as well as

$$\sqrt{g_\phi g_l}/m_{Z'} \lesssim 2.17 \times 10^4 \left(\frac{m_\phi}{\mathrm{MeV}}\right)^{1/4} \mathrm{TeV}^{-1} \,.$$

Both bounds are weaker than those obtained above, and are not shown in Figs. 6.4, 6.5, 7.3 and 7.4.

In addition, if ϕ constitutes DM, its self-interaction may change the shape and density profile of DM halos, and the kinematics of colliding clusters. Such self-interaction is apparently very weak in the heavy F-mediated model. The self-scattering cross section averaged over $\phi\phi \to \phi\phi$, $\phi\phi^* \to \phi\phi^*$ and $\phi^*\phi^* \to \phi^*\phi^*$ in the Z'-mediated model reads [440]

$$\sigma_{\mathrm{SI}}^{\phi\phi} = \frac{3 g_\phi^4 m_\phi^2}{8\pi m_{Z'}^4} \,, \tag{8.4}$$

where velocity-suppressed terms have been neglected[2]. However, the current bound, $\sigma_{\mathrm{SI}}/m_\phi \leq 0.5\,\mathrm{cm}^2/\mathrm{g}$ from cluster observations [441–445], is also not able to provide any meaningful bounds on the Z'-mediated model with $m_{Z'} = 10\,\mathrm{GeV}$.

8.5 Anomalous supernovae cooling

An important constraint arises from the anomalous energy loss via ϕ production in hot stars, especially inside supernovae (SN), as we consider $m_\phi = \mathcal{O}(\mathrm{MeV–GeV})$ which has overlap with the SN core temperature. To avoid the suppression of neutrino emission from the SN core after explosion, we impose the so-called "Raffelt criterion", which states that the energy loss via dark particle production has to be smaller than the luminosity in neutrinos, $L_\nu = 3 \times 10^{52}\,\mathrm{erg/s}$ [193][3]. Here we follow the method detailed in Chap. 3, and adopt the SN1987A numerical model of [213] with a total size $r_{\mathrm{SN}} = 35\,\mathrm{km}$, to derive the bounds on the leptophilic DM models above.

[2] At $m_{Z'} \sim 2m_\phi$ the velocity suppression in s-channel $\phi\phi^* \to \phi\phi^*$ can be compensated by the resonant enhancement. Such resonant contribution never dominates and thus is not considered.

[3] The bounds from SN1987A are derived from the cooling of the proto-neutron star; doubts exist if SN1987A was a neutrino-driven explosion [201] in which case the limits become invalidated. Such speculation could be resolved once the remnant of SN1987A is firmly observed [446].

The dominant ϕ production channel is pair-creation from electron-positron annihilation. As our mediator particles, F or Z', are much heavier than the core temperature of SN, we can safely neglect thermal corrections. Quantitatively, the lower boundaries of the exclusion regions are derived by requiring

$$\int_0^{r_c} d^3r \int \frac{d^3p_{e^-} d^3p_{e^+}}{(2\pi)^6} f_{e^-} f_{e^+} \left(\sigma_{e^-e^+\to\phi\phi^*} v_M\right) \sqrt{s} \lesssim L_\nu \,, \tag{8.5}$$

where r_c is the core size of SN1987A, taken as 15 km here and f_{e^-,e^+} are Fermi-Dirac distributions for electron and positron.

On the flip side, if the coupling between ϕ and SM particles inside the SN core is so strong that the ϕ becomes trapped inside the core, the energy loss via ϕ emission diminishes and again drops below the neutrino luminosity[4]. For the detailed treatment of the trapping limit, we refer the reader to our paper [P1].

The resulting SN1987A exclusion regions, combining both lower and upper boundaries, are given in the right panels of Figs. 7.3 and 7.4. Our lower boundaries agree well with previous results [234, 448]. Regarding the upper boundaries, the Pauli blocking plays an important role in suppressing ϕ-electron scattering. Meanwhile, although there is little Pauli blocking in ϕ-nucleon scattering, ϕ only couples to quarks at loop level, yielding a suppression by another factor m_ϕ^2/m_F^2 for the F-mediated model and α/π for the Z'-mediated model. It hence turns out that ϕ-electron scattering dominates the capture in the parameter regions studied here.

[4]For even stronger couplings, the abundance of ϕ particles trapped inside SN may help to capture SM neutrinos, leading to an observable reduction in SN neutrino emission [447]. This may affect the parameter region studied in Sec. V of Ref. [P3] for $m_\phi \lesssim 10\,\mathrm{MeV}$.

CHAPTER 9

Summary of Part II

In this part, we consider the possibility that DM is a complex scalar particle ϕ with a mass below the GeV-scale. The particle is assumed to couple to SM leptons, either via a heavy fermion F or via a vector boson Z'. These models fare among the simplest UV-complete extensions to the SM, and have been contemplated as sub-GeV DM candidates well before the field exploded with activity in this mass bracket. Among other reasons, they draw their attention from the fact that ϕ annihilation today might explain the galactic INTEGRAL excess and/or bring into reconciliation the prediction and observation of the anomalous magnetic moment of the muon.

Given the tremendous recent activity devoted to the search of light new physics, it is only timely to revisit these models of scalar DM in light of much new data. These particles can be probed in the laboratory such as in electron-beam experiments, and by astrophysical and cosmological observations. We collate the latest observational and experimental data and subject the model to all relevant bounds and provide forecasts on the sensitivity of proposed future experiments.

Respecting the bounds on charged particles from high-energy colliders LEP and LHC, we consider F to be at or above the EW scale. The combination m_F/c_F^2 is inherent to most observables and can be interpreted as the effective UV-scale Λ_F for that model. We calculate the production of ϕ-pairs, mediated by the exchange of off-shell F, in the fixed-target experiments NA64 and LDMX, beam-dump experiments mQ and BDX, as well in e^-e^+ colliders BaBar and Belle II. When the production is kinematically unsuppressed, the best bound is $\Lambda_F \gtrsim 250\,\mathrm{GeV}$ by BaBar, currently surpassed by LEP with $\Lambda_F \gtrsim 1\,\mathrm{TeV}$. LDMX-II can improve on this number to 5 TeV. Turning to the Z'-mediated model, we consider only heavy vector mediator. If Z' remains off-shell in all experiments, we may take the combination $m_{Z'}/\sqrt{g_\phi g_l}$ as the effective UV scale $\Lambda_{Z'}$. In this case, BaBar points to $\Lambda_{Z'} \gtrsim 35\,\mathrm{GeV}$ to be improved by Belle-II to $\Lambda_{Z'} \gtrsim 170\,\mathrm{GeV}$ at best, weaker than the current LEP bound of $\Lambda_{Z'} \gtrsim 346\,\mathrm{GeV}$.

These direct limits are then compared to loop-induced precision observables, concretely, to $g-2$, to the invisible width of the Z and to Z-boson oblique corrections. We explicitly revisit all those calculations, confirming previously presented scaling relations in the limit $m_{\phi,l}/m_F \ll 1$ or $m_{\phi,l}/m_{Z'} \ll 1$, and, as an added value, provide the full expressions of the

loop integrals. We find that for the F-mediated model, the improved limit obtained from $g-2$ of the electron surpasses all direct observables, with $\Lambda_F \gtrsim 10^4\,\text{TeV}$, while for the Z'-mediated model, they do not play a role in the phenomenology. We also complement those constraints with limits that arise from the freedom in the chiral structure of the models, using the parity asymmetry in polarized electron scattering. Finally, we discuss limits from lepton flavor violation that are dependent on the concrete UV-content of the models.

Turning to astrophysical constraints, we derive the anomalous energy loss induced by ϕ-pair production in the assumed proto-neutron star of SN1987A. This adds strong and complementary new limits on the parameter space for $m_\phi \lesssim 100\,\text{MeV}$ down to $\Lambda_F \gtrsim 10^5\,\text{TeV}$ and $\Lambda_{Z'} \gtrsim 3\,\text{TeV}$. We furthermore consider constraints from direct detection, structure formation, CMB energy injection, and DM-self scattering. Here, the CMB puts stringent constraints on the s-wave annihilation mediated by F. In turn, for the p-wave annihilation mediated by Z' the bounds are sub-leading. For those reasons, a thermal freeze-out in the F-mediated model is firmly excluded, whereas the Z'-mediated model remains little constrained from energy injection.

Regarding the DM interpretation of the INTEGRAL 511 keV line, we show that it is excluded in both the F-mediated model as well as in the Z'-mediated model with $m_{Z'} \geq 10\,\text{GeV}$. In the model with charged F, the crucial constraints come from the $(g-2)_e$ data, from the CMB, and from SN1987A. For the Z'-mediated model, intensity-frontier experiments and direct detection via electron recoils play the major role. However, a caveat exists: if the annihilation is resonant, $m_{Z'} \simeq 2m_\phi$, the INTEGRAL signal may still be explained in conjunction with a light $m_{Z'} \leq 10\,\text{GeV}$ while at the same time being experimentally allowed.

As an outlook, we comment on the resonant region which is not studied here. For $m_{Z'} \simeq 2m_\phi$, the annihilation cross section is greatly enhanced and the required value on g_l coming from the annihilation cross section diminishes. This hampers the direct experimental sensitivity considered in this part. In turn, however, it opens the possibility of using displaced vertex searches in fixed-target experiments, depending on the decay mode of Z'. Dialing down the Z'-mass further, $m_{Z'} < 2m_\phi$ the annihilation via $\phi\phi^* \to Z'^{(*)}Z'^{(*)} \to 2e^-2e^+$ will eventually come to dominate. As the process is not velocity suppressed, we then re-enter the regime where stringent CMB bounds apply.

CHAPTER 10

Conclusion and Outlook

10.1 Main findings

In this thesis, we study in detail probes of light dark sectors made up of sub-GeV dark states. We demonstrate the sensitivity of each experiment and environment using two showcases: the "photon portal" and scalar dark matter with a fermion/vector mediator. In the case of the photon portal, the fermionic dark state χ interacts with the photon via various electromagnetic form factors, including a millicharge, magnetic/electric dipole moments, and the mass-dimension 6 operators anapole moment/charge radius. We can quantify the "darkness" by testing the interaction between the dark state and photon in various observables. On the other hand, the scalar dark matter ϕ talks to SM leptons through a new heavy fermion F or a new dark gauge boson Z'. Although the phenomenology of the two scenarios is different, they both represent rather minimal extensions of the Standard Model; thus, it is intuitive to treat them as benchmarks for augmentation of a light, sub-GeV dark sector to the Standard Model.

A sub-GeV dark sector can be a potential solution to several observed anomalies. This thesis focuses on the long-standing muon $g-2$ anomaly and the INTEGRAL 511 keV line excess. Both phenomena may point to physics beyond the Standard Model. For the muon $g-2$, we re-derive the complete analytical formulas for the contribution to $(g-2)_\mu$ for the considered models. The result is in agreement with the literature, such that the presence of either ϕ or Z' can alleviate the tension. For the INTEGRAL 511 keV γ-line, we first give a summary on the current status of this excess, and then we derive the favored parameter space for the ensuing models assuming a correct dark matter relic abundance through thermal freeze-out. In summary, we identify regions of parameter space in both vector and fermion portals that can address the above two hints simultaneously. After re-confirming the models' validity in solving these puzzles, we examine if they are allowed in various experiments and searches, summarized in the following.

We first notice that a sub-GeV, or better, a sub-MeV dark sector can have implications in stellar physics, as the temperature and plasma frequency are in this ballpark, *e.g.*, globular clusters, the Sun and the supernova SN1987A. In Chap. 3, we analyze the production of

dark sector particles via electron-positron annihilation, plasmon decay, Compton-like scattering, and electron-nucleus bremsstrahlung. Furthermore, we provide an overview of how to decompose the above processes in a thermal medium, related to the essential quantity: the imaginary part of the photon's self-energy in medium. There is double counting between different processes when the s-channel photon becomes on-shell, which is not adequately considered in the literature. We establish a framework to avoid this additional contribution systematically. Through the non-observation of stellar anomalies, we limit the overall dark luminosity, resulting in constraints on the underlying particle model.

Besides being produced in stellar systems, dark sector particles can manifest themselves in the laboratory. For direct production, the facilities with high-intensity and detectors of high energy/angular resolution are suitable for a sub-GeV dark-state search. In this thesis, we study both electron and proton facilities. Depending on the experimental configurations, the electron-beam experiments can be categorized into electron-positron colliders (BaBar/Belle II), fixed-target experiments (NA64/LDMX), and beam-dump experiments (mQ/BDX), with the signal channels being mono-γ with missing transverse energy, missing energy inferred from a measurement of the final-state electron, and dark-state induced recoils in a downstream detector, respectively. The signal rate for each kind of experiment is analytically derived, including the formulas for cross sections of electron-positron annihilation with initial-state radiation and the electron-nucleus bremsstrahlung. Furthermore, the full analytical 4-body phase space, needed for the bremsstrahlung production, is derived in the appendix. It is shown that the constraints from the electron-beam facilities are essential for ruling out the Z' scenario as a possible explanation for the INTEGRAL 511 keV line excess.

The dark states production mechanism in the proton-beam experiments is distinct from that of the electron-beam one; considering that we need QCD to describe the result from a beam-target collision, such as meson production and the direct production of dark states from the Drell-Yan process, we resort to numerical simulations. In this thesis, we focus on the production of χ from the Drell-Yan process and meson decay. While the estimation of the Drell-Yan process mainly relies on numerical tools, we build a complete framework for computing the energy spectrum and angular distribution of the dark states sourced from meson decay, including two-body decay for a vector meson and three-body decay for a scalar meson. The formulas for the differential decay rates and the transformation from the meson rest frame to the lab frame are derived. We are interested in the electron recoil and hadronic shower caused by the dark states in the downstream detector. We observe the dependence on the center-of-mass energy of operators with different mass-dimension in the ensuing constraints. For mass-dimension 5 operators, future proton-beam experiments can probe the parameter space beyond the LEP bound.

These light dark states can also be directly produced in high-energy colliders such as LEP and LHC. All the dark states considered in this thesis can be created in these colliders,

resulting in missing energy signals. Besides, the heavy mediator can be produced on-shell, yielding a displaced vertex signal from a long-lived particle. In this thesis, we focus on the missing energy search in LEP, in which the center-of-mass energy is around the Z-pole mass. While its sensitivity is not extraordinary for lower mass-dimension operators due to their weaker UV-dependence, the LEP missing-energy bound remains essential for anapole moment and charge radius operators. Beyond the Z-pole, one may consider analyzing the existing LHC data and studying future colliders' sensitivity to test the presence of beyond TeV particles. To do so, we need to have detailed collider simulations, integrating the collision of particle beams, the cascade of final-state particles, and their detection; this is reserved for dedicated future work.

Indirectly, the dark states can take part in loop processes, affecting various electroweak precision observables. For example, new heavy charged particles can appear in the photon's self-energy, altering the fine-structure constant's running. Another example is the lepton $g-2$: new particles that couple to Standard Model leptons can engage in the typical triangle loop and contribute to the anomalous magnetic moment. We have shown that the value of a_e inferred from the fine-structure constant measurement can lead to stringent limits on the dark sector models. Finally, dark states' appearance can modify the decay width of Standard Model particles, *e.g.*, the Z-invisible decay, which is measured precisely. We have detailed the calculation of various loop diagrams, and a generalization to other types of dark-visible interactions can be made from there. If the dark sector is described by a chiral theory or non-flavor-universal one, it can act as a source of extra parity violation or result in lepton flavor violating processes. Parity violation is present in the Standard Model weak interaction, precisely measured in terms of polarized electron-electron scattering. With the current sensitivity, the potential dark chiral interaction can be strongly constrained. In the latter case, lepton flavor violating processes such as $\mu \to e\gamma$ are forbidden in the Standard Model; therefore, the presence of lepton flavor violating processes can be a smoking gun for new physics. We have utilized current measurements of the asymmetry parameter for the parity violation and the absence of $\mu \to e\gamma$ to derive constraints on the underlying models.

In addition to a thermal component, we entertain the possibility of having a non-thermal component of dark states. We consider an intuitive way to build a non-thermal population: particle decay. To be specific, we study the process of dark matter decays to dark radiation. Through the two-body decay, the energy spectrum of dark radiation is only related to the mass and lifetime of the parent dark matter; thus, dark radiation can have a distinct energy spectrum from the thermal cosmic radiation backgrounds. A non-thermal energy spectrum also boosts the detection potential of dark radiation in terrestrial experiments such as the direct detection experiments and neutrino experiments, as long as their thresholds are low enough. First, we establish the framework of computing the event rate of Standard Model particles' recoil with an incoming relativistic dark flux. We then derive the sensitivity of current experiments such as XENON1T, Borexino and Super-Kamiokande, as well as proposed

ones, *e.g.*, DUNE and Hyper-Kamiokande. Besides, we find the recent XENON1T excess can be fitted with the dark radiation carrying mass-dimension 4 and 6 EM form factors, without conflicting the constraints from stellar energy loss argument.

The conventional direct and indirect dark matter searches are still essential for sub-GeV dark states but with different strategies. For the direct detection, we study scattering between a non-relativistic dark matter and an atomic electron, which has a smaller ionizing threshold than the nuclear recoil in order to be detectable. We update the current constraints on the benchmark models with a combination of experiments and further consider a solar-reflected flux. On the other hand, the pair-annihilation of dark states leaves imprints both in the early and local universe. In the former case, the energy injection from the s-wave annihilation modifies the ionization history, affecting the Cosmic Microwave Background anisotropy power spectra. The velocity-suppressed p-wave annihilation, on the other hand, can be less suppressed at lower redshifts in virilized dark matter halos, yielding detectable signals in observatories such as Voyager I considered in this thesis.

We demonstrate that the two benchmark sub-GeV dark sector models can only be weakly-coupled to the visible sector by scrutinizing the aforementioned probes, together with cosmological observables such as $N_{\rm eff}$ and structure formation. In addition, the electromagnetic form factors of the dark states are constrained to be small; namely, the dark sector is indeed "dark" to a large degree. We also rule out scalar dark matter, either through fermion or vector portal, as an explanation of the muon $g-2$ anomaly and the INTEGRAL 511 keV line excess. Furthermore, the parameter space for a correct thermal dark matter relic of the two portals is excluded. In summary, we illustrate how current and future searches, equipped with high-intensity source and high-resolution detectors, can improve our understanding of a light, sub-GeV dark sector.

10.2 Future perspectives

Although rough estimates may be sufficient for setting overall constraints, we note that some aspects discussed in this thesis may require further investigation, listed in the following:

- Neutrino kinetic decoupling (ongoing work): in the early universe, this process naturally leads to $N_{\rm eff} \neq 3$. We note that in the literature, the calculation usually assumes dark matter thermalizes with either the electron or neutrino sector initially. However, dark matter may interact with both electron and neutrino with comparable strength, such as the Z'-portal discussed in this thesis. To obtain the correct value of $N_{\rm eff}$ and robust constraints on the parameter space, one needs to co-evolute the three sectors' thermodynamics.
- On-shell production of portal particles: with high enough center-of-mass energy, heavy mediators such as F and Z' can be produced on-shell in laboratories. In this case,

the observables are strongly related to their decay width and the associated branching ratios to different final states. The signal can be missing energy (if it mainly decays into the dark states) or a displaced vertex (if it mainly decays into Standard Model particles). Therefore, a detailed study considering both individual effects or even the combination is required to probe the whole parameter space firmly.

- UV completion of the "photon portal": the UV physics may be important in deriving valid constraints on the parameter space of the photon portal from high-energy colliders including LEP and LHC, as the center-of-mass energy may be comparable to the UV scale. In an UV-completed model, electromagnetic form factors of dark states can be induced by some heavy charged states appearing in loops. Furthermore, these heavy states can be millcharged to avoid collider constraints on charged particles at electroweak scale. On the other hand, one can search for distinct signatures in colliders, *e.g.*, displaced vertex signals from heavy particle decay, which requires detailed detector simulations.
- Precise calculation of DM-electron scattering (ongoing work): in this thesis, we use atomic form factors based on the non-relativistic wavefunctions of electrons in our calculations of DM-electron scattering. In the high momentum transfer regime $\vec{q} \cdot \vec{r} \gtrsim 1$ where $\vec{r}$ is the electron coordinate, it turns out that fully relativistic electron wavefunctions are necessary to compute accurate atomic form factors.

In conclusion, this thesis provides a comprehensive framework for probing a light dark sector in the sub-GeV mass range. Through two minimal extensions of the Standard Model, we demonstrate the sensitivity reaches of different experiments and searches, ranging from laboratory to astrophysics and cosmology. We have shown that current constraints suggest that the dark states only carry minute electromagnetic form factors and exclude a potential explanation for some long-standing anomalies. Sub-GeV dark sectors remain an active research area, with plenty of new ideas on model building and experimental designs. The formalism developed in this thesis is thus timely and can be employed in other more involved models. In the future, this framework can be extended to include searches that are not considered in this thesis, *e.g.*, the 21 cm cosmology at the cosmic dawn and missing energy/displaced vertex events in LHC.

Appendix

A Derivation of Phase Space

In this appendix, we derive the Lorentz-invariant phase space integrals in frames, relevant in the computation of decay rates and cross sections in this thesis. We start from the three-body phase space which appears in the decay rate of the scalar meson (Sec. 4.2.2) and in Compton-like production of the dark states (Sec. 3.2.4). Then we resolve the formidable four-body phase space, relevant for the bremsstrahlung process considered in this thesis; see Sec. 3.2.5 and Sec. 7.1.

One useful technique to simplify the phase space integral is decomposing the full one into a sequence of fundamental two-body phase space elements. We first combine any two particles into one "quasi-particle" with 4-momentum $q_{12} = p_1 + p_2$ by inserting the integrals:

$$\int d^4q_{12}\,\delta^4(q_{12} - p_1 - p_2)\Theta(q_{12}^0) = 1\,, \tag{A.1}$$

and

$$\int ds_{12}\,\delta(s_{12} - q_{12}^2) = 1\,, \tag{A.2}$$

where s_{12} can be seen as the squared mass of the quasi-particle. Utilizing the identity,

$$\int \frac{d^3q_{12}}{2E_{12}} = \int d^4q_{12}\,\delta(s_{12} - q_{12}^2)\Theta(q_{12}^0)\,, \tag{A.3}$$

to integrate out the q_{12}^0 dependence, we obtain

$$\int \frac{ds_{12}}{2\pi} \int \frac{d^3q_{12}}{(2\pi)^3 2E_{12}}\,(2\pi)^4\delta^4(q_{12} - p_1 - p_2) = 1\,, \tag{A.4}$$

where $E_{12} = q_{12}^0$. Because the overall phase space integral is Lorentz-invariant, in principle we can carry out the integral in any frame, in which the most convenient one is the rest frame of q_{12}. Therefore, in this way we can simplify part of the many-body phase space; for example, we can integrate the Lorentz-invariant phase space $d\Pi_i = \prod_i d^3\vec{p}_i(2\pi)^{-3}(2E_i)^{-1}$ with the delta function in Eq. (A.4), yielding a two-body phase space:

$$\begin{aligned}\int d\Phi_2 &= \int d\Pi_{i=1,2}\,(2\pi)^4\delta^4(q_{12} - p_1 - p_2) \\ &= \frac{\bar{\beta}(s_{12}, m_1, m_2)}{8\pi} \int \frac{d\Omega_{12}}{4\pi}\,,\end{aligned} \tag{A.5}$$

with

$$\bar{\beta}(s_{12}, m_1^2, m_2^2) = \sqrt{1 - \frac{2(m_1^2 + m_2^2)}{s_{12}} + \frac{(m_1^2 - m_2^2)^2}{s_{12}^2}}\,.$$

A.1 Three-body phase space

First, we consider the three-body decay process $p_1 \to p_2 + p_3 + p_4$. The most general form of the three-body phase space integral reads

$$\int d\Phi_3 = \int d\Pi_{i=2,3,4}\,(2\pi)^4 \delta^4(p_1 - p_2 - p_3 - p_4)\,. \tag{A.6}$$

To simplify Eq. (A.6), we only need to apply the aforementioned technique once. Combining p_3 and p_4 as one quasi-particle, we can rewrite Eq. (A.6) as

$$\begin{aligned}\int d\Phi_3 &= \int d\Pi_{i=2,3,4} \int \frac{ds_{34}}{2\pi} \int \frac{d^3 q_{34}}{(2\pi)^3 2E_{34}} (2\pi)^4 \delta^4(q_{34} - q_3 - q_4)(2\pi)^4 \delta^4(p_1 - p_2 - q_{34}) \\ &= \int \frac{ds_{34}}{2\pi} \int d\Phi_2(p_2, q_{34}) \int d\Phi_2(p_3, p_4) \\ &= \int \frac{ds_{34}}{2\pi} \int \frac{d\Omega_2}{4\pi} \frac{\bar{\beta}(m_1^2, m_2^2, s_{34})}{8\pi} \int \frac{d\Omega_{34}}{4\pi} \frac{\bar{\beta}(s_{34}, m_3^2, m_4^2)}{8\pi}\,.\end{aligned} \tag{A.7}$$

Note that here $d\Omega_2$ represents the overall solid angle of the whole system, and $d\Omega_{34}$ is the angular phase space element between $\vec{p}_2$ and $\vec{p}_3$-$\vec{p}_4$ plane. To further simplify the phase space integral, we choose to compute in the frame that $\vec{p}_3 + \vec{p}_4 = 0$ (denoted as "R34")[1]. As we are interested in an isotropic decay, the overall solid angle of the system can be integrated out. Furthermore, we can define the polar angle $\cos\theta_{34}^{\mathrm{R34}}$ with respect to $\vec{p}_2$ such that the dependence on the azimuthal angle ϕ_{34} can be seen as an overall rotation of $\vec{p}_3$ and $\vec{p}_4$ with respect to $\vec{p}_2$. After integrating out the trivial rotational degrees of freedom, the three-body phase space integral becomes

$$\int d\Phi_3 = \frac{1}{32(2\pi)^3} \int ds_{34} \int d\cos\theta_{34}^{\mathrm{R34}}\, \bar{\beta}(m_1^2, m_2^2, s_{34}) \bar{\beta}(s_{34}, m_3^2, m_4^2)\,. \tag{A.8}$$

In general, it is more convenient to trade the frame-dependent variable $\cos\theta_{34}^{\mathrm{R34}}$ with certain Lorentz-invariant quantities such as $s_{23} \equiv (p_2 + p_3)^2$. In the R34 frame, we have

$$s_{23} = m_2^2 + m_3^2 + 2E_2^{\mathrm{R34}} E_3^{\mathrm{R34}} - 2|\vec{p}_2|^{\mathrm{R34}} |\vec{p}_3|^{\mathrm{R34}} \cos\theta_{34}^{\mathrm{R34}}\,. \tag{A.9}$$

It is straightforward to express energies and momenta in the R34 frame in terms of s_{34} and the masses,

$$E_1^{\mathrm{R34}} = \frac{m_1^2 - m_2^2 + s_{34}}{2\sqrt{s_{34}}}\,, \quad |\vec{p}_1|^{\mathrm{R34}} = \frac{m_1^2}{2\sqrt{s_{34}}} \bar{\beta}(m_1^2, m_2^2, s_{34})\,,$$

[1] Compared to the frame used here, it is not so straightforward to use the rest frame of the decaying particle to simplify the phase space integral.

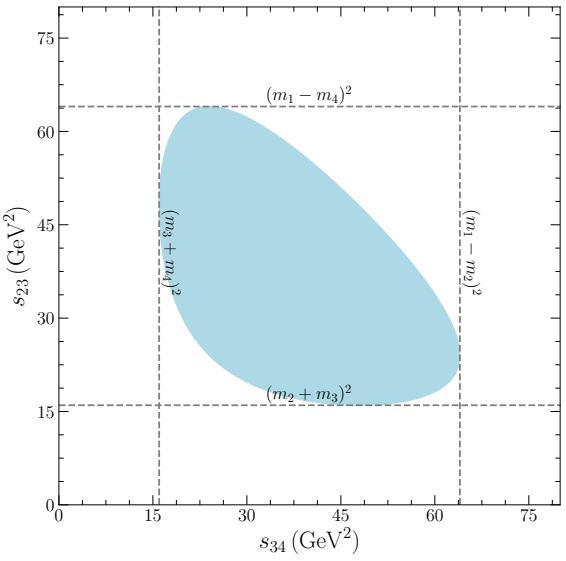

Figure A.2: The Dalitz plot demonstrating the allowed kinematic region (light blue shaded) for two Lorentz-invariant variables s_{23} and s_{34}. The kinematic boundaries are represented by four dashed lines with the corresponding values labelled. Here we take $m_1 = 10\,\mathrm{GeV}$ and $m_2 = m_3 = m_4 = 2\,\mathrm{GeV}$.

$$
\begin{aligned}
E_2^{\mathrm{R34}} &= \frac{m_1^2 - m_2^2 - s_{34}}{2\sqrt{s_{34}}}\,, \quad |\vec{p}_2|^{\mathrm{R34}} = \frac{m_1^2}{2\sqrt{s_{34}}}\bar{\beta}(m_1^2, m_2^2, s_{34})\,,\\
E_3^{\mathrm{R34}} &= \frac{m_3^2 - m_4^2 + s_{34}}{2\sqrt{s_{34}}}\,, \quad |\vec{p}_3|^{\mathrm{R34}} = \frac{m_3^2}{2\sqrt{s_{34}}}\bar{\beta}(m_3^2, m_4^2, s_{34})\,,\\
E_4^{\mathrm{R34}} &= \frac{m_3^2 - m_4^2 - s_{34}}{2\sqrt{s_{34}}}\,, \quad |\vec{p}_4|^{\mathrm{R34}} = \frac{m_3^2}{2\sqrt{s_{34}}}\bar{\beta}(m_3^2, m_4^2, s_{34})\,.
\end{aligned}
$$

We can then express $\cos\theta_{34}^{\mathrm{R34}}$ in terms of Lorentz-invariant variables as

$$
\cos\theta_{34}^{\mathrm{R34}} = \frac{s_{34}(m_1^2 + m_2^2 + m_3^2 + m_4^2 - 2s_{23}) + (m_1^2 - m_2^2)(m_3^2 - m_4^2) - s_{34}^2}{m_1^2 m_3^2 \bar{\beta}(m_1^2, m_2^2, s_{34})\bar{\beta}(m_3^2, m_4^2, s_{34})}\,. \tag{A.10}
$$

To replace the integration variable, we need the Jacobian,

$$
\left|\frac{\partial \cos\theta_{34}^{\mathrm{R34}}}{\partial s_{23}}\right| = \frac{2s_{34}}{m_1^2 m_3^2 \bar{\beta}(m_1^2, m_2^2, s_{34})\bar{\beta}(m_3^2, m_4^2, s_{34})}\,, \tag{A.11}
$$

with which the three-body phase space integral can be written as

$$
\begin{aligned}
\int d\Phi_3 &= \frac{1}{32(2\pi)^3}\int ds_{34}\int ds_{23}\left|\frac{\partial \cos\theta_{34}^{\mathrm{R34}}}{\partial s_{23}}\right|\bar{\beta}(m_1^2, m_2^2, s_{34})\bar{\beta}(s_{34}, m_3^2, m_4^2)\\
&= \frac{1}{16(2\pi)^3 m_1^2}\int ds_{34}\int ds_{23}\,,
\end{aligned} \tag{A.12}
$$

where we use the fact that $m_3^2\bar{\beta}(m_3^2, m_4^2, s_{34}) = s_{34}\bar{\beta}(s_{34}, m_3^2, m_4^2)$. The integration boundaries of s_{34} are given by

$$
(m_3 + m_4)^2 \leq s_{34} \leq (m_1 - m_2)^2\,,
$$

while that of s_{23} read

$$[s_{23}]^{\pm} = m_2^2 + m_3^2 + 2E_2^{\rm R34}E_3^{\rm R34} \pm 2|\vec{p}_2|^{\rm R34}|\vec{p}_3|^{\rm R34}\,,$$

corresponding to the case $\cos\theta_{34}^{\rm R34} = \mp 1$. The variables, s_{23} and s_{34}, are usually called *Dalitz variables*, and the integration boundaries of them form the famous *Dalitz plot* shown in Fig. A.2.

Note that Eq. (A.12) is general and fully Lorentz-invariant, hence it can be applied to other specific frames. For example, to obtain the energy spectrum of the dark states produced from the scalar meson decay sm $\to \gamma + \chi + \bar{\chi}$, we need to first compute the differential decay rate $d\Gamma_\chi/dE_\chi^*$ in the rest frame of the meson in which the decay is isotropic, and then boost the whole system to the lab frame. In this case we simply trade one of the Lorentz-invariant variables in Eq. (A.12) with E_χ^*; see App. B.2.1 for details. For the Compton-like production of χ-pair $e^- + \gamma \to e^- + \chi + \bar{\chi}$ discussed in Sec. 3.2.4, as the energy spectrum and the direction of the emitted dark states are not important, we can regard χ-pair as a quasi-particle with squared invariant mass $s_{\chi\bar{\chi}}$ to compute the three-body phase phase. The resulting differential cross section is given in Eq. (3.19). One may switch to other specific frame choices, depending on the problem at hand; we refer the reader to [449] for the formulas in different frames.

A.2 Four-body phase space

The four-body phase space integral is especially relevant for the bremsstrahlung process $p_1 + p_2 \to p_3 + p_4 + p_5 + p_6$ that appears many times in this thesis. The most general form of the four-body phase space integral reads

$$\int d\Phi_4 = \int d\Pi_{i=3,4,5,6}\,(2\pi)^4\delta^4(p_1 + p_2 - p_3 - p_4 - p_5 - p_6)\,. \tag{A.13}$$

Including the delta function for the four-momentum conservation as well as an overall rotation around $\vec{p}_1 + \vec{p}_2$, we still have 7 degrees of freedom. In the following, we simplify Eq. (A.13) case by case, including the bremsstrahlung production of dark states in stellar objects, in fixed-target experiments, and in beam-dump experiments.

For the emission in stars, we consider the process $e(p_1) + N(p_2) \to e(p_3) + N/X_n(p_4) + \chi(p_5) + \bar{\chi}(p_6)$ and compute the energy loss rate in the lab frame $\vec{p}_2 = 0$. In case of an inelastic process on the target nucleus, the final-state N is replaced by X_n, where X_n denotes an inclusive final state. First, because we are only interested in the total energy loss by $\chi(\bar{\chi})$ per collision, the energy spectrum and the angular distribution of the dark states are not relevant; therefore, we can factor out the phase space of the dark states, resulting in

$$\int d\Phi_4 = \int d\Pi_{i=3,4,k}\,(2\pi)^4\delta^4(p_1 + p_2 - p_3 - p_4 - k) \int \frac{ds_{\chi\bar{\chi}}}{2\pi} \int d\Pi_{i=5,6}\,(2\pi)^4\delta^4(k - p_5 - p_6)$$

$$= \int \frac{ds_{\chi\bar{\chi}}}{2\pi} \int d\Phi_3(p_3, p_4, k) \frac{\bar{\beta}(s_{\chi\bar{\chi}}, m_\chi^2, m_\chi^2)}{8\pi} \int \frac{d\Omega_{\chi\bar{\chi}}^{\mathrm{R}}}{4\pi}\,, \tag{A.14}$$

where $k = p_5 + p_6$ and $s_{\chi\bar{\chi}} = k^2$. The phase space of the χ-pair can be integrated in their rest frame together with the dark current to yield $f(s_{\chi\bar{\chi}})$; see Eq. (2.5). Now we are left with a three-body phase space integral that is independent of the dark states, for which we introduce Lorentz-invariant variables to replace the frame-dependent variables. First, we introduce $s_4 = \omega^2 = (p_4 + k)^2 = (p_1 + p_2 - p_3)^2$ such that the three-body phase space integral reads

$$\begin{aligned}
\int d\Phi_3 &= \int d\Pi_3 \int d\Pi_{i=4,k}\, (2\pi)^4 \delta^4(\omega - p_4 - k) \\
&= \int d\Pi_3 \, \frac{\bar{\beta}(s_4, m_{N/X}^2, s_{\chi\bar{\chi}})}{8\pi} \int \frac{d\Omega_{4k}^{\mathrm{R4k}}}{4\pi} \\
&= \frac{1}{16(2\pi)^4} \int dE_3 \int d\cos\theta_3\, |\vec{p}_3| \bar{\beta}(s_4, m_{N/X}^2, s_{\chi\bar{\chi}}) \int d\Omega_{4k}^{\mathrm{R4k}}\,,
\end{aligned} \tag{A.15}$$

where the overall azimuthal angle between $\vec{p}_3$ and $\vec{p}_1 + \vec{p}_2$ is integrated out and "R4k" denotes the frame $\vec{p}_4 + \vec{k} = 0$. The two frame-dependent variables, E_3 and $\cos\theta_3$, can be replaced by s_4 and $t_1 = (p_1 - p_3)^2 = q_1^2$ with the formulas:

$$\begin{aligned}
s_4 &= 2m_e^2 + m_N^2 + 2(E_1 - E_3)m_N - 2E_1E_3 + 2\sqrt{E_1^2 - m_e^2}\sqrt{E_3^2 - m_e^2}\cos\theta_3\,, \\
t_1 &= 2m_e^2 - 2E_1E_3 + \sqrt{E_1^2 - m_e^2}\sqrt{E_3^2 - m_e^2}\cos\theta_3\,,
\end{aligned}$$

with $E_1 = (s - m_e^2 - m_N^2)/(2m_N)$, where $s = (p_1 + p_2)^2$ is the squared CM energy of the system. The Jacobian for changing the variables reads

$$\left| \frac{\partial(E_3, \cos\theta_3)}{\partial(s_4, t_1)} \right| = \frac{1}{2|\vec{p}_3|\sqrt{\lambda(s, m_e^2, m_N^2)}}\,, \tag{A.16}$$

where $\lambda(a, b, c) = a^2 + b^2 + c^2 - 2(ab + ac + bc)$ is the triangle function and its relation with $\bar{\beta}$ is

$$\sqrt{\lambda(a, b, c)} = a \times \bar{\beta}(a, b, c)\,.$$

In terms of s_4 and t_1, the three-body phase space integral can be rewritten as

$$\int d\Phi_3 = \frac{1}{32(2\pi)^4} \frac{1}{\sqrt{\lambda(s, m_e^2, m_N^2)}} \int ds_4 \int dt_1\, \bar{\beta}(s_4, m_{N/X}^2, s_{\chi\bar{\chi}}) \int d\Omega_{4k}^{\mathrm{R4k}}\,. \tag{A.17}$$

Now the only frame-dependent part is $d\Omega_{4k}^{\mathrm{R4k}} = d\cos\theta_{4k}^{\mathrm{R4k}} d\phi_{4k}^{\mathrm{R4k}}$, in which the polar angle can be replaced by another Lorentz-invariant variable $t_2 = (p_2 - p_4)^2 = q_2^2$, in the R4k frame, which reads[2]

$$t_2 = m_N^2 + m_{N/X}^2 - \frac{1}{2s_4}\Big[(s_4 + m_N^2 - t_1)(s_4 + m_{N/X}^2 - s_{\chi\bar{\chi}})$$

[2] See the discussion on "t-channel cut" in [449].

$$- \sqrt{\lambda(s_4, m_N^2, t_1)\lambda(s_4, m_{N/X}^2, s_{\chi\bar{\chi}})}\cos\theta_{4k}^{\mathrm{R4k}}\Big] .$$

The corresponding Jacobian is then

$$\left|\frac{\partial \cos\theta_{4k}^{\mathrm{R4k}}}{\partial t_2}\right| = \frac{2s_4}{\sqrt{\lambda(s_4, m_N^2, t_1)\lambda(s_4, m_{N/X}^2, s_{\chi\bar{\chi}})}} . \tag{A.18}$$

The azimuthal angle can be seen as the angle between planes $(\vec{q}_1, \vec{p}_1)$ and $(\vec{q}_1, \vec{k})$ in the lab frame. In terms of $n \times n$ unsymmetrical G_n and symmetrical Δ_n Gram determinants[3], we introduce another Lorentz-invariant variable,

$$\begin{aligned} p_{1k} \equiv p_1 \cdot k = &\frac{(p_2 \cdot p_1)G_2(p_2, q_1; q_1, k) - (q_1 \cdot p_1)G_2(p_2, q_1; p_2, k)}{-\Delta_2(p_2, q_1)} \\ &+ \frac{\sqrt{\Delta_3(p_2, q_1, p_1)\Delta_3(p_2, q_1, k)}\cos\phi_{4k}^{\mathrm{R4k}}}{-\Delta_2(p_2, q_1)} , \end{aligned}$$

from which we can read off the Jacobian:

$$\left|\frac{\partial \phi_4^{R4k}}{\partial p_{1k}}\right| = -\frac{\sqrt{-\Delta_2(p_2, q_1)}}{\sqrt{-\Delta_4(p_2, q_1, p_1, k)}} . \tag{A.19}$$

Note that when switching to p_{1k} we need an extra factor of 2 to account for the fact that ϕ_{4k}^{R4k} ranges from 0 to 2π.

Finally, we can write down the Lorentz-invariant formula for the three-body phase space integral considered here,

$$\int d\Phi_3 = \frac{1}{8(2\pi)^4}\frac{1}{\sqrt{\lambda(s, m_e^2, m_N^2)}}\int ds_4 \int dt_1 \frac{1}{\sqrt{\lambda(s_4, m_N^2, t_1)}}\int dt_2 \int dp_{1k} \left|\frac{\partial \phi_{4k}^{\mathrm{R4k}}}{\partial p_{1k}}\right| . \tag{A.20}$$

Combining Eq. (A.20) with $|\mathcal{M}|_{2\to3}$, we can derive $\sigma_{2\to3}$ in Eq. (B.67); the integration boundaries for each variable are given below Eq. (B.67)[4]. Including the phase space of the χ-pair, the full four-body phase space reads

$$\begin{aligned} \int d\Phi_4 = &\frac{1}{32(2\pi)^6}\frac{1}{\sqrt{\lambda(s, m_e^2, m_N^2)}}\int s_{\chi\bar{\chi}} \int ds_4 \int dt_1 \frac{\bar{\beta}(s_{\chi\bar{\chi}}, m_\chi^2, m_\chi^2)}{\sqrt{\lambda(s_4, m_N^2, t_1)}} \\ &\times \int dt_2 \int dp_{1k} \left|\frac{\partial \phi_{4k}^{\mathrm{R4k}}}{\partial p_{1k}}\right| \int \frac{d\Omega_{\chi\bar{\chi}}^{\mathrm{R}}}{4\pi} . \end{aligned} \tag{A.21}$$

[3] See [449] for the definitions of G_n and Δ_n.

[4] For the s-channel variables such as s_4, the integration boundaries are simply the overall kinematic constraints. On the contrary, for the t-channel variables such as t_1 and t_2, the boundaries are determined by the extremal value of the cosine of the following angles.

For the production of ϕ-pair in fixed-target experiment considered in Sec. 7.1.2, we infer the missing energy by measuring the final-state electron; therefore, we need to obtain the energy spectrum and angular distribution of p_3,

$$\int \frac{d\Phi_4}{dE_3 d\cos\theta_3} = \frac{\sqrt{E_3^2 - m_e^2}}{16(2\pi)^6} \int s_{\phi\phi} \frac{\bar{\beta}(s_{\phi\phi}, m_\phi^2, m_\phi^2)}{\sqrt{\lambda(s_4, m_N^2, t_1)}} \int dt_2 \int dp_{1k} \left| \frac{\partial \phi_{4k}^{\rm R4k}}{\partial p_{1k}} \right| \int \frac{d\Omega_{\phi\phi}^{\rm R}}{4\pi} , \quad \text{(A.22)}$$

where we simply apply the inverse of Eq. (A.16) to Eq. (A.21). The 2-to-4 differential cross section (C.108) can then be derived based on Eq. (A.22).

For beam-dump experiments such as mQ and BDX, we probe the particle recoil caused by dark states at a downstream detector, for which we solve for the energy spectrum and angular distribution of the produced dark states. Therefore, we can no longer combine dark state pair as one quasi-particle; instead, we decompose the four-body phase space integral as follows:

$$\begin{aligned} \int d\Phi_4 &= \int \frac{ds_{36}}{2\pi} \int d\Pi_{i=4,5,k_{36}} (2\pi)^4 \delta^4(p_1 + p_2 - p_4 - p_5 - k_{36}) \int d\Pi_{i=3,6} (2\pi)^4 \delta^4(k_{36} - p_3 - p_6) \\ &= \int \frac{ds_{36}}{2\pi} \int d\Phi_3(p_4, p_5, k_{36}) \frac{\bar{\beta}(s_{36}, m_e^2, m_\phi^2)}{8\pi} \int \frac{d\Omega_{36}^{\rm R36}}{4\pi} , \end{aligned} \quad \text{(A.23)}$$

where $s_{36} = (p_3 + p_6)^2 = k_{36}^2$. Introducing a t-channel cut, the polar part of $d\Omega_{36}^{\rm R36}$ (polar angle between $\vec{p}_3$ and $\vec{p}_1 + \vec{p}_2$) can be traded with a Lorentz-invariant variable $t_{23} = (p_2 - p_3)^2$, expressed by

$$\begin{aligned} t_{23} = m_N^2 + m_e^2 - \frac{1}{2s_{36}} \Bigg\{ & \left[s_{36} + m_N^2 - (p_1 - p_4 - p_5)^2 \right] (s_{36} + m_e^2 - m_\phi^2) \\ & - \sqrt{\lambda(s_{36}, m_N^2, (p_1 - p_4 - p_5)^2) \lambda(s_{36}, m_e^2, m_\phi^2)} \cos\theta_{36}^{\rm R36} \Bigg\} , \end{aligned}$$

with the Jacobian being

$$\left| \frac{\partial \cos\theta_{36}^{\rm R36}}{\partial t_{23}} \right| = \frac{2s_{36}}{\sqrt{\lambda(s_{36}, m_N^2, (p_1 - p_4 - p_5)^2) \lambda(s_{36}, m_e^2, m_\phi^2)}} . \quad \text{(A.24)}$$

In the lab frame, the azimuthal angle $\phi_{36}^{\rm R36}$ is then the angle between planes $(\vec{p}_1 - \vec{p}_4 - \vec{p}_5, \vec{p}_3)$ and $(\vec{p}_1 - \vec{p}_4 - \vec{p}_5, \vec{p}_4)$, which can be reformulated as the Lorentz-invariant variable:

$$\begin{aligned} p_{34} \equiv p_3 \cdot p_4 = & \frac{(p_2 \cdot p_4) G_2(p_2, p_1 - p_4 - p_5; p_1 - p_4 - p_5, p_3)}{-\Delta_2(p_2, p_1 - p_4 - p_5)} \\ & - \frac{[(p_1 - p_4 - p_5) \cdot p_4] \, G_2(p_2, p_1 - p_4 - p_5; p_2, p_3)}{-\Delta_2(p_2, p_1 - p_4 - p_5)} \\ & - \frac{\sqrt{\Delta_3(p_2, p_1 - p_4 - p_5, p_4) \Delta_3(p_2, p_1 - p_4 - p_5, p_3)} \cos\phi_{36}^{\rm R36}}{-\Delta_2(p_2, p_1 - p_4 - p_5)} . \end{aligned}$$

The Jacobian can be derived analogous to Eq. (A.19). The residual three-body phase space integral reads

$$\begin{aligned}\int d\Phi_3 &= \int d\Pi_5 \int d\Pi_{i=4,k_{36}} (2\pi)^4 (p_1 + p_2 - p_4 - p_5 - k_{36}) \\ &= \frac{1}{2(2\pi)^2} \int dE_5 \int d\cos\theta_5 \, |\vec{p}_5| \int d\Pi_{i=4,k_{36}} (2\pi)^4 (k_{436} - p_4 - k_{36}) \\ &= \frac{1}{2(2\pi)^2} \int dE_5 \int d\cos\theta_5 \, |\vec{p}_5| \frac{\bar{\beta}(s_{436}, m_{N/X}^2, s_{36})}{8\pi} \int \frac{d\Omega_{436}^{\mathrm{R436}}}{4\pi} \,, \end{aligned} \tag{A.25}$$

with $s_{436} = (p_4 + k_{36})^2 = k_{436}^2$. Again, with a t-channel cut $p_2 + (p_1 - p_5)^2 \to p_4 + k_{36}$, we can introduce

$$\begin{aligned} t_2 = m_N^2 + m_{N/X}^2 - \frac{1}{2s_{436}} \Big[&(s_{436} + m_N^2 - t_{15}^2)(s_{436} + m_{N/X}^2 - s_{36}) \\ &- \sqrt{\lambda(s_{436}, m_N^2, t_{15}) \lambda(s_{436}, m_{N/X}^2, s_{36})} \cos\theta_{436}^{\mathrm{R436}} \Big] \,, \end{aligned}$$

where $t_{15} \equiv (p_1 - p_5)^2$. The corresponding Jacobian is

$$\left| \frac{\partial \cos\theta_{436}^{\mathrm{R436}}}{\partial t_2} \right| = \frac{2 s_{436}}{\sqrt{\lambda(s_{436}, m_N^2, t_{15}) \lambda(s_{436}, m_{N/X}^2, s_{36})}} \,. \tag{A.26}$$

The two variables, s_{436} and t_{15}, can be expressed in terms of lab frame variables as

$$\begin{aligned} s_{436} &= m_e^2 + m_N^2 + m_\phi^2 + 2E_1 m_N - 2E_5 m_N - 2E_1 E_5 + 2\sqrt{E_1^2 - m_e^2}\sqrt{E_5^2 - m_\phi^2} \cos\theta_5 \,, \\ t_{15} &= m_e^2 + m_\phi^2 - 2E_1 E_5 2\sqrt{E_1^2 - m_e^2}\sqrt{E_5^2 - m_\phi^2} \cos\theta_5 \,. \end{aligned}$$

Note that

$$(p_1 - p_4 - p_5)^2 = m_N^2 + m_{N/X}^2 + s_{36} + t_{15} - s_{436} - t_2 \,.$$

While the azimuthal angle $\phi_{436}^{\mathrm{R436}}$ can be seen as the angle between planes $(\vec{p}_1 - \vec{p}_5, \vec{p}_1)$ and $(\vec{p}_1 - \vec{p}_5, \vec{p}_4)$ in the lab frame, we can define

$$\begin{aligned} p_{14} \equiv p_1 \cdot p_4 = &\frac{(p_2 \cdot p_1) G_2(p_2, p_1 - p_5; p_1 - p_5, p_4) - [(p_1 - p_5) \cdot p_1] \, G_2(p_2, p_1 - p_5; p_2, p_4)}{-\Delta_2(p_2, p_1 - p_5)} \\ &- \frac{\sqrt{\Delta_3(p_2, p_1 - p_5, p_1) \Delta_3(p_2, p_1 - p_5, p_4)} \cos\phi_{436}^{\mathrm{R436}}}{-\Delta_2(p_2, p_1 - p_5)} \,. \end{aligned}$$

The Jacobian can be read off accordingly. Collecting all pieces of the phase space integral, we find

$$\int \frac{d\Phi_4}{dE_5 \cos\theta_5} = \frac{\sqrt{E_5^2 - m_\phi^5}}{8(2\pi)^7} \frac{\int ds_{36} \int t_{23} \int dp_{34} \int dt_2 \int dp_{14} \left| \frac{\partial \phi_{36}^{\mathrm{R36}}}{\partial p_{34}} \right| \left| \frac{\partial \phi_{436}^{\mathrm{R436}}}{\partial p_{14}} \right|}{\sqrt{\lambda(s_{36}, m_N^2, (p_1 - p_4 - p_5)^2) \lambda(s_{436}, m_N^2, t_{15})}}$$

$$= \frac{\sqrt{E_5^2 - m_\phi^5}}{32(2\pi)^7} \frac{\int ds_{36} \int t_{23} \int d\phi_{36}^{\mathrm{R36}} \int dt_2 \int d\phi_{436}^{\mathrm{R436}}}{\sqrt{\lambda(s_{36}, m_N^2, (p_1 - p_4 - p_5)^2)\lambda(s_{436}, m_N^2, t_{15})}} , \tag{A.27}$$

where the factor of 4 difference is due the fact that both ϕ_{36}^{R36} and $\phi_{436}^{\mathrm{R436}}$ go from 0 to 2π. In Eq. (C.109), we apply the latter case and replace the subscript "5" with ϕ in Eq. (A.27).

As a final remark of this appendix, in the derivation of the scatteing amplitude, one needs to define an additional Lorentz-invariant variable[5] $p_{56} \equiv p_5 \cdot p_6$ such that every scalar product of four-momenta can be written in terms of a combination of Lorentz-invariant variables [183]. Using the fact that, in a four-dimensional space-time, any five 4-vectors cannot be linearly independent, we can express p_{56} as a function of other Lorentz-invariant variables by solving $\det(M) = 0$, where the (i, j) entry of the 5×5 matrix M is $p_i \cdot p_j$ and $i, j = 1, \cdots, 5$. There are two solutions of p_{56} corresponding to $\phi_{36}^{\mathrm{R36}} \in [0, \pi)$ and $\phi_{36}^{\mathrm{R36}} \in [\pi, 2\pi)$. Other Lorentz-invariant variables are not affected by $\phi_{36}^{\mathrm{R36}} \to 2\pi - \phi_{36}^{\mathrm{R36}}$. For a pictorial demonstration, see Fig. 12 in [183].

B Appendix for Part I

B.1 Stellar Probes

B.1.1 Photons in a thermal medium

The processes depicted in Fig. 3.1 are fundamentally affected (or enabled) by the in-medium modified photon dispersion. Here we collect the central results that go into the computation of the energy loss rates (our convention largely follows [193]). The central quantity measuring the strength of the medium-effect is the plasma frequency ω_p, obtained through

$$\omega_p^2 = \frac{4\alpha}{\pi} \int_0^\infty dp \, \frac{p^2}{E} \left(1 - \frac{1}{3}v^2\right) \left(f_{e^-} + f_{e^+}\right) , \tag{B.28}$$

where $v = p/E$ is the velocity of electrons or positrons, and f_{e^-} and f_{e^+} are their respective Fermi-Dirac distributions, $f_{e^\pm} = [e^{(E \pm \mu_e)/T} + 1]^{-1}$.

Eq. (B.28) takes on the following analytic forms in the classical, degenerate and relativistic limit respectively,

$$\omega_p^2 \simeq \begin{cases} \dfrac{4\pi\alpha n_e}{m_e} \left(1 - \dfrac{5}{2}\dfrac{T}{m_e}\right) & \text{classical} \\ \dfrac{4\pi\alpha n_e}{E_F} = \dfrac{4\alpha}{3\pi} p_F^2 v_F & \text{degenerate} \\ \dfrac{4\alpha}{3\pi}\left(\mu_e^2 + \dfrac{1}{3}\pi^2 T^2\right) & \text{relativistic} \end{cases} , \tag{B.29}$$

[5] Here the choice of this additional Lorentz-invariant variable is not unique.

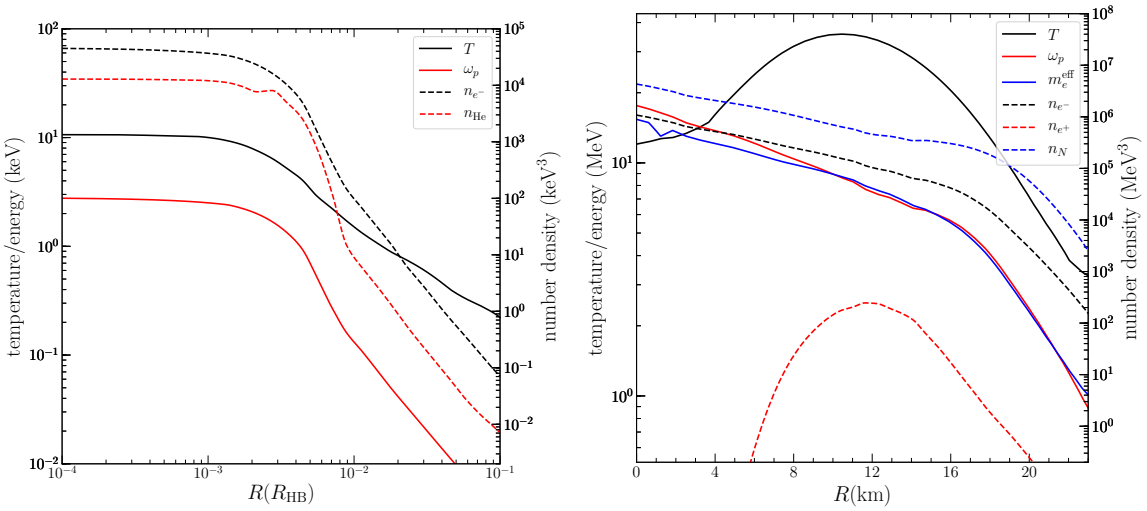

Figure B.3: Reproduced profiles of a representative $0.8M_\odot$ HB star [211] (left) and of a PNS of a $18M_\odot$ progenitor [213] (right) that are adopted in this thesis. In each panel, the left vertical axis corresponds to the values of temperature and plasma frequency (solid lines) at each radius, in units of keV (HB) or MeV (PNS), and the right vertical axis gives the number densities (dashed lines) of each particle species, in keV^3 (HB) or MeV^3 (PNS). For SN, the effective electron mass $m_e^{\rm eff}$ is also displayed.

where α is the fine-structure constant, n_e is the number density of electrons, $p_F = (3\pi^2 n_e)^{1/3}$ is the Fermi momentum, $E_F = \sqrt{m_e^2 + p_F^2}$ is the Fermi energy and $v_F = p_F/E_F$ is the Fermi velocity. Here "classical" refers to a non-relativistic ($T \ll m_e$) and non-degenerate ($T \gg \mu_e - m_e$) plasma.

The PNS core of a SN is both in a relativistic and degenerate regime and we find that the relativistic limit above yields a better fit to the general form of ω_p in Eq. (B.28) than the degenerate limit; the latter exhibits a 10% deviation. The core of a RG star is non-relativistic but degenerate whereas HB stars and the Sun are well described by the classical limit. In our numerical calculations, we adopt ω_p computed from Eq. (B.28), avoiding any ambiguities of taking limiting cases. Representative values of ω_p at the cores of all stellar objects are summarized as

$$\omega_p \sim \begin{cases} 0.3\,\text{keV} & \text{Sun's core} \\ 2.6\,\text{keV} & \text{HB's core} \\ 8.6\,\text{keV} & \text{RG's core} \\ 17.6\,\text{keV} & \text{SN's core} \end{cases} . \tag{B.30}$$

The computation of most of the processes requires the in-medium photon propagator. Picking Coulomb gauge, for a photon carrying 4-momentum $k = (\omega, \vec{k})$, the latter divides into

longitudinal (L) and transverse (T) parts [450]:

$$D_{00} = \frac{k^2}{|\vec{k}|^2(k^2 - \Pi_{\rm L})}\, g_{00}\,,$$
$$D_{ij} = \frac{1}{k^2 - \Pi_{\rm T}} \left(\delta_{ij} - \frac{k_i k_j}{|\vec{k}|^2}\right)\,, \tag{B.31}$$

where k_i is the Cartesian component of the photon three-momentum (magnitude $|\vec{k}|$). Using [450] and adopting the conventions of [171, 193], the real part of the polarization functions $\Pi_{\rm T,L}$ in the rest frame of the (isotropic) thermal bath reads

$$\mathrm{Re}\,\Pi_{\rm T} = \frac{3\omega^2}{2v_*^2|\vec{k}|^2}\omega_p^2 \left(1 - \frac{\omega^2 - v_*^2|\vec{k}|^2}{2\omega v_*|\vec{k}|} \ln\frac{\omega + v_*|\vec{k}|}{\omega - v_*|\vec{k}|}\right)\,,$$
$$\mathrm{Re}\,\Pi_{\rm L} = 3\omega_p^2 \left(\frac{\omega^2 - |\vec{k}|^2}{v_*^2|\vec{k}|^2}\right)\left(\frac{\omega}{2v_*|\vec{k}|}\ln\frac{\omega + v_*|\vec{k}|}{\omega - v_*|\vec{k}|} - 1\right)\,. \tag{B.32}$$

The full expressions for the dispersion relations $k^2 - \Pi_{\rm T,L} = 0$ then relate the energies of an on-shell photon, $\omega_{\rm T,L}$, to its momentum $\vec{k}$ to order α [450], via

$$\omega_{\rm T}^2 = |\vec{k}|^2 + \omega_p^2 \frac{3\omega_{\rm T}^2}{2v_*^2|\vec{k}|^2}\left(1 - \frac{\omega_{\rm T}^2 - v_*^2|\vec{k}|^2}{2\omega_{\rm T} v_*|\vec{k}|}\ln\frac{\omega_{\rm T} + v_*|\vec{k}|}{\omega_{\rm T} - v_*|\vec{k}|}\right)\,,$$
$$\omega_{\rm L}^2 = \omega_p^2 \frac{3\omega_{\rm L}^2}{v_*^2|\vec{k}|^2}\left(\frac{\omega_{\rm L}}{2v_*|\vec{k}|}\ln\frac{\omega_{\rm L} + v_*|\vec{k}|}{\omega_{\rm L} - v_*|\vec{k}|} - 1\right)\,. \tag{B.33}$$

Eq. (B.33) are also valid to order $|\vec{k}|^2$ at small $|\vec{k}|$ for all temperatures and electron number densities. Throughout the thesis, we always use $\omega_{\rm T,L}$, as functions of $|\vec{k}|$, to denote the energy of an on-shell thermal photon, which satisfies Eq. (B.33), and use ω for off-shell photons.

Longitudinal photons are populated up to a wavenumber $k_{\rm max}$, beyond which the longitudinal dispersion relation crosses the light cone and L-modes become damped, with

$$k_{\rm max} = \left[\frac{3}{v_*^2}\left(\frac{1}{2v_*}\ln\frac{1+v_*}{1-v_*} - 1\right)\right]^{1/2}\omega_p\,, \tag{B.34}$$

and in the relativistic limit $k_{\rm max} \to \infty$. In these equations, the mobility of charges is captured by the typical velocity of electrons, $v_* \equiv \omega_1/\omega_p$, where

$$\omega_1^2 = \frac{4\alpha}{\pi}\int_0^\infty dp\, \frac{p^2}{E}\left(\frac{5}{3}v^2 - v^4\right)\left(f_{e^-} + f_{e^+}\right)\,. \tag{B.35}$$

In the three limits mentioned previously, v_* can be approximated as

$$v_* \simeq \begin{cases} \sqrt{5T/m_e} & \text{classical} \\ v_F & \text{degenerate} \\ 1 & \text{relativistic} \end{cases}\,. \tag{B.36}$$

Finally, as alluded to in the main text, the processes we consider are non-resonant in the photon exchange and $\mathrm{Im}\,\Pi_{\mathrm{T,L}}$ can be neglected throughout.

In turn, the computation of in-medium photon decay, *i.e.*, process described by Eq. (3.5), requires the description of external in-medium photon states. For propagation in the z-direction, *i.e.*, $k_x = k_y = 0$, the transverse and longitudinal polarization vectors are given by

$$\epsilon^\mu_{\mathrm{T}} = (0, 1(0), 0(1), 0)\,, \quad \epsilon^\mu_{\mathrm{L}} = \frac{1}{\sqrt{\omega^2_{\mathrm{L}} - |\vec{k}|^2}}(|\vec{k}|, 0, 0, \omega_{\mathrm{L}})\,. \tag{B.37}$$

In all cases $\epsilon^\mu \epsilon_\mu = -1$ and $\epsilon^\mu k_\mu = 0$.

Furthermore, the in-medium coupling of the photon to the EM current is modified by the vertex renormalization constants $Z_{\mathrm{T,L}} \equiv (1 - \partial\Pi_{\mathrm{T,L}}/\partial\omega^2_{\mathrm{T,L}})^{-1}$. For the convention adopted here, they are equivalent to the ones given in [193],

$$\begin{aligned} Z_{\mathrm{T}} &= \frac{2\omega^2_{\mathrm{T}}(\omega^2_{\mathrm{T}} - v^2_*|\vec{k}|^2)}{3\omega^2_p\omega^2_{\mathrm{T}} + (\omega^2_{\mathrm{T}} + |\vec{k}|^2)(\omega^2_{\mathrm{T}} - v^2_*|\vec{k}|^2) - 2\omega^2_{\mathrm{T}}(\omega^2_{\mathrm{T}} - |\vec{k}|^2)}\,, \\ Z_{\mathrm{L}} &= \frac{2(\omega^2_{\mathrm{L}} - v^2_*|\vec{k}|^2)}{3\omega^2_p - (\omega^2_{\mathrm{L}} - v^2_*|\vec{k}|^2)}\frac{\omega^2_{\mathrm{L}}}{\omega^2_{\mathrm{L}} - |\vec{k}|^2}\,, \end{aligned} \tag{B.38}$$

These factors are attached to each zero-temperature vertex factor involving an external photon state. For internal photons, this effect is already accounted for in the momentum-dependent self-energy $\Pi_{\mathrm{T,L}}(\omega, \vec{k})$.

For thermal corrections to the electron mass which is relevant for PNS, we closely follow [451]. For an electron with a general 4-momentum $p = (E, \vec{p})$ in a neutral medium where the positron number density is negligible, we first introduce the four functions below:

$$A_e = \frac{-\alpha}{4\pi|\vec{p}|}\int_0^\infty dq\,\frac{q\,f_{e^-}(q)}{\sqrt{q^2 + m_e^2}}\left[4|\vec{p}|q - (p^2 + m_e^2)L_2\right]\,, \tag{B.39a}$$

$$C_e = \frac{\alpha m_e}{\pi|\vec{p}|}\int_0^\infty dq\,\frac{q\,f_{e^-}(q)}{\sqrt{q^2 + m_e^2}}\,(-L_2)\,, \tag{B.39b}$$

$$A_\gamma = \frac{-\alpha}{4\pi|\vec{p}|}\int_0^\infty dq\,f_\gamma(q)\left[8|\vec{p}|q + (p^2 + m_e^2)(L_3 - L_4)\right]\,, \tag{B.39c}$$

$$C_\gamma = \frac{\alpha m_e}{\pi|\vec{p}|}\int_0^\infty dq\,f_\gamma(q)\,(L_3 - L_4)\,, \tag{B.39d}$$

where q here is the absolute value of the 3-momentum of medium particles (electron, photon) that is integrated over and $L_{2,3,4}$ are functions of q in terms of

$$L_2(q) = \ln\left[\frac{2(E\sqrt{q^2 + m_e^2} + |\vec{p}|q) + p^2 + m_e^2}{2(E\sqrt{q^2 + m_e^2} - |\vec{p}|q) + p^2 + m_e^2}\right]\,, \tag{B.40a}$$

$$L_3(q) = \ln\left[\frac{2(Eq + |\vec{p}|q) + p^2 - m_e^2}{2(Eq - |\vec{p}|q) + p^2 - m_e^2}\right], \tag{B.40b}$$

$$L_4(q) = \ln\left[\frac{2(Eq + |\vec{p}|q) - p^2 + m_e^2}{2(Eq - |\vec{p}|q) - p^2 + m_e^2}\right]. \tag{B.40c}$$

Here m_e is the zero-temperature mass of electron, 0.511 MeV, while $f_\gamma(p)$ and $f_{e^-}(p)$ give the thermal momentum distribution functions of photon and electron (per degree of freedom). We have set $f_{e^+}(p) = 0$ in the above equations. In the end, we take the approximation made in [452] to obtain that

$$m_e^{\text{eff}}(p) = \sqrt{m_e^2 - 2(A_\gamma + A_e) - 2m_e(C_\gamma + C_e)}\,. \tag{B.41}$$

We have neglected thermal corrections to χ states. In the phenomenologically relevant regime, their coupling to the thermal bath is very weak.

Finally, we have reproduced the profiles of the HB star model from [211], and PNS model from [213], adopted in this thesis, as shown in Fig. B.3, where neutrality and $\mu_{e^-} + \mu_{e^+} = 0$ at each radius have been taken for granted for the PNS profile.

B.1.2 Full expression of χ-pair production rate

For any process that produces a $\chi\bar{\chi}$-pair through a photon propagator of 4-momentum $k = (\omega, \vec{k})$, its spin-summed squared matrix element can be written as

$$\sum_{\text{spins}} |\mathcal{M}|^2 = D_{\mu\nu}(k) D^*_{\rho\sigma}(k) \mathcal{T}^{\mu\rho}_{\text{SM}} \mathcal{T}^{\nu\sigma}_{\chi}\,, \tag{B.42}$$

where the in-medium photon propagator $D_{\mu\nu}$ is given by Eq. (B.31), while $\mathcal{T}^{\mu\rho}_{\text{SM}}$ and $\mathcal{T}^{\nu\sigma}_{\chi}$ represent the corresponding squared matrix elements of the SM current, *i.e.*, SM $\to \gamma^*(k)$ $(+\,\text{SM}')$, and the dark current, *i.e.*, $\gamma^*(k) \to \chi(p_\chi) + \bar{\chi}(p_{\bar{\chi}})$, of which the latter is given by Eq. (2.4). Generalizing Eq. (5.156) of [205] yields an expression for the exact $\chi\bar{\chi}$ differential production rate per volume:

$$\frac{d\dot{N}_\chi}{d^4k} = \frac{1}{(2\pi)^4} D_{\mu\nu}(k) D^*_{\rho\sigma}(k) \left(\frac{2\,\text{Im}\,\Pi^{\mu\rho}(k)}{e^{\omega/T} - 1}\right) I^{\nu\sigma}_\chi\,, \tag{B.43}$$

where $\text{Im}\,\Pi^{\mu\rho}$ is the imaginary part of the thermal photon self-energy induced by all possible SM currents. In the medium it is decomposed into longitudinal and transverse components, $\text{Im}\,\Pi_{\text{T,L}}$, as shown in Eq. (3.11) in the main text. The factor $I^{\nu\sigma}_\chi$ is the 2-body final state integrated over its phase space,

$$I^{\nu\sigma}_\chi = \int d\Pi_{i=\chi,\bar{\chi}}\, (2\pi)^4 \delta^4(k - p_\chi - p_{\bar{\chi}}) \mathcal{T}^{\nu\sigma}_\chi\,, \tag{B.44}$$

where $d\Pi_i = \prod_i d^3\vec{p}_i(2\pi)^{-3}(2E_i)^{-1}$, as mentioned in the main text. The integration can be executed in an arbitrary frame, and in particular in the rest frame of the thermal bath by adopting Lenard's formula [453], generalized to massive final states. We find

$$\int d\Pi_{i=\chi,\bar{\chi}}\,(2\pi)^4\delta^4(k-p_\chi-p_{\bar{\chi}})p_\chi^\mu p_{\bar{\chi}}^\nu = \frac{1}{96\pi}(Ak^2 g^{\mu\nu}+2Bk^\mu k^\nu)\,, \tag{B.45}$$

where the coefficients A and B are given by

$$A=\left(1-\frac{4m_\chi^2}{s_{\chi\bar{\chi}}}\right)^{3/2}\,,\quad B=\sqrt{1-\frac{4m_\chi^2}{s_{\chi\bar{\chi}}}}\left(1+\frac{2m_\chi^2}{s_{\chi\bar{\chi}}}\right)\,,$$

with $s_{\chi\bar{\chi}}=k^2$. In terms of the functions $f(s_{\chi\bar{\chi}})$ defined in Eq. (2.6), the factor $I_\chi^{\nu\sigma}$ is then explicitly given by

$$I_\chi^{\nu\sigma}=\frac{1}{8\pi}\sqrt{1-\frac{4m_\chi^2}{s_{\chi\bar{\chi}}}}f(s_{\chi\bar{\chi}})\left(-g^{\nu\sigma}+\frac{k^\nu k^\sigma}{s_{\chi\bar{\chi}}}\right)\,. \tag{B.46}$$

Putting all of the above together, we obtain the differential production rate per volume, Eq. (3.11), found in the main text, which we repeat here for convenience,

$$\frac{d\dot{N}_\chi}{d^4k}=\frac{1}{64\pi^5}\left[-\frac{2\,\mathrm{Im}\,\Pi_\mathrm{T}(k)}{|s_{\chi\bar{\chi}}-\Pi_\mathrm{T}|^2}-\frac{\mathrm{Im}\,\Pi_\mathrm{L}(k)}{|s_{\chi\bar{\chi}}-\Pi_\mathrm{L}|^2}\right]f_B(\omega)f(s_{\chi\bar{\chi}})\sqrt{1-\frac{4m_\chi^2}{s_{\chi\bar{\chi}}}}\,, \tag{B.47}$$

where $f_B(\omega)=(e^{\omega/T}-1)^{-1}$ is the Bose-Einstein momentum distribution of thermal bosons. During the derivation we have used that

$$-g^{\nu\sigma}+\frac{k^\nu k^\sigma}{s_{\chi\bar{\chi}}}=\epsilon_{\mathrm{T},1}^\nu\epsilon_{\mathrm{T},1}^\sigma+\epsilon_{\mathrm{T},2}^\nu\epsilon_{\mathrm{T},2}^\sigma+\epsilon_\mathrm{L}^\nu\epsilon_\mathrm{L}^\sigma\,.$$

B.1.3 Leading contributions to $\mathrm{Im}\,\Pi_{\mathrm{T,L}}$

We now demonstrate that Eq. (3.11) or, equivalently, Eq. (B.43) contain the leading production mechanisms considered in this paper. In particular we clarify the role of resonances, and that they are accounted for by the process $\gamma_{\mathrm{T,L}}\to\chi\bar{\chi}$. First, for the presence of an on-shell transverse/longitudinal photon, one needs to take the limit $\omega\to\omega_{\mathrm{T,L}}$ of the total production rate. Using the L'Hôpital's rule, we find

$$\lim_{\omega\to\omega_{\mathrm{T,L}}}\frac{1}{|s_{\chi\bar{\chi}}-\Pi_{\mathrm{T,L}}|^2}=\left.\frac{(1-\partial\Pi_{\mathrm{T,L}}/\partial\omega^2)^{-1}}{|\omega^2-|\vec{k}|^2-\Pi_{\mathrm{T,L}}|^2}\right|_{\omega=\omega_{\mathrm{T,L}}}=\frac{Z_{\mathrm{T,L}}}{|s_{\chi\bar{\chi}}-\Pi_{\mathrm{T,L}}|^2}\,, \tag{B.48}$$

with the vertex renormalization constants $Z_{\mathrm{T,L}}$ given in Eq. (B.38). Second, we isolate the pole contribution to the total production rate, *i.e.*, the case $s_{\chi\bar{\chi}}=\mathrm{Re}\,\Pi_{\mathrm{T,L}}$, and adopt the narrow width approximation:

$$\lim_{\mathrm{Im}\,\Pi_{\mathrm{T,L}}\to 0}\frac{-\,\mathrm{Im}\,\Pi_{\mathrm{T,L}}(k)}{\pi|s_{\chi\bar{\chi}}-\Pi_{\mathrm{T,L}}|^2}=\delta(s_{\chi\bar{\chi}}-\mathrm{Re}\,\Pi_{\mathrm{T,L}})\,, \tag{B.49}$$

where $\mathrm{Im}\,\Pi_{\mathrm{T,L}} < 0$. Then noting that $\mathrm{Re}\,\Pi_{\mathrm{T,L}}$ is also a function of $s_{\chi\bar{\chi}}$ and writing $d^4k = d^3\vec{k}\,ds_{\chi\bar{\chi}}/(2\omega)$ yields

$$\dot{N}_{\chi}^{\mathrm{T,L}} = g_{\mathrm{T,L}} \int \frac{d^3\vec{k}}{(2\pi)^3}\, f_B(\omega_{\mathrm{T,L}}) \left[\frac{Z_{\mathrm{T,L}} f(\mathrm{Re}\,\Pi_{\mathrm{T,L}})}{16\pi\omega_{\mathrm{T,L}}} \sqrt{1 - \frac{4m_\chi^2}{\mathrm{Re}\,\Pi_{\mathrm{T,L}}}} \right] , \tag{B.50}$$

where $g_{\mathrm{T}} = 2$ and $g_{\mathrm{L}} = 1$, counting the degrees of freedom of the photon modes. Now both $\omega_{\mathrm{T,L}}$ and $\mathrm{Re}\,\Pi_{\mathrm{T,L}}$ need to satisfy the photon dispersion relation with a 3-momentum $\vec{k}$ due to the δ-function above. As will be calculated below and given explicitly in Eq. (3.12), the term in the parentheses is exactly the decay rate of $\gamma_{\mathrm{T,L}}$ into χ-pairs.

In a next step, we further verify that the contribution of the one electron loop (OEL) to $\mathrm{Im}\,\Pi^{\mu\rho}$ induces the production rate of χ from electron-positron annihilation[6], process Eq. (3.6). In this case, it is easier to start with Eq. (B.43), where according to the in-medium optical theorem (see Fig. 3.2) we may write

$$2\,\mathrm{Im}\,\Pi^{\mu\rho}|_{\mathrm{OEL}} = \int d\Pi_{i=1,2}\, \mathcal{T}_e^{\mu\rho} (1 - f_{e^-} - f_{e^+}) (2\pi)^4 \delta^4(k - p_1 - p_2)\,, \tag{B.51}$$

where

$$\mathcal{T}_e^{\mu\rho} = \mathcal{M}^{\mu}_{\gamma^* \to e^+e^-} \mathcal{M}^{\rho}_{e^+e^- \to \gamma^*}\,,$$

and $f_{e^\mp}$ gives the momentum distribution function of $e^-(p_1)$, $e^+(p_2)$ per degree of freedom as defined above. Moreover, terms that are kinetically forbidden for $k^2 > 0$ have been neglected [202]. The presence of $(1 - f_{e^-} - f_{e^+})$ is due to quantum statistics, and would disappear for classical particles. Substituting this expression into Eq. (B.43) gives

$$\left.\frac{d\dot{N}_\chi}{d^4k}\right|_{\mathrm{OEL}} = \int d\Pi_{i=1,2,\chi,\bar{\chi}}\, |\mathcal{M}_{\mathrm{ann}}|^2 (1 - f_{e^-} - f_{e^+}) f_B(\omega) (2\pi)^4 \delta^4(k - p_1 - p_2) \delta^4(k - p_\chi - p_{\bar{\chi}})\,. \tag{B.52}$$

Then for the Fermi-Dirac distribution function $f_{e^\pm}$ and the Bose-Einstein distribution $f_B(\omega)$ with the energy conservation $E_1 + E_2 = \omega$, there exists the relation,

$$\left(\frac{f_{e^-}}{1 - f_{e^-}}\right) \left(\frac{f_{e^+}}{1 - f_{e^+}}\right) = \frac{f_B(\omega)}{1 + f_B(\omega)}\,, \tag{B.53}$$

allowing us to rewrite the number production rate per volume above as

$$\dot{N}_\chi\Big|_{\mathrm{OEL}} = \int d\Pi_{i=1,2,\chi,\bar{\chi}}\, |\mathcal{M}_{\mathrm{ann}}|^2 f_{e^-} f_{e^+} (2\pi)^4 \delta^4(p_1 + p_2 - p_\chi - p_{\bar{\chi}})\,. \tag{B.54}$$

after integrating over d^4k on both sides. The last expression transforms precisely to the corresponding energy loss rate Eq. (3.17), once both the energy-loss factor $(E_1 + E_2)$ and fermionic degrees of freedom $f_{e^\pm}$ are taken in account.

[6]The contribution of the two and three electron loops to $\mathrm{Im}\,\Pi^{\mu\rho}$ correspond to Compton scattering and bremsstrahlung, respectively.

B.1.4 $\gamma_{\rm T,L}$ decay to dark states

In the following appendices, we calculate the leading processes in the Feynman-diagrammatic approach using tree-level perturbation theory augmented by the thermal corrections outlined in App. B.1.1. The decay of a transverse or longitudinal photon of 4-momentum k to a pair of dark states $\bar{\chi}(p_{\bar{\chi}}) + \chi(p_\chi)$ is described by the spin-summed squared matrix element,

$$\sum_{\rm spins} |\mathcal{M}_{\rm T,L}|^2 = Z_{\rm T,L}\epsilon_\mu(k)\epsilon^*_\nu(k)\mathcal{T}^{\mu\nu}_\chi \,, \tag{B.55}$$

where $Z_{\rm T,L}$ is the vertex renormalization factor in Eq. (B.38), ϵ_μ is the photon polarization vector and $\mathcal{T}^{\mu\nu}_\chi$ is given in Eq. (2.4). The decay rate is given by the phase-space integral:

$$\Gamma_{\rm T,L} = \int d\Pi_{i=\chi,\bar{\chi}}\,(2\pi)^4\delta^4(k - p_\chi - p_{\bar{\chi}})\frac{1}{2\omega_{\rm T,L}}\sum_{\rm spins}|\mathcal{M}_{\rm T,L}|^2 \,, \tag{B.56}$$

where $\omega_{\rm T,L}$ is the energy of the external transverse or longitudinal photon. It is useful to employ Eq. (B.45). In terms of $I^{\nu\sigma}$ defined in Eq. (B.46), we can write the decay rate as

$$\Gamma_{\rm T,L} = \frac{1}{2\omega_{\rm T,L}} Z_{\rm T,L}\epsilon_\mu(k)\epsilon^*_\nu(k) I^{\mu\nu}_\chi . \tag{B.57}$$

The explicit expression, given by Eq. (3.12) in the main text, is then found by using the expressions in Eq. (B.37) for the polarization vectors when the initial state propagates in positive z-direction, *i.e.*, for $k^\mu = (\omega, 0, 0, k)$; note that the term proportional to $k^\mu k^\nu$ in $I^{\mu\nu}_\chi$ does not contribute due to the Ward identity.

B.1.5 e^-e^+ annihilation to dark states

Here we consider the process $e^-(p_1) + e^+(p_2) \to \chi(p_\chi) + \bar{\chi}(p_{\bar{\chi}})$. By setting $p_i = (E_i, \vec{p_i})$ and $k = p_1 + p_2$, one can define the cross sections[7] in terms of the squared matrix element for annihilation $|\mathcal{M}_{\rm ann}|^2$,

$$\begin{aligned}\sigma &= \int \frac{d\Pi_{i=\chi,\bar{\chi}}}{4E_1E_2v_M}\,(2\pi)^4\delta^4(k - p_\chi - p_{\bar{\chi}})\frac{1}{4}\sum_{\rm spins}|\mathcal{M}_{\rm ann}|^2 \\ &= \frac{\pi\alpha}{4E_1E_2v_M} D_{\mu\nu}D^*_{\rho\sigma}\mathcal{T}^{\mu\rho}_e I^{\nu\sigma}_\chi \,,\end{aligned} \tag{B.58}$$

where $\mathcal{T}^{\mu\rho}_e$ reads

$$\mathcal{T}^{\mu\rho}_e = -2\left(sg^{\mu\rho} - 2p_1^\mu p_2^\rho - 2p_1^\rho p_2^\mu\right) \,, \tag{B.59}$$

and $I^{\nu\sigma}_\chi$ is given in Eq. (B.46); here $s = k^2$. Furthermore, v_M is the Møller velocity defined as $v_M = F/(E_1E_2)$ and the flux factor F is given by

$$F = \left[(p_1\cdot p_2)^2 - m_e^4\right]^{1/2} = \frac{1}{2}\sqrt{s(s-4m_e^2)}\,. \tag{B.60}$$

[7] In the limit that $\Pi_{\rm T,L} \to 0$, it becomes the zero-temperature e^-e^+ annihilation cross section.

Contracting the Lorentz indices then yields

$$\sigma = \sigma_{\rm T} + \sigma_{\rm L}\,, \tag{B.61}$$

where the interference term vanishes in the Coulomb gauge, as can also be seen from Eq. (3.11), and the cross section for each polarization mode is given as Eq. (3.15) and Eq. (3.16) in the main text.

B.1.6 Compton production of dark states

In this appendix, we collect the ingredients for computing the energy loss from the process $e^- + \gamma_{\rm T,L} \to e^- + \chi + \bar{\chi}$. By separating out the χ-pair phase space element, the 2-to-3 cross section can be written in terms of the cross section of the process $e^-(p_1) + \gamma_{\rm T,L}(p_2) \to \gamma^*(p_3) + e^-(p_4)$ with γ^* being an off-shell photon with invariant mass $\sqrt{s_{\chi\bar{\chi}}}$; see Eq. (3.19). In the numerical calculation, we treat the transverse and longitudinal modes of the initial photon separately, as they are described by distinct dispersion relations and different polarization vectors. The finite-temperature effects are summarized in App. B.1.1. Note that here we neglect the thermal effect of γ^* to avoid the double counting with plasmon decay; see main text for explanation.

In terms of Lorentz-invariant variables $s = (p_1 + p_2)^2$ and $t = (p_1 - p_3)^2$, the 2-to-2 cross sections for T and L modes, before multiplied by the vertex renormalization factors (B.38), read

$$\begin{aligned}
\sigma^{\rm T}_{2\to2} = {}& \frac{\pi\alpha^2}{(m_e^2-s)^2\left[m_\gamma^4 - 2m_\gamma^2(m_e^2+s) + (m_e^2-s)^2\right]^2}\Big\{t^2(s-m_e^2)\left[m_\gamma^4 - 2m_\gamma^2 m_e^2 + (m_e^2-s)^2\right] \\
& - 2t\Big\{m_\gamma^6(2s+s_{\chi\bar{\chi}}) + m_\gamma^4\left[m_e^4 - m_e^2(7s+4s_{\chi\bar{\chi}}) - 2s^2\right] + m_\gamma^2(m_e^2-s)\left[m_e^2(2s+3s_{\chi\bar{\chi}}) - 3ss_{\chi\bar{\chi}}\right] \\
& - (m_e^2-s)^2(m_e^4 - 5m_e^2 s - 2ss_{\chi\bar{\chi}})\Big\} - \frac{2(m_e^2-s)^2(2m_e^2+s_{\chi\bar{\chi}})}{m_e^2-t}\Big\{m_\gamma^6 - 2m_\gamma^4(m_e^2+s-s_{\chi\bar{\chi}}) \\
& + m_\gamma^2\left[-2s_{\chi\bar{\chi}}(3m_e^2+s) + (m_e^2-s)^2 + 2s_{\chi\bar{\chi}}^2\right] + 2(m_e^3-m_e s)^2\Big\} + 2(m_e^2-s)\ln(m_e^2-t)\Big\{2m_\gamma^8 \\
& + m_\gamma^6\left[4s_{\chi\bar{\chi}} - 6(m_e^2+s)\right] + m_\gamma^4\left[7m_e^4 + 2m_e^2(s-5s_{\chi\bar{\chi}}) + 7s^2 - 6ss_{\chi\bar{\chi}} + 2s_{\chi\bar{\chi}}^2\right] \\
& + 2m_\gamma^2(m_e^2-s)(m_e^4 - 3m_e^2 s + 2s^2 - 2ss_{\chi\bar{\chi}} - s_{\chi\bar{\chi}}) \\
& - (m_e^2-s)^2\left[3m_e^4 + m_e^2(6s-2s_{\chi\bar{\chi}}) - s^2 + 2ss_{\chi\bar{\chi}} - 2s_{\chi\bar{\chi}}^2\right]\Big\}\Big\}\Big|_{t=t^+-t^-}\,,
\end{aligned} \tag{B.62}$$

$$\begin{aligned}
\sigma^{\rm L}_{2\to2} = {}& \frac{8m_\gamma^2\pi\alpha^2}{(m_e^2-s)^2\left[m_\gamma^4 - 2m_\gamma^2(m_e^2+s) + (m_e^2-s)^2\right]^2}\Big\{-\frac{s(s-m_e^2)t^2}{2} \\
& + \frac{(m_e^2-s)^2(2m_e^2+s_{\chi\bar{\chi}})\left[(2m_e^2-s_{\chi\bar{\chi}})(m_e^2+s-s_{\chi\bar{\chi}}) + m_\gamma^2(-m_e^2+s_{\chi\bar{\chi}})\right]}{m_e^2-t}
\end{aligned}$$

$$
\begin{aligned}
&+ t\Big\{ - m_e^6 + 6m_e^2 s^2 - s^2(s - 3s_{\chi\bar{\chi}}) + m_e^4(4s + s_{\chi\bar{\chi}}) + m_\gamma^2 \left[m_e^4 + s^2 - m_e^2(4s + s_{\chi\bar{\chi}}) \right] \Big\} \\
&- (m_e^2 - s)\ln(m_e^2 - t)\Big\{ m_e^2 \left[2m_\gamma^4 - 6m_\gamma^2(m_e^2 + s) + (3m_e^2 + s)(m_e^2 + 3s) \right] \\
&+ 2(m_\gamma^2 - s)(m_e^2 - s)s_{\chi\bar{\chi}} - (m_e^2 + 3s)s_{\chi\bar{\chi}}^2 \Big\} \Big\} \Big|_{t=t^+-t^-} ,
\end{aligned} \tag{B.63}
$$

where m_γ is the thermal mass of initial $\gamma_{\mathrm{T,L}}$. In the zero-temperature limit ($m_\gamma \to 0$), one finds $\sigma^{\mathrm{L}}_{2\to2} = 0$ as expected.

The boundaries for t are

$$
\begin{aligned}
[t]^\pm = m_e^2 + s_{\chi\bar{\chi}} - \frac{(-m_\gamma^2 + m_e^2 + s)(-m_e^2 + s + s_{\chi\bar{\chi}})}{2s} \\
\pm \frac{\sqrt{[m_\gamma^4 - 2m_\gamma^2(m_e^2 + s) + (m_e^2 - s)^2][m_e^4 - 2m_e^2(s + s_{\chi\bar{\chi}}) + (s - s_{\chi\bar{\chi}})^2]}}{2s} ,
\end{aligned}
$$

while $4m_\chi^2 \le s_{\chi\bar{\chi}} \le (\sqrt{s} - m_e)^2$. When computing the energy loss rate (3.20), we integrate with the medium-frame variables $|\vec{p}_1| = [0, \infty]$, $|\vec{p}_2| = [0, \infty]$ and s, with

$$
[s]^\pm = m_e^2 + m_\gamma^2 + 2\sqrt{|\vec{p}_1|^2 + m_e^2}\sqrt{|\vec{p}_2|^2 + m_\gamma^2} \pm 2|\vec{p}_1||\vec{p}_2| .
$$

The energy loss E_{loss} carried by χ-pair in the medium frame reads

$$
E_{\mathrm{loss}} = \frac{s_{\chi\bar{\chi}} - m_e^2 + s}{2\sqrt{s}} . \tag{B.64}
$$

B.1.7 eN bremsstrahlung production of dark states

The $2 \to 3$ amplitude squared $|\mathcal{M}_{2\to3}|^2$ can be split into three parts as

$$
\sum_{\mathrm{spins}} \frac{|\mathcal{M}_{2\to3}|^2}{(4\pi\alpha)^2 g_1 g_2} = D^{\rho\beta}(q) D^{\sigma\gamma *}(q) W_{\rho\sigma} L^{\mu\nu}_{\beta\gamma} \epsilon^*_\mu(k) \epsilon_\nu(k) , \tag{B.65}
$$

where $q = p_2 - p_4$ is the momentum transfer between the initial states, $L^{\mu\nu}_{\beta\gamma}$ stands for the leptonic part, $W_{\rho\sigma}$ is the hadronic tensor and $\epsilon_\nu(k)$ is the polarization vector of the emitted photon of virtual squared mass $s_{\chi\bar{\chi}} = k^2$. Detailed forms for $L^{\mu\nu}_{\beta\gamma}$ and $W_{\rho\sigma}$ are given in the App. A in [183].

The $2 \to 3$ cross section reads

$$
\sigma_{2\to3} = \frac{1}{4 g_1 g_2 E_1 E_2 v_M} \int d\Pi_{i=3,4,k} \sum_{\mathrm{spins}} |\mathcal{M}_{2\to3}|^2 , \tag{B.66}
$$

where v_M is the Møller velocity, as defined in the main text. The phase space integrations, when written in terms of Lorentz-invariant variables reads

$$
\sigma_{2\to3} = \frac{1}{32(2\pi)^4 E_1 E_2 v_M} \frac{1}{\sqrt{\lambda(s, m_e^2, m_N^2)}} \int ds_4 \int dt_1 \frac{1}{\sqrt{\lambda(s_4, m_N^2, t_1)}} \int dt_2 \int dp_{1k} \left| \frac{\partial \phi^{\mathrm{R4k}}_{4k}}{\partial p_{1k}} \right|
$$

$$\times \frac{1}{g_1 g_2} \sum_{\text{spins}} |\mathcal{M}_{2\to 3}|^2 \,, \tag{B.67}$$

see App. A.2 for the derivation of the phase space integral.

The integration boundaries of s_4 are given by

$$(m_N + \sqrt{s_{\chi\bar{\chi}}})^2 \leq s_4 \leq (\sqrt{s} - m_e)^2 \,,$$

and the boundaries of t_1 and t_2 are given by

$$[t_1]^{\pm} = 2m_e^2 - \frac{1}{2s}\left[(s + m_e^2 - m_N^2)(s + m_e^2 - s_4) \mp \sqrt{\lambda(s, m_e^2, m_N^2)\lambda(s, m_e^2, s_4)}\right] \,,$$
$$[t_2]^{\pm} = 2m_N^2 - \frac{1}{2s_4}\left[(s_4 + m_N^2 - t_1)(s_4 + m_N^2 - s_{\chi\bar{\chi}}) \mp \sqrt{\lambda(s_4, m_N^2, t_1)\lambda(s_4, m_N^2, s_{\chi\bar{\chi}})}\right] \,.$$

The physical region for p_{1k} reads

$$[p_{1k}]^{\pm} = \frac{(p_2 \cdot p_1)G_2(p_2, q_1; q_1, k) - (q_1 \cdot p_1)G_2(p_2, q_1; p_2, k) \pm \sqrt{\Delta_3(p_2, q_1, p_1)\Delta_3(p_2, q_1, k)}}{-\Delta_2(p_2, \sqrt{t_1})} \,.$$

Putting everything together, the full $2 \to 4$ cross section is given by

$$\sigma_{2\to 4} = \int ds_{\chi\bar{\chi}}\, \sigma_{2\to 3}(s_{\chi\bar{\chi}}) \frac{f(s_{\chi\bar{\chi}})}{16\pi^2 s_{\chi\bar{\chi}}^2} \sqrt{1 - \frac{4m_\chi^2}{s_{\chi\bar{\chi}}}} \,. \tag{B.68}$$

The integration boundaries of $s_{\chi\bar{\chi}}$ are given by

$$4m_\chi^2 \leq s_{\chi\bar{\chi}} \leq (\sqrt{s} - m_e - m_N)^2 \,.$$

The energy loss per bremsstrahlung process in terms of Lorentz-invariant variables reads

$$E_{\text{loss}} = \frac{t_2 - t_1 + s_4 - m_N^2}{2m_N} \,. \tag{B.69}$$

B.1.8 Soft-photon approximation for bremsstrahlung

Here we discuss the soft-photon approximation for bremsstrahlung, its regime of validity and explain where it fails in calculating the $2 \to 4$ cross section. In the soft limit, that is, if the emitted photon energy is small compared to the available kinetic energy $\omega \ll E_{\text{kin}}$, the $2 \to 3$ cross section can be factorized into an elastic scattering and an emission part[8],

$$d\sigma_{2\to 3}^{\text{soft}} = d\sigma_{2\to 2} \int \frac{d^3k}{(2\pi)^3 2\omega} 4\pi\alpha \left| \frac{p_3 \cdot \epsilon^*}{p_3 \cdot k} - \frac{p_1 \cdot \epsilon^*}{p_1 \cdot k} \right|^2 \,, \tag{B.70}$$

[8] The emission part here describes the emission off one of the particles. If both particles can emit photons, the emission part has to be adjusted correspondingly.

where $\omega^2 = |\vec{k}|^2 + s_{\chi\bar{\chi}}$ and ϵ_μ is the polarization vector of the emitted photon. In this approximation, a simple form of the differential $2 \to 3$ cross section can be obtained in the non-relativistic and ultra-relativistic limit respectively [454],

$$\omega \frac{d\sigma^{\text{soft}}_{2\to3}}{d\omega} = \begin{cases} \dfrac{16}{3}\dfrac{\alpha^3}{\mu^2 v^2} \ln\left[\dfrac{1+\sqrt{1-\omega/E_{\text{kin}}}}{1-\sqrt{1-\omega/E_{\text{kin}}}}\right], \\ \dfrac{4\alpha^3}{\mu^2}\dfrac{E'}{E}\left(\dfrac{E}{E'}+\dfrac{E'}{E}-\dfrac{2}{3}\right)\left(\ln\dfrac{E^2E'}{\mu^2\omega}-\dfrac{1}{2}\right), \end{cases} \tag{B.71}$$

where μ is the reduced mass, v is the relative velocity and E (E') is the initial (final) total CM energy of the colliding particles. Even though in deriving the expression in Eq. (B.71) we have assumed $\sqrt{s_{\chi\bar{\chi}}} \ll E_{\text{kin}}$ and $\omega \ll E_{\text{kin}}$, integrating Eq. (B.71) over ω in the region $\sqrt{s_{\chi\bar{\chi}}} < \omega < E_{\text{kin}}$ still gives a very good approximation to the full cross section. Obviously, the approximation breaks down if $\sqrt{s_{\chi\bar{\chi}}} \sim E_{\text{kin}}$ where the integration region of ω gets very small and the integral is dominated by large emission energies.

To obtain the $2 \to 4$ cross section from the $2 \to 3$ cross section in Eq. (3.21), $\sigma^{\text{soft}}_{2\to3}$ gets multiplied by the factors in Eq. (2.6) corresponding to the EM form factor interactions. This leads to the following parametric dependence on $s_{\chi\bar{\chi}}$:

$$d\sigma^{\text{soft}}_{2\to4} \propto \begin{cases} d\sigma^{\text{soft}}_{2\to3}\, ds_{\chi\bar{\chi}}/s_{\chi\bar{\chi}} & \text{(mass-dimension 4)}, \\ d\sigma^{\text{soft}}_{2\to3}\, ds_{\chi\bar{\chi}} & \text{(mass-dimension 5)}, \\ d\sigma^{\text{soft}}_{2\to3}\, ds_{\chi\bar{\chi}}\, s_{\chi\bar{\chi}} & \text{(mass-dimension 6)}, \end{cases} \tag{B.72}$$

that is, for mass-dimension 4 operators, like millicharged states, the $2 \to 4$ cross section is dominated by small $s_{\chi\bar{\chi}}$, whereas for higher dimensional operators, the expression is UV-biased. Hence, the main contribution to the integral comes from $s_{\chi\bar{\chi}}$-values for which the soft approximation breaks down as one probes the kinematic endpoint region. It turns out that in the non-relativistic regime and for $m_\chi + m_{\bar{\chi}} \ll E_{\text{kin}}$, using Eq. (B.71) reproduces the exact $2 \to 4$ cross section up to a factor 2 or 3. However, for relativistic particles, the error at $\sqrt{s_{\chi\bar{\chi}}} \sim E_{\text{kin}}$ gets larger. Due to the $s_{\chi\bar{\chi}}$-dependence in Eq. (B.72), this still results in a decent description of millicharged $\chi\bar{\chi}$-emission, but produces errors of several orders of magnitude in the relativistic regime for the mass-dimension 5 and 6 EM form factors.

Equation (B.70) can be further simplified by separating the phase space. This is possible, if the elastic scattering cross section is insensitive to an angular cut-off in the forward or backward direction, *e.g.*, if the interaction is mediated by a massive particle such as the pion in np scattering[9]. Then,

$$\sigma^{\text{soft}}_{2\to3} = \sigma^{\text{t}}_{2\to2}\, \mathcal{I}(s_{\chi\bar{\chi}}), \tag{B.73}$$

[9]For ep scattering, on the other hand, the phase space separation is not possible, since the elastic cross section is forward divergent. In these cases, 3-body kinematics is required.

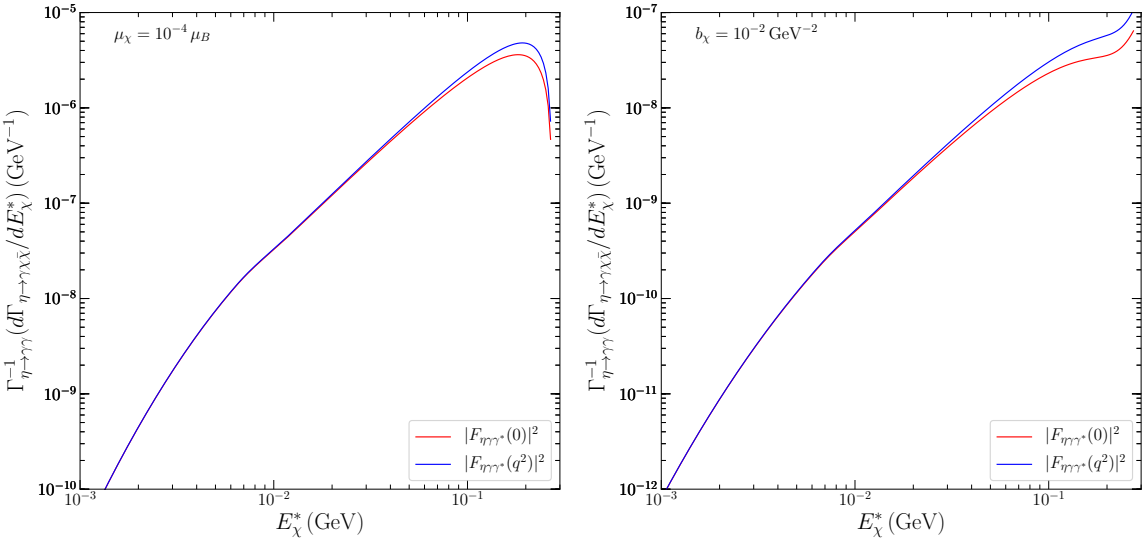

Figure B.4: Comparison of differential decay rate of η meson into dark states without (red) or with (blue) meson transition form factor for MDM (left) and CR (right) with $m_\chi = 1\,\mathrm{MeV}$. The decay rates are normalized with $\Gamma^{-1}_{\eta\to\gamma\gamma}$.

where $\sigma^{\mathrm{t}}_{2\to2}$ is the transport cross section,

$$\sigma^{\mathrm{t}}_{2\to2} = \int_{-1}^{1} d\cos\theta\, \frac{d\sigma_{2\to2}}{d\cos\theta}(1-\cos\theta)\,,$$

and the emission piece $\mathcal{I}(s_{\chi\bar{\chi}})$ is obtained by executing the integral in Eq. (B.70),

$$\begin{aligned}\mathcal{I}(s_{\chi\bar{\chi}}) &= \frac{1}{1-\cos\theta}\int \frac{d^3k}{(2\pi)^3 2\omega}\,4\pi\alpha\left|\frac{p_3\cdot\epsilon^*}{p_3\cdot k}-\frac{p_1\cdot\epsilon^*}{p_1\cdot k}\right|^2 \\ &= \frac{\alpha}{3\pi}\int_{\sqrt{s_{\chi\bar{\chi}}}}^{E_{\mathrm{kin}}} d\omega\,\frac{\sqrt{\omega^2-s_{\chi\bar{\chi}}}\left(s_{\chi\bar{\chi}}/2+\omega^2\right)}{\omega^4}\,. \end{aligned} \tag{B.74}$$

In the first line, we have divided by $(1-\cos\theta)$ to cancel the θ-dependent part in the emission piece, which we have absorbed into the transport cross section.

B.2 Proton-beam Experiments

B.2.1 Decay rates of scalar mesons

The decay rate of scalar mesons into a photon plus a χ-pair, $\Gamma_\chi \equiv \Gamma_{\mathrm{sm}\to\gamma\chi\bar{\chi}}$, is given by

$$\Gamma_\chi = \int_{4m_\chi^2}^{m_{\mathrm{sm}}^2} ds_{\chi\bar{\chi}}\,\Gamma_{\mathrm{sm}\to\gamma\gamma^*}(s_{\chi\bar{\chi}})\,\frac{f(s_{\chi\bar{\chi}})}{16\pi^2 s^2_{\chi\bar{\chi}}}\sqrt{1-\frac{4m_\chi^2}{s_{\chi\bar{\chi}}}}\,, \tag{B.75}$$

where $\Gamma_{\mathrm{sm}\to\gamma\gamma^*}$ is the decay rate with an off-shell photon,

$$\Gamma_{\mathrm{sm}\to\gamma\gamma^*}(s_{\chi\bar{\chi}}) = \frac{\alpha^2(m_{\mathrm{sm}}^2 - s_{\chi\bar{\chi}})^3}{32\pi^3 m_{\mathrm{sm}}^3 F_{\mathrm{sm}}^2}\,, \tag{B.76}$$

with F_{sm} being the decay constant of the meson. Since we are allowed to neglect the momentum-dependence of the EM transition form factors of the scalar mesons (shown below), F_{sm} will drop out in the branching ratio, Eq. (4.2). The explicit expressions of $f(s_{\chi\bar{\chi}})$ for various EM form factor interactions are given in Eq. (2.6). Analogously, the expression for $f_e(m_{\mathrm{vm}}^2)$, used for vector meson decay in Sec. 4.2.2, is given by

$$f_e(m_{\mathrm{vm}}^2) = \frac{16\pi\alpha}{3} m_{\mathrm{vm}}^2 \left(1 + \frac{2m_e^2}{m_{\mathrm{vm}}^2}\right). \tag{B.77}$$

To infer the energy spectrum of χ from scalar meson decay, we also need to know the differential decay rate $d\Gamma_\chi/dE_\chi^*$ in the rest frame of the meson ($\vec{p}_1 = 0$). To this end, we first compute the amplitude of the process $\mathrm{sm}(p_1) \to \gamma(p_2) + \chi(p_3) + \bar{\chi}(p_4)$ and define the two Lorentz-invariant variables $s_{23} = (p_2 + p_3)^2$ and $s_{42} = (p_4 + p_2)^2$, so that $s_{\chi\bar{\chi}}$ becomes $s_{\chi\bar{\chi}} = m_{\mathrm{sm}}^2 + 2m_\chi^2 - s_{23} - s_{42}$. The corresponding squared amplitudes, summed over the spin of final states for each EM form factor are obtained as follows:

$$\begin{aligned}\text{mQ:}\ \sum_{\text{spins}} |\mathcal{M}|^2 = {}& \frac{4\alpha^3\epsilon^2}{\pi F_{\mathrm{sm}}^2 (2m_\chi^2 + m_{\mathrm{sm}}^2 - s_{23} - s_{42})^2} \times \Big\{12m_\chi^6 + 2m_\chi^4\left[m_{\mathrm{sm}}^2 - 7(s_{23}+s_{42})\right] \\ & + m_\chi^2\left[-2m_{\mathrm{sm}}^2(s_{23}+s_{42}) + 6s_{23}^2 + 8s_{23}s_{42} + 6s_{42}^2\right] + (s_{23}^2 + s_{42}^2)(m_{\mathrm{sm}}^2 - s_{23} - s_{42})\Big\}\,,\end{aligned} \tag{B.78a}$$

$$\begin{aligned}\text{MDM:}\ \sum_{\text{spins}} |\mathcal{M}|^2 = {}& \frac{2\alpha^2\mu_\chi^2}{\pi^2 F_{\mathrm{sm}}^2 (2m_\chi^2 + m_{\mathrm{sm}}^2 - s_{23} - s_{42})} \times \Big\{6m_\chi^6 + m_\chi^4\left[m_{\mathrm{sm}}^2 - 7(s_{23}+s_{42})\right] \\ & + m_\chi^2\left[2(s_{23}^2 + 3s_{23}s_{42} + s_{42}^2) - m_{\mathrm{sm}}^2(s_{23}+s_{42})\right] - s_{23}s_{42}(-m_{\mathrm{sm}}^2 + s_{23} + s_{42})\Big\}\,,\end{aligned} \tag{B.78b}$$

$$\begin{aligned}\text{EDM:}\ \sum_{\text{spins}} |\mathcal{M}|^2 = {}& \frac{-2\alpha^2 d_\chi^2}{\pi^2 F_{\mathrm{sm}}^2 (2m_\chi^2 + m_{\mathrm{sm}}^2 - s_{23} - s_{42})} \times \Big\{2m_\chi^6 - m_\chi^4(m_{\mathrm{sm}}^2 + s_{23} + s_{42}) \\ & + m_\chi^2\left[m_{\mathrm{sm}}^2(s_{23}+s_{42}) - 2s_{23}s_{42}\right] + s_{23}s_{42}(-m_{\mathrm{sm}}^2 + s_{23} + s_{42})\Big\}\,,\end{aligned} \tag{B.78c}$$

$$\begin{aligned}\text{AM:}\ \sum_{\text{spins}} |\mathcal{M}|^2 = {}& \frac{-\alpha^2 a_\chi^2}{\pi^2 F_{\mathrm{sm}}^2} \times \Big\{4m_\chi^6 - 2m_\chi^4(m_{\mathrm{sm}}^2 + s_{23} + s_{42}) \\ & + 2m_\chi^2\left[m_{\mathrm{sm}}^2(s_{23}+s_{42}) - s_{23}^2 - s_{42}^2\right] - (s_{23}^2 + s_{42}^2)(m_{\mathrm{sm}}^2 - s_{23} - s_{42})\Big\}\,,\end{aligned} \tag{B.78d}$$

$$\text{CR:}\ \sum_{\text{spins}} |\mathcal{M}|^2 = \frac{\alpha^2 b_\chi^2}{\pi^2 F_{\mathrm{sm}}^2} \times \Big\{12m_\chi^6 + 2m_\chi^4\left[m_{\mathrm{sm}}^2 - 7(s_{23}+s_{42})\right]$$

$$-m_\chi^2\left[2m_{\rm sm}^2(s_{23}+s_{42})-6s_{23}^2-8s_{23}s_{42}-6s_{42}^2\right]+(s_{23}^2+s_{42}^2)(m_{\rm sm}^2-s_{23}-s_{42})\Big\}\,. \tag{B.78e}$$

Then the Dalitz plot (see Fig. A.2) allows us to express the differential decay rate in the rest frame of the meson as

$$\frac{d\Gamma_\chi}{dE_\chi^*}=\frac{1}{128\pi^3 m_{\rm sm}^2}\int ds_{23}\sum_{\rm spins}|\mathcal{M}|^2\,, \tag{B.79}$$

where the integration boundaries of s_{23} are given by

$$\begin{aligned}[s_{23}]^\pm=\frac{1}{2s_{42}}\Big[&(m_\chi^2-s_{42})(m_\chi^2-m_{\rm sm}^2+s_{42})+2m_\chi^2 s_{42}\\ &\mp(m_\chi^2-s_{42})\sqrt{m_\chi^4-2m_\chi^2(m_{\rm sm}^2+s_{42})+(m_{\rm sm}^2-s_{42})^2}\Big]\,.\end{aligned} \tag{B.80}$$

Here, s_{42} is

$$s_{42}=m_\chi^2+m_{\rm sm}^2-2E_\chi^* m_{\rm sm}\,. \tag{B.81}$$

The allowed kinematic range of E_χ^* is $m_\chi\le E_\chi^*\le m_{\rm sm}/2$. At last we arrive at the differential branching ratio via

$$\frac{d{\rm Br}_\chi}{dE_\chi^*}={\rm Br}_{{\rm sm}\to\gamma\gamma}\times\frac{1}{\Gamma_{{\rm sm}\to\gamma\gamma}}\frac{d\Gamma_\chi}{dE_\chi^*}\,, \tag{B.82}$$

from which one can directly see that the meson decay constant, $F_{\rm sm}$, cancels out in the ratio of Γ_χ and $\Gamma_{{\rm sm}\to\gamma\gamma}$.

At the end of this section, we comment on the assumption of using constant transition form factors for scalar meson decay. Vector meson dominance suggests that the assumption holds well for $m_{\rm sm}^2\ll m_\rho^2$, which is the case for π^0 decays. For the heavier scalar mesons considered in this work, η/η', we have numerically evaluated the differential decay rate using the EM transition form factor. For the η meson [455], the results are given in Fig. B.4, which shows that the shape of $d{\rm Br}_\chi/dE_\chi^*$ is only affected mildly by the (kinematically limited) virtuality of the intermediate photon. In the total decay rate for $m_\chi=1\,(100)\,{\rm MeV}$, ${\rm Br}_\chi$ would increase by a factor of 1.3 (1.7) in the case of MDM/EDM, and by a factor of 1.8 (1.9) in the case of AM/CR. Hence, neglecting the momentum-dependence of the transition form factors leads to slightly weaker bounds, and is hence conservative.

B.2.2 χ distribution from meson decay

In this section, the derivation of Eq. (4.4) is provided. In general, the number of χ particles produced from a certain meson distribution is given by

$$N_\chi=\int dE_m\,d\cos\theta_m\,\frac{d^2N_m}{dE_m\,d\cos\theta_m}\times 2{\rm Br}_\chi$$

$$= \int dE_m \, d\cos\theta_m \, \frac{d^2 N_m}{dE_m \, d\cos\theta_m} \times \int dE_\chi^* \, d\cos\theta^* d\phi^* \, \frac{d^3 \hat{N}_\chi}{dE_\chi^* \, d\cos\theta^* d\phi^*} \,, \tag{B.83}$$

where E_m and θ_m are the energy of meson and angle between the meson momentum and the beam axis in the lab frame, respectively. The energy of χ in the rest frame of the meson is denoted by E_χ^*. Finally, θ^*, ϕ^* are the polar and azimuthal angles of the χ momentum in the rest frame of the meson with respect to the lab-frame meson momentum.

In practice, we are interested in the distribution of χ particles in terms of E_χ and θ_χ, which are the energy of χ and the polar angle of the χ momentum with respect to the beam axis in the lab frame. A Lorentz transformation allows to express the last quantities as functions of E_m, $\cos\theta_m$, E_χ^*, $\cos\theta^*$ and ϕ^*. Then, by inserting the two delta-functions,

$$\int dE_\chi \, \delta\left[E_\chi - E_\chi(E_m, \cos\theta_m, E_\chi^*, \cos\theta^*, \phi^*)\right] = 1 \,,$$
$$\int d\cos\theta_\chi \, \delta\left[\cos\theta_\chi - \cos\theta_\chi(E_m, \cos\theta_m, E_\chi^*, \cos\theta^*, \phi^*)\right] = 1 \,,$$

into Eq. (B.83) and using the fact that the decay is isotropic in the meson rest frame, we arrive at

$$N_\chi = \int \frac{d\cos\theta^* d\phi^*}{4\pi} dE_\chi^* \, dE_m \, d\cos\theta_m \, dE_\chi \, d\cos\theta_\chi \, \frac{d\hat{N}_\chi}{dE_\chi^*} \frac{d^2 N_m}{dE_m \, d\cos\theta_m}$$
$$\times \, \delta\left[E_\chi - E_\chi(E_m, \cos\theta_m, E_\chi^*, \cos\theta^*, \phi^*)\right] \delta\left[\cos\theta_\chi - \cos\theta_\chi(E_m, \cos\theta_m, E_\chi^*, \cos\theta^*, \phi^*)\right] \,. \tag{B.84}$$

Next we use the two delta functions to perform the integrals over E_m and θ_m leading to

$$N_\chi = \int \frac{d\cos\theta^* d\phi^*}{4\pi} dE_\chi^* \, dE_\chi \, d\cos\theta_\chi \times \frac{d\hat{N}_\chi}{dE_\chi^*} \, \frac{d^2 N_m}{dE_m \, d\cos\theta_m} \left| \frac{\partial(E_m, \cos\theta_m)}{\partial(E_\chi, \cos\theta_\chi)} \right| \,. \tag{B.85}$$

where the last factor $|\partial(\dots)/\partial(\dots)|$ is the Jacobian of the variable transformation. In the end, the distribution function of χ particles from meson decay in the lab frame in terms of E_χ and θ_χ reads

$$\frac{d^2 N_\chi}{dE_\chi d\cos\theta_\chi} = \int \frac{d\cos\theta^* d\phi^*}{4\pi} dE_\chi^* \, \frac{d\hat{N}_\chi}{dE_\chi^*} \times \frac{d^2 N_m}{dE_m \, d\cos\theta_m} \left| \frac{\partial(E_m, \cos\theta_m)}{\partial(E_\chi, \cos\theta_\chi)} \right| \,, \tag{B.86}$$

Summing up the contribution from each meson, we retrieve Eq. (4.4) of the main text.

B.2.3 $L_{\mu\nu} W^{\mu\nu}$ in DIS cross section

The DIS differential cross section, given in Eq. (4.10), contains the contraction of dark and hadronic matrix element $L_{\mu\nu} W^{\mu\nu}$. In the following we list $L_{\mu\nu} W^{\mu\nu}$ for each EM form factor interaction:

$$\text{mQ: } L_{\mu\nu} W^{\mu\nu} = 4\pi\alpha\epsilon^2 \left\{ 2F_1(Q^2 - 2m_\chi^2) - \frac{m_N F_2}{\nu} \left[4E_\chi(\nu - E_\chi) + Q^2 \right] \right\} \,, \tag{B.87a}$$

$$\text{MDM: } L_{\mu\nu}W^{\mu\nu} = \mu_\chi^2\Bigg\{Q^2F_1(8m_\chi^2 - Q^2) + \frac{m_N F_2}{\nu}\left[4E_\chi^2Q^2 - 4E_\chi\nu Q^2 - 4m_\chi^2(\nu^2+Q^2) + \nu^2Q^2\right]\Bigg\}, \tag{B.87b}$$

$$\text{EDM: } L_{\mu\nu}W^{\mu\nu} = d_\chi^2\left\{-Q^2F_1(4m_\chi^2+Q^2) + \frac{m_N F_2}{\nu}Q^2(\nu-2E_\chi)^2\right\}, \tag{B.87c}$$

$$\text{AM: } L_{\mu\nu}W^{\mu\nu} = a_\chi^2\Bigg\{2Q^4F_1(4m_\chi^2+Q^2) - \frac{m_N F_2}{\nu}Q^2\left[-4E_\chi^2Q^2 + 4E_\chi\nu Q^2 + 4m_\chi^2(\nu^2+Q^2) + Q^4\right]\Bigg\}, \tag{B.87d}$$

$$\text{CR: } L_{\mu\nu}W^{\mu\nu} = b_\chi^2\left\{2Q^4F_1(Q^2-2m_\chi^2) - \frac{m_N F_2}{\nu}Q^4\left[4E_\chi(\nu-E_\chi)+Q^2\right]\right\}. \tag{B.87e}$$

B.3 Terrestrial Probes

B.3.1 Recoil cross section on bound electron

For scattering on bound electrons, the differential cross section for massive DR that may either be relativistic or non-relativistic reads [163]

$$\left.\frac{d\sigma v}{dq dE_R}\right|_{(n,l)} = \frac{\bar\sigma_e}{8\mu_{\chi e}^2 E_R}\frac{m_\chi^2}{p_\chi E_\chi}\int d\Omega_{\vec p_e'}\, q|f_{n,l}(q)|^2|F_\chi(q,E_\chi)|^2, \tag{B.88}$$

where E_R is the electron recoil energy, v is the relative velocity, $\mu_{\chi e}$ is the reduced mass between χ and e^-, q is the momentum transfer, $d\Omega_{\vec p_e'}$ is the solid angle element of the final-state electron and $|f_{n,l}(q)|^2$ is the atomic form factor for the atomic state (n,l) [160, 428][10]. In this thesis, we use the numerical result of $|f_{n,l}(q)|^2$ that was obtained from an atomic calculation described in [165]. We normalize our results to the non-relativistic effective scattering cross section $\bar\sigma_e$ on a free electron, evaluated at a typical atomic momentum transfer $q_0 \simeq \alpha m_e$ and at vanishing kinetic energy, $E_\chi = m_\chi$,

$$\bar\sigma_e = \frac{\mu_{\chi e}^2}{16\pi m_\chi^2 m_e^2}\overline{|\mathcal{M}(q=q_0, E_\chi = m_\chi)|}^2, \tag{B.89}$$

where $\overline{|\mathcal{M}|}^2$ is the squared amplitude averaged over the initial-state spins and summed over the final-state spins. We assume m_e is much larger than the momentum transfer q and the deposited energy ΔE, which is valid when we consider the scattering with bound electrons in Chap. 5. We then expand $\overline{|\mathcal{M}(q,E_\chi)|}^2$ in $q/m_e = O(\alpha)$ and are careful to additionally retain the leading terms in a velocity-expansion that become relevant in the non-relativistic limit

[10] Note that often $|f_{\rm ion}(q)|^2 = \int d\Omega_{\vec p_e'}\,|f_{n,l}(q)|^2$ is written in the literature.

$v < \alpha$. For mQ, EDM, CR the leading order terms in both expansions coincide; for MDM and AM, the leading order term in q/m_e is velocity suppressed in the non-relativistic limit, and we add the term that is not velocity suppressed but of higher order in q/m_e. We find

$$\text{mQ: } \bar{\sigma}_e = \epsilon^2 \pi \alpha^2 \frac{16 m_\chi^2 m_e^2}{q_0^4 (m_\chi + m_e)^2}\,, \tag{B.90a}$$

$$\text{MDM: } \bar{\sigma}_e = \mu_\chi^2 \alpha \frac{m_\chi^2}{(m_\chi + m_e)^2}\,, \tag{B.90b}$$

$$\text{EDM: } \bar{\sigma}_e = d_\chi^2 \alpha \frac{4 m_\chi^2 m_e^2}{q_0^2 (m_\chi + m_e)^2}\,, \tag{B.90c}$$

$$\text{AM: } \bar{\sigma}_e = a_\chi^2 \alpha \frac{q_0^2 m_\chi^2}{(m_\chi + m_e)^2}\,, \tag{B.90d}$$

$$\text{CR: } \bar{\sigma}_e = b_\chi^2 \alpha \frac{4 m_\chi^2 m_e^2}{(m_\chi + m_e)^2}\,, \tag{B.90e}$$

where ϵ is the millicharge of χ in units of the elementary charge e, μ_χ and d_χ are the magnetic and electric dipole moment of χ, and a_χ and b_χ are the anapole moment and charge radius coupling of χ. The listed non-relativistic effective scattering cross sections agrees with the ones found in [160, 183].

The dark matter form factor is defined as

$$|F_\chi(q, E_\chi)|^2 = \frac{\overline{|\mathcal{M}(q, E_\chi)|}^2}{\overline{|\mathcal{M}(q = q_0, E_\chi = m_\chi)|}^2}\,, \tag{B.91}$$

with the concrete expressions for the respective effective operators given by

$$\text{mQ: } |F_\chi(q, E_\chi)|^2 = \frac{E_\chi^2 q_0^4}{m_\chi^2 q^4}\,, \tag{B.92a}$$

$$\text{MDM: } |F_\chi(q, E_\chi)|^2 = \frac{4 m_e^2 \left(E_\chi^2 - m_\chi^2\right)}{q^2 m_\chi^2} + 1\,, \tag{B.92b}$$

$$\text{EDM: } |F_\chi(q, E_\chi)|^2 = \frac{E_\chi^2 q_0^2}{m_\chi^2 q^2}\,, \tag{B.92c}$$

$$\text{AM: } |F_\chi(q, E_\chi)|^2 = \frac{4 m_e^2 \left(E_\chi^2 - m_\chi^2\right) + q^2 m_\chi^2}{q_0^2 m_\chi^2}\,, \tag{B.92d}$$

$$\text{CR: } |F_\chi(q, E_\chi)|^2 = \frac{E_\chi^2}{m_\chi^2}\,. \tag{B.92e}$$

Unlike in the direct detection literature that is concerned with chiefly non-relativistic scatterings, the form factors defined here carry an additional dependence on E_χ as is generally the case for relativistic scattering processes. When taking the non-relativistic limit $E_\chi \simeq m_\chi$, we

retrieve the non-relativistic dark matter form factors found in the literature [160, 183]. In addition, in the relativistic limit, $E_\chi \gg m_\chi$, the helicity suppression introduced by γ^5 drops out, and the respective mass-dimension 5 and 6 form factors become equivalent. We conclude the dark matter form factors presented here are applicable across the entire kinematic region.

For massless DR, $m_\chi = 0$, the differential cross section can be written as

$$\left.\frac{d\sigma v}{dq dE_R}\right|_{(n,l)} = \frac{\bar{\sigma}_e}{8E_R p_\chi^2} \int d\Omega_{\vec{p}'_e}\, q |f_{n,l}(q)|^2 |F_\chi(q, p_\chi)|^2 \,. \tag{B.93}$$

It should be noted that $\bar{\sigma}_e$ in Eq. (B.89) is ill-defined for $m_\chi \to 0$, but in the product $\bar{\sigma}_e |F_\chi(q, E_\chi)|^2$ the mass-dependence cancels out. Hence, in practice, keeping with the usually adopted convention for the definition of $\bar{\sigma}_e$ does not pose any obstruction.

B.3.2 Recoil cross section on free particle

In agreement with the previous work on the dark sector-photon interactions [183], we list here for completeness the recoil cross sections for scattering on free electrons,

$$\text{mQ: } \frac{d\sigma_{\chi e}}{dE_R} = \epsilon^2 \pi \alpha^2 \frac{m_e(E_R^2 + 2E_\chi^2) - E_R(2E_\chi m_e + m_e^2 + m_\chi^2)}{(E_\chi^2 - m_\chi^2) E_R^2 m_e^2} \,, \tag{B.94a}$$

$$\text{MDM: } \frac{d\sigma_{\chi e}}{dE_R} = \mu_\chi^2 \alpha \frac{(E_R - 2m_e)m_\chi^2 - 2(E_R - E_\chi)E_\chi m_e}{2(E_\chi^2 - m_\chi^2) E_R m_e} \,, \tag{B.94b}$$

$$\text{EDM: } \frac{d\sigma_{\chi e}}{dE_R} = d_\chi^2 \alpha \frac{2E_\chi m_e(E_\chi - E_R) - E_R m_\chi^2}{2(E_\chi^2 - m_\chi^2) E_R m_e} \,, \tag{B.94c}$$

$$\text{AM: } \frac{d\sigma_{\chi e}}{dE_R} = a_\chi^2 \alpha \frac{m_e \left[E_R^2 - E_R(2E_\chi + m_e) + 2E_\chi^2\right] + m_\chi^2(E_R - 2m_e)}{E_\chi^2 - m_\chi^2} \,, \tag{B.94d}$$

$$\text{CR: } \frac{d\sigma_{\chi e}}{dE_R} = b_\chi^2 \alpha \frac{E_R^2 m_e - E_R(2E_\chi m_e + m_e^2 + m_\chi^2) + 2E_\chi^2 m_e}{E_\chi^2 - m_\chi^2} \,. \tag{B.94e}$$

For the general expressions that are applicable for the analogous scattering on nuclei, see App. E in [183].

C Appendix for Part II

C.1 Contribution to lepton $g-2$

In general, we can write the amplitude of the 1-loop diagram as $\mathcal{M}_\mu = e\bar{u}(p_2) W_\mu(p, q) u(p_1)$, where $W_\mu(p, q)$ entails the interaction included in the loop, with $p = (p_1 + p_2)/2$ and the

momentum transfer $q = p_2 - p_1$. The contribution to a_l can then be expressed in terms of projection operators, V^μ and $T^{\mu\nu}$, as [456]

$$a_l = \frac{1}{(d-1)(d-2)m^2}\mathrm{Tr}\Big\{\frac{d-2}{2}\left[m_l^2\gamma_\mu - dp_\mu \not{p} - (d-1)m_l p_\mu\right]V^\mu + \frac{m_l}{4}(\not{p}+m)[\gamma_\nu,\gamma_\mu](\not{p}+m)T^{\mu\nu}\Big\}, \tag{C.95}$$

in which we use the dimensional regularization with $d = 4-\epsilon$. The projection operators can be obtained by Taylor-expanding $W_\mu(p,q)$ in the limit $q \to 0$, which reads

$$W_\mu(p,q) \simeq W_\mu(p,0) + \Delta_\nu \frac{\partial}{\partial \Delta_\nu} W_\mu(p,q)\Big|_{q=0} \equiv V_\mu(p) + \Delta_\nu T^\nu_\mu(p)\,,$$

with $\Delta_\nu = -q_\nu$ and $p\cdot q = 0$.

From explicit calculation for the $(g-2)_l$ contribution in the representative models as shown in Fig. 6.3 we obtain

$$\Delta a_l^F = \int_0^1 dz\, \frac{m_l(z-1)^2\left[m_l z(c_L^{l\,2}+c_R^{l\,2}) + 2c_L^l c_R^l m_F\right]}{16\pi^2\left[m_F^2(1-z)+m_\phi^2 z\right]},$$
$$\Delta a_l^{Z'} = \int_0^1 dz\, \frac{m_l^2 z(z-1)\left[g_L^2(z+1) - 4g_L g_R + g_R^2(z+1)\right]}{8\pi^2\left[m_l^2(z-1)^2 + m_{Z'}^2 z\right]}. \tag{C.96}$$

Taking only the leading order terms and setting $g_L = g_R \equiv g_l$, we recover Eq. (6.9) and Eq. (6.12) of the main text.

C.1.1 ϕ-pair annihilation

Here we give the non-relativistic expansion of the DM annihilation cross section via a t-channel fermion F, to second order of the relative velocity, assuming the hierarchy $m_F \gg m_\phi > m_l$,

$$\sigma_{\mathrm{ann},F} v_M = \frac{\left(c_L^2 m_l + c_R^2 m_l + 2c_L c_R m_F\right)^2}{16\pi(m_F^2 + m_\phi^2 - m_l^2)^2}\left(1 - \frac{m_l^2}{m_\phi^2}\right)^{\frac{3}{2}} + v_{\mathrm{rel}}^2\left[\frac{(c_L^4 - 12c_L^2c_R^2 + c_R^4)m_\phi^2}{48\pi m_F^4} + \frac{3c_L^2c_R^2 m_l^2}{32\pi m_F^2 m_\phi^2} - \frac{(c_L^4 - 14c_L^2c_R^2 + c_R^4)m_l^2}{64\pi m_F^4}\right]. \tag{C.97}$$

Here we have neglected terms of $\mathcal{O}(m_{l,\phi}^5/m_F^5)$. By taking only the leading order in $\mathcal{O}(m_{l,\phi}/m_F)$ and replacing v_{rel} with $2v_\phi$, we retrieve the s-wave expression of Eq. (1) in [362], while our p-wave result differs. The difference arises from the general mismatch between v_{rel} and v_M. We prefer to use the non-relativistic expansion of the Lorentz-invariant quantity $\sigma_{\mathrm{ann}} v_M$ [209]; our scattering amplitude agrees with the one given in the appendix of [362]. For the special

case $c_L c_R = 0$ and for $m_l = 0$, the s-wave component in Eq. (C.97) vanishes and the process becomes p-wave dominated, scaling as $v_{\rm rel}^2 m_\phi^2/m_F^4$.

For real scalar DM, $\phi = \phi^*$, the annihilation process via a u-channel fermion F needs to be added, and the cross section in the same approximation becomes

$$\sigma_{\text{ann},F}^{\text{real }\phi} v_M = \frac{\left(c_L^2 m_l + c_R^2 m_l + 2c_L c_R m_F\right)^2}{4\pi(m_F^2 + m_\phi^2 - m_l^2)^2}\left(1 - \frac{m_l^2}{m_\phi^2}\right)^{\frac{3}{2}} + v_{\rm rel}^2\left[\frac{3c_L^2 c_R^2 m_l^2}{8\pi m_F^2 m_\phi^2} + \frac{3c_L c_R(c_L^2 + c_R^2)m_l^3}{8\pi m_F^3 m_\phi^2} - \frac{c_L^2 c_R^2 m_\phi^2}{\pi m_F^4} + \frac{3c_L^2 c_R^2 m_l^2}{4\pi m_F^4}\right]. \tag{C.98}$$

C.1.2 $e^- e^+$ annihilation with initial state radiation

First, we detail the annihilation cross section associated with ISR, corresponding to Fig. 7.1. Following [183], the differential cross section with ISR is formulated as the cross section without ISR times the improved Altarelli-Parisi radiator function. The annihilation cross sections, without ISR and with s denoting the squared CM energy, to order $\mathcal{O}(m_{e,\phi}^3/m_F^3)$ and after an average over the initial-state spins has been performed, reads

$$\sigma_{e^-e^+\to\phi\phi}^{F} = \frac{c_L^2 c_R^2}{32\pi m_F^2}\sqrt{\frac{s-4m_\phi^2}{s-4m_e^2}}\left(1 - \frac{4m_e^2}{s}\right), \tag{C.99}$$

$$\sigma_{e^-e^+\to\phi\phi}^{Z'} = g_\phi^2(s-4m_\phi^2)\sqrt{\frac{s-4m_\phi^2}{s-4m_e^2}}\left[\frac{s(g_L^2+g_R^2) - m_e^2(g_L^2 - 6g_L g_R + g_R^2)}{96\pi s(s-m_{Z'}^2)^2}\right]. \tag{C.100}$$

C.1.3 eN bremsstrahlung

For the fixed-target and beam-dump experiments, we consider the production of ϕ-pairs via electron-nucleus bremsstrahlung depicted in Fig. 7.2. Here, we need to compute the 2-to-4 cross section $\sigma_{2\to4}$ for the process $e^-(p_1) + N(p_2) \to e^-(p_3) + N/X_n(p_4) + \phi(p_\phi) + \phi^*(p_{\phi^*})$. We define $k = p_\phi + p_\phi^*$ with $k^2 \equiv s_{\phi\phi}$, $q_1 = p_1 - p_3$ with $q_1^2 \equiv t_1$ and $q_2 = p_2 - p_4$ with $q_2^2 \equiv t_2$ such that $k = q_1 + q_2$ given that total momentum is conserved. The differential cross section is then written as

$$d\sigma_{2\to4} = \frac{1}{4E_1 E_2 v_M}\frac{1}{g_1 g_2}\sum_{\text{spins}}|\mathcal{M}|^2 d\Phi, \tag{C.101}$$

where g_1 and g_2 are the spin degrees of freedom of electron and nucleus, $|\mathcal{M}|^2$ is the squared amplitude, and $d\Phi$ is the total phase space. By introducing an integral with respect to $s_X \equiv m_X^2 = p_4^2$ to account for the potential inelastic scattering, in the lab frame Eq. (C.101) becomes

$$d\sigma_{2\to4} = \frac{(4\pi\alpha)^2}{2|\vec{p}_1|m_N g_2 q_2^4} L^{\mu\nu,\rho\sigma}\phi_{\rho\sigma}W_{\mu\nu}(-q_2)ds_X d\Phi_4,$$

where $L^{\mu\nu,\rho\sigma}$ contains the leptonic average over g_1, $\phi_{\rho\sigma}$ includes the ϕ-emission piece together with the heavy mediator propagator, $W_{\mu\nu}$ is the hadronic tensor with its concrete form given in [183] and $d\Phi_4$ is the 4-body phase space integral which is analytically computed in [183] and derived again in App. A.2.

The leptonic tensor from the two diagrams and their interference can be expressed as

$$L^{\mu\nu,\rho\sigma} = \frac{L_a^{\mu\nu,\rho\sigma}}{\left[(p_3+k)^2 - m_e^2\right]^2} + \frac{L_b^{\mu\nu,\rho\sigma}}{\left[(p_1-k)^2 - m_e^2\right]^2} + \frac{L_{ab}^{\mu\nu,\rho\sigma}}{\left[(p_3+k)^2 - m_e^2\right]\left[(p_1-k)^2 - m_e^2\right]}\,, \tag{C.102}$$

where, for completeness, we spell out the individual traces in the following. For the F-mediated model they read

$$\begin{aligned}
L_{a,F}^{\mu\nu,\rho\sigma} &= \frac{\mathbb{1}^{\rho\sigma}}{g_1 m_F^2}\mathrm{Tr}\Big[(\not{p}_3 + m_e)(c_L P_L + c_R P_R)(c_L P_R + c_R P_L)(\not{p}_3 + \not{k} + m_e)\gamma^\mu(\not{p}_1 + m_e)\gamma^\nu \\
&\qquad (\not{p}_3 + \not{k} + m_e)(c_L P_L + c_R P_R)(c_L P_R + c_R P_L)\Big]\,, \\
L_{b,F}^{\mu\nu,\rho\sigma} &= \frac{\mathbb{1}^{\rho\sigma}}{g_1 m_F^2}\mathrm{Tr}\Big[(\not{p}_1 + m_e)(c_L P_L + c_R P_R)(c_L P_R + c_R P_L)(\not{p}_1 - \not{k} + m_e)\gamma^\nu(\not{p}_3 + m_e)\gamma^\mu \\
&\qquad (\not{p}_1 - \not{k} + m_e)(c_L P_L + c_R P_R)(c_L P_R + c_R P_L)\Big]\,, \\
L_{ab,F}^{\mu\nu,\rho\sigma} &= \frac{\mathbb{1}^{\rho\sigma}}{g_1 m_F^2}\Big\{\mathrm{Tr}\Big[(\not{p}_3 + m_e)(c_L P_L + c_R P_R)(c_L P_R + c_R P_L)(\not{p}_3 + \not{k} + m_e)\gamma^\mu(\not{p}_1 + m_e) \\
&\qquad (c_L P_L + c_R P_R)(c_L P_R + c_R P_L)(\not{p}_1 - \not{k} + m_e)\gamma^\nu\Big] + \mathrm{Tr}\Big[(\not{p}_3 + m_e)\gamma^\mu(\not{p}_1 - \not{k} + m_e) \\
&\qquad (c_L P_L + c_R P_R)(c_L P_R + c_R P_L)(\not{p}_1 + m_e)\gamma^\nu(\not{p}_3 + \not{k} + m_e)(c_L P_L + c_R P_R)(c_L P_R + c_R P_L)\Big]\Big\}\,,
\end{aligned} \tag{C.103}$$

where $\mathbb{1}^{\rho\sigma}$ is an identity matrix with indices ρ, σ. For the Z'-mediated model we obtain for the traces:

$$\begin{aligned}
L_{a,Z'}^{\mu\nu,\rho\sigma} &= \frac{1}{g_1}\mathrm{Tr}\Big[(\not{p}_3 + m_e)\gamma^\rho(g_L P_L + g_R P_R)(\not{p}_3 + \not{k} + m_e)\gamma^\mu(\not{p}_1 + m_e)\gamma^\nu(\not{p}_3 + \not{k} + m_e) \\
&\qquad (g_L P_R + g_R P_L)\gamma^\sigma\Big]\,, \\
L_{b,Z'}^{\mu\nu,\rho\sigma} &= \frac{1}{g_1}\mathrm{Tr}\Big[(\not{p}_1 + m_e)(g_L P_R + g_R P_L)\gamma^\sigma(\not{p}_1 - \not{k} + m_e)\gamma^\nu(\not{p}_3 + m_e)\gamma^\mu(\not{p}_1 - \not{k} + m_e) \\
&\qquad \gamma^\rho(g_L P_L + g_R P_R)\Big]\,, \\
L_{ab,Z'}^{\mu\nu,\rho\sigma} &= \frac{1}{g_1}\Big\{\mathrm{Tr}\Big[(\not{p}_3 + m_e)\gamma^\rho(g_L P_L + g_R P_R)(\not{p}_3 + \not{k} + m_e)\gamma^\mu(\not{p}_1 + m_e)(g_L P_R + g_R P_L) \\
&\qquad \gamma^\sigma(\not{p}_1 - \not{k} + m_e)\gamma^\nu\Big] + \mathrm{Tr}\Big[(\not{p}_3 + m_e)\gamma^\mu(\not{p}_1 - \not{k} + m_e)\gamma^\rho(g_L P_L + g_R P_R)(\not{p}_1 + m_e) \\
&\qquad \gamma^\nu(\not{p}_3 + \not{k} + m_e)(g_L P_R + g_R P_L)\gamma^\sigma\Big]\Big\}\,.
\end{aligned} \tag{C.104}$$

In the case that ϕ-emission proceeds by F mediation, we may simplify the calculation by utilizing the fact that $m_F = 1\,\text{TeV}$ is much larger than any momentum transfer considered here and approximate the the F propagator as

$$\frac{i\,(\not{k} + m_F)}{k^2 - m_F^2} \to \frac{-i}{m_F}\,, \tag{C.105}$$

where k is the four-momentum flowing in the propagator. We hence write the $ll\phi\phi$ interaction as an effective operator suppressed by m_F. The ϕ-emission piece is thus $\phi^F_{\rho\sigma} = \mathbb{1}_{\rho\sigma}$, and the integral over the product of Lorentz-invariant phase space of ϕ and ϕ^* denoted by $d\Pi_{\phi,\phi^*}$, is given by

$$\int d\Pi_{\phi,\phi^*}\,(2\pi)^4\delta^{(4)}(k - p_\phi - p_{\phi^*})\phi^F_{\rho\sigma} = \frac{\mathbb{1}_{\rho\sigma}}{8\pi}\sqrt{1 - \frac{4m_\phi^2}{s_{\phi\phi}}}\,.$$

The ϕ-emission piece $\phi^{Z'}_{\rho\sigma}$ in the Z'-mediated case reads

$$\phi^{Z'}_{\rho\sigma} = \frac{g_\phi^2}{\left(s_{\phi\phi} - m_{Z'}^2\right)^2}\left(k^\alpha k^\beta - 2p_\phi^\alpha p_{\phi^*}^\beta - 2p_{\phi^*}^\alpha p_\phi^\beta\right)\left(g_{\rho\alpha} - \frac{k_\rho k_\alpha}{m_{Z'}^2}\right)\left(g_{\sigma\beta} - \frac{k_\sigma k_\beta}{m_{Z'}^2}\right)\,. \tag{C.106}$$

Terms containing p_ϕ and p_{ϕ^*} can be integrated over the ϕ-pair phase space using a modified version of Lenard's formula [P1] for massive final states, yielding

$$\int d\Pi_{\phi,\phi^*}\,(2\pi)^4\delta^{(4)}(k - p_\phi - p_{\phi^*})\phi^{Z'}_{\rho\sigma} = \frac{1}{8\pi\left(s_{\phi\phi} - m_{Z'}^2\right)^2}\sqrt{1 - \frac{4m_\phi^2}{s_{\phi\phi}}}f_{Z'}(s_{\phi\phi})\left(-g_{\rho\sigma} + \frac{k_\rho k_\sigma}{s_{\phi\phi}}\right).$$

Here, the function $f(s_{\phi\phi})$ following the convention used in [183] and [P1, P2], and for the Z'-mediated model reads

$$f_{Z'}(s_{\phi\phi}) = \frac{1}{3}g_\phi^2 s_{\phi\phi}\left(1 - \frac{4m_\phi^2}{s_{\phi\phi}}\right). \tag{C.107}$$

When considering the experiments NA64 and LDMX where final-state electrons are measured, we utilize the following differential cross section:

$$\begin{aligned}
\frac{d\sigma^F_{2\to4}}{dE_3 d\cos\theta_3} &= \frac{\alpha^2}{8\pi^2 g_2 m_N}\sqrt{\frac{E_3^2 - m_e^2}{E_1^2 - m_e^2}}\int ds_X \int ds_{\phi\phi}\int dt_2 \int dp_{1k}\left|\frac{\partial\phi_{4k}^{\text{R4k}}}{\partial p_{1k}}\right|\frac{1}{t_2^2}\frac{1}{\sqrt{\lambda(s_4, m_N^2, t_1)}} \\
&\quad\times L_F^{\mu\nu,\rho\sigma}W_{\mu\nu}(-q_2)\frac{\mathbb{1}_{\rho\sigma}}{16\pi^2}\sqrt{1 - \frac{4m_\phi^2}{s_{\phi\phi}}}\,, \\
\frac{d\sigma^{Z'}_{2\to4}}{dE_3 d\cos\theta_3} &= \frac{\alpha^2}{8\pi^2 g_2 m_N}\sqrt{\frac{E_3^2 - m_e^2}{E_1^2 - m_e^2}}\int ds_X \int ds_{\phi\phi}\int dt_2 \int dp_{1k}\left|\frac{\partial\phi_{4k}^{\text{R4k}}}{\partial p_{1k}}\right|\frac{1}{t_2^2}\frac{1}{\sqrt{\lambda(s_4, m_N^2, t_1)}}
\end{aligned}$$

$$\times L_{Z'}^{\mu\nu,\rho\sigma} W_{\mu\nu}(-q_2) \frac{1}{16\pi^2 (s_{\phi\phi} - m_{Z'}^2)^2} \sqrt{1 - \frac{4m_\phi^2}{s_{\phi\phi}}} f_{Z'}(s_{\phi\phi}) \left(-g_{\rho\sigma} + \frac{k_\rho k_\sigma}{s_{\phi\phi}} \right) . \tag{C.108}$$

The derivation of the differential four-body phase space integral is given in App. A.2.

For the experiments mQ and BDX, we need the spectrum and distribution of the produced ϕ particles. Therefore, we use

$$\begin{aligned} \frac{d\sigma_{2\to4}^{F,Z'}}{dE_\phi d\cos\theta_\phi} = & \frac{\alpha^2}{16(2\pi)^5 g_2 m_N} \sqrt{\frac{E_\phi^2 - m_\phi^2}{E_1^2 - m_e^2}} \int ds_X \int ds_{36} \int dt_{23} \int d\phi_{36}^{\mathrm{R36}} \int t_2 \int d\phi_{436}^{\mathrm{R436}} \\ & \times \frac{1}{t_2^2} \frac{1}{\sqrt{\lambda(s_{36}, m_N^2, (p_1 - p_4 - p_\phi)^2) \lambda(s_{436}, m_N^2, t_{15})}} L_{F,Z'}^{\mu\nu,\rho\sigma} W_{\mu\nu}(-q_2) \phi_{\rho\sigma}^{F,Z'} . \end{aligned} \tag{C.109}$$

See App. A.2 for the definitions of each variable and Eq. (A.27) for the formula of differential four-body phase space integral in this case.

C.1.4 ϕe scattering

To leading order, the differential recoil cross section $d\sigma_{\phi e}/dE_R$ as a function of the incoming ϕ-energy, E_ϕ, and the recoil energy of the electron, E_R, for the F-mediated (s- and u-channel scattering) and Z'-mediated (t-channel scattering) cases read as follows:

$$\frac{d\sigma_{\phi e}^F}{dE_R} = \frac{c_L^2 c_R^2 (E_R + 2m_e)}{4\pi (E_\phi^2 - m_\phi^2) m_F^2} \qquad (m_{e,\phi} \ll m_F) , \tag{C.110}$$

$$\frac{d\sigma_{\phi e}^{Z'}}{dE_R} = \frac{g_\phi^2 g_l^2 \left[2E_\phi m_e (E_\phi - E_R) - E_R m_\phi^2 \right]}{4\pi (E_\phi^2 - m_\phi^2)(2E_R m_e + m_{Z'}^2)^2} , \tag{C.111}$$

where we use $g_L = g_R \equiv g_l$ for the sake of presenting a more compact formula. The equations above are used in computing the electron scattering signal in mQ and BDX.

To properly account for the Pauli blocking factor in the computation of the upper boundaries of the SN1987A exclusion region, we also provide the differential cross sections in terms of Mandelstam variable t, taking again the limit of heavy mediators,

$$\frac{d\sigma_{\phi e}^F}{dt} = \frac{c_L^2 c_R^2}{4\pi m_F^2} \frac{4m_e^2 - t}{(m_e^2 + m_\phi^2 - s)^2 - 4m_e^2 m_\phi^2} , \tag{C.112}$$

$$\frac{d\sigma_{\phi e}^{Z'}}{dt} = \frac{g_l^2 g_\phi^2}{4\pi m_{Z'}^4} \frac{(m_e^2 + m_\phi^2 - s)^2 + t(s - m_e^2)}{(m_e^2 + m_\phi^2 - s)^2 - 4m_e^2 m_\phi^2} . \tag{C.113}$$

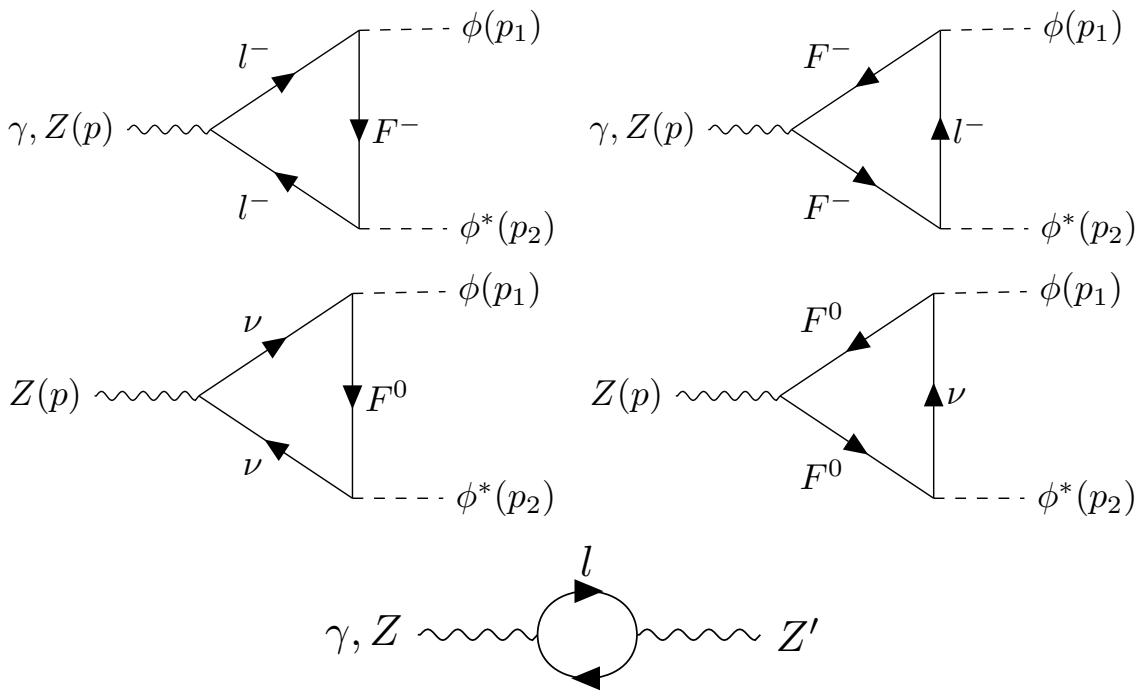

Figure C.5: *Top panel:* Triangle loop coupling ϕ to Z or γ with one charged F (left) and two charged F (right). *Middle panel:* Triangle loop coupling ϕ to Z with one (left) or two (right) neutral F states. *Bottom panel:* Loop-induced γ-Z' and Z-Z' mixing, which also contribute to the coupling to a ϕ-pair.

C.2 Further 1-loop diagrams

The presence of heavy new charged fermions, $F^\pm$, induces effective interactions between ϕ and SM gauge bosons through a set of triangle loops containing $F^\pm$ and SM charged leptons, demonstrated in Fig. C.5. This loop-induced charge radius interaction can, *e.g.*, be probed in direct detection experiments [367, 457].

Here we detail the calculation of the coupling of the ϕ-pair to an off-shell photon via the aforementioned triangle loops. The amplitude that needs to be dotted into the off-shell photon reads

$$i\mathcal{M}_{F,\mu} = \sum_l \left(i\mathcal{M}^l_{1F,\mu} + i\mathcal{M}^l_{2F,\mu} \right) , \tag{C.114}$$

where $i\mathcal{M}^l_{1F,\mu}$ and $i\mathcal{M}^l_{2F,\mu}$ correspond to the diagrams containing one and two $F^\pm$ in the loop, respectively. Note that we take one charged SM lepton as an example, and denote its mass by m_l. Here left- and right-handed SM leptons contribute equally, so we further set $c_L = c_R \equiv c_F$.

After using Feynman parametrization and dimensional regularization to perform the loop integral, we find that the divergences in $\mathcal{M}^l_{1F,\mu}$ and $\mathcal{M}^l_{2F,\mu}$ mutually cancel. The remaining

finite terms read

$$i\mathcal{M}^l_{1F,\mu} = -i\frac{ec_F^2}{4\pi^2}\int_0^1 dz\int_0^{1-z} dx\left\{p_{2,\mu}\left[\frac{m_l^2(z-1)+2m_lm_Fz+g_a(p^2,m_\phi^2)}{\Delta_{1F}}+(3z+1)\ln\Delta_{1F}\right]\right.$$
$$\left.+p_\mu\left[\frac{m_l^2x+m_lm_F(2x-1)+g_b(p^2,m_\phi^2)}{\Delta_{1F}}+(3x-2)\ln\Delta_{1F}\right]\right\}, \tag{C.115}$$

$$i\mathcal{M}^l_{2F,\mu} = i\frac{ec_F^2}{4\pi^2}\int_0^1 dz\int_0^{1-z} dx\left\{p_{2,\mu}\left[\frac{m_F^2(z-1)+2m_lm_Fz+g_a(p^2,m_\phi^2)}{\Delta_{2F}}+(3z+1)\ln\Delta_{2F}\right]\right.$$
$$\left.+p_\mu\left[\frac{m_F^2x+m_lm_F(2x-1)+g_b(p^2,m_\phi^2)}{\Delta_{2F}}+(3x-2)\ln\Delta_{2F}\right]\right\}, \tag{C.116}$$

with p_μ being the four-momentum of the photon, $p_{2,\mu}$ being the four-momentum of one of the outgoing ϕ particles, and

$$\begin{aligned}
g_a(p^2,m_\phi^2) &= m_\phi^2(z-1)z^2+p^2x(z+1)(x+z-1)\,,\\
g_b(p^2,m_\phi^2) &= m_\phi^2z(xz-z-2x+1)+p^2x(x-1)(x+z-1)\,,\\
\Delta_{1F} &= -m_l^2(z-1)+z\big[m_F^2+m_\phi^2(z-1)\big]+p^2x(x+z-1)\,,\\
\Delta_{2F} &= -m_F^2(z-1)+z\big[m_l^2+m_\phi^2(z-1)\big]+p^2x(x+z-1)\,.
\end{aligned}$$

Note that if $m_l = m_F$, the total amplitude vanishes, as a manifestation of Furry's theorem. One can also directly write the combination of the two diagrams as an effective charge radius operator if we integrate out the heavy F,

$$-b_\phi\partial_\mu\phi\partial_\nu\phi^*F^{\mu\nu}\,, \tag{C.117}$$

where $F^{\mu\nu}$ is the field strength tensor of the SM photon. We have checked that our loop calculation correctly matches onto this effective operator, with the Wilson coefficient:

$$b_\phi = \frac{ec_F^2}{4\pi^2}\int_0^1 dz\int_0^{1-z} dx$$
$$\times\left\{\frac{x(x+z-1)\big[m_l^2(z^2+z-2)+2m_lm_Fz-z(z+1)m_F^2-z(z-1)m_\phi^2\big]}{\big[m_l^2(z-1)-zm_F^2-z(z-1)m_\phi^2\big]^2}-(m_l\leftrightarrow m_F)\right\}, \tag{C.118}$$

in numerical agreement with previous results [367, 457]. Note that a sum over the contributions from all SM leptons needs to be performed in the actual evaluation.

The above calculation can be generalized to infer the additional contribution to the invisible Z decay width by replacing the relevant couplings in the above amplitudes by the weak charges,

$$e\to\frac{e}{2s_Wc_W}g_V\,, \tag{C.119}$$

where $s_W = \sin\theta_W$, $c_W = \cos\theta_W$ with θ_W being the weak angle, and g_V being the usual vector coupling of weak current; axial vector currents do not contribute when $c_L = c_R$. Note that one also needs to include the contribution from diagrams containing neutral leptons as shown in the middle panel of Fig. C.5. We have checked that the resulting bound on c_F is rather weak, and is thus not shown in the constraint plots.

In the Z'-mediated case, the SM photon or Z-boson gains an effective coupling to ϕ via mixing with Z', originating from a SM lepton loop, shown in the bottom panel of Fig. C.5. To estimate the mixing, we need to compute the polarization mixing tensor $i\Pi^{\mu\nu}$ given by the usual Lorentz structure, $i\Pi^{\mu\nu} = i\left(p^2 g^{\mu\nu} - p^\mu p^\nu\right)\Pi(p^2)$. For the SM photon and taking $g_L = g_R \equiv g_l$, we find in dimensional regularization the mixing self-energy:

$$\Pi(p^2) = -\frac{e g_l}{2\pi^2}\int_0^1 dx\, x(1-x)\left[\frac{2}{\epsilon} + \ln\frac{\tilde{\mu}^2}{\Delta} + \mathcal{O}(\epsilon)\right], \tag{C.120}$$

where ϵ is an infinitesimal number, $\tilde{\mu}^2 = 4\pi e^{-\gamma_E}\mu^2$ with the Euler-Mascheroni constant γ_E, the renormalization scale μ, and $\Delta = m_l^2 - x(1-x)p^2$. Equivalently, one can also re-write the self-energy of Eq. (C.120) in terms of the standard Passarino-Veltman integrals [458–460] as

$$\Pi(p^2) = \frac{e g_l}{12\pi^2 p^2}\left[2A_0(m_l^2) - (p^2 + 2m_l^2)B_0(p^2, m_l^2, m_l^2)\right]. \tag{C.121}$$

The divergence in $\Pi(p^2)$ can be cancelled by a counterterm, that is, after specifying a renormalization condition, the effective mixing can be evaluated. The mixing between Z and Z' is computed in the same way but with Eq. (C.119). Nevertheless, the ensuing constraint on $\sqrt{g_\phi g_l}$ from the Z invisible decay is fully covered by the LEP bound.

Bibliography

[1] X. Chu, J.-L. Kuo, J. Pradler, and L. Semmelrock, *Stellar probes of dark sector-photon interactions*. Phys. Rev. D **100** (2019) no. 8, 083002, arXiv:1908.00553 [hep-ph].

[2] X. Chu, J.-L. Kuo, and J. Pradler, *Dark sector-photon interactions in proton-beam experiments*. Phys. Rev. D **101** (2020) no. 7, 075035, arXiv:2001.06042 [hep-ph].

[3] C. Boehm, X. Chu, J.-L. Kuo, and J. Pradler, *Scalar Dark Matter Candidates – Revisited*. Phys. Rev. D **103** (2021) 075005, arXiv:2010.02954 [hep-ph].

[4] J.-L. Kuo, M. Pospelov, and J. Pradler, *Terrestrial Probes of Electromagnetically Interacting Dark Radiation*. arXiv:2102.08409 [hep-ph].

[5] **Particle Data Group** Collaboration, P. Zyla *et al.*, *Review of Particle Physics*. PTEP **2020** (2020) no. 8, 083C01.

[6] C. Bouchiat, J. Iliopoulos, and P. Meyer, *An Anomaly Free Version of Weinberg's Model*. Phys. Lett. B **38** (1972) 519–523.

[7] J. A. Minahan, P. Ramond, and R. C. Warner, *A Comment on Anomaly Cancellation in the Standard Model*. Phys. Rev. D **41** (1990) 715.

[8] F. Englert and R. Brout, *Broken Symmetry and the Mass of Gauge Vector Mesons*. Phys. Rev. Lett. **13** (1964) 321–323.

[9] P. W. Higgs, *Broken Symmetries and the Masses of Gauge Bosons*. Phys. Rev. Lett. **13** (1964) 508–509.

[10] G. S. Guralnik, C. R. Hagen, and T. W. B. Kibble, *Global Conservation Laws and Massless Particles*. Phys. Rev. Lett. **13** (1964) 585–587.

[11] **CMS** Collaboration, S. Chatrchyan *et al.*, *Observation of a New Boson at a Mass of 125 GeV with the CMS Experiment at the LHC*. Phys. Lett. B **716** (2012) 30–61, arXiv:1207.7235 [hep-ex].

[12] **ATLAS** Collaboration, G. Aad *et al.*, *Observation of a new particle in the search for the Standard Model Higgs boson with the ATLAS detector at the LHC*. Phys. Lett. B **716** (2012) 1–29, arXiv:1207.7214 [hep-ex].

[13] J. Erler and M. Schott, *Electroweak Precision Tests of the Standard Model after the Discovery of the Higgs Boson*. Prog. Part. Nucl. Phys. **106** (2019) 68–119, arXiv:1902.05142 [hep-ph].

[14] H. Georgi and S. L. Glashow, *Unity of All Elementary Particle Forces*. Phys. Rev. Lett. **32** (1974) 438–441.

[15] J. C. Pati and A. Salam, *Lepton Number as the Fourth Color*. Phys. Rev. D **10** (1974) 275–289. [Erratum: Phys.Rev.D 11, 703–703 (1975)].

[16] A. J. Buras, J. R. Ellis, M. K. Gaillard, and D. V. Nanopoulos, *Aspects of the Grand Unification of Strong, Weak and Electromagnetic Interactions*. Nucl. Phys. B **135** (1978) 66–92.

[17] J. Wess and B. Zumino, *Supergauge Transformations in Four-Dimensions*. Nucl. Phys. B **70** (1974) 39–50.

[18] P. Fayet and S. Ferrara, *Supersymmetry*. Phys. Rept. **32** (1977) 249–334.

[19] P. Fayet, *Spontaneously Broken Supersymmetric Theories of Weak, Electromagnetic and Strong Interactions*. Phys. Lett. B **69** (1977) 489.

[20] I. Brivio and M. Trott, *The Standard Model as an Effective Field Theory*. Phys. Rept. **793** (2019) 1–98, arXiv:1706.08945 [hep-ph].

[21] G. Arcadi, M. Dutra, P. Ghosh, M. Lindner, Y. Mambrini, M. Pierre, S. Profumo, and F. S. Queiroz, *The waning of the WIMP? A review of models, searches, and constraints*. Eur. Phys. J. C **78** (2018) no. 3, 203, arXiv:1703.07364 [hep-ph].

[22] **CTEQ** Collaboration, R. Brock *et al.*, *Handbook of perturbative QCD: Version 1.0*. Rev. Mod. Phys. **67** (1995) 157–248.

[23] H. Georgi, *An Effective Field Theory for Heavy Quarks at Low-energies*. Phys. Lett. B **240** (1990) 447–450.

[24] H. Leutwyler, *On the foundations of chiral perturbation theory*. Annals Phys. **235** (1994) 165–203, arXiv:hep-ph/9311274.

[25] N. Brambilla, A. Pineda, J. Soto, and A. Vairo, *Potential NRQCD: An Effective theory for heavy quarkonium*. Nucl. Phys. B **566** (2000) 275, arXiv:hep-ph/9907240.

[26] S. Aoki *et al.*, *Review of lattice results concerning low-energy particle physics*. Eur. Phys. J. C **77** (2017) no. 2, 112, arXiv:1607.00299 [hep-lat].

[27] F. Jegerlehner and A. Nyffeler, *The Muon g-2*. Phys. Rept. **477** (2009) 1–110, arXiv:0902.3360 [hep-ph].

[28] **Muon g-2** Collaboration, G. Bennett *et al.*, *Final Report of the Muon E821 Anomalous Magnetic Moment Measurement at BNL*. Phys. Rev. D **73** (2006) 072003, arXiv:hep-ex/0602035.

[29] **Muon g-2** Collaboration, B. Abi *et al.*, *Measurement of the Positive Muon Anomalous Magnetic Moment to 0.46 ppm*. Phys. Rev. Lett. **126** (2021) no. 14, 141801, arXiv:2104.03281 [hep-ex].

[30] B. Pontecorvo, *Inverse beta processes and nonconservation of lepton charge*. Zh. Eksp. Teor. Fiz. **34** (1957) 247.

[31] **Super-Kamiokande** Collaboration, Y. Fukuda *et al.*, *Evidence for oscillation of atmospheric neutrinos*. Phys. Rev. Lett. **81** (1998) 1562–1567, arXiv:hep-ex/9807003.

[32] P. Minkowski, $\mu \to e\gamma$ *at a Rate of One Out of* 10^9 *Muon Decays?* Phys. Lett. B **67** (1977) 421–428.

[33] R. N. Mohapatra and G. Senjanovic, *Neutrino Mass and Spontaneous Parity Nonconservation*. Phys. Rev. Lett. **44** (1980) 912.

[34] T. Yanagida, *Horizontal Symmetry and Masses of Neutrinos*. Prog. Theor. Phys. **64** (1980) 1103.

[35] J. Schechter and J. W. F. Valle, *Neutrino Masses in SU(2) x U(1) Theories*. Phys. Rev. D **22** (1980) 2227.

[36] Z. Maki, M. Nakagawa, and S. Sakata, *Remarks on the unified model of elementary particles*. Prog. Theor. Phys. **28** (1962) 870–880.

[37] I. Esteban, M. C. Gonzalez-Garcia, A. Hernandez-Cabezudo, M. Maltoni, and T. Schwetz, *Global analysis of three-flavour neutrino oscillations: synergies and tensions in the determination of* θ_{23}*,* δ_{CP}*, and the mass ordering*. JHEP **01** (2019) 106, arXiv:1811.05487 [hep-ph].

[38] N. Cabibbo, *Unitary Symmetry and Leptonic Decays*. Phys. Rev. Lett. **10** (1963) 531–533.

[39] M. Kobayashi and T. Maskawa, *CP Violation in the Renormalizable Theory of Weak Interaction*. Prog. Theor. Phys. **49** (1973) 652–657.

[40] D. Buttazzo, A. Greljo, G. Isidori, and D. Marzocca, *B-physics anomalies: a guide to combined explanations*. JHEP **11** (2017) 044, arXiv:1706.07808 [hep-ph].

[41] R. D. Peccei and H. R. Quinn, *CP Conservation in the Presence of Instantons*. Phys. Rev. Lett. **38** (1977) 1440–1443.

[42] R. D. Peccei and H. R. Quinn, *Constraints Imposed by CP Conservation in the Presence of Instantons*. Phys. Rev. D **16** (1977) 1791–1797.

[43] S. Weinberg, *A New Light Boson?* Phys. Rev. Lett. **40** (1978) 223–226.

[44] R. D. Peccei, *The Strong CP problem and axions*. Lect. Notes Phys. **741** (2008) 3–17, arXiv:hep-ph/0607268.

[45] E. Witten, *Mass Hierarchies in Supersymmetric Theories*. Phys. Lett. B **105** (1981) 267.

[46] I. Antoniadis, N. Arkani-Hamed, S. Dimopoulos, and G. R. Dvali, *New dimensions at a millimeter to a Fermi and superstrings at a TeV*. Phys. Lett. B **436** (1998) 257–263, arXiv:hep-ph/9804398.

[47] L. Randall and R. Sundrum, *A Large mass hierarchy from a small extra dimension*. Phys. Rev. Lett. **83** (1999) 3370–3373, arXiv:hep-ph/9905221.

[48] F. Zwicky, *Die Rotverschiebung von extragalaktischen Nebeln*. Helv. Phys. Acta **6** (1933) 110–127.

[49] V. C. Rubin and W. K. Ford, Jr., *Rotation of the Andromeda Nebula from a Spectroscopic Survey of Emission Regions*. Astrophys. J. **159** (1970) 379–403.

[50] V. C. Rubin, N. Thonnard, and W. K. Ford, Jr., *Rotational properties of 21 SC galaxies with a large range of luminosities and radii, from NGC 4605 /R = 4kpc/ to UGC 2885 /R = 122 kpc/*. Astrophys. J. **238** (1980) 471.

[51] D. Clowe, A. Gonzalez, and M. Markevitch, *Weak lensing mass reconstruction of the interacting cluster 1E0657-558: Direct evidence for the existence of dark matter*. Astrophys. J. **604** (2004) 596–603, arXiv:astro-ph/0312273.

[52] **Supernova Search Team** Collaboration, A. G. Riess *et al.*, *Observational evidence from supernovae for an accelerating universe and a cosmological constant*. Astron. J. **116** (1998) 1009–1038, arXiv:astro-ph/9805201.

[53] **Supernova Cosmology Project** Collaboration, S. Perlmutter *et al.*, *Measurements of Ω and Λ from 42 high redshift supernovae*. Astrophys. J. **517** (1999) 565–586, arXiv:astro-ph/9812133.

[54] S. Perlmutter, M. S. Turner, and M. J. White, *Constraining dark energy with SNe Ia and large scale structure*. Phys. Rev. Lett. **83** (1999) 670–673, arXiv:astro-ph/9901052.

[55] E. Hubble, *A relation between distance and radial velocity among extra-galactic nebulae*. Proc. Nat. Acad. Sci. **15** (1929) 168–173.

[56] G. R. Farrar and P. J. E. Peebles, *Interacting dark matter and dark energy.* Astrophys. J. **604** (2004) 1–11, arXiv:astro-ph/0307316.

[57] A. A. Costa, R. C. G. Landim, B. Wang, and E. Abdalla, *Interacting Dark Energy: Possible Explanation for 21-cm Absorption at Cosmic Dawn.* Eur. Phys. J. C **78** (2018) no. 9, 746, arXiv:1803.06944 [astro-ph.CO].

[58] W. Yang, A. Mukherjee, E. Di Valentino, and S. Pan, *Interacting dark energy with time varying equation of state and the H_0 tension.* Phys. Rev. D **98** (2018) no. 12, 123527, arXiv:1809.06883 [astro-ph.CO].

[59] V. Poulin, T. L. Smith, T. Karwal, and M. Kamionkowski, *Early Dark Energy Can Resolve The Hubble Tension.* Phys. Rev. Lett. **122** (2019) no. 22, 221301, arXiv:1811.04083 [astro-ph.CO].

[60] M. Viel, J. Lesgourgues, M. G. Haehnelt, S. Matarrese, and A. Riotto, *Constraining warm dark matter candidates including sterile neutrinos and light gravitinos with WMAP and the Lyman-alpha forest.* Phys. Rev. D **71** (2005) 063534, arXiv:astro-ph/0501562.

[61] M. Viel, G. D. Becker, J. S. Bolton, and M. G. Haehnelt, *Warm dark matter as a solution to the small scale crisis: New constraints from high redshift Lyman-α forest data.* Phys. Rev. D **88** (2013) 043502, arXiv:1306.2314 [astro-ph.CO].

[62] B. Carr, F. Kuhnel, and M. Sandstad, *Primordial Black Holes as Dark Matter.* Phys. Rev. D **94** (2016) no. 8, 083504, arXiv:1607.06077 [astro-ph.CO].

[63] J. L. Feng, *Dark Matter Candidates from Particle Physics and Methods of Detection.* Ann. Rev. Astron. Astrophys. **48** (2010) 495–545, arXiv:1003.0904 [astro-ph.CO].

[64] G. Jungman, M. Kamionkowski, and K. Griest, *Supersymmetric dark matter.* Phys. Rept. **267** (1996) 195–373, arXiv:hep-ph/9506380.

[65] ", US Cosmic Visions: New Ideas in Dark Matter 2017: Community Reportt," in *U.S. Cosmic Visions: New Ideas in Dark Matter*. 7, 2017. arXiv:1707.04591 [hep-ph].

[66] W. Hu, R. Barkana, and A. Gruzinov, *Cold and fuzzy dark matter.* Phys. Rev. Lett. **85** (2000) 1158–1161, arXiv:astro-ph/0003365.

[67] L. Hui, J. P. Ostriker, S. Tremaine, and E. Witten, *Ultralight scalars as cosmological dark matter.* Phys. Rev. D **95** (2017) no. 4, 043541, arXiv:1610.08297 [astro-ph.CO].

[68] M. Pospelov, *Secluded U(1) below the weak scale.* Phys. Rev. D **80** (2009) 095002, arXiv:0811.1030 [hep-ph].

[69] M. Vogelsberger, J. Zavala, F.-Y. Cyr-Racine, C. Pfrommer, T. Bringmann, and K. Sigurdson, *ETHOS – an effective theory of structure formation: dark matter physics as a possible explanation of the small-scale CDM problems*. Mon. Not. Roy. Astron. Soc. **460** (2016) no. 2, 1399–1416, arXiv:1512.05349 [astro-ph.CO].

[70] K. Petraki and R. R. Volkas, *Review of asymmetric dark matter*. Int. J. Mod. Phys. A **28** (2013) 1330028, arXiv:1305.4939 [hep-ph].

[71] Y. Farzan and E. Ma, *Dirac neutrino mass generation from dark matter*. Phys. Rev. D **86** (2012) 033007, arXiv:1204.4890 [hep-ph].

[72] P. Jean *et al.*, *Early SPI / INTEGRAL measurements of 511 keV line emission from the 4th quadrant of the Galaxy*. Astron. Astrophys. **407** (2003) L55, arXiv:astro-ph/0309484 [astro-ph].

[73] J. Knodlseder *et al.*, *Early SPI / INTEGRAL contraints on the morphology of the 511 keV line emission in the 4th galactic quadrant*. Astron. Astrophys. **411** (2003) L457–L460, arXiv:astro-ph/0309442.

[74] E. Bulbul, M. Markevitch, A. Foster, R. K. Smith, M. Loewenstein, and S. W. Randall, *Detection of An Unidentified Emission Line in the Stacked X-ray spectrum of Galaxy Clusters*. Astrophys. J. **789** (2014) 13, arXiv:1402.2301 [astro-ph.CO].

[75] A. Boyarsky, O. Ruchayskiy, D. Iakubovskyi, and J. Franse, *Unidentified Line in X-Ray Spectra of the Andromeda Galaxy and Perseus Galaxy Cluster*. Phys. Rev. Lett. **113** (2014) 251301, arXiv:1402.4119 [astro-ph.CO].

[76] D. Hooper and L. Goodenough, *Dark Matter Annihilation in The Galactic Center As Seen by the Fermi Gamma Ray Space Telescope*. Phys. Lett. B **697** (2011) 412–428, arXiv:1010.2752 [hep-ph].

[77] A. H. Guth, *The Inflationary Universe: A Possible Solution to the Horizon and Flatness Problems*. Phys. Rev. D **23** (1981) 347–356.

[78] A. D. Linde, *A New Inflationary Universe Scenario: A Possible Solution of the Horizon, Flatness, Homogeneity, Isotropy and Primordial Monopole Problems*. Phys. Lett. B **108** (1982) 389–393.

[79] L. Kofman, A. D. Linde, and A. A. Starobinsky, *Reheating after inflation*. Phys. Rev. Lett. **73** (1994) 3195–3198, arXiv:hep-th/9405187.

[80] P. Petreczky, *Lattice QCD at non-zero temperature*. J. Phys. G **39** (2012) 093002, arXiv:1203.5320 [hep-lat].

[81] D. J. Gross, R. D. Pisarski, and L. G. Yaffe, *QCD and Instantons at Finite Temperature*. Rev. Mod. Phys. **53** (1981) 43.

[82] E. Witten, *Cosmic Separation of Phases*. Phys. Rev. D **30** (1984) 272–285.

[83] Y. Aoki, G. Endrodi, Z. Fodor, S. D. Katz, and K. K. Szabo, *The Order of the quantum chromodynamics transition predicted by the standard model of particle physics*. Nature **443** (2006) 675–678, arXiv:hep-lat/0611014.

[84] M. Pospelov and J. Pradler, *Big Bang Nucleosynthesis as a Probe of New Physics*. Ann. Rev. Nucl. Part. Sci. **60** (2010) 539–568, arXiv:1011.1054 [hep-ph].

[85] R. H. Cyburt, B. D. Fields, K. A. Olive, and T.-H. Yeh, *Big Bang Nucleosynthesis: 2015*. Rev. Mod. Phys. **88** (2016) 015004, arXiv:1505.01076 [astro-ph.CO].

[86] **Planck** Collaboration, N. Aghanim *et al.*, *Planck 2018 results. VI. Cosmological parameters*. arXiv:1807.06209 [astro-ph.CO].

[87] **SDSS** Collaboration, W. J. Percival *et al.*, *Baryon Acoustic Oscillations in the Sloan Digital Sky Survey Data Release 7 Galaxy Sample*. Mon. Not. Roy. Astron. Soc. **401** (2010) 2148–2168, arXiv:0907.1660 [astro-ph.CO].

[88] F. Beutler, C. Blake, M. Colless, D. H. Jones, L. Staveley-Smith, L. Campbell, Q. Parker, W. Saunders, and F. Watson, *The 6dF Galaxy Survey: Baryon Acoustic Oscillations and the Local Hubble Constant*. Mon. Not. Roy. Astron. Soc. **416** (2011) 3017–3032, arXiv:1106.3366 [astro-ph.CO].

[89] S. Naoz, S. Noter, and R. Barkana, *The first stars in the universe*. Mon. Not. Roy. Astron. Soc. **373** (2006) L98, arXiv:astro-ph/0604050.

[90] T. Abel, G. L. Bryan, and M. L. Norman, *The formation of the first star in the Universe*. Science **295** (2002) 93, arXiv:astro-ph/0112088.

[91] S. A. Wouthuysen, *On the excitation mechanism of the 21-cm (radio-frequency) interstellar hydrogen emission line.*Astron. J. **57** (Jan., 1952) 31–32.

[92] G. B. Field, *Excitation of the Hydrogen 21-CM Line*Proceedings of the IRE **46** (Jan., 1958) 240–250.

[93] C. M. Hirata, *Wouthuysen-Field coupling strength and application to high-redshift 21 cm radiation*. Mon. Not. Roy. Astron. Soc. **367** (2006) 259–274, arXiv:astro-ph/0507102.

[94] J. R. Pritchard and A. Loeb, *21-cm cosmology*. Rept. Prog. Phys. **75** (2012) 086901, arXiv:1109.6012 [astro-ph.CO].

[95] J. E. Gunn and B. A. Peterson, *On the Density of Neutral Hydrogen in Intergalactic Space*. Astrophys. J. **142** (1965) 1633.

[96] **SDSS** Collaboration, R. H. Becker *et al.*, *Evidence for Reionization at Z ~ 6: Detection of a Gunn-Peterson trough in a Z = 6.28 Quasar*. Astron. J. **122** (2001) 2850, arXiv:astro-ph/0108097.

[97] G. R. Blumenthal, S. M. Faber, J. R. Primack, and M. J. Rees, *Formation of Galaxies and Large Scale Structure with Cold Dark Matter*. Nature **311** (1984) 517–525.

[98] M. Davis, G. Efstathiou, C. S. Frenk, and S. D. M. White, *The Evolution of Large Scale Structure in a Universe Dominated by Cold Dark Matter*. Astrophys. J. **292** (1985) 371–394.

[99] J. R. Bond, L. Kofman, and D. Pogosyan, *How filaments are woven into the cosmic web*. Nature **380** (1996) 603–606, arXiv:astro-ph/9512141.

[100] A. G. Riess *et al.*, *A 2.4% Determination of the Local Value of the Hubble Constant*. Astrophys. J. **826** (2016) no. 1, 56, arXiv:1604.01424 [astro-ph.CO].

[101] C.-T. Chiang and A. Slosar, *Inferences of H_0 in presence of a non-standard recombination*. arXiv:1811.03624 [astro-ph.CO].

[102] K. Jedamzik and L. Pogosian, *Relieving the Hubble tension with primordial magnetic fields*. Phys. Rev. Lett. **125** (2020) no. 18, 181302, arXiv:2004.09487 [astro-ph.CO].

[103] K. K. Boddy, V. Gluscevic, V. Poulin, E. D. Kovetz, M. Kamionkowski, and R. Barkana, *Critical assessment of CMB limits on dark matter-baryon scattering: New treatment of the relative bulk velocity*. Phys. Rev. D **98** (2018) no. 12, 123506, arXiv:1808.00001 [astro-ph.CO].

[104] B. D. Fields, *The primordial lithium problem*. Ann. Rev. Nucl. Part. Sci. **61** (2011) 47–68, arXiv:1203.3551 [astro-ph.CO].

[105] K. Jedamzik, *Neutralinos and Big Bang nucleosynthesis*. Phys. Rev. D **70** (2004) 083510, arXiv:astro-ph/0405583.

[106] K. Hamaguchi, T. Hatsuda, M. Kamimura, Y. Kino, and T. T. Yanagida, *Stau-catalyzed ^{6}Li Production in Big-Bang Nucleosynthesis*. Phys. Lett. B **650** (2007) 268–274, arXiv:hep-ph/0702274.

[107] A. Coc, N. J. Nunes, K. A. Olive, J.-P. Uzan, and E. Vangioni, *Coupled Variations of Fundamental Couplings and Primordial Nucleosynthesis*. Phys. Rev. D **76** (2007) 023511, arXiv:astro-ph/0610733.

[108] M. Regis and C. Clarkson, *Do primordial Lithium abundances imply there's no Dark Energy?* Gen. Rel. Grav. **44** (2012) 567–579, arXiv:1003.1043 [astro-ph.CO].

[109] C. Angulo *et al.*, *The $Be^7(d,p)2\alpha$ cross section at big bang energies and the primordial Li^7 abundances.* Astrophys. J. Lett. **630** (2005) L105–L108, arXiv:astro-ph/0508454.

[110] R. H. Cyburt and M. Pospelov, *Resonant enhancement of nuclear reactions as a possible solution to the cosmological lithium problem.* Int. J. Mod. Phys. E **21** (2012) 1250004, arXiv:0906.4373 [astro-ph.CO].

[111] N. Chakraborty, B. D. Fields, and K. A. Olive, *Resonant Destruction as a Possible Solution to the Cosmological Lithium Problem.* Phys. Rev. D **83** (2011) 063006, arXiv:1011.0722 [astro-ph.CO].

[112] C. Broggini, L. Canton, G. Fiorentini, and F. L. Villante, *The cosmological 7Li problem from a nuclear physics perspective.* JCAP **06** (2012) 030, arXiv:1202.5232 [astro-ph.CO].

[113] B. Follin, L. Knox, M. Millea, and Z. Pan, *First Detection of the Acoustic Oscillation Phase Shift Expected from the Cosmic Neutrino Background.* Phys. Rev. Lett. **115** (2015) no. 9, 091301, arXiv:1503.07863 [astro-ph.CO].

[114] A. Faessler, R. Hodak, S. Kovalenko, and F. Simkovic, *Can one measure the Cosmic Neutrino Background?* Int. J. Mod. Phys. E **26** (2017) no. 01n02, 1740008, arXiv:1602.03347 [nucl-th].

[115] C. Grojean and G. Servant, *Gravitational Waves from Phase Transitions at the Electroweak Scale and Beyond.* Phys. Rev. D **75** (2007) 043507, arXiv:hep-ph/0607107.

[116] C. Caprini *et al.*, *Science with the space-based interferometer eLISA. II: Gravitational waves from cosmological phase transitions.* JCAP **04** (2016) 001, arXiv:1512.06239 [astro-ph.CO].

[117] M. Dine and A. Kusenko, *The Origin of the matter - antimatter asymmetry.* Rev. Mod. Phys. **76** (2003) 1, arXiv:hep-ph/0303065.

[118] M. Fukugita and T. Yanagida, *Baryogenesis Without Grand Unification.* Phys. Lett. B **174** (1986) 45–47.

[119] D. E. Morrissey and M. J. Ramsey-Musolf, *Electroweak baryogenesis.* New J. Phys. **14** (2012) 125003, arXiv:1206.2942 [hep-ph].

[120] M. A. Luty, *Baryogenesis via leptogenesis.* Phys. Rev. D **45** (1992) 455–465.

[121] S. Davidson, E. Nardi, and Y. Nir, *Leptogenesis*. Phys. Rept. **466** (2008) 105–177, arXiv:0802.2962 [hep-ph].

[122] **BICEP2, Planck** Collaboration, P. A. R. Ade *et al.*, *Joint Analysis of BICEP2/KeckArray and Planck Data*. Phys. Rev. Lett. **114** (2015) 101301, arXiv:1502.00612 [astro-ph.CO].

[123] G. Kauffmann, S. D. M. White, and B. Guiderdoni, *The Formation and Evolution of Galaxies Within Merging Dark Matter Haloes*. Mon. Not. Roy. Astron. Soc. **264** (1993) 201.

[124] A. A. Klypin, A. V. Kravtsov, O. Valenzuela, and F. Prada, *Where are the missing Galactic satellites?* Astrophys. J. **522** (1999) 82–92, arXiv:astro-ph/9901240.

[125] B. Moore, S. Ghigna, F. Governato, G. Lake, T. R. Quinn, J. Stadel, and P. Tozzi, *Dark matter substructure within galactic halos*. Astrophys. J. Lett. **524** (1999) L19–L22, arXiv:astro-ph/9907411.

[126] M. Boylan-Kolchin, J. S. Bullock, and M. Kaplinghat, *Too big to fail? The puzzling darkness of massive Milky Way subhaloes*. Mon. Not. Roy. Astron. Soc. **415** (2011) L40, arXiv:1103.0007 [astro-ph.CO].

[127] M. Boylan-Kolchin, J. S. Bullock, and M. Kaplinghat, *The Milky Way's bright satellites as an apparent failure of LCDM*. Mon. Not. Roy. Astron. Soc. **422** (2012) 1203–1218, arXiv:1111.2048 [astro-ph.CO].

[128] D. N. Spergel and P. J. Steinhardt, *Observational evidence for selfinteracting cold dark matter*. Phys. Rev. Lett. **84** (2000) 3760–3763, arXiv:astro-ph/9909386.

[129] A. M. Brooks, M. Kuhlen, A. Zolotov, and D. Hooper, *A Baryonic Solution to the Missing Satellites Problem*. Astrophys. J. **765** (2013) 22, arXiv:1209.5394 [astro-ph.CO].

[130] A. M. Brooks and A. Zolotov, *Why Baryons Matter: The Kinematics of Dwarf Spheroidal Satellites*. Astrophys. J. **786** (2014) 87, arXiv:1207.2468 [astro-ph.CO].

[131] D. H. Weinberg, J. S. Bullock, F. Governato, R. Kuzio de Naray, and A. H. G. Peter, *Cold dark matter: controversies on small scales*. Proc. Nat. Acad. Sci. **112** (2015) 12249–12255, arXiv:1306.0913 [astro-ph.CO].

[132] Q. Zhu, F. Marinacci, M. Maji, Y. Li, V. Springel, and L. Hernquist, *Baryonic impact on the dark matter distribution in Milky Way-sized galaxies and their satellites*. Mon. Not. Roy. Astron. Soc. **458** (2016) no. 2, 1559–1580, arXiv:1506.05537 [astro-ph.CO].

[133] **BOSS** Collaboration, K. S. Dawson *et al.*, *The Baryon Oscillation Spectroscopic Survey of SDSS-III*. Astron. J. **145** (2013) 10, arXiv:1208.0022 [astro-ph.CO].

[134] J. D. Bowman, A. E. E. Rogers, R. A. Monsalve, T. J. Mozdzen, and N. Mahesh, *An absorption profile centred at 78 megahertz in the sky-averaged spectrum*. Nature **555** (2018) no. 7694, 67–70, arXiv:1810.05912 [astro-ph.CO].

[135] J. B. Muñoz and A. Loeb, *A small amount of mini-charged dark matter could cool the baryons in the early Universe*. Nature **557** (2018) no. 7707, 684, arXiv:1802.10094 [astro-ph.CO].

[136] M. Pospelov, J. Pradler, J. T. Ruderman, and A. Urbano, *Room for New Physics in the Rayleigh-Jeans Tail of the Cosmic Microwave Background*. Phys. Rev. Lett. **121** (2018) no. 3, 031103, arXiv:1803.07048 [hep-ph].

[137] A. Fialkov and R. Barkana, *Signature of Excess Radio Background in the 21-cm Global Signal and Power Spectrum*. Mon. Not. Roy. Astron. Soc. **486** (2019) no. 2, 1763–1773, arXiv:1902.02438 [astro-ph.CO].

[138] G. D'Amico, P. Panci, and A. Strumia, *Bounds on Dark Matter annihilations from 21 cm data*. Phys. Rev. Lett. **121** (2018) no. 1, 011103, arXiv:1803.03629 [astro-ph.CO].

[139] K. Cheung, J.-L. Kuo, K.-W. Ng, and Y.-L. S. Tsai, *The impact of EDGES 21-cm data on dark matter interactions*. Phys. Lett. B **789** (2019) 137–144, arXiv:1803.09398 [astro-ph.CO].

[140] H. Liu and T. R. Slatyer, *Implications of a 21-cm signal for dark matter annihilation and decay*. Phys. Rev. D **98** (2018) no. 2, 023501, arXiv:1803.09739 [astro-ph.CO].

[141] S. Fraser *et al.*, *The EDGES 21 cm Anomaly and Properties of Dark Matter*. Phys. Lett. B **785** (2018) 159–164, arXiv:1803.03245 [hep-ph].

[142] A. Schneider, *Constraining noncold dark matter models with the global 21-cm signal*. Phys. Rev. D **98** (2018) no. 6, 063021, arXiv:1805.00021 [astro-ph.CO].

[143] S. Furlanetto, S. P. Oh, and F. Briggs, *Cosmology at Low Frequencies: The 21 cm Transition and the High-Redshift Universe*. Phys. Rept. **433** (2006) 181–301, arXiv:astro-ph/0608032.

[144] L. J. Hall, K. Jedamzik, J. March-Russell, and S. M. West, *Freeze-In Production of FIMP Dark Matter*. JHEP **03** (2010) 080, arXiv:0911.1120 [hep-ph].

[145] W. Chao, X.-F. Li, and L. Wang, *Filtered pseudo-scalar dark matter and gravitational waves from first order phase transition*. arXiv:2012.15113 [hep-ph].

[146] A. Azatov, M. Vanvlasselaer, and W. Yin, *Dark Matter production from relativistic bubble walls*. arXiv:2101.05721 [hep-ph].

[147] B. W. Lee and S. Weinberg, *Cosmological Lower Bound on Heavy Neutrino Masses*. Phys. Rev. Lett. **39** (1977) 165–168.

[148] K. Griest and M. Kamionkowski, *Unitarity Limits on the Mass and Radius of Dark Matter Particles*. Phys. Rev. Lett. **64** (1990) 615.

[149] J. Smirnov and J. F. Beacom, *TeV-Scale Thermal WIMPs: Unitarity and its Consequences*. Phys. Rev. D **100** (2019) no. 4, 043029, arXiv:1904.11503 [hep-ph].

[150] S. Tremaine and J. E. Gunn, *Dynamical Role of Light Neutral Leptons in Cosmology*. Phys. Rev. Lett. **42** (1979) 407–410.

[151] A. Boyarsky, O. Ruchayskiy, and D. Iakubovskyi, *A Lower bound on the mass of Dark Matter particles*. JCAP **03** (2009) 005, arXiv:0808.3902 [hep-ph].

[152] H. Davoudiasl, P. B. Denton, and D. A. McGady, *Ultralight Fermionic Dark Matter*. Phys. Rev. D **103** (2021) 055014, arXiv:2008.06505 [hep-ph].

[153] O. Buchmueller, C. Doglioni, and L. T. Wang, *Search for dark matter at colliders*. Nature Phys. **13** (2017) no. 3, 217–223, arXiv:1912.12739 [hep-ex].

[154] J. M. Gaskins, *A review of indirect searches for particle dark matter*. Contemp. Phys. **57** (2016) no. 4, 496–525, arXiv:1604.00014 [astro-ph.HE].

[155] M. Schumann, *Direct Detection of WIMP Dark Matter: Concepts and Status*. J. Phys. G **46** (2019) no. 10, 103003, arXiv:1903.03026 [astro-ph.CO].

[156] N. Borodatchenkova, D. Choudhury, and M. Drees, *Probing MeV dark matter at low-energy e+e- colliders*. Phys. Rev. Lett. **96** (2006) 141802, arXiv:hep-ph/0510147.

[157] B. Batell, M. Pospelov, and A. Ritz, *Exploring Portals to a Hidden Sector Through Fixed Targets*. Phys. Rev. D **80** (2009) 095024, arXiv:0906.5614 [hep-ph].

[158] P. deNiverville, M. Pospelov, and A. Ritz, *Observing a light dark matter beam with neutrino experiments*. Phys. Rev. D **84** (2011) 075020, arXiv:1107.4580 [hep-ph].

[159] P. deNiverville, D. McKeen, and A. Ritz, *Signatures of sub-GeV dark matter beams at neutrino experiments*. Phys. Rev. D **86** (2012) 035022, arXiv:1205.3499 [hep-ph].

[160] R. Essig, J. Mardon, and T. Volansky, *Direct Detection of Sub-GeV Dark Matter*. Phys. Rev. **D85** (2012) 076007, arXiv:1108.5383 [hep-ph].

[161] C. Kouvaris and J. Pradler, *Probing sub-GeV Dark Matter with conventional detectors*. Phys. Rev. Lett. **118** (2017) no. 3, 031803, arXiv:1607.01789 [hep-ph].

[162] T. Bringmann and M. Pospelov, *Novel direct detection constraints on light dark matter*. Phys. Rev. Lett. **122** (2019) no. 17, 171801, arXiv:1810.10543 [hep-ph].

[163] H. An, M. Pospelov, J. Pradler, and A. Ritz, *Directly Detecting MeV-scale Dark Matter via Solar Reflection*. Phys. Rev. Lett. **120** (2018) no. 14, 141801, arXiv:1708.03642 [hep-ph].

[164] M. Ibe, W. Nakano, Y. Shoji, and K. Suzuki, *Migdal Effect in Dark Matter Direct Detection Experiments*. JHEP **03** (2018) 194, arXiv:1707.07258 [hep-ph].

[165] R. Essig, J. Pradler, M. Sholapurkar, and T.-T. Yu, *Relation between the Migdal Effect and Dark Matter-Electron Scattering in Isolated Atoms and Semiconductors*. Phys. Rev. Lett. **124** (2020) no. 2, 021801, arXiv:1908.10881 [hep-ph].

[166] T. Lin, *Dark matter models and direct detection*. PoS **333** (2019) 009, arXiv:1904.07915 [hep-ph].

[167] R. Essig, E. Kuflik, S. D. McDermott, T. Volansky, and K. M. Zurek, *Constraining Light Dark Matter with Diffuse X-Ray and Gamma-Ray Observations*. JHEP **11** (2013) 193, arXiv:1309.4091 [hep-ph].

[168] S. Galli, F. Iocco, G. Bertone, and A. Melchiorri, *CMB constraints on Dark Matter models with large annihilation cross-section*. Phys. Rev. D **80** (2009) 023505, arXiv:0905.0003 [astro-ph.CO].

[169] T. R. Slatyer, N. Padmanabhan, and D. P. Finkbeiner, *CMB Constraints on WIMP Annihilation: Energy Absorption During the Recombination Epoch*. Phys. Rev. D **80** (2009) 043526, arXiv:0906.1197 [astro-ph.CO].

[170] S. Davidson, S. Hannestad, and G. Raffelt, *Updated bounds on millicharged particles*. JHEP **05** (2000) 003, arXiv:hep-ph/0001179.

[171] H. An, M. Pospelov, and J. Pradler, *New stellar constraints on dark photons*. Phys. Lett. **B725** (2013) 190–195, arXiv:1302.3884 [hep-ph].

[172] J. H. Chang, R. Essig, and S. D. McDermott, *Revisiting Supernova 1987A Constraints on Dark Photons*. JHEP **01** (2017) 107, arXiv:1611.03864 [hep-ph].

[173] J. H. Chang, R. Essig, and S. D. McDermott, *Supernova 1987A Constraints on Sub-GeV Dark Sectors, Millicharged Particles, the QCD Axion, and an Axion-like Particle*. JHEP **09** (2018) 051, arXiv:1803.00993 [hep-ph].

[174] M. Rocha, A. H. G. Peter, J. S. Bullock, M. Kaplinghat, S. Garrison-Kimmel, J. Onorbe, and L. A. Moustakas, *Cosmological Simulations with Self-Interacting Dark Matter I: Constant Density Cores and Substructure*. Mon. Not. Roy. Astron. Soc. **430** (2013) 81–104, arXiv:1208.3025 [astro-ph.CO].

[175] P. Fayet, *U-boson production in e+ e- annihilations, psi and Upsilon decays, and Light Dark Matter*. Phys. Rev. D **75** (2007) 115017, arXiv:hep-ph/0702176.

[176] C. Boehm, D. Hooper, J. Silk, M. Casse, and J. Paul, *MeV dark matter: Has it been detected?* Phys. Rev. Lett. **92** (2004) 101301, arXiv:astro-ph/0309686 [astro-ph].

[177] B. Holdom, *Two U(1)'s and Epsilon Charge Shifts*. Phys. Lett. B **166** (1986) 196–198.

[178] B. Patt and F. Wilczek, *Higgs-field portal into hidden sectors*. arXiv:hep-ph/0605188.

[179] A. Falkowski, J. Juknevich, and J. Shelton, *Dark Matter Through the Neutrino Portal*. arXiv:0908.1790 [hep-ph].

[180] J. F. Cherry, A. Friedland, and I. M. Shoemaker, *Neutrino Portal Dark Matter: From Dwarf Galaxies to IceCube*. arXiv:1411.1071 [hep-ph].

[181] M. Blennow, E. Fernandez-Martinez, A. Olivares-Del Campo, S. Pascoli, S. Rosauro-Alcaraz, and A. V. Titov, *Neutrino Portals to Dark Matter*. Eur. Phys. J. C **79** (2019) no. 7, 555, arXiv:1903.00006 [hep-ph].

[182] ", Working Group Report: New Light Weakly Coupled Particlest," in *Community Summer Study 2013: Snowmass on the Mississippi*. 10, 2013. arXiv:1311.0029 [hep-ph].

[183] X. Chu, J. Pradler, and L. Semmelrock, *Light dark states with electromagnetic form factors*. Phys. Rev. **D99** (2019) no. 1, 015040, arXiv:1811.04095 [hep-ph].

[184] B. J. Kavanagh, P. Panci, and R. Ziegler, *Faint Light from Dark Matter: Classifying and Constraining Dark Matter-Photon Effective Operators*. JHEP **04** (2019) 089, arXiv:1810.00033 [hep-ph].

[185] I. B. Zel'Dovich, *Electromagnetic Interaction with Parity Violation*Soviet Journal of Experimental and Theoretical Physics **6** (Jan., 1958) 1184.

[186] C. S. Wood, S. C. Bennett, D. Cho, B. P. Masterson, J. L. Roberts, C. E. Tanner, and C. E. Wieman, *Measurement of parity nonconservation and an anapole moment in cesium*. Science **275** (1997) 1759–1763.

[187] C. Giunti and A. Studenikin, *Neutrino electromagnetic interactions: a window to new physics*. Rev. Mod. Phys. **87** (2015) 531, arXiv:1403.6344 [hep-ph].

[188] J. Bagnasco, M. Dine, and S. D. Thomas, *Detecting technibaryon dark matter*. Phys. Lett. **B320** (1994) 99–104, arXiv:hep-ph/9310290 [hep-ph].

[189] R. Foadi, M. T. Frandsen, and F. Sannino, *Technicolor Dark Matter*. Phys. Rev. **D80** (2009) 037702, arXiv:0812.3406 [hep-ph].

[190] O. Antipin, M. Redi, A. Strumia, and E. Vigiani, *Accidental Composite Dark Matter*. JHEP **07** (2015) 039, arXiv:1503.08749 [hep-ph].

[191] S. Raby and G. West, *Experimental Consequences and Constraints for Magninos*. Phys. Lett. **B194** (1987) 557–562.

[192] M. Pospelov and A. Ritz, *Resonant scattering and recombination of pseudo-degenerate WIMPs*. Phys. Rev. **D78** (2008) 055003, arXiv:0803.2251 [hep-ph].

[193] G. G. Raffelt, *Stars as laboratories for fundamental physics*. 1996. http://wwwth.mpp.mpg.de/members/raffelt/mypapers/199613.pdf.

[194] N. Viaux, M. Catelan, P. B. Stetson, G. Raffelt, J. Redondo, A. A. R. Valcarce, and A. Weiss, *Neutrino and axion bounds from the globular cluster M5 (NGC 5904)*. Phys. Rev. Lett. **111** (2013) 231301, arXiv:1311.1669 [astro-ph.SR].

[195] J. A. Frieman, S. Dimopoulos, and M. S. Turner, *Axions and Stars*. Phys. Rev. **D36** (1987) 2201.

[196] G. G. Raffelt and G. D. Starkman, *STELLAR ENERGY TRANSFER BY keV MASS SCALARS*. Phys. Rev. **D40** (1989) 942.

[197] J. Redondo and G. Raffelt, *Solar constraints on hidden photons re-visited*. JCAP **1308** (2013) 034, arXiv:1305.2920 [hep-ph].

[198] N. Grevesse and A. J. Sauval, *Standard Solar Composition*. Space Sci. Rev. **85** (1998) 161–174.

[199] M. Asplund, N. Grevesse, A. J. Sauval, and P. Scott, *The chemical composition of the Sun*. Ann. Rev. Astron. Astrophys. **47** (2009) 481–522, arXiv:0909.0948 [astro-ph.SR].

[200] K. Blum and D. Kushnir, *Neutrino Signal of Collapse-induced Thermonuclear Supernovae: the Case for Prompt Black Hole Formation in SN1987A*. Astrophys. J. **828** (2016) no. 1, 31, arXiv:1601.03422 [astro-ph.HE].

[201] N. Bar, K. Blum, and G. D'Amico, *Is there a supernova bound on axions?* Phys. Rev. D **101** (2020) no. 12, 123025, arXiv:1907.05020 [hep-ph].

[202] H. A. Weldon, *Simple Rules for Discontinuities in Finite Temperature Field Theory*. Phys. Rev. **D28** (1983) 2007.

[203] M. E. Carrington, H. Defu, and R. Kobes, *Scattering amplitudes at finite temperature*. Phys. Rev. **D67** (2003) 025021, arXiv:hep-ph/0207115 [hep-ph].

[204] J. Alam, S. Sarkar, P. Roy, T. Hatsuda, and B. Sinha, *Thermal photons and lepton pairs from quark gluon plasma and hot hadronic matter*. Annals Phys. **286** (2001) 159–248, arXiv:hep-ph/9909267 [hep-ph].

[205] M. L. Bellac, *Thermal Field Theory*. Cambridge Monographs on Mathematical Physics. Cambridge University Press, 2011. http://www.cambridge.org/mw/academic/subjects/physics/theoretical-physics-and-mathematical-physics/thermal-field-theory?format=AR.

[206] E. Braaten, *Emissivity of a hot plasma from photon and plasmon decay*. Phys. Rev. Lett. **66** (1991) 1655.

[207] E. Vitagliano, J. Redondo, and G. Raffelt, *Solar neutrino flux at keV energies*. JCAP **1712** (2017) no. 12, 010, arXiv:1708.02248 [hep-ph].

[208] G. G. Raffelt, *Plasmon Decay Into Low Mass Bosons in Stars*. Phys. Rev. **D37** (1988) 1356.

[209] P. Gondolo and G. Gelmini, *Cosmic abundances of stable particles: Improved analysis*. Nucl. Phys. B **360** (1991) 145–179.

[210] J. Edsjo and P. Gondolo, *Neutralino relic density including coannihilations*. Phys. Rev. **D56** (1997) 1879–1894, arXiv:hep-ph/9704361 [hep-ph].

[211] D. Dearborn, G. Raffelt, P. Salati, J. Silk, and A. Bouquet, *Dark Matter and Thermal Pulses in Horizontal Branch Stars*. Astrophys. J. **354** (1990) 568.

[212] J. N. Bahcall, A. M. Serenelli, and S. Basu, *New solar opacities, abundances, helioseismology, and neutrino fluxes*. Astrophys. J. **621** (2005) L85–L88, arXiv:astro-ph/0412440 [astro-ph].

[213] T. Fischer, S. Chakraborty, M. Giannotti, A. Mirizzi, A. Payez, and A. Ringwald, *Probing axions with the neutrino signal from the next galactic supernova*. Phys. Rev. **D94** (2016) no. 8, 085012, arXiv:1605.08780 [astro-ph.HE].

[214] **Particle Data Group** Collaboration, M. Tanabashi *et al.*, *Review of Particle Physics*. Phys. Rev. **D98** (2018) no. 3, 030001.

[215] G. G. Raffelt, *New bound on neutrino dipole moments from globular cluster stars*. Phys. Rev. Lett. **64** (1990) 2856–2858.

[216] N. Viaux, M. Catelan, P. B. Stetson, G. Raffelt, J. Redondo, A. A. R. Valcarce, and A. Weiss, *Particle-physics constraints from the globular cluster M5: Neutrino Dipole Moments*. Astron. Astrophys. **558** (2013) A12, arXiv:1308.4627 [astro-ph.SR].

[217] S. Arceo-Díaz, K. P. Schröder, K. Zuber, and D. Jack, *Constraint on the magnetic dipole moment of neutrinos by the tip-RGB luminosity in ω-Centauri*. Astropart. Phys. **70** (2015) 1–11.

[218] M. Fukugita and S. Yazaki, *Reexamination of Astrophysical and Cosmological Constraints on the Magnetic Moment of Neutrinos*. Phys. Rev. **D36** (1987) 3817.

[219] G. G. Raffelt and D. S. P. Dearborn, *Bounds on Weakly Interacting Particles From Observational Lifetimes of Helium Burning Stars*. Phys. Rev. **D37** (1988) 549–551.

[220] G. G. Raffelt, *Limits on neutrino electromagnetic properties: An update*. Phys. Rept. **320** (1999) 319–327.

[221] J. H. Chang, R. Essig, and A. Reinert, *Light(ly)-coupled Dark Matter in the keV Range: Freeze-In and Constraints*. JHEP **03** (2021) 141, arXiv:1911.03389 [hep-ph].

[222] J. A. Grifols and E. Masso, *Charge Radius of the Neutrino: A Limit From SN1987A*. Phys. Rev. **D40** (1989) 3819.

[223] G. Steigman, *Primordial Helium And the Cosmic Background Radiation*. JCAP **1004** (2010) 029, arXiv:1002.3604 [astro-ph.CO].

[224] G. Mangano and P. D. Serpico, *A robust upper limit on $N_{\rm eff}$ from BBN, circa 2011*. Phys. Lett. **B701** (2011) 296–299, arXiv:1103.1261 [astro-ph.CO].

[225] J. Hamann, S. Hannestad, G. G. Raffelt, and Y. Y. Y. Wong, *Sterile neutrinos with eV masses in cosmology: How disfavoured exactly?* JCAP **1109** (2011) 034, arXiv:1108.4136 [astro-ph.CO].

[226] J. Alwall, R. Frederix, S. Frixione, V. Hirschi, F. Maltoni, O. Mattelaer, H. S. Shao, T. Stelzer, P. Torrielli, and M. Zaro, *The automated computation of tree-level and next-to-leading order differential cross sections, and their matching to parton shower simulations*. JHEP **07** (2014) 079, arXiv:1405.0301 [hep-ph].

[227] S. Alekhin *et al.*, *A facility to Search for Hidden Particles at the CERN SPS: the SHiP physics case*. Rept. Prog. Phys. **79** (2016) no. 12, 124201, arXiv:1504.04855 [hep-ph].

[228] R. Harnik, Z. Liu, and O. Palamara, *Millicharged Particles in Liquid Argon Neutrino Experiments*. JHEP **07** (2019) 170, arXiv:1902.03246 [hep-ph].

[229] M. Hoferichter, B. Kubis, S. Leupold, F. Niecknig, and S. P. Schneider, *Dispersive analysis of the pion transition form factor*. Eur. Phys. J. **C74** (2014) 3180, arXiv:1410.4691 [hep-ph].

[230] R. Escribano, P. Masjuan, and P. Sanchez-Puertas, *The η transition form factor from space- and time-like experimental data*. Eur. Phys. J. **C75** (2015) no. 9, 414, arXiv:1504.07742 [hep-ph].

[231] T. Husek, *Radiative corrections in Dalitz decays of π^0, η and η' mesons*. EPJ Web Conf. **199** (2019) 02015, arXiv:1811.12350 [hep-ph].

[232] T. Sjostrand, S. Mrenna, and P. Z. Skands, *PYTHIA 6.4 Physics and Manual*. JHEP **05** (2006) 026, arXiv:hep-ph/0603175 [hep-ph].

[233] T. Sjöstrand, S. Ask, J. R. Christiansen, R. Corke, N. Desai, P. Ilten, S. Mrenna, S. Prestel, C. O. Rasmussen, and P. Z. Skands, *An Introduction to PYTHIA 8.2*. Comput. Phys. Commun. **191** (2015) 159–177, arXiv:1410.3012 [hep-ph].

[234] L. Darmé, S. A. R. Ellis, and T. You, *Light Dark Sectors through the Fermion Portal*. arXiv:2001.01490 [hep-ph].

[235] B. Krusche, *Photoproduction of mesons from nuclei: In-medium properties of hadrons*. Prog. Part. Nucl. Phys. **55** (2005) 46–70, arXiv:nucl-ex/0411033 [nucl-ex].

[236] B. Batell, P. deNiverville, D. McKeen, M. Pospelov, and A. Ritz, *Leptophobic Dark Matter at Neutrino Factories*. Phys. Rev. **D90** (2014) no. 11, 115014, arXiv:1405.7049 [hep-ph].

[237] P. deNiverville, *Searching for hidden sector dark matter with fixed target neutrino experiments*. PhD thesis, U. Victoria (main), 2016-08-30. https://dspace.library.uvic.ca/handle/1828/7502.

[238] *SHiP sensitivity to Dark Photons*SHiP Collaboration (Sep, 2016) , CERN-SHiP-NOTE-2016-004. https://cds.cern.ch/record/2214092.

[239] P. deNiverville and C. Frugiuele, *Hunting sub-GeV dark matter with the NOνA near detector*. Phys. Rev. **D99** (2019) no. 5, 051701, arXiv:1807.06501 [hep-ph].

[240] V. De Romeri, K. J. Kelly, and P. A. N. Machado, *DUNE-PRISM Sensitivity to Light Dark Matter*. Phys. Rev. **D100** (2019) no. 9, 095010, arXiv:1903.10505 [hep-ph].

[241] B. Döbrich, J. Jaeckel, and T. Spadaro, *Light in the beam dump. Axion-Like Particle production from decay photons in proton beam-dumps*. JHEP **05** (2019) 213, arXiv:1904.02091 [hep-ph].

[242] E. Fermi. Z. Phys. **29** (1924) 315.

[243] C. F. von Weizsacker, *Radiation emitted in collisions of very fast electrons*. Z. Phys. **88** (1934) 612–625.

[244] E. J. Williams. Phys. Rev. **45** (1934) .

[245] J. Blümlein and J. Brunner, *New Exclusion Limits on Dark Gauge Forces from Proton Bremsstrahlung in Beam-Dump Data*. Phys. Lett. **B731** (2014) 320–326, arXiv:1311.3870 [hep-ph].

[246] P. deNiverville, C.-Y. Chen, M. Pospelov, and A. Ritz, *Light dark matter in neutrino beams: production modelling and scattering signatures at MiniBooNE, T2K and SHiP*. Phys. Rev. **D95** (2017) no. 3, 035006, arXiv:1609.01770 [hep-ph].

[247] J. L. Feng, I. Galon, F. Kling, and S. Trojanowski, *ForwArd Search ExpeRiment at the LHC*. Phys. Rev. **D97** (2018) no. 3, 035001, arXiv:1708.09389 [hep-ph].

[248] Y.-D. Tsai, P. deNiverville, and M. X. Liu, *The High-Energy Frontier of the Intensity Frontier: Closing the Dark Photon, Inelastic Dark Matter, and Muon g-2 Windows*. arXiv:1908.07525 [hep-ph].

[249] A. Faessler, M. I. Krivoruchenko, and B. V. Martemyanov, *Once more on electromagnetic form factors of nucleons in extended vector meson dominance model*. Phys. Rev. **C82** (2010) 038201, arXiv:0910.5589 [hep-ph].

[250] P. Coloma, B. A. Dobrescu, C. Frugiuele, and R. Harnik, *Dark matter beams at LBNF*. JHEP **04** (2016) 047, arXiv:1512.03852 [hep-ph].

[251] C. Frugiuele, *Probing sub-GeV dark sectors via high energy proton beams at LBNF/DUNE and MiniBooNE*. Phys. Rev. **D96** (2017) no. 1, 015029, arXiv:1701.05464 [hep-ph].

[252] A. de Gouvêa, P. J. Fox, R. Harnik, K. J. Kelly, and Y. Zhang, *Dark Tridents at Off-Axis Liquid Argon Neutrino Detectors*. JHEP **01** (2019) 001, arXiv:1809.06388 [hep-ph].

[253] D. E. Soper, M. Spannowsky, C. J. Wallace, and T. M. P. Tait, *Scattering of Dark Particles with Light Mediators*. Phys. Rev. **D90** (2014) no. 11, 115005, arXiv:1407.2623 [hep-ph].

[254] M. Hirai, S. Kumano, and T. H. Nagai, *Determination of nuclear parton distribution functions and their uncertainties in next-to-leading order*. Phys. Rev. **C76** (2007) 065207, arXiv:0709.3038 [hep-ph].

[255] **LSND** Collaboration, C. Athanassopoulos *et al.*, *The Liquid scintillator neutrino detector and LAMPF neutrino source*. Nucl. Instrum. Meth. **A388** (1997) 149–172, arXiv:nucl-ex/9605002 [nucl-ex].

[256] **MiniBooNE DM** Collaboration, A. A. Aguilar-Arevalo *et al.*, *Dark Matter Search in Nucleon, Pion, and Electron Channels from a Proton Beam Dump with MiniBooNE.* Phys. Rev. **D98** (2018) no. 11, 112004, arXiv:1807.06137 [hep-ex].

[257] **CHARM-II** Collaboration, K. De Winter *et al.*, *A Detector for the Study of Neutrino - Electron Scattering.* Nucl. Instrum. Meth. **A278** (1989) 670.

[258] **CHARM-II** Collaboration, P. Vilain *et al.*, *Precision measurement of electroweak parameters from the scattering of muon-neutrinos on electrons.* Phys. Lett. **B335** (1994) 246–252.

[259] G. R. Brown, *Sensitivity Study for Low Mass Dark Matter Search at DUNE.* Diploma Thesis, Texas U., Arlington, 2018. http://lss.fnal.gov/archive/masters/fermilab-masters-2018-02.pdf.

[260] M. Hostert, *Hidden Physics at the Neutrino Frontier: Tridents, Dark Forces, and Hidden Particles.* PhD thesis, Durham U., 2019. http://etheses.dur.ac.uk/13289/.

[261] **SHiP** Collaboration, M. Anelli *et al.*, *A facility to Search for Hidden Particles (SHiP) at the CERN SPS.* arXiv:1504.04956 [physics.ins-det].

[262] L. Buonocore, C. Frugiuele, F. Maltoni, O. Mattelaer, and F. Tramontano, *Event generation for beam dump experiments.* JHEP **05** (2019) 028, arXiv:1812.06771 [hep-ph].

[263] R. Ball *et al.*, *The neutrino beam dump experiment at Fermilab (E613).* eConf **C801002** (1980) 172–174.

[264] **LSND** Collaboration, ", Results from LSND on Neutrino Physicst," in *Proceedings, 34th Rencontres de Moriond on Electroweak Interactions and Unified Theories: Les Arcs, France, Mar 13-20, 1999*, pp. 41–52, The Gioi. The Gioi, Hanoi, 2001.

[265] F. Shimizu, Y. Kubota, H. Koiso, F. Sai, S. Sakamoto, and S. S. Yamamoto, *Measurement of the pp Cross-sections in the Momentum Range 0.9-2.0 GeV/c.* Nucl. Phys. **A386** (1982) 571–588.

[266] A. Achilli, R. M. Godbole, A. Grau, G. Pancheri, O. Shekhovtsova, and Y. N. Srivastava, *Total and inelastic cross-sections at LHC at sqrts* $= 7 - TeV$ *and beyond.* Phys. Rev. **D84** (2011) 094009, arXiv:1102.1949 [hep-ph].

[267] R. C. Allen, H. H. Chen, M. E. Potter, R. L. Burman, J. B. Donahue, D. A. Krakauer, R. L. Talaga, E. S. Smith, and A. C. Dodd, *A Measurement of the Neutrino Flux From a Stopped Pion Source.* Nucl. Instrum. Meth. **A284** (1989) 347.

[268] **COHERENT** Collaboration, D. Akimov *et al.*, *Sensitivity of the COHERENT Experiment to Accelerator-Produced Dark Matter*. arXiv:1911.06422 [hep-ex].

[269] **LSND** Collaboration, L. B. Auerbach *et al.*, *Measurement of electron - neutrino - electron elastic scattering*. Phys. Rev. **D63** (2001) 112001, arXiv:hep-ex/0101039 [hep-ex].

[270] **MiniBooNE** Collaboration, A. A. Aguilar-Arevalo *et al.*, *The MiniBooNE Detector*. Nucl. Instrum. Meth. **A599** (2009) 28–46, arXiv:0806.4201 [hep-ex].

[271] **MiniBooNE** Collaboration, A. A. Aguilar-Arevalo *et al.*, *Observation of a Significant Excess of Electron-Like Events in the MiniBooNE Short-Baseline Neutrino Experiment*. arXiv:1805.12028 [hep-ex].

[272] **MiniBooNE** Collaboration, R. Dharmapalan *et al.*, *Low Mass WIMP Searches with a Neutrino Experiment: A Proposal for Further MiniBooNE Running*. arXiv:1211.2258 [hep-ex].

[273] **DUNE** Collaboration, R. Acciarri *et al.*, *Long-Baseline Neutrino Facility (LBNF) and Deep Underground Neutrino Experiment (DUNE)*. arXiv:1512.06148 [physics.ins-det].

[274] **DUNE** Collaboration, B. Abi *et al.*, *The Single-Phase ProtoDUNE Technical Design Report*. arXiv:1706.07081 [physics.ins-det].

[275] **SHiP Collaboration** Collaboration, S. collaboration, *SHiP Experiment - Comprehensive Design Study report* Tech. Rep. CERN-SPSC-2019-049. SPSC-SR-263, CERN, Geneva, Dec, 2019. https://cds.cern.ch/record/2704147.

[276] K. Jodłowski, F. Kling, L. Roszkowski, and S. Trojanowski, *Extending the reach of FASER, MATHUSLA and SHiP towards smaller lifetimes using secondary production*. arXiv:1911.11346 [hep-ph].

[277] S. Mohanty and S. Rao, *Detecting Dipolar Dark Matter in Beam Dump Experiments*. arXiv:1506.06462 [hep-ph].

[278] **COHERENT** Collaboration, D. Akimov *et al.*, *Observation of Coherent Elastic Neutrino-Nucleus Scattering*. Science **357** (2017) no. 6356, 1123–1126, arXiv:1708.01294 [nucl-ex].

[279] S. Ajimura *et al.*, *Technical Design Report (TDR): Searching for a Sterile Neutrino at J-PARC MLF (E56, JSNS2)*. arXiv:1705.08629 [physics.ins-det].

[280] **NOvA** Collaboration, P. Adamson *et al.*, *Measurement of the neutrino mixing angle θ_{23} in NOvA*. Phys. Rev. Lett. **118** (2017) no. 15, 151802, arXiv:1701.05891 [hep-ex].

[281] **BEBC WA66** Collaboration, M. Talebzadeh *et al.*, *Search for ν_τ Interactions in the BEBC Beam Dump Experiment.* Nucl. Phys. **B291** (1987) 503–515.

[282] A. M. Cooper-Sarkar, S. Sarkar, J. Guy, W. Venus, P. O. Hulth, and K. Hultqvist, *Bound on the tau-neutrino magnetic moment from the BEBC beam dump experiment.* Phys. Lett. **B280** (1992) 153–158.

[283] S.-F. Ge and I. M. Shoemaker, *Constraining Photon Portal Dark Matter with Texono and Coherent Data.* JHEP **11** (2018) 066, arXiv:1710.10889 [hep-ph].

[284] J. R. Jordan, Y. Kahn, G. Krnjaic, M. Moschella, and J. Spitz, *Signatures of Pseudo-Dirac Dark Matter at High-Intensity Neutrino Experiments.* Phys. Rev. **D98** (2018) no. 7, 075020, arXiv:1806.05185 [hep-ph].

[285] L. Buonocore, P. deNiverville, and C. Frugiuele, *The hunt for sub-GeV dark matter at neutrino facilities: a survey of past and present experiments.* arXiv:1912.09346 [hep-ph].

[286] G. Marocco and S. Sarkar, *Blast from the past: Constraints on the dark sector from the BEBC WA66 beam dump experiment.* SciPost Phys. **10** (2021) 043, arXiv:2011.08153 [hep-ph].

[287] **NA62** Collaboration, E. Cortina Gil *et al.*, *Search for production of an invisible dark photon in π^0 decays.* JHEP **05** (2019) 182, arXiv:1903.08767 [hep-ex].

[288] J. L. Pinfold, *The MoEDAL Experiment at the LHC—A Progress Report.* Universe **5** (2019) no. 2, 47.

[289] A. Haas, C. S. Hill, E. Izaguirre, and I. Yavin, *Looking for milli-charged particles with a new experiment at the LHC.* Phys. Lett. **B746** (2015) 117–120, arXiv:1410.6816 [hep-ph].

[290] A. Ball *et al.*, *A Letter of Intent to Install a milli-charged Particle Detector at LHC P5.* arXiv:1607.04669 [physics.ins-det].

[291] S. Foroughi-Abari, F. Kling, and Y.-D. Tsai, *FORMOSA: Looking Forward to Millicharged Dark Sectors.* arXiv:2010.07941 [hep-ph].

[292] M. Sher and J. Stevens, *Detecting a heavy neutrino electric dipole moment at the LHC.* Phys. Lett. **B777** (2018) 246–249, arXiv:1710.06894 [hep-ph].

[293] M. Frank, M. de Montigny, P.-P. A. Ouimet, J. Pinfold, A. Shaa, and M. Staelens, *Searching for Heavy Neutrinos with the MoEDAL-MAPP Detector at the LHC.* arXiv:1909.05216 [hep-ph].

[294] K. Kadota and J. Silk, *Constraints on Light Magnetic Dipole Dark Matter from the ILC and SN 1987A*. Phys. Rev. **D89** (2014) no. 10, 103528, arXiv:1402.7295 [hep-ph].

[295] R. Primulando, E. Salvioni, and Y. Tsai, *The Dark Penguin Shines Light at Colliders*. JHEP **07** (2015) 031, arXiv:1503.04204 [hep-ph].

[296] A. Alves, A. C. O. Santos, and K. Sinha, *Collider Detection of Dark Matter Electromagnetic Anapole Moments*. Phys. Rev. **D97** (2018) no. 5, 055023, arXiv:1710.11290 [hep-ph].

[297] A. A. Prinz *et al.*, *Search for millicharged particles at SLAC*. Phys. Rev. Lett. **81** (1998) 1175–1178, arXiv:hep-ex/9804008 [hep-ex].

[298] G. Magill, R. Plestid, M. Pospelov, and Y.-D. Tsai, *Millicharged particles in neutrino experiments*. Phys. Rev. Lett. **122** (2019) no. 7, 071801, arXiv:1806.03310 [hep-ph].

[299] Z. Liu and Y. Zhang, *Probing millicharge at BESIII*. arXiv:1808.00983 [hep-ph].

[300] S. N. Gninenko, D. V. Kirpichnikov, and N. V. Krasnikov, *Probing millicharged particles with NA64 experiment at CERN*. Phys. Rev. **D100** (2019) no. 3, 035003, arXiv:1810.06856 [hep-ph].

[301] E. Golowich and R. W. Robinett, *Limits on Millicharged Matter From Beam Dump Experiments*. Phys. Rev. **D35** (1987) 391.

[302] **ArgoNeuT** Collaboration, R. Acciarri *et al.*, *Improved Limits on Millicharged Particles Using the ArgoNeuT Experiment at Fermilab*. arXiv:1911.07996 [hep-ex].

[303] J. Liang, Z. Liu, Y. Ma, and Y. Zhang, *Millicharged particles at electron colliders*. arXiv:1909.06847 [hep-ph].

[304] K. Akita and M. Yamaguchi, *A precision calculation of relic neutrino decoupling*. JCAP **08** (2020) 012, arXiv:2005.07047 [hep-ph].

[305] J. Froustey, C. Pitrou, and M. C. Volpe, *Neutrino decoupling including flavour oscillations and primordial nucleosynthesis*. JCAP **12** (2020) 015, arXiv:2008.01074 [hep-ph].

[306] G. Mangano and P. D. Serpico, *A robust upper limit on $N_{\rm eff}$ from BBN, circa 2011*. Physics Letters B **701** (July, 2011) 296–299, arXiv:1103.1261 [astro-ph.CO].

[307] J. F. Navarro, C. S. Frenk, and S. D. White, *The Structure of cold dark matter halos*. Astrophys. J. **462** (1996) 563–575, arXiv:astro-ph/9508025.

[308] Y. Cui, M. Pospelov, and J. Pradler, *Signatures of Dark Radiation in Neutrino and Dark Matter Detectors*. Phys. Rev. **D97** (2018) no. 10, 103004, arXiv:1711.04531 [hep-ph].

[309] **DES** Collaboration, A. Chen *et al.*, *Constraints on Decaying Dark Matter with DES-Y1 and external data*. arXiv:2011.04606 [astro-ph.CO].

[310] **Planck** Collaboration, N. Aghanim *et al.*, *Planck 2018 results. V. CMB power spectra and likelihoods*. Astron. Astrophys. **641** (2020) A5, arXiv:1907.12875 [astro-ph.CO].

[311] D. Scolnic *et al.*, *The Complete Light-curve Sample of Spectroscopically Confirmed SNe Ia from Pan-STARRS1 and Cosmological Constraints from the Combined Pantheon Sample*. Astrophys. J. **859** (2018) no. 2, 101, arXiv:1710.00845 [astro-ph.CO].

[312] F. Beutler, C. Blake, M. Colless, D. H. Jones, L. Staveley-Smith, G. B. Poole, L. Campbell, Q. Parker, W. Saunders, and F. Watson, *The 6dF Galaxy Survey: $z\approx 0$ measurements of the growth rate and σ_8*"Mon. Not. Roy. Astron. Soc." **423** (July, 2012) 3430–3444, arXiv:1204.4725 [astro-ph.CO].

[313] A. J. Ross, L. Samushia, C. Howlett, W. J. Percival, A. Burden, and M. Manera, *The clustering of the SDSS DR7 main Galaxy sample – I. A 4 per cent distance measure at $z = 0.15$*. Mon. Not. Roy. Astron. Soc. **449** (2015) no. 1, 835–847, arXiv:1409.3242 [astro-ph.CO].

[314] **BOSS** Collaboration, S. Alam *et al.*, *The clustering of galaxies in the completed SDSS-III Baryon Oscillation Spectroscopic Survey: cosmological analysis of the DR12 galaxy sample*. Mon. Not. Roy. Astron. Soc. **470** (2017) no. 3, 2617–2652, arXiv:1607.03155 [astro-ph.CO].

[315] K. Enqvist, S. Nadathur, T. Sekiguchi, and T. Takahashi, *Decaying dark matter and the tension in σ_8*. JCAP **09** (2015) 067, arXiv:1505.05511 [astro-ph.CO].

[316] V. Poulin, P. D. Serpico, and J. Lesgourgues, *A fresh look at linear cosmological constraints on a decaying dark matter component*. JCAP **1608** (2016) no. 08, 036, arXiv:1606.02073 [astro-ph.CO].

[317] A. Nygaard, T. Tram, and S. Hannestad, *Updated constraints on decaying cold dark matter*. arXiv:2011.01632 [astro-ph.CO].

[318] J. N. Bahcall and R. K. Ulrich, *Solar Models, Neutrino Experiments and Helioseismology*. Rev. Mod. Phys. **60** (1988) 297–372.

[319] J. N. Bahcall, E. Lisi, D. Alburger, L. De Braeckeleer, S. Freedman, and J. Napolitano, *Standard neutrino spectrum from B-8 decay*. Phys. Rev. C **54** (1996) 411–422, arXiv:nucl-th/9601044.

[320] J. N. Bahcall, *Gallium solar neutrino experiments: Absorption cross-sections, neutrino spectra, and predicted event rates*. Phys. Rev. C **56** (1997) 3391–3409, arXiv:hep-ph/9710491.

[321] **XENON** Collaboration, E. Aprile *et al.*, *Observation of Excess Electronic Recoil Events in XENON1T*. arXiv:2006.09721 [hep-ex].

[322] **XENON** Collaboration, E. Aprile *et al.*, *Light Dark Matter Search with Ionization Signals in XENON1T*. Phys. Rev. Lett. **123** (2019) no. 25, 251801, arXiv:1907.11485 [hep-ex].

[323] **Borexino** Collaboration, M. Agostini *et al.*, *Sensitivity to neutrinos from the solar CNO cycle in Borexino*. arXiv:2005.12829 [hep-ex].

[324] **BOREXINO** Collaboration, M. Agostini *et al.*, *First Direct Experimental Evidence of CNO neutrinos*. arXiv:2006.15115 [hep-ex].

[325] **Super-Kamiokande** Collaboration, K. Bays *et al.*, *Supernova Relic Neutrino Search at Super-Kamiokande*. Phys. Rev. **D85** (2012) 052007, arXiv:1111.5031 [hep-ex].

[326] **Super-Kamiokande** Collaboration, C. Kachulis *et al.*, *Search for Boosted Dark Matter Interacting With Electrons in Super-Kamiokande*. arXiv:1711.05278 [hep-ex].

[327] K. Abe *et al.*, *Letter of Intent: The Hyper-Kamiokande Experiment — Detector Design and Physics Potential —*. arXiv:1109.3262 [hep-ex].

[328] **Hyper-Kamiokande Working Group** Collaboration, ", Hyper-Kamiokande Physics Opportunitiest," in *Community Summer Study 2013: Snowmass on the Mississippi*. 9, 2013. arXiv:1309.0184 [hep-ex].

[329] L. Necib, J. Moon, T. Wongjirad, and J. M. Conrad, *Boosted Dark Matter at Neutrino Experiments*. Phys. Rev. **D95** (2017) 075018, arXiv:1610.03486 [hep-ph].

[330] M. Szydagis, C. Levy, G. Blockinger, A. Kamaha, N. Parveen, and G. Rischbieter, *Investigating the XENON1T Low-Energy Electronic Recoil Excess Using NEST*. arXiv:2007.00528 [hep-ex].

[331] H. An, M. Pospelov, J. Pradler, and A. Ritz, *New limits on dark photons from solar emission and keV scale dark matter*. arXiv:2006.13929 [hep-ph].

[332] **Borexino** Collaboration, G. Alimonti *et al.*, *The Borexino detector at the Laboratori Nazionali del Gran Sasso*. Nucl. Instrum. Meth. **A600** (2009) 568–593, arXiv:0806.2400 [physics.ins-det].

[333] A. L. Read, *Presentation of search results: The CL(s) technique*. J. Phys. G **28** (2002) 2693–2704.

[334] M. Pospelov and J. Pradler, *Elastic scattering signals of solar neutrinos with enhanced baryonic currents*. Phys.Rev. **D85** (2012) 113016, arXiv:1203.0545 [hep-ph].

[335] C. Cappiello and J. F. Beacom, *Strong New Limits on Light Dark Matter from Neutrino Experiments*. Phys. Rev. D **100** (2019) no. 10, 103011, arXiv:1906.11283 [hep-ph].

[336] K. Kadota, T. Sekiguchi, and H. Tashiro, *A new constraint on millicharged dark matter from galaxy clusters*. arXiv:1602.04009 [astro-ph.CO].

[337] A. Caputo, L. Sberna, M. Frias, D. Blas, P. Pani, L. Shao, and W. Yan, *Constraints on millicharged dark matter and axionlike particles from timing of radio waves*. Phys. Rev. D **100** (2019) no. 6, 063515, arXiv:1902.02695 [astro-ph.CO].

[338] **PandaX-II** Collaboration, X. Zhou *et al.*, *A search for solar axions and anomalous neutrino magnetic moment with the complete PandaX-II data*. arXiv:2008.06485 [hep-ex].

[339] C. Boehm, D. G. Cerdeno, M. Fairbairn, P. A. Machado, and A. C. Vincent, *Light new physics in XENON1T*. arXiv:2006.11250 [hep-ph].

[340] P. Jean, J. Knodlseder, W. Gillard, N. Guessoum, K. Ferriere, A. Marcowith, V. Lonjou, and J. P. Roques, *Spectral analysis of the galactic e+ e- annihilation emission*. Astron. Astrophys. **445** (2006) 579–589, arXiv:astro-ph/0509298.

[341] N. Prantzos *et al.*, *The 511 keV emission from positron annihilation in the Galaxy*. Rev. Mod. Phys. **83** (2011) 1001–1056, arXiv:1009.4620 [astro-ph.HE].

[342] T. Siegert, R. Diehl, G. Khachatryan, M. G. Krause, F. Guglielmetti, J. Greiner, A. W. Strong, and X. Zhang, *Gamma-ray spectroscopy of Positron Annihilation in the Milky Way*. Astron. Astrophys. **586** (2016) A84, arXiv:1512.00325 [astro-ph.HE].

[343] C. Boehm, T. Ensslin, and J. Silk, *Can Annihilating dark matter be lighter than a few GeVs?* J. Phys. G **30** (2004) 279–286, arXiv:astro-ph/0208458.

[344] J. F. Beacom, N. F. Bell, and G. Bertone, *Gamma-ray constraint on Galactic positron production by MeV dark matter*. Phys. Rev. Lett. **94** (2005) 171301, arXiv:astro-ph/0409403.

[345] Y. Rasera, R. Teyssier, P. Sizun, B. Cordier, J. Paul, M. Casse, and P. Fayet, *Soft gamma-ray background and light dark matter annihilation.* Phys. Rev. D **73** (2006) 103518, arXiv:astro-ph/0507707.

[346] F. H. Panther, R. M. Crocker, Y. Birnboim, I. R. Seitenzahl, and A. J. Ruiter, *Positron Annihilation in the Nuclear Outflows of the Milky Way.* Mon. Not. Roy. Astron. Soc. **474** (2018) no. 1, L17–L21, arXiv:1710.02613 [astro-ph.HE].

[347] C. Boehm and Y. Ascasibar, *More evidence in favour of light dark matter particles?* Phys. Rev. **D70** (2004) 115013, arXiv:hep-ph/0408213 [hep-ph].

[348] Y. Ascasibar, P. Jean, C. Boehm, and J. Knoedlseder, *Constraints on dark matter and the shape of the Milky Way dark halo from the 511-keV line.* Mon. Not. Roy. Astron. Soc. **368** (2006) 1695–1705, arXiv:astro-ph/0507142 [astro-ph].

[349] A. C. Vincent, P. Martin, and J. M. Cline, *Interacting dark matter contribution to the Galactic 511 keV gamma ray emission: constraining the morphology with INTEGRAL/SPI observations.* JCAP **04** (2012) 022, arXiv:1201.0997 [hep-ph].

[350] J. C. Higdon, R. E. Lingenfelter, and R. E. Rothschild, *The Galactic Positron Annihilation Radiation \& The Propagation of Positrons in the Interstellar Medium.* Astrophys. J. **698** (2009) 350–379, arXiv:0711.3008 [astro-ph].

[351] R. E. Lingenfelter, J. C. Higdon, and R. E. Rothschild, *Is There a Dark Matter Signal in the Galactic Positron Annihilation Radiation?* Phys. Rev. Lett. **103** (2009) 031301, arXiv:0904.1025 [astro-ph.HE].

[352] C. A. Kierans *et al.*, *Positron Annihilation in the Galaxy.* arXiv:1903.05569 [astro-ph.HE].

[353] C. Boehm and P. Uwer, *Revisiting Bremsstrahlung emission associated with Light Dark Matter annihilations.* arXiv:hep-ph/0606058.

[354] M. Boudaud, J. Lavalle, and P. Salati, *Novel cosmic-ray electron and positron constraints on MeV dark matter particles.* Phys. Rev. Lett. **119** (2017) no. 2, 021103, arXiv:1612.07698 [astro-ph.HE].

[355] J. F. Beacom and H. Yuksel, *Stringent constraint on galactic positron production.* Phys. Rev. Lett. **97** (2006) 071102, arXiv:astro-ph/0512411.

[356] P. Sizun, M. Casse, and S. Schanne, *Continuum gamma-ray emission from light dark matter positrons and electrons.* Phys. Rev. D **74** (2006) 063514, arXiv:astro-ph/0607374.

[357] M. Cirelli, N. Fornengo, B. J. Kavanagh, and E. Pinetti, *Integral X-ray constraints on sub-GeV Dark Matter*. arXiv:2007.11493 [hep-ph].

[358] R. Bartels, D. Gaggero, and C. Weniger, *Prospects for indirect dark matter searches with MeV photons*. JCAP **05** (2017) 001, arXiv:1703.02546 [astro-ph.HE].

[359] T. Blum, A. Denig, I. Logashenko, E. de Rafael, B. L. Roberts, T. Teubner, and G. Venanzoni, *The Muon (g-2) Theory Value: Present and Future*. arXiv:1311.2198 [hep-ph].

[360] T. Aoyama *et al.*, *The anomalous magnetic moment of the muon in the Standard Model*. Phys. Rept. **887** (2020) 1–166, arXiv:2006.04822 [hep-ph].

[361] E. W. Kolb and M. S. Turner, *The Early Universe*, vol. 69. 1990.

[362] C. Boehm and P. Fayet, *Scalar dark matter candidates*. Nucl. Phys. **B683** (2004) 219–263, arXiv:hep-ph/0305261 [hep-ph].

[363] P. Agrawal, S. Blanchet, Z. Chacko, and C. Kilic, *Flavored Dark Matter, and Its Implications for Direct Detection and Colliders*. Phys. Rev. D **86** (2012) 055002, arXiv:1109.3516 [hep-ph].

[364] D. Schmidt, T. Schwetz, and T. Toma, *Direct Detection of Leptophilic Dark Matter in a Model with Radiative Neutrino Masses*. Phys. Rev. D **85** (2012) 073009, arXiv:1201.0906 [hep-ph].

[365] Y. Zhang, *Top Quark Mediated Dark Matter*. Phys. Lett. B **720** (2013) 137–141, arXiv:1212.2730 [hep-ph].

[366] Y. Bai and J. Berger, *Fermion Portal Dark Matter*. JHEP **11** (2013) 171, arXiv:1308.0612 [hep-ph].

[367] Y. Bai and J. Berger, *Lepton Portal Dark Matter*. JHEP **08** (2014) 153, arXiv:1402.6696 [hep-ph].

[368] P. Agrawal, B. Batell, D. Hooper, and T. Lin, *Flavored Dark Matter and the Galactic Center Gamma-Ray Excess*. Phys. Rev. D **90** (2014) no. 6, 063512, arXiv:1404.1373 [hep-ph].

[369] J. Kile, A. Kobach, and A. Soni, *Lepton-Flavored Dark Matter*. Phys. Lett. B **744** (2015) 330–338, arXiv:1411.1407 [hep-ph].

[370] D. Egana-Ugrinovic, M. Low, and J. T. Ruderman, *Charged Fermions Below 100 GeV*. JHEP **05** (2018) 012, arXiv:1801.05432 [hep-ph].

[371] J. P. Leveille, *The Second Order Weak Correction to (G-2) of the Muon in Arbitrary Gauge Models*. Nucl. Phys. **B137** (1978) 63–76.

[372] T. Toma, *Internal Bremsstrahlung Signature of Real Scalar Dark Matter and Consistency with Thermal Relic Density*. Phys. Rev. Lett. **111** (2013) 091301, arXiv:1307.6181 [hep-ph].

[373] F. Giacchino, L. Lopez-Honorez, and M. H. Tytgat, *Scalar Dark Matter Models with Significant Internal Bremsstrahlung*. JCAP **10** (2013) 025, arXiv:1307.6480 [hep-ph].

[374] F. Giacchino, L. Lopez-Honorez, and M. H. Tytgat, *Bremsstrahlung and Gamma Ray Lines in 3 Scenarios of Dark Matter Annihilation*. JCAP **08** (2014) 046, arXiv:1405.6921 [hep-ph].

[375] C. Boehm, Y. Farzan, T. Hambye, S. Palomares-Ruiz, and S. Pascoli, *Is it possible to explain neutrino masses with scalar dark matter?* Phys. Rev. D **77** (2008) 043516, arXiv:hep-ph/0612228.

[376] R. J. Wilkinson, A. C. Vincent, C. Boehm, and C. McCabe, *Ruling out the light weakly interacting massive particle explanation of the Galactic 511 keV line*. Phys. Rev. D **94** (2016) no. 10, 103525, arXiv:1602.01114 [astro-ph.CO].

[377] P. Langacker, *The Physics of Heavy Z' Gauge Bosons*. Rev. Mod. Phys. **81** (2009) 1199–1228, arXiv:0801.1345 [hep-ph].

[378] P. J. Fox and E. Poppitz, *Leptophilic Dark Matter*. Phys. Rev. D **79** (2009) 083528, arXiv:0811.0399 [hep-ph].

[379] X.-J. Bi, X.-G. He, and Q. Yuan, *Parameters in a class of leptophilic models from PAMELA, ATIC and FERMI*. Phys. Lett. B **678** (2009) 168–173, arXiv:0903.0122 [hep-ph].

[380] N. F. Bell, Y. Cai, R. K. Leane, and A. D. Medina, *Leptophilic dark matter with Z' interactions*. Phys. Rev. D **90** (2014) no. 3, 035027, arXiv:1407.3001 [hep-ph].

[381] C. Boehm and J. Silk, *A New test of the light dark matter hypothesis*. Phys. Lett. **B661** (2008) 287–289, arXiv:0708.2768 [hep-ph].

[382] P. Agrawal, Z. Chacko, and C. B. Verhaaren, *Leptophilic Dark Matter and the Anomalous Magnetic Moment of the Muon*. JHEP **08** (2014) 147, arXiv:1402.7369 [hep-ph].

[383] S. Bilmis, I. Turan, T. Aliev, M. Deniz, L. Singh, and H. Wong, *Constraints on Dark Photon from Neutrino-Electron Scattering Experiments*. Phys. Rev. D **92** (2015) no. 3, 033009, arXiv:1502.07763 [hep-ph].

[384] M. Cadeddu, N. Cargioli, F. Dordei, C. Giunti, Y. Li, E. Picciau, and Y. Zhang, *Constraints on light vector mediators through coherent elastic neutrino nucleus scattering data from COHERENT*. arXiv:2008.05022 [hep-ph].

[385] M. Pospelov and A. Ritz, *Astrophysical Signatures of Secluded Dark Matter*. Phys. Lett. B **671** (2009) 391–397, arXiv:0810.1502 [hep-ph].

[386] M. Ibe, H. Murayama, and T. Yanagida, *Breit-Wigner Enhancement of Dark Matter Annihilation*. Phys. Rev. D **79** (2009) 095009, arXiv:0812.0072 [hep-ph].

[387] J. M. Cline, H. Liu, T. Slatyer, and W. Xue, *Enabling Forbidden Dark Matter*. Phys. Rev. D **96** (2017) no. 8, 083521, arXiv:1702.07716 [hep-ph].

[388] R. H. Parker, C. Yu, W. Zhong, B. Estey, and H. Müller, *Measurement of the fine-structure constant as a test of the Standard Model*. Science **360** (2018) 191, arXiv:1812.04130 [physics.atom-ph].

[389] L. Morel, Z. Yao, P. Cladé, and S. Guellati-Khélifa, *Determination of the fine-structure constant with an accuracy of 81 parts per trillion*. Nature **588** (2020) no. 7836, 61–65.

[390] **BaBar** Collaboration, B. Aubert *et al.*, *The BaBar detector*. Nucl. Instrum. Meth. **A479** (2002) 1–116, arXiv:hep-ex/0105044 [hep-ex].

[391] **NA64** Collaboration, D. Banerjee *et al.*, *Search for vector mediator of Dark Matter production in invisible decay mode*. arXiv:1710.00971 [hep-ex].

[392] **NA64 Collaboration** Collaboration, S. Gninenko, *NA64 Status Report 2020* Tech. Rep. CERN-SPSC-2020-017. SPSC-SR-273, CERN, Geneva, Jun, 2020. http://cds.cern.ch/record/2719646.

[393] A. A. Prinz, *The Search for millicharged particles at SLAC*. PhD thesis, Stanford U., Phys. Dept., 2001. http://wwwlib.umi.com/dissertations/fullcit?p3002033.

[394] A. Abashian *et al.*, *The Belle Detector*. Nucl. Instrum. Meth. **A479** (2002) 117–232.

[395] **Belle-II** Collaboration, T. Abe *et al.*, *Belle II Technical Design Report*. arXiv:1011.0352 [physics.ins-det].

[396] **LDMX** Collaboration, J. Mans, *The LDMX Experiment*. EPJ Web Conf. **142** (2017) 01020.

[397] **BDX** Collaboration, M. Battaglieri *et al.*, *Dark matter search in a Beam-Dump eXperiment (BDX) at Jefferson Lab: an update on PR12-16-001*. arXiv:1712.01518 [physics.ins-det].

[398] O. Nicrosini and L. Trentadue, *Transverse Degrees of Freedom in {QED} Evolution.* Phys. Lett. B **231** (1989) 487–491.

[399] G. Montagna, O. Nicrosini, F. Piccinini, and L. Trentadue, *Invisible events with radiative photons at LEP.* Nucl. Phys. B **452** (1995) 161–172, arXiv:hep-ph/9506258.

[400] R. Essig, J. Mardon, M. Papucci, T. Volansky, and Y.-M. Zhong, *Constraining Light Dark Matter with Low-Energy e^+e^- Colliders.* JHEP **11** (2013) 167, arXiv:1309.5084 [hep-ph].

[401] **BDX** Collaboration, M. Battaglieri *et al.*, *Dark Matter Search in a Beam-Dump EXperiment (BDX) at Jefferson Lab – 2018 Update to PR12-16-001.* arXiv:1910.03532 [physics.ins-det].

[402] **L3** Collaboration, P. Achard *et al.*, *Single photon and multiphoton events with missing energy in e^+e^- collisions at LEP.* Phys. Lett. B **587** (2004) 16–32, arXiv:hep-ex/0402002.

[403] F. Rossi-Torres and C. Moura, *Scalar dark matter in light of LEP and proposed ILC experiments.* Phys. Rev. D **92** (2015) no. 11, 115022, arXiv:1503.06475 [hep-ph].

[404] P. J. Fox, R. Harnik, J. Kopp, and Y. Tsai, *LEP Shines Light on Dark Matter.* Phys. Rev. D **84** (2011) 014028, arXiv:1103.0240 [hep-ph].

[405] K. Cheung, P.-Y. Tseng, Y.-L. S. Tsai, and T.-C. Yuan, *Global Constraints on Effective Dark Matter Interactions: Relic Density, Direct Detection, Indirect Detection, and Collider.* JCAP **05** (2012) 001, arXiv:1201.3402 [hep-ph].

[406] P. Ilten, Y. Soreq, M. Williams, and W. Xue, *Serendipity in dark photon searches.* JHEP **06** (2018) 004, arXiv:1801.04847 [hep-ph].

[407] A. Freitas and S. Westhoff, *Leptophilic Dark Matter in Lepton Interactions at LEP and ILC.* JHEP **10** (2014) 116, arXiv:1408.1959 [hep-ph].

[408] A. Freitas, J. Lykken, S. Kell, and S. Westhoff, *Testing the Muon g-2 Anomaly at the LHC.* JHEP **05** (2014) 145, arXiv:1402.7065 [hep-ph]. [Erratum: JHEP 09, 155 (2014)].

[409] F. del Aguila, M. Chala, J. Santiago, and Y. Yamamoto, *Collider limits on leptophilic interactions.* JHEP **03** (2015) 059, arXiv:1411.7394 [hep-ph].

[410] N. Chen, J. Wang, and X.-P. Wang, *The leptophilic dark matter with Z' interaction: from indirect searches to future e^+e^- collider searches.* arXiv:1501.04486 [hep-ph].

[411] H. Davoudiasl, H.-S. Lee, and W. J. Marciano, *'Dark' Z implications for Parity Violation, Rare Meson Decays, and Higgs Physics*. Phys. Rev. D **85** (2012) 115019, arXiv:1203.2947 [hep-ph].

[412] F. D'Eramo, B. J. Kavanagh, and P. Panci, *Probing Leptophilic Dark Sectors with Hadronic Processes*. Phys. Lett. B **771** (2017) 339–348, arXiv:1702.00016 [hep-ph].

[413] D. Hanneke, S. Fogwell, and G. Gabrielse, *New Measurement of the Electron Magnetic Moment and the Fine Structure Constant*. Phys. Rev. Lett. **100** (2008) 120801, arXiv:0801.1134 [physics.atom-ph].

[414] C. S. Wu, E. Ambler, R. W. Hayward, D. D. Hoppes, and R. P. Hudson, *Experimental Test of Parity Conservation in β Decay*. Phys. Rev. **105** (1957) 1413–1414.

[415] J. H. Christenson, J. W. Cronin, V. L. Fitch, and R. Turlay, *Evidence for the 2π Decay of the K_2^0 Meson*. Phys. Rev. Lett. **13** (1964) 138–140.

[416] A. Czarnecki and W. J. Marciano, *Polarized Moller scattering asymmetries*. Int. J. Mod. Phys. A **15** (2000) 2365–2376, arXiv:hep-ph/0003049.

[417] **SLAC E158** Collaboration, P. Anthony *et al.*, *Precision measurement of the weak mixing angle in Moller scattering*. Phys. Rev. Lett. **95** (2005) 081601, arXiv:hep-ex/0504049.

[418] Y. Kuno and Y. Okada, *Muon decay and physics beyond the standard model*. Rev. Mod. Phys. **73** (2001) 151–202, arXiv:hep-ph/9909265.

[419] **MEG** Collaboration, A. Baldini *et al.*, *Search for the lepton flavour violating decay $\mu^+ \to e^+\gamma$ with the full dataset of the MEG experiment*. Eur. Phys. J. C **76** (2016) no. 8, 434, arXiv:1605.05081 [hep-ex].

[420] C. Boehm, M. J. Dolan, and C. McCabe, *A Lower Bound on the Mass of Cold Thermal Dark Matter from Planck*. JCAP **08** (2013) 041, arXiv:1303.6270 [hep-ph].

[421] J. H. Heo and C. Kim, *Light Dark Matter and Dark Radiation*. J. Korean Phys. Soc. **68** (2016) no. 5, 715–721, arXiv:1504.00773 [astro-ph.HE].

[422] N. Fornengo, C. Kim, and J. Song, *Finite temperature effects on the neutrino decoupling in the early universe*. Phys. Rev. D **56** (1997) 5123–5134, arXiv:hep-ph/9702324.

[423] M. Escudero, *Neutrino decoupling beyond the Standard Model: CMB constraints on the Dark Matter mass with a fast and precise $N_{\rm eff}$ evaluation*. JCAP **02** (2019) 007, arXiv:1812.05605 [hep-ph].

[424] P. F. Depta, M. Hufnagel, K. Schmidt-Hoberg, and S. Wild, *BBN constraints on the annihilation of MeV-scale dark matter*. JCAP **04** (2019) 029, arXiv:1901.06944 [hep-ph].

[425] N. Sabti, J. Alvey, M. Escudero, M. Fairbairn, and D. Blas, *Refined Bounds on MeV-scale Thermal Dark Sectors from BBN and the CMB*. JCAP **01** (2020) 004, arXiv:1910.01649 [hep-ph].

[426] K. N. Abazajian and J. Heeck, *Observing Dirac neutrinos in the cosmic microwave background*. Phys. Rev. D **100** (2019) 075027, arXiv:1908.03286 [hep-ph].

[427] **SENSEI** Collaboration, L. Barak *et al.*, *SENSEI: Direct-Detection Results on sub-GeV Dark Matter from a New Skipper-CCD*. arXiv:2004.11378 [astro-ph.CO].

[428] R. Essig, A. Manalaysay, J. Mardon, P. Sorensen, and T. Volansky, *First Direct Detection Limits on sub-GeV Dark Matter from XENON10*. Phys. Rev. Lett. **109** (2012) 021301, arXiv:1206.2644 [astro-ph.CO].

[429] R. Essig, T. Volansky, and T.-T. Yu, *New Constraints and Prospects for sub-GeV Dark Matter Scattering off Electrons in Xenon*. Phys. Rev. D **96** (2017) no. 4, 043017, arXiv:1703.00910 [hep-ph].

[430] M. Hufnagel, K. Schmidt-Hoberg, and S. Wild, *BBN constraints on MeV-scale dark sectors. Part I. Sterile decays*. JCAP **02** (2018) 044, arXiv:1712.03972 [hep-ph].

[431] H. Liu, T. R. Slatyer, and J. Zavala, *Contributions to cosmic reionization from dark matter annihilation and decay*. Phys. Rev. D **94** (2016) no. 6, 063507, arXiv:1604.02457 [astro-ph.CO].

[432] E. C. Stone, A. C. Cummings, F. B. McDonald, B. C. Heikkila, N. Lal, and W. R. Webber, *Voyager 1 Observes Low-Energy Galactic Cosmic Rays in a Region Depleted of Heliospheric Ions*. Science **341** (2013) no. 6142, 150–153, https://science.sciencemag.org/content/341/6142/150.full.pdf. https://science.sciencemag.org/content/341/6142/150.

[433] M. Boudaud, T. Lacroix, M. Stref, and J. Lavalle, *Robust cosmic-ray constraints on p-wave annihilating MeV dark matter*. Phys. Rev. D **99** (2019) no. 6, 061302, arXiv:1810.01680 [astro-ph.HE].

[434] **e-ASTROGAM** Collaboration, A. De Angelis *et al.*, *The e-ASTROGAM mission*. Exper. Astron. **44** (2017) no. 1, 25–82, arXiv:1611.02232 [astro-ph.HE].

[435] **AMEGO** Collaboration, R. Caputo *et al.*, *All-sky Medium Energy Gamma-ray Observatory: Exploring the Extreme Multimessenger Universe*. arXiv:1907.07558 [astro-ph.IM].

[436] C. Boehm, P. Fayet, and R. Schaeffer, *Constraining dark matter candidates from structure formation*. Phys. Lett. B **518** (2001) 8–14, arXiv:astro-ph/0012504.

[437] C. Boehm and R. Schaeffer, *Constraints on dark matter interactions from structure formation: Damping lengths*. Astron. Astrophys. **438** (2005) 419–442, arXiv:astro-ph/0410591.

[438] R. J. Wilkinson, C. Boehm, and J. Lesgourgues, *Constraining Dark Matter-Neutrino Interactions using the CMB and Large-Scale Structure*. JCAP **05** (2014) 011, arXiv:1401.7597 [astro-ph.CO].

[439] A. Arhrib, C. Bœ hm, E. Ma, and T.-C. Yuan, *Radiative Model of Neutrino Mass with Neutrino Interacting MeV Dark Matter*. JCAP **04** (2016) 049, arXiv:1512.08796 [hep-ph].

[440] X. Chu, C. Garcia-Cely, and T. Hambye, *Can the relic density of self-interacting dark matter be due to annihilations into Standard Model particles?* JHEP **11** (2016) 048, arXiv:1609.00399 [hep-ph].

[441] S. W. Randall, M. Markevitch, D. Clowe, A. H. Gonzalez, and M. Bradac, *Constraints on the Self-Interaction Cross-Section of Dark Matter from Numerical Simulations of the Merging Galaxy Cluster 1E 0657-56*. Astrophys. J. **679** (2008) 1173–1180, arXiv:0704.0261 [astro-ph].

[442] D. Harvey, R. Massey, T. Kitching, A. Taylor, and E. Tittley, *The non-gravitational interactions of dark matter in colliding galaxy clusters*. Science **347** (2015) 1462–1465, arXiv:1503.07675 [astro-ph.CO].

[443] A. Robertson, R. Massey, and V. Eke, *What does the Bullet Cluster tell us about self-interacting dark matter?* Mon. Not. Roy. Astron. Soc. **465** (2017) no. 1, 569–587, arXiv:1605.04307 [astro-ph.CO].

[444] D. Harvey, A. Robertson, R. Massey, and I. G. McCarthy, *Observable tests of self-interacting dark matter in galaxy clusters: BCG wobbles in a constant density core*. Mon. Not. Roy. Astron. Soc. **488** (2019) no. 2, 1572–1579, arXiv:1812.06981 [astro-ph.CO].

[445] K. Bondarenko, A. Boyarsky, T. Bringmann, and A. Sokolenko, *Constraining self-interacting dark matter with scaling laws of observed halo surface densities*. JCAP **1804** (2018) no. 04, 049, arXiv:1712.06602 [astro-ph.CO].

[446] D. Page, M. V. Beznogov, I. Garibay, J. M. Lattimer, M. Prakash, and H.-T. Janka, *NS 1987A in SN 1987A*. Astrophys. J. **898** (2020) no. 2, 125, arXiv:2004.06078 [astro-ph.HE].

[447] P. Fayet, D. Hooper, and G. Sigl, *Constraints on light dark matter from core-collapse supernovae*. Phys. Rev. Lett. **96** (2006) 211302, arXiv:hep-ph/0602169.

[448] A. Guha, P. B. Dev, and P. K. Das, *Model-independent Astrophysical Constraints on Leptophilic Dark Matter in the Framework of Tsallis Statistics*. JCAP **02** (2019) 032, arXiv:1810.00399 [hep-ph].

[449] E. Byckling and K. Kajantie, *Particle Kinematics: (Chapters I-VI, X)*. University of Jyvaskyla, Jyvaskyla, Finland, 1971.

[450] E. Braaten and D. Segel, *Neutrino energy loss from the plasma process at all temperatures and densities*. Phys. Rev. **D48** (1993) 1478–1491, arXiv:hep-ph/9302213 [hep-ph].

[451] S. J. Hardy, *The effective electron mass in core-collapse supernovae*. Astron. Astrophys. **342** (1999) 614–621, arXiv:astro-ph/9811466 [astro-ph].

[452] J. F. Donoghue and B. R. Holstein, *Renormalization and Radiative Corrections at Finite Temperature*. Phys. Rev. **D28** (1983) 340. [Erratum: Phys. Rev.D29,3004(1984)].

[453] A. Lenard, *Inner Bremsstrahlung in μ-Meson Decay*Phys. Rev. **90** (Jun, 1953) 968–973. https://link.aps.org/doi/10.1103/PhysRev.90.968.

[454] V. Berestetskii, E. Lifshitz, and L. Pitaevskii, *Quantum Electrodynamics*. Course of theoretical physics. Butterworth-Heinemann, 1982.

[455] ", Radiative corrections for Dalitz decays of π^0, $\eta^{(\prime)}$ and Σ^0t," in *22nd High-Energy Physics International Conference in Quantum Chromodynamics (QCD 19) Montpellier, Languedoc, France, July 2-5, 2019*. 2019. arXiv:1911.06820 [hep-ph].

[456] R. Barbieri and E. Remiddi, *Electron and Muon 1/2(g-2) from Vacuum Polarization Insertions*. Nucl. Phys. B **90** (1975) 233–266.

[457] A. Hamze, C. Kilic, J. Koeller, C. Trendafilova, and J.-H. Yu, *Lepton-Flavored Asymmetric Dark Matter and Interference in Direct Detection*. Phys. Rev. D **91** (2015) no. 3, 035009, arXiv:1410.3030 [hep-ph].

[458] G. Passarino and M. Veltman, *One Loop Corrections for e+ e- Annihilation Into mu+ mu- in the Weinberg Model*. Nucl. Phys. B **160** (1979) 151–207.

[459] G. 't Hooft and M. Veltman, *Scalar One Loop Integrals*. Nucl. Phys. B **153** (1979) 365–401.

[460] T. Hahn, *Automatic loop calculations with FeynArts, FormCalc, and LoopTools*. Nucl. Phys. B Proc. Suppl. **89** (2000) 231–236, arXiv:hep-ph/0005029.